

AN ABSTRACT OF THE DISSERTATION OF

Joseph N. Tang for the degree of Doctor of Philosophy in Chemistry presented on November 8, 2018.

Title: Exploratory Studies Within the Exotic Lyonsite Structure

Abstract approved: _____

Munirpallam A. Subramanian

Structure-property relationships have always underpinned the field of solid state chemistry; dependable structural descriptions are integral to understanding and controlling the physical properties of inorganic compounds old and new. While a handful of crystal structures are celebrated for their versatility, flexibility, and functionality, the existence of more exotic structures is often ignored. Without methodical study, potential solutions to contemporary material challenges may repeatedly escape notice. The lyonsite structure is one such under-studied system. Existing research has shown that some lyonsites exhibit behaviors that may be favorable for usage as inexpensive photocatalysts, wavelength-selective optical filters, or microwave dielectrics. This dissertation therefore systematically investigates the structural flexibility and physical properties of a series of lyonsite oxides.

Incorporation of Co^{2+} into the $\text{Zn}_{2.5-x}\text{Co}_x\text{VMoO}_8$ system was successful and the subsequent effect on the Zn site preference was explored. All samples were annealed

between 700 and 1000 °C, resulting in green-colored pastilles. Powder X-ray diffraction (PXRD) and neutron powder diffraction (NPD) confirmed the solid solution range to be $0 \leq x \leq 2.5$, with all members isostructural with the parent compound. Magnetic susceptibility measurements indicated Curie-Weiss behavior in the high T region, confirming the presence of Co^{2+} . Diffuse reflectance measurements are also presented to explain the color mechanisms of this series.

Next, a comparative investigation was carried out within the $\text{Zn}_{2.5-x}\text{A}_x\text{VMoO}_8$ ($\text{A}^{2+} = \text{Mn}, \text{Ni}, \text{Cu}$) system. Samples were prepared between 700 and 1000 °C, resulting in various colors. All three solid solutions were found to exhibit a miscibility gap before or at the midpoint, beyond which phase separation occurs. X-ray and neutron powder diffraction were used to elucidate the cause of these solubility limits and diffuse reflectance measurements reveal varying color mechanisms. All phase pure members of the solid solutions are found to be similar to the parent compound, and magnetic susceptibility measurements confirmed the +2 oxidation state for all substitutions, with tendency towards antiferromagnetic exchange as x increases.

Finally, the demonstrated cationic flexibility of this structure was exploited in an investigation of the vacancy tolerance in the A site. In the parent compound $\text{Co}_{3.75}\text{V}_{1.5}\text{Mo}_{1.5}\text{O}_{12}$, it is apparent that a stoichiometric vacancy of 0.25 is unavoidable, as a result of both coulombic repulsion and simple charge balance. This work focuses on the systematic elimination of said vacancies by introducing increasing Li content, with varying V content for charge balance. A full solid solution was found to exist with the formula $\square_{0.25-\frac{1}{8}x}\text{Li}_x\text{Co}_{3.75-\frac{7}{8}x}\text{V}_{1.5-\frac{3}{4}x}\text{Mo}_{1.5+\frac{3}{4}x}\text{O}_{12}$ ($0 \leq x \leq 2$), terminating at the known end member $\text{Li}_2\text{Co}_2\text{Mo}_3\text{O}_{12}$. Samples were synthesized using high temperature

solid state reaction methods in air under ambient pressure. Lattice refinements on PXRD data confirmed the isostructural nature of the whole series. Structure-property relationships were also explored via magnetic susceptibility, optical, and dielectric measurements.

©Copyright by Joseph N. Tang
November 8, 2018
All Rights Reserved

Exploratory Studies Within the Exotic Lyonsite Structure

by

Joseph N. Tang

A DISSERTATION

submitted to

Oregon State University

in partial fulfillment of
the requirements for the
degree of

Doctor of Philosophy

Presented November 8, 2018

Commencement June 2019

Doctor of Philosophy dissertation of Joseph N. Tang presented on November 8, 2018.

APPROVED:

Major Professor, representing Chemistry

Head of the Department of Chemistry

Dean of the Graduate School

I understand that my dissertation will become part of the permanent collection of Oregon State University libraries. My signature below authorizes release of my dissertation to any reader upon request.

Joseph N. Tang, Author

ACKNOWLEDGEMENTS

First, I would like to acknowledge and thank Dr. Mas Subramanian, for the guidance and support that he has shown me over the course of my graduate career. Even though I came from a different academic background, his unwavering patience has allowed me to develop and improve my skills as a solid state chemist. He has provided many professional development opportunities, including conferences, internships, and employment prospects. The standard I am held to in Dr. Subramanian's lab have shaped me as a researcher and I will continue to uphold that standard in my future scientific endeavors.

I would like to thank Drs. Michael Lerner, Paul Cheong, Greg Herman, and William Warnes for their time and commitment as my committee members. I would like to acknowledge Dr. Ngọc Nguyễn, who patiently guided me through my internship. During our meetings, I learned an invaluable amount of information, and his insightful perspectives on solid state sciences have helped me become a more rounded scientist.

I am grateful to all the past and present members of the Subramanian group who I've had the pleasure of working with. Though the membership has changed over the years, there was always a sense of camaraderie. Many thanks to the "Masketeers": Drs. Geneva Laurita, Rosa Grajczyk, and Whitney Schmidt for sharing their expertise when I was new and getting my research wheels running. I would like to especially thank Dr. Joshua Flynn for his patience when teaching me and answering my "stupid" questions; I would not be half the researcher I am today without his help. I would also like to express my gratitude to Dr. Jun Li, who has been an invaluable resource and

mentor in research, as well as a source of wisdom during our various life discussions. I thank my labmates Dr. Elena Medina, Sarah Synnestvedt, Maxwell Wallace, Elizabeth Sobalvarro, and Brett Duell for creating a fun work environment and helping me solidify my understanding of chemistry through numerous research discussions. I thank my undergraduate mentees Andrea Domen, Dillon Crook, Blake Day, and Jesse La Jeunesse for supporting me through my research and the struggles that accompanied them.

During my time at Oregon State University, I have enjoyed the company of departmental friends who have commiserated with me about graduate student life: Drs. Wesley Surta, Hanyang Zhang, Nicholas Larkey, Ryan McQuade, Maduka Ogba, Zhifei Li, and Clement Bommier.

I am very grateful to Dr. Richard Nafshun, Margie Haak, and Dr. James Krueger, for providing me with numerous teaching-related opportunities across all levels of chemistry, and inspiring me to continually make effective science education a priority in my life.

I want to express my sincerest gratitude to my prior chemistry professors: Dr. Henry Altmiller, who encouraged me to embark on graduate school at Oregon State University and endlessly inspired me with his life lessons, and Drs. Donald Wharry, Mary Kopecki, and J.D. Lewis, for sparking my interest in chemistry. I would certainly not be a chemist without their inspiration.

I would like to thank my friends for being a solid support system and for keeping me grounded throughout this journey: Mai-Anh Vãn-Đình, Kevin Hinh, Elizabeth Kaweesa, and Staci and Alex Ebadirad. In addition, I thank my siblings Timothy

Nguyễn and Justin Nguyễn for motivating me to be the best role model I can be for them. I thank my uncle Thành Tăng for introducing me to science at an early age, and my parents for pushing me to fulfill my potential in anything I attempt. Lastly but certainly not least, I thank my husband, Bin Zhang. Your kindness, selflessness, and unconditional love and support inspires me and pushes me to be the best version of myself.

CONTRIBUTION OF AUTHORS

Chapter 3: Dr. Jun Li contributed in the review of the manuscript on which this chapter is primarily based; J. N. Tang, J. Li, M. A. Subramanian, Structural investigation and selected properties of $\text{Zn}_{2.5-x}\text{Co}_x\text{VMoO}_8$ lyonsites, *J. Solid State Chem.* 266 (2018) 155–160. Dr. Jun Li also contributed to discussions of structural analysis for the neutron diffraction experiments.

Chapter 5: Dillon Crook assisted in sample synthesis and preparation for property measurements for the manuscript on which this chapter is primarily based; J. N. Tang, D. M. Crook, M. A. Subramanian, Vacancy tuning in Li,V-substituted lyonsites, (*In Progress*).

Appendix A: Maxwell Wallace performed electrical resistivity measurements and contributed in the preparation and review of the manuscript on which this chapter is primarily based; J. N. Tang, S. Svadlenak, M. K. Wallace, M. A. Subramanian, Structure-property relationships and charge distribution in $\text{LiMn}_{2-x}\text{Rh}_x\text{O}_4$ spinels, (*In Progress*). Paradronektrakoontara synthesized samples and assisted in preparation for property measurements. Scott Svadlenak performed preliminary structural analysis for the neutron diffraction experiments.

Appendix C: Maxwell Wallace contributed in converting the completed Python script to a Windows executable.

TABLE OF CONTENTS

	<u>Page</u>
1 General Overview and Introduction to Lyonsite Type Oxides	1
1.1 Introduction to Transition Metal Oxides	1
1.1.1 Classifications	1
1.1.2 Orbital Splitting	9
1.2 A Survey of Framework Structures	11
1.2.1 Ionic Conductivity	12
1.2.2 Photocatalysis	14
1.2.3 Nonlinear Optics (NLO)	17
1.2.4 Luminescence	19
1.2.5 Transparent Conducting Oxides (TCO)	20
1.2.6 Photovoltaics (PV)	21
1.3 The Lyonsite Structure	22
1.3.1 Structural Description	23
1.3.2 Molybdates	27
1.3.3 Vanadates	27
1.3.4 Vanadomolybdates	28
1.3.5 Tungstates/Vanadotungstates	30
1.3.6 Physical Properties	30
1.4 Other Structure Types in this Dissertation	32
1.4.1 The Spinel Structure	32
References	33
2 Synthesis and Characterization Methods	43
2.1 Preparation of Bulk Oxides	43
2.1.1 Ceramic Method	43
2.1.2 Citrate Gel Method	45
2.2 Structural Characterization	46
2.2.1 Scattering Techniques	46
2.2.2 X-ray Diffraction	48
2.2.3 Neutron Diffraction	51
2.2.4 Diffraction Instrumentation	52
2.2.5 Structure Modeling	53
2.3 Physical Property Characterization	56
2.3.1 Magnetic Properties	56
2.3.2 Optical Properties	64

TABLE OF CONTENTS (Continued)

	<u>Page</u>
2.3.3 Dielectric Properties	69
2.3.4 Photocatalytic Activity	73
References	77
3 Structural investigation and selected properties of $Zn_{2.5-x}Co_xVMoO_8$ lyonsites	80
3.1 Abstract	80
3.2 Introduction/Motivation	82
3.3 Experimental	84
3.4 Results/Discussion	85
3.4.1 Crystal Structure	85
3.4.2 Magnetic Properties	98
3.4.3 Optical Properties	101
3.5 Conclusions	103
3.6 Supporting Information	104
References	108
4 Novel compositions and physical property comparisons for $(A, A')_{2.5}VMoO_8$ lyonsites ($A = Zn, A' = Mn, Ni, Cu$)	111
4.1 Abstract	111
4.2 Introduction/Motivation	113
4.3 Experimental	115
4.4 Results/Discussion	116
4.4.1 Crystal Structure	116
4.4.2 Magnetic Properties	127
4.4.3 Optical Properties	130
4.5 Conclusions	135
4.6 Supporting Information	135
References	138
5 Vacancy Tuning in Li,V-Substituted Lyonsites	143
5.1 Abstract	143

TABLE OF CONTENTS (Continued)

	<u>Page</u>
5.2 Introduction/Motivation	145
5.3 Experimental	148
5.4 Results/Discussion	149
5.4.1 Crystal Structure	149
5.4.2 Magnetic Properties	153
5.4.3 Optical Properties	155
5.4.4 Dielectric Properties	162
5.5 Conclusions	164
References	165
General Conclusions and Future Work	169
Bibliography	172
Appendices	185
A Structure-Property Relationships and Charge Distribution in $\text{LiMn}_{2-x}\text{Rh}_x\text{O}_4$ Spinels	186
B Alternate Synthesis and Photocatalytic Activity for Select Lyonsite-Type Oxides	200
C A Rudimentary Standalone Dielectric Density Calculator	214

LIST OF FIGURES

<u>Figure</u>	<u>Page</u>
1.1 A unit cell representing a layered honeycomb ordered structure ($\text{Li}_3\text{Zn}_2\text{SbO}_6$, $C2/m$). Li = green, ZnO_6 octahedra = gray, SbO_6 octahedra = orange, O = red.	3
1.2 A unit cell representing a typical perovskite (SrTiO_3 , $Pm\bar{3}m$). Sr = green, Ti = blue, O = red.	4
1.3 Representative unit cells of TBP-containing structure types: $\text{YIn}_{1-x}\text{Mn}_x\text{O}_3$ (left), andalusite (middle), and hibonite (right). In $\text{YIn}_{1-x}\text{Mn}_x\text{O}_3$: Y = gray, $(\text{In}, \text{Mn})\text{O}_5$ TBP = blue, O = red. In andalusite (Al_2SiO_5 , $Pnmm$): AlO_5 TBP = green, AlO_6 octahedra = gray, SiO_4 tetrahedra = blue. In hibonite ($\text{CaAl}_{12}\text{O}_{19}$, $P6_3/mmc$): Ca = gray, AlO_5 TBP = purple, AlO_6 octahedra = pink/cyan/yellow, and AlO_4 tetrahedra = green.	4
1.4 Generic representation of the trigonal prismatic site formed in ABBA... stacking. Trigonal prismatic site = yellow, octahedra = blue, O = red.	5
1.5 Comparison between the fluorite (left) and pyrochlore (right) structures. Cation polyhedra = blue and yellow, O = red, F = pale blue.	6
1.6 Comparison between rutile (left), hollandite (middle), and todorokite (right) structures. Cation polyhedra = gray, O = red.	7
1.7 Representation of a skutterudite (left) and a β -gallia rutile (BGR) intergrowth structure (right). In the skutterudite: In = gray, Co-centered octahedra = blue, Sb = brown. In the BGR: K = purple, gallia blocks = green, rutile blocks = gray.	8
1.8 A unit cell representing the A_2X' network of the pyrochlore. A = gray, O = red, $X'A_4$ tetrahedron = red, distorted AXX' cube = purple.	9
1.9 Crystal field splitting diagrams for ideal octahedral (left) and trigonal prism (right) environments in a hypothetical d^7 spin state.	11
1.10 The β -gallia structure, with unit cell outline shown in dashed lines. Ga-centered polyhedra = green, O = red.	13
1.11 The NASICON structure, as viewed along the c axis, with unit cell outline shown in dotted lines. Na = white, ZrO_6 octahedra = green, SiO_4 tetrahedra = blue.	14

LIST OF FIGURES (Continued)

Figure	Page
1.12 The BaTi_4O_9 structure, with tunnels viewable along the b axis. Ba = green, TiO_6 octahedra = blue.	15
1.13 Examples of tunneled β -gallia rutile intergrowth titanates, with unit cell outlines shown in dashed lines. $\text{Na}_{0.7}\text{Ga}_{4.7}\text{Ti}_{0.3}\text{O}_8$ (top), $\text{Na}_{0.8}\text{Ga}_{4.8}\text{Ti}_{1.2}\text{O}_{10}$ (middle), $\text{Na}_{0.8}\text{Ga}_{4.8}\text{Ti}_{2.2}\text{O}_{12}$ (bottom). Na = purple, β -gallia blocks = green, rutile blocks = gray.	16
1.14 The LiB_3O_5 structure, with unit cell outlines shown in dashed lines. Li = gray, BO_4 tetrahedra and BO_3 trigonal planes = brown, O = red .	18
1.15 The KBBF (left), SBBO (middle), and $\text{K}_3\text{Ba}_3\text{Li}_2\text{Al}_4\text{B}_6\text{O}_{20}\text{F}$ (right) structures. K = white, Sr = gray, Ba = yellow, BeO_4 tetrahedra = green, BO_3 trigonal planes = brown, LiO_4 tetrahedra = dark gray, AlO_4 tetrahedra = black, O = red, F = pale blue.	19
1.16 The Åkermanite structure, with unit cell outlines shown in dashed lines. Ca = white, MgO_4 tetrahedra = orange, SiO_4 tetrahedra = black, O = red.	20
1.17 The sphalerite (left), roquesite (middle), and kesterite (right) structures, with unit cell outlines shown in dashed lines. Zn-centered tetrahedra = gray, Cu-centered tetrahedra = blue, In-centered tetrahedra = pink, Sn-centered tetrahedra = dark gray, S = yellow.	22
1.18 The primary tunnel motif of the $\text{Al}_7\text{BO}_3(\text{SiO}_4)_3\text{O}_3$ ($Pm\bar{c}n$) member of the dumortierite mineral family. AlO_6 face-sharing octahedra = red, AlO_6 edge-sharing octahedra = purple, black, AlO_6 face- and edge-sharing octahedra = dark green, SiO_4 tetrahedra = gray, BO_3 trigonal planes = green, Al = pale blue, Si = blue, B = green.	24
1.19 The lyonsite crystal structure as viewed along the a axis (A1 = blue, A2 = green, A3 = gray, M1, M2 = purple). Left: primary tunnel motif of the lyonsite. Right: representation of broader structure, with unit cell outline shown in dashed lines.	26
1.20 A unit cell representing the spinel structure (CoAl_2O_4 , $Fd\bar{3}m$). CoO_4 tetrahedra = blue, AlO_6 octahedra = gray, O = red.	32

LIST OF FIGURES (Continued)

<u>Figure</u>	<u>Page</u>
2.1 A representation of the ceramic method, in which precursors (red/blue) are mixed, forming the product phase at the interfaces through diffusion (purple). These particles are broken up to facilitate further reaction.	44
2.2 A comparison between the scattering behaviors of electrons, X-rays, and neutrons impinging on a sample surface	47
2.3 Basic schematic of an X-ray diffraction experiment.	49
2.4 A representation of the conditions required for Bragg diffraction.	50
2.5 The broad categories of magnetic spin interactions: paramagnetism (left), ferromagnetism (middle), and antiferromagnetism (right).	57
2.6 The Quantum Design Physical Property Measurement System (PPMS). The Model 6000 controller is housed in the white cabinet (left), while the sample chamber is housed in the He containment dewar (black, center). The cryopump (He level control via a second stage and condenser) is integrated into the dewar, and is connected to a compressor (not shown). Not shown: Scroll pump housing unit (temperature control), diaphragm pump housing unit (pressure control).	58
2.7 Sample preparation for ACMS: sample powders are packed into a straw (left), fitted to a sample rod (middle), and inserted through the DC servo motor (right).	59
2.8 Electronic configurations for the t_{2g} orbitals. Highlighted in purple are the spin states that are expected to have an unquenched orbital angular momentum contribution.	64
2.9 Schematic of the internal cross-section of the bifurcated optical fiber and the pathways for incident and reflected light.	66
2.10 Schematic of the integrating sphere for a Jasco V-670 spectrophotometer and the pathways for incident and reflected light.	67
2.11 In-house parallel plate capacitor setup, with schematic of an idealized setup	70
2.12 Capacitor phasor diagram, showing the phase angles between an ideal capacitor and a capacitor containing a lossy dielectric.	72

LIST OF FIGURES (Continued)

<u>Figure</u>	<u>Page</u>
2.13 The general photocatalysis mechanism. A particle (green/white) suspended in solution (blue background) is irradiated with an incident light (yellow) with an energy $E > E_g$, forming an exciton, which migrates to the surface, causing single-electron reduction/oxidation reactions with adsorbed molecules. For water splitting, the reduction reaction is $O_2 + e^- \longrightarrow O_2^\bullet$ and the oxidation reaction is $H_2O + h^+ \longrightarrow OH^\bullet + H^+$. .	74
2.14 Schematic of a reactor setup for photocatalysis experiments. Powder samples (green) are suspended in solution with the degradation target and irradiated with incident light (yellow), all housed in a dark box. Aliquots are centrifuged and decanted, and degradation is monitored with a spectrophotometer.	76
3.1 Lyonsite crystal structure (A1 = purple, A2 = blue, A3 = green, M1 = gray, M2 = navy).	83
3.2 Powder X-ray diffraction patterns for $Zn_{2.5-x}Co_xVMoO_8$	86
3.3 Lattice parameters for $Zn_{2.5-x}Co_xVMoO_8$. The ranges for the a , b , and c parameters are set to the same size (0.6 Å) for direct comparisons. .	87
3.4 TOF neutron diffraction pattern for $Zn_{1.25}Co_{1.25}VMoO_8$. Display includes calculated intensities (red), difference curve (blue), and allowed reflections for $Pnma$ (magenta).	88
3.5 Fragments of the $Zn_{1.20}Co_{1.30}V_{0.98}Mo_{1.02}O_8$ unit cell, with the M1 (a) and M2 (b) sites' bond lengths labeled. Other structural features are provided for context. Atom colors: V = gray, Mo = purple, O = red.	91
3.6 Lattice parameter comparisons for $Zn_{2.5-x}Co_xVMoO_8$ against literature values [21, 24].	92
3.7 A3 site symmetry comparisons between Wang et al. [21] (left) and this work (right). Black line indicates (001) plane. Top row: projection viewed along the b axis, bottom row: along the a axis. Atom colors: Zn = gray, Co = blue, O = red.	94

LIST OF FIGURES (Continued)

Figure	Page	
3.8	Isolated polyhedra for $\text{Zn}_{1.20}\text{Co}_{1.30}\text{V}_{0.98}\text{Mo}_{1.02}\text{O}_8$, labeled with (a) select A1 interatomic distances, and (b) A1(left)/A3(right) bond angles. Top row: Wang et al. [21], bottom row: this work. Atom colors: Zn = dark gray, Co = blue, \square = light gray, O = red.	96
3.9	Magnetic susceptibility plots for $\text{Zn}_{2.5-x}\text{Co}_x\text{VMoO}_8$ and corresponding effective moments.	100
3.10	Optical properties for $\text{Zn}_{2.5-x}\text{Co}_x\text{VMoO}_8$. Displayed are (a) Crystal field splitting diagrams for ideal octahedra and trigonal prisms, (b) powder pictures from $x = 0$ (left) to $x = 2.5$ (right), (c) UV-vis diffuse reflectance spectra, and (d) vis-NIR diffuse reflectance spectra, following the same legend scheme as (c).	102
3.11	Powder neutron diffraction analysis for the nominal $\text{Zn}_{1.25}\text{Co}_{1.25}\text{VMoO}_8$ between Banks 2 (a) and 4 (b) from POWGEN. Overlapping d -spacing regions are boxed in red to indicate intensity mismatch between banks. Bank 2 was omitted from further refinement due to the lower data quality.	104
3.12	A site vacancy localization simulations on the A2 (a) and A3 (b) sites for the nominal $\text{Zn}_{1.25}\text{Co}_{1.25}\text{VMoO}_8$	104
3.13	Visual representation of the M site under different vacancy simulations for the nominal $\text{Zn}_{1.25}\text{Co}_{1.25}\text{VMoO}_8$ as obtained from neutron diffraction analysis. Shortened M -O bond lengths resulting from O displacement towards the M cation are bolded.	106
3.14	Site occupancy trends for the nominal $\text{Zn}_{1.25}\text{Co}_{1.25}\text{VMoO}_8$ as obtained from neutron diffraction analysis.	107
3.15	Combined A site polyhedral distortion comparison for the nominal $\text{Zn}_{1.25}\text{Co}_{1.25}\text{VMoO}_8$ as obtained from neutron diffraction analysis. Quadratic elongation (a) and bond length distortion (b) ($\times 10^3$).	107
4.1	Lyonsite crystal structure (A1 = red, A2 = purple, A3 = gray, M1 = orange, M2 = green).	113
4.2	Powder X-ray diffraction pattern (a) and lattice parameters (b) for $\text{Zn}_{2.5-x}\text{A}'_x\text{VMoO}_8$, in which $A' = \text{Mn}^{2+}$. The ranges for the a , b , and c parameters are set to the same size (0.7 Å) for direct comparisons. .	118

LIST OF FIGURES (Continued)

<u>Figure</u>	<u>Page</u>
4.3 Powder X-ray diffraction pattern (a) and lattice parameters (b) for $\text{Zn}_{2.5-x}\text{A}'_x\text{VMoO}_8$, in which $\text{A}' = \text{Ni}^{2+}$. The ranges for the a , b , and c parameters are set to the same size (0.7 Å) for direct comparisons. . .	119
4.4 Powder X-ray diffraction pattern (a) and lattice parameters (b) for $\text{Zn}_{2.5-x}\text{A}'_x\text{VMoO}_8$, in which $\text{A}' = \text{Cu}^{2+}$. The ranges for the a , b , and c parameters are set to the same size (0.7 Å) for direct comparisons. . .	120
4.5 Neutron diffraction patterns for $\text{Zn}_2\text{A}'_{0.5}\text{VMoO}_8$, in which $\text{A}' = \text{Mn}^{2+}$ (a), Ni^{2+} (b), and Cu^{2+} (c). Display includes calculated intensities (red), difference curve (blue), and allowed reflections for $Pnma$ (magenta). .	122
4.6 A site occupancy comparisons for $\text{Zn}_{2.5-x}\text{A}'_x\text{VMoO}_8$ ($x = 0.5$), in which $\text{A}' = \text{Mn}^{2+}$ (a), Ni^{2+} (b), and Cu^{2+} (c). Display includes overall polyhedral framework as viewed along the a axis (faded gray) and least-occupied sites (labeled). Atom colors: Zn = dark gray, Mn = purple, Ni = yellow, Cu = blue, \square = white.	127
4.7 Magnetic susceptibility plots for $\text{Zn}_{2.5-x}\text{A}'_x\text{VMoO}_8$, in which $\text{A}' = \text{Mn}^{2+}$ (a), Ni^{2+} (b), and Cu^{2+} (c).	129
4.8 UV-vis diffuse reflectance spectra and powder pictures for $\text{Zn}_{2.5-x}\text{A}'_x\text{VMoO}_8$, in which $\text{A}' = \text{Mn}^{2+}$ (a,b), Ni^{2+} (c,d), and Cu^{2+} (e,f).	132
4.9 Vis-NIR diffuse reflectance spectra for $\text{Zn}_{2.5-x}\text{A}'_x\text{VMoO}_8$, in which $\text{A}' = \text{Mn}^{2+}$ (a), Ni^{2+} (b), and Cu^{2+} (c).	134
4.10 Site occupancy trends for the nominal $\text{Zn}_2\text{Mn}_{0.5}\text{VMoO}_8$ (a), $\text{Zn}_2\text{Ni}_{0.5}\text{VMoO}_8$ (b), $\text{Zn}_2\text{Cu}_{0.5}\text{VMoO}_8$ (c), and a combined A site occupancy comparison for each substituted cation (d) as obtained from neutron diffraction analysis.	137
4.11 A site polyhedral distortion parameters for $\text{A}' = \text{Mn}^{2+}$. Quadratic elongation (a): $\lambda = \frac{1}{n} \sum_{i=1}^n \left(\frac{l_i}{l_o}\right)^2$ [34] and bond length distortion (b): $\Delta = \frac{1}{n} \sum_{i=1}^n \left(\frac{l_i-l_o}{l_o}\right)^2$ [35] ($\times 10^3$). n = number of bonds, l_o = idealized bond length (taken by summing radii), l_i = bond length.	138
4.12 Combined A site polyhedral distortion comparison for each substituted cation. Quadratic elongation (a) and bond length distortion (b) ($\times 10^3$).138	

LIST OF FIGURES (Continued)

<u>Figure</u>	<u>Page</u>	
5.1	The lyonsite crystal structure as viewed along the a axis (A1 = blue, A2 = green, A3 = gray, M1,M2 = purple). Left: primary tunnel motif of the lyonsite. Right: representation of broader structure, with unit cell outline shown in dashed lines.	146
5.2	Powder X-ray diffraction patterns for $\square_{0.25-\frac{1}{8}x}\text{Li}_x\text{Co}_{3.75-\frac{7}{8}x}\text{V}_{1.5-\frac{3}{4}x}\text{Mo}_{1.5+\frac{3}{4}x}\text{O}_{12}$. hkl tick marks: $x = 0$ end member (green), $x = 2$ end member (blue).	150
5.3	Lattice parameters for $\square_{0.25-\frac{1}{8}x}\text{Li}_x\text{Co}_{3.75-\frac{7}{8}x}\text{V}_{1.5-\frac{3}{4}x}\text{Mo}_{1.5+\frac{3}{4}x}\text{O}_{12}$. The ranges for the a , b , and c parameters are set to the same size (0.7 Å) for direct comparisons.	151
5.4	CW neutron diffraction pattern (top) and synchrotron X-ray diffraction pattern (bottom) for $\square_{0.25-\frac{1}{8}x}\text{Li}_x\text{Co}_{3.75-\frac{7}{8}x}\text{V}_{1.5-\frac{3}{4}x}\text{Mo}_{1.5+\frac{3}{4}x}\text{O}_{12}$ at $x = 1.25$. Display includes calculated intensities (red), difference curve (blue), and allowed reflections for $Pnma$ (magenta).	153
5.5	Magnetic susceptibility plots for $\square_{0.25-\frac{1}{8}x}\text{Li}_x\text{Co}_{3.75-\frac{7}{8}x}\text{V}_{1.5-\frac{3}{4}x}\text{Mo}_{1.5+\frac{3}{4}x}\text{O}_{12}$	154
5.6	Powder pictures for $\square_{0.25-\frac{1}{8}x}\text{Li}_x\text{Co}_{3.75-\frac{7}{8}x}\text{V}_{1.5-\frac{3}{4}x}\text{Mo}_{1.5+\frac{3}{4}x}\text{O}_{12}$	156
5.7	Visible wavelength diffuse reflectance spectra for $\square_{0.25-\frac{1}{8}x}\text{Li}_x\text{Co}_{3.75-\frac{7}{8}x}\text{V}_{1.5-\frac{3}{4}x}\text{Mo}_{1.5+\frac{3}{4}x}\text{O}_{12}$	157
5.8	Vis-NIR diffuse reflectance spectra for $\square_{0.25-\frac{1}{8}x}\text{Li}_x\text{Co}_{3.75-\frac{7}{8}x}\text{V}_{1.5-\frac{3}{4}x}\text{Mo}_{1.5+\frac{3}{4}x}\text{O}_{12}$, following the same legend scheme as Fig. 5.7.	158
5.9	McLean analysis for $\square_{0.25-\frac{1}{8}x}\text{Li}_x\text{Co}_{3.75-\frac{7}{8}x}\text{V}_{1.5-\frac{3}{4}x}\text{Mo}_{1.5+\frac{3}{4}x}\text{O}_{12}$	160
5.10	Tauc plots for $\square_{0.25-\frac{1}{8}x}\text{Li}_x\text{Co}_{3.75-\frac{7}{8}x}\text{V}_{1.5-\frac{3}{4}x}\text{Mo}_{1.5+\frac{3}{4}x}\text{O}_{12}$	161
5.11	Dielectric constant and loss tangent plots for the $x = 0$ member of the $\square_{0.25-\frac{1}{8}x}\text{Li}_x\text{Co}_{3.75-\frac{7}{8}x}\text{V}_{1.5-\frac{3}{4}x}\text{Mo}_{1.5+\frac{3}{4}x}\text{O}_{12}$ solid solution.	163
5.12	Dielectric constant and loss tangent plots for the $x = 2$ member of the $\square_{0.25-\frac{1}{8}x}\text{Li}_x\text{Co}_{3.75-\frac{7}{8}x}\text{V}_{1.5-\frac{3}{4}x}\text{Mo}_{1.5+\frac{3}{4}x}\text{O}_{12}$ solid solution.	164

LIST OF TABLES

Table	Page
3.1 Unit cell coordinates, occupancies, and displacement parameters for $\text{Zn}_{1.25}\text{Co}_{1.25}\text{VMoO}_8$ ($Pnma$). $a = 5.0497(1)$ Å, $b = 10.389(1)$ Å, $c = 17.497(1)$ Å, $V = 918.00(5)$ Å ³ . Reliability parameters $\chi^2 = 2.85$, $wR_p = 2.27$ %. *Refined anisotropic U values can be found in the available CIF file (CSD no. 434587).	90
3.2 Polyhedral distortion parameters: (a) quadratic elongation and (b) bond length distortion ($\times 10^3$). n = number of bonds, l_o = idealized bond length (taken by summing radii), l_i = bond length.	98
3.3 Summary of A site vacancy simulations for the nominal $\text{Zn}_{1.25}\text{Co}_{1.25}\text{VMoO}_8$ as obtained from neutron diffraction analysis. *Values deemed unreasonable, thereby invalidating that simulation	105
3.4 Summary of M -O site bond lengths (Å) under different vacancy simulations for the nominal $\text{Zn}_{1.25}\text{Co}_{1.25}\text{VMoO}_8$ as obtained from neutron diffraction analysis. *Values indicate O displacement towards M cation.	105
3.5 Bond valence sums for the nominal $\text{Zn}_{1.25}\text{Co}_{1.25}\text{VMoO}_8$ as obtained from neutron diffraction analysis.	106
4.1 Crystallographic information for $\text{Zn}_{2.5-x}\text{A}'_x\text{VMoO}_8$ ($x = 0.5$) ($Pnma$).	123
4.2 Unit cell coordinates, occupancies, and displacement parameters for the nominal $\text{Zn}_2\text{Mn}_{0.5}\text{VMoO}_8$. *Refined anisotropic U values can be found in the available CIF file (CCDC no. 1866822).	123
4.3 Unit cell coordinates, occupancies, and displacement parameters for the nominal $\text{Zn}_2\text{Ni}_{0.5}\text{VMoO}_8$. *Refined anisotropic U values can be found in the available CIF file (CCDC no. 1866823).	124
4.4 Unit cell coordinates, occupancies, and displacement parameters for the nominal $\text{Zn}_2\text{Cu}_{0.5}\text{VMoO}_8$. *Refined anisotropic U values can be found in the available CIF file (CCDC no. 1866824).	125
4.5 A site occupancy comparisons for $\text{Zn}_{2.5-x}\text{A}'_x\text{VMoO}_8$ ($x = 0.5$) ($Pnma$) as obtained from neutron diffraction analysis.	127
4.6 Effective magnetic moments for $\text{Zn}_{2.5-x}\text{A}'_x\text{VMoO}_8$	130

LIST OF TABLES (Continued)

<u>Table</u>	<u>Page</u>
4.7 Bond valence sums for the nominal $\text{Zn}_2\text{Mn}_{0.5}\text{VMoO}_8$ (a), $\text{Zn}_2\text{Ni}_{0.5}\text{VMoO}_8$ (b), and $\text{Zn}_2\text{Cu}_{0.5}\text{VMoO}_8$ (c) as obtained from neutron diffraction analysis.	136
5.1 Effective magnetic moments for $\square_{0.25-\frac{1}{8}x}\text{Li}_x\text{Co}_{3.75-\frac{7}{8}x}\text{V}_{1.5-\frac{3}{4}x}\text{Mo}_{1.5+\frac{3}{4}x}\text{O}_{12}$.	155
5.2 Possible band-to-band absorption transitions for a given material. . .	159
5.3 Estimated optical band gaps for $\square_{0.25-\frac{1}{8}x}\text{Li}_x\text{Co}_{3.75-\frac{7}{8}x}\text{V}_{1.5-\frac{3}{4}x}\text{Mo}_{1.5+\frac{3}{4}x}\text{O}_{12}$.	162

LIST OF APPENDIX FIGURES

Figure	Page
A.1 Powder X-ray diffraction patterns for $\text{LiMn}_{2-x}\text{Rh}_x\text{O}_4$. <i>hkl</i> tick marks (black) are shown for allowed reflections for $Fd\bar{3}m$	191
A.2 <i>a</i> lattice parameter for $\text{LiMn}_{2-x}\text{Rh}_x\text{O}_4$	192
A.3 Magnetic susceptibility plots for $\text{LiMn}_{2-x}\text{Rh}_x\text{O}_4$	193
A.4 Crystal field splitting diagrams and possible spin states for $\text{LiMn}_{2-x}\text{Rh}_x\text{O}_4$	195
B.1 Powder X-ray diffraction patterns for $\text{Zn}_2\text{Ni}_{0.5}\text{VMoO}_8$. <i>hkl</i> tick marks (black) are shown for allowed reflections for <i>Pnma</i> . Inset figure displays the peak broadening associated with the smaller particle size (resulting from the citrate gel method).	202
B.2 UV-vis absorbance spectra for MB after 2 h irradiation time (truncated for λ_{max}).	203
B.3 Average degradation plot for MB over 2 h irradiation time.	204
B.4 Degradation plot comparison for MB-only (black) and MB loaded with TiO_2 (red) over 2 h irradiation time.	205
B.5 Degradation plot comparison for $\text{Zn}_2\text{Cu}_{0.5}\text{VMoO}_8$ (black), MB-only (red), and MB loaded with TiO_2 (blue) over 2 h irradiation time.	206
B.6 Degradation plot comparison for $\text{Zn}_2\text{Ni}_{0.5}\text{VMoO}_8$ (black), MB-only (red), and MB loaded with TiO_2 (blue) over 2 h irradiation time.	207
B.7 Degradation plot comparison for $\text{Li}_3\text{CrMo}_3\text{O}_{12}$ (black), MB-only (red), and MB loaded with TiO_2 (blue) over 2 h irradiation time.	208
B.8 UV-vis absorbance spectra for MB loaded with $\text{Li}_3\text{Ti}_{0.75}\text{Mo}_3\text{O}_{12}$ after 2 h irradiation time. Also shown is the initial absorbance taken prior to the 2 h dark phase (labeled as $t = -120$ min.).	210
B.9 Degradation plot comparison for MB-only (blue triangles), MB loaded with TiO_2 (blue diamonds), and MB loaded with $\text{Li}_3\text{Ti}_{0.75}\text{Mo}_3\text{O}_{12}$ measured at two wavelengths, over 2 h irradiation time. Also shown is the initial absorbance taken prior to the 2 h dark phase (labeled as $x = -120$ min.).	211

LIST OF APPENDIX FIGURES (Continued)

<u>Figure</u>	<u>Page</u>
B.10 Powder X-ray diffraction patterns for $\text{Li}_3\text{Ti}_{0.75}\text{Mo}_3\text{O}_{12}$. <i>hkl</i> tick marks (black) are shown for allowed reflections for <i>Pnma</i>	212
C.1 General workflow for the proposed program.	216
C.2 General workflow for the running program.	218

LIST OF APPENDIX TABLES

<u>Table</u>		<u>Page</u>
A.1	Possible oxidation state and stoichiometries for $\text{LiMn}_{2-x}\text{Rh}_x\text{O}_4$	196
A.2	Effective magnetic moments and modeling conditions for $\text{LiMn}_{2-x}\text{Rh}_x\text{O}_4$.	196

Chapter 1: General Overview and Introduction to Lyonsite Type Oxides

1.1 Introduction to Transition Metal Oxides

Structure-property relationships have always underpinned the field of solid state chemistry; dependable structural descriptions are integral to understanding and controlling the physical properties of inorganic compounds old and new. While a handful of crystal structures are celebrated for their versatility, flexibility, and functionality, the existence of more exotic structures is often ignored. Without methodical study, potential solutions to contemporary material challenges may repeatedly escape notice. In the following sections, an overview of transition metal oxide structures is presented, which will contextualize a discussion on the structure type at the heart of this dissertation: the lyonsite structure.

1.1.1 Classifications

At first glance, structure categorization may seem a trivial use of time. In reality, an understanding of structure families is often critical to understanding past-observed properties, as well as providing perspective towards future properties. Regardless of classification style, all crystalline materials can be described by one of the 230 space groups, subdivided into seven crystal systems: cubic, hexagonal, trigonal (rhombohedral), tetragonal, orthorhombic, monoclinic, and triclinic [1, 2]. Using

Hermann-Mauguin notation, these space groups are expressed by a combination of a letter (signifying the Bravais lattice centering) and three terms (signifying the highest symmetry elements with respect to the crystallographic directions for each system). For example, the $Fd\bar{3}m$ space group encodes the following information, from left to right: face-centered unit cell (F), diamond glide parallel to the a , b , and c axes (d), 3-fold rotation with inversion center along the body diagonals ($\bar{3}$), and mirror plane orthogonal to the face diagonals (m). An example relevant to this dissertation can be found in the space group $Pnma$, which denotes that the unit cell is primitive and possesses the three symmetry operations: n glide orthogonal to the a axis, mirror plane orthogonal to the b axis, and a glide orthogonal to the c axis.

Fundamentally, the most common way to understand and describe oxide crystal structures is through the stacking of atoms or ions. By assuming ions are spherical in shape, two forms of stacking are most commonly observed: cubic and hexagonal. Typically, oxygen anions form the basis for these packing schemes, creating void spaces for cations to occupy. If layers are labeled alphabetically, and an initial layer of densely arranged spheres is designated A, the subsequent layers can either be stacked in an ABA... or ABC... fashion. In ABA stacking, layer B is placed above the first such that the spheres are not directly above those of A, and a third layer is placed above B, flush with the spheres of A; this sequence is also notated as a hexagonal close packed (hcp) array. Structure types that fall into this category are honeycomb layered structures (Fig. 1.1) and delafossites [3].

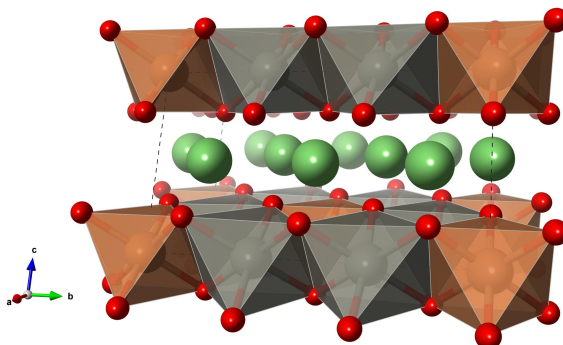


Figure 1.1: A unit cell representing a layered honeycomb ordered structure ($\text{Li}_3\text{Zn}_2\text{SbO}_6$, $C2/m$). Li = green, ZnO_6 octahedra = gray, SbO_6 octahedra = orange, O = red.

If the third layer is offset from both A and B, it is notated as C, and this scheme is considered a cubic close packed (ccp) array. Many famous structures adopt this stacking sequence, e.g., perovskites (Fig.1.2) and spinels [4]. For a perovskite (which takes the general formula ABX_3), the ccp array consists of the X anions, with 1/4 of the anion positions replaced with an A cation, forming layers of AX_3 . The B cation then occupies 1/4 of the interstitial octahedral voids. A description of the spinel structure is given in section 1.4.1. It should be noted that the chemical formula gives no indication of structure type. For example, the YMO_3 ($M = \text{In}, \text{Mn}$) formula matches that of a perovskite, but is in fact a hexagonal phase ($P6_3cm$) (Fig. 1.3). Instead of octahedra, the coordination of interest in this structure is the uncommon trigonal bipyramidal (TBP) site (which exists in minerals like andalusite [5], and has been exploited to great effect as a chromophore in pigment research [6–8]).

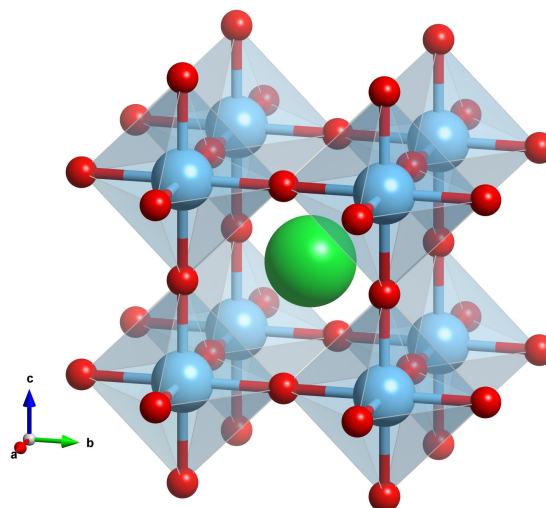


Figure 1.2: A unit cell representing a typical perovskite (SrTiO_3 , $Pm\bar{3}m$). Sr = green, Ti = blue, O = red.

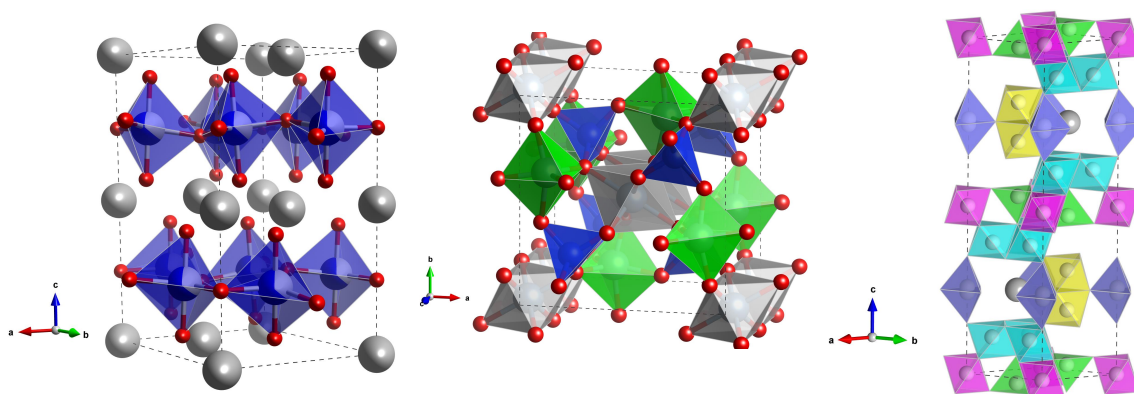


Figure 1.3: Representative unit cells of TBP-containing structure types: $\text{YIn}_{1-x}\text{Mn}_x\text{O}_3$ (left), andalusite (middle), and hibonite (right). In $\text{YIn}_{1-x}\text{Mn}_x\text{O}_3$: Y = gray, (In,Mn) O_5 TBP = blue, O = red. In andalusite (Al_2SiO_5 , $Pn\bar{1}m$): AlO_5 TBP = green, AlO_6 octahedra = gray, SiO_4 tetrahedra = blue. In hibonite ($\text{CaAl}_{12}\text{O}_{19}$, $P6_3/mmc$): Ca = gray, AlO_5 TBP = purple, AlO_6 octahedra = pink/cyan/yellow, and AlO_4 tetrahedra = green.

When the stacking sequences become more complex than the simple descriptions

above, different coordination environments (besides octahedral and tetrahedral) become possible, and categorization becomes difficult. For example, if a layer repeats itself, i.e. ABBA..., a trigonal prismatic coordination environment is created for the interstitial site between the BB layers (Fig. 1.4) [9, 10]. Many derivative structures can be

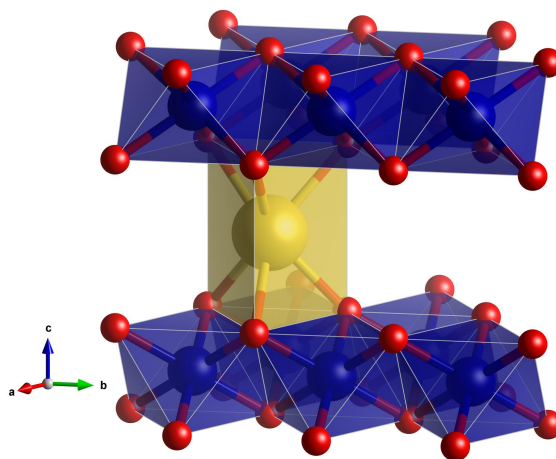


Figure 1.4: Generic representation of the trigonal prismatic site formed in ABBA... stacking. Trigonal prismatic site = yellow, octahedra = blue, O = red.

described by distorting or modifying the basic structures; for example, introducing defects into the fluorite structure can yield the well-known pyrochlore family (which takes the general formula $A_2M_2O_6O'$ and adopts the cubic $Fd\bar{3}m$ space group) (Fig. 1.5). In the fluorite structure (AX_2 , or A_4X_8 for comparison with the pyrochlores), the cations form a ccp array, and the anions occupy all the tetrahedral voids. Removal of an oxygen from the formula unit results in distinct crystallographic sites for the cations ($A_2M_2X_7$); the A cation's cubic coordination environment then distorts, while the M cation occupies the octahedral site, thereby forming the pyrochlore structure [4, 11].

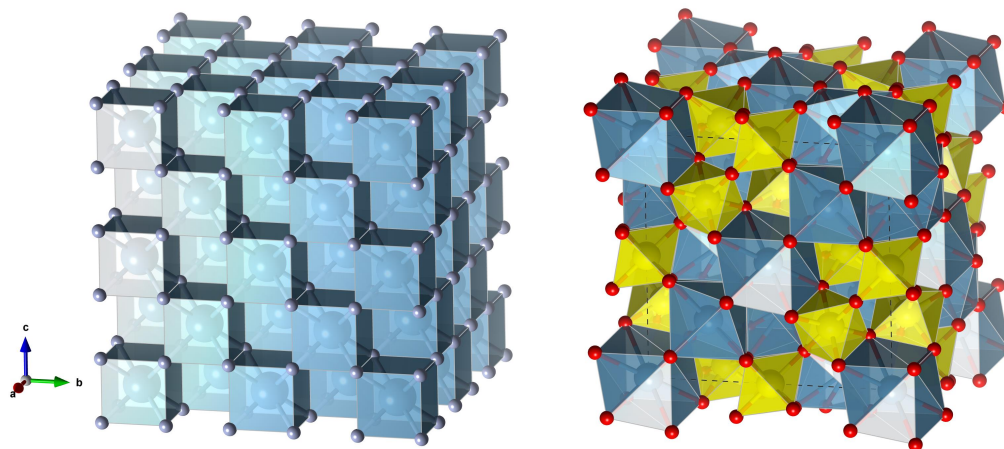


Figure 1.5: Comparison between the fluorite (left) and pyrochlore (right) structures. Cation polyhedra = blue and yellow, O = red, F = pale blue.

As the complexity further increases, describing structures by stacking sequences becomes impractical, and structural motifs are used instead. For example, the rutile, hollandite, and todorokite structures are all arranged in channels/tunnels, and are aptly referred to as tunneled structures (Fig. 1.6). The rutile structure, epitomized by the oxide TiO_2 , can be described as a hcp lattice of anions with $1/2$ of the octahedral voids filled [4]. The TiO_6 octahedra form edge-sharing chains, and are connected by corner-sharing octahedra, to form a $1 \times 1 \times 1 \times 1$ chain tunnel structure (tetragonal $P4_2/mnm$). However, in the hollandite structure (which takes the general formula $A_xM_4O_8$ and adopts the tetragonal $I4/m$ space group), the MO_6 octahedra retain the tunneling characteristics of the rutile structure, but the channel is created by two edge-sharing chains, creating a $2 \times 2 \times 2 \times 2$ channel [4]. Todorokites extend this further, forming $3 \times 3 \times 3 \times 3$ channels comprised of central cations like Mg^{2+} , Al^{3+} , Mn^{3+} , or Mn^{4+} [12].

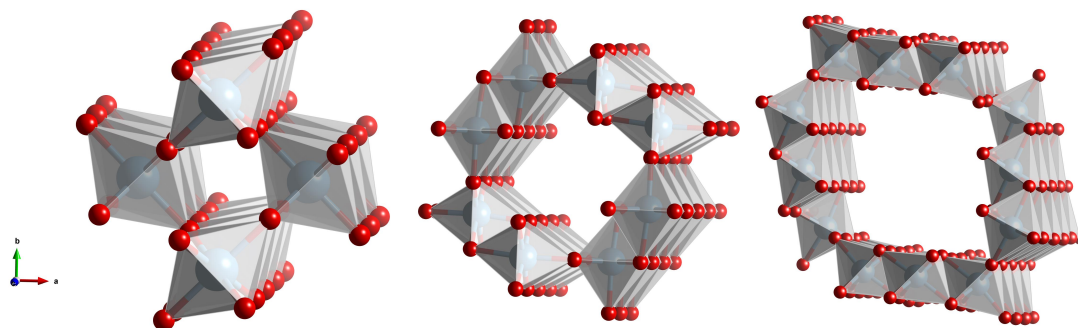


Figure 1.6: Comparison between rutile (left), hollandite (middle), and todorokite (right) structures. Cation polyhedra = gray, O = red.

The difference in structure is reflected in the properties, as the channels in the hollandites are large enough to house a large A^+ cation ($A^+ = \text{K, Rb, Cs}$) or Ba^{2+} and exhibit one-dimensional ionic conductivity, while rutile cannot accommodate such cations [13, 14]. The tunnels in the todorokite are even larger, accommodating ions like Ca^{2+} , Na^+ , K^+ , or rigid bodies like H_2O [12]. Variations on these features also exist, as psilomelane ($\text{Ba}_x\text{Mn}_5\text{O}_{16}(2-x)\text{H}_2\text{O}$, space group $A2/m$), is comprised of 2×3 tunnels, while ramsdellite ($\gamma\text{-MnO}_2$, space group $Pbnm$) is comprised of 1×2 tunnels [15].

Categories can also be quite broad, as with the case of so-called extended "framework" structures. Zeolites, skutterudites, and β -gallia-rutile (BGR) are all examples of unrelated frameworks with unique features, and properties that are just as distinct. Zeolites contain large channels and are useful in ion exchange applications [4], skutterudites have "rattler" sites and are oft-studied thermoelectric materials [16], and BGR structures have shown promise as inexpensive photocatalytic materials (Fig. 1.7) [17].

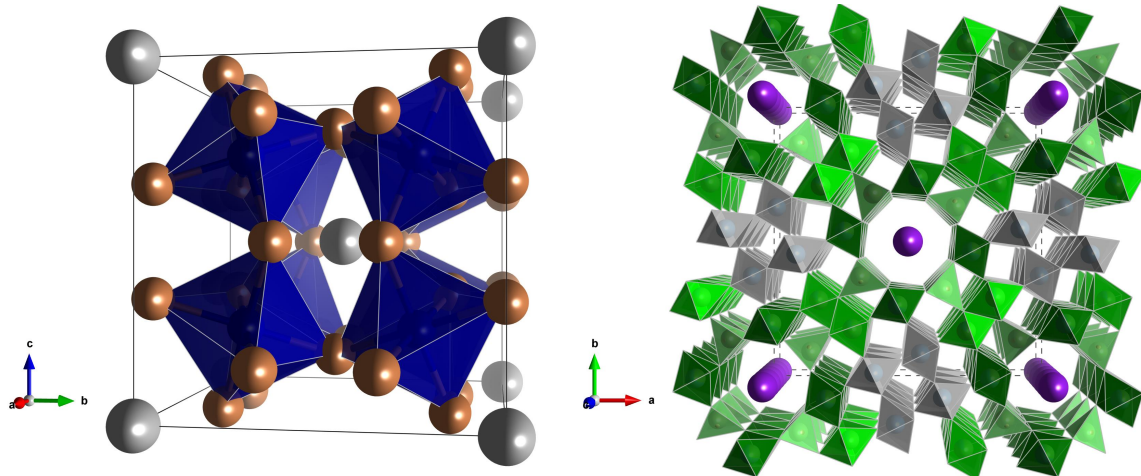


Figure 1.7: Representation of a skutterudite (left) and a β -gallia rutile (BGR) intergrowth structure (right). In the skutterudite: In = gray, Co-centered octahedra = blue, Sb = brown. In the BGR: K = purple, gallia blocks = green, rutile blocks = gray.

These categories are also not mutually exclusive; for example, it is also common to describe the pyrochlore structure as interpenetrating 3D networks: corner-sharing MX_6 octahedra and linearly-coordinated A_2X' chains, linked by a framework of $X'A_4$ tetrahedra (Fig. 1.8) [11].

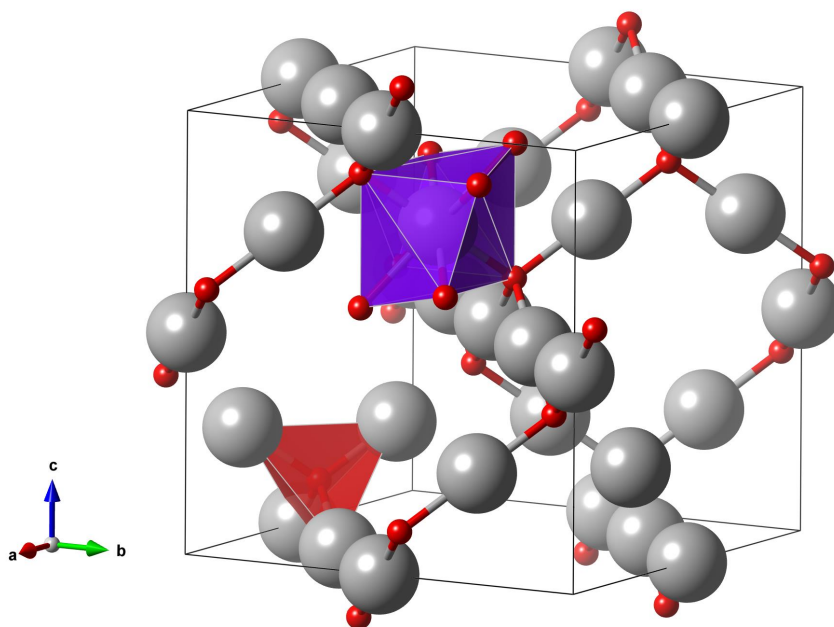


Figure 1.8: A unit cell representing the A_2X' network of the pyrochlore. A = gray, O = red, $X'A_4$ tetrahedron = red, distorted $AX'X'$ cube = purple.

1.1.2 *Orbital Splitting*

Within the sweeping categories solid state chemists use, there are just as many quirks within structure families, i.e. unusual coordination environments and local chemical distortions. These oddities have many origins, including but not limited to: metal identity, ligand identity, and metal-ligand interactions. In Crystal Field

Theory, a given transition metal has five degenerate d orbitals; approaching ligands perturb these orbitals, removing their degeneracy [18]. The nature of this perturbation is dependent on several factors, including the ligand's identity/charge, approach direction, electron density and directionality. Repulsion along the bonding axes raises the energies of the respective orbitals, while lowering the energies of the orbitals with less metal-ligand overlap [18]. In the classic octahedral example, the ligands approach along the x , y , and z axes, raising the energies of the $d_{x^2-y^2}$ and d_{z^2} orbitals (e_g), and lower those of the d_{xy} , d_{yz} , and d_{xz} orbitals (t_{2g}) (Fig. 1.9). Although most cases involve nuanced discussions for octahedral or tetrahedral coordinations, the trigonal prismatic coordination is also important to this dissertation. This environment is also six-coordinate, but the directionality differs dramatically from that of the octahedral coordination, and is relatively uncommon in oxides [19]; the ligands overlap strongly with the off-axis orbitals (d_{xz} and d_{yz}), raising their energies (e'') [20]. The d_{z^2} orbital incidentally also experiences repulsive forces from mild overlap, though not to the extent the e'' orbitals do, and is therefore lower in energy (a'). The on-axis orbitals $d_{x^2-y^2}$ and d_{xy} overlap the least and are lowest in energy (e'). The overall crystal field splitting diagram for the trigonal prismatic environment can be seen in Fig. 1.9.

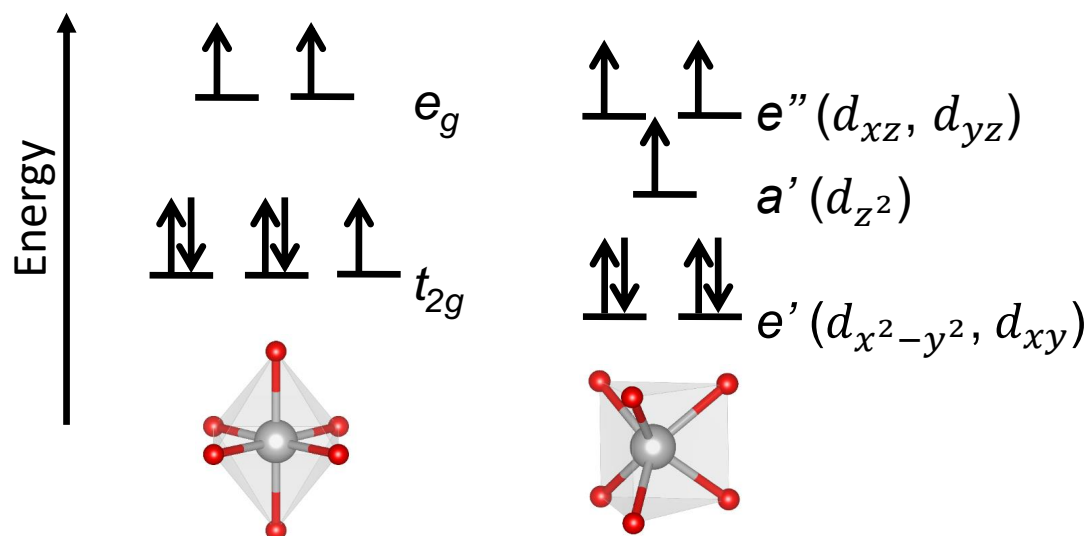


Figure 1.9: Crystal field splitting diagrams for ideal octahedral (left) and trigonal prism (right) environments in a hypothetical d^7 spin state.

Further splitting can be induced when uneven electron filling occurs in the upper orbitals; this is known as Jahn-Teller distortion [21]. The metal-ligand orbital overlap shortens the bond lengths and creates an increased repulsive force with the relevant orbitals. The degeneracy of these orbitals is further removed, resulting in axial compression or elongation. This phenomenon can often have profound implications in the bonding structure and the physical properties (e.g., magnetic properties, optical spectra).

1.2 A Survey of Framework Structures

Adaptable structures have been highly useful in a variety of applications, as evident from families like the perovskites, apatites, and garnets; the tunable structures result

in tunable physical properties. For example, the perovskites are well known to be capable of incorporating over 50% of the elements onto at least one of the three lattice sites. This adaptability extends even into organic substitutions, e.g., $\text{CH}_3\text{NH}_3^+\text{PbI}_3$ is an organohalide perovskite that has found recent interest as a photovoltaic material for solar cells or quantum dot light-emitting diodes [22, 23]. In addition, removing a B cation and replacing it with a vacancy yields a whole family of vacancy-ordered double perovskites (A_2BX_6) [24].

1.2.1 Ionic Conductivity

As mentioned, some tunneled structures, such as hollandite and todorokite, can accommodate alkali cations and exhibit ionic conductivity. The most typical hollandite (also known as cryptomelane and coronadite), $\alpha\text{-MnO}_2$, has a conductivity of $\sim 10^{-2}$ S/cm [14]. Some complex hollandites, such as $\text{K}_{1.6}\text{Mg}_{0.8}\text{Ti}_{7.2}\text{O}_{16}$, can exhibit temperature-independent ionic conductivity [13]. For todorokites, an example is found in $(\text{Bi}_6\text{O}_5)\text{Rh}_8^{3+}\text{Rh}_4^{4+}\text{O}_{24}$ ($C2/m$), with a room temperature conductivity σ_{300} as low as 3 S/cm, decreasing to $\sim 10^{-5}$ S/cm with decreasing temperature. A large Seebeck of 280 $\mu\text{V}/\text{K}$ is also observed at 200 K, indicating semiconducting behavior. The combination of the high Seebeck and high conductivity make this a promising low temperature thermoelectric material [12]. The simplest tunneled relative, rutile, has also been computationally predicted to exhibit topologically insulating effects upon nanostructuring [25].

There are also many framework structures that do not feature tunnel systems;

e.g., β -gallia (Ga_2O_3 , $C2/m$) can be described as almost-ccp, with double edge-shared ribbons of GaO_6 octahedra, joined together by corner-sharing GaO_4 tetrahedra (Fig. 1.10) [15].

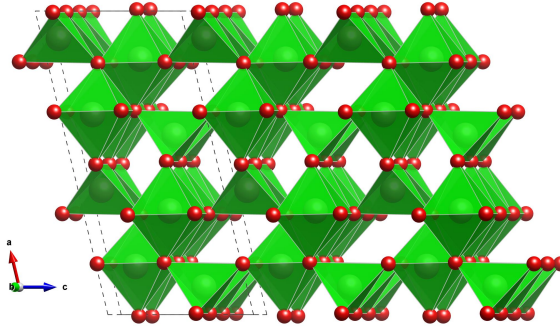


Figure 1.10: The β -gallia structure, with unit cell outline shown in dashed lines. Ga-centered polyhedra = green, O = red.

Fast Na^+ ion transport has been demonstrated in the well-known NASICON (Na super ionic conductor) family, generalized as $A_xM_2(\text{XO}_4)_3$, in which $A^+ = \text{Li}, \text{Na}$, $M = \text{Ti}, \text{Fe}, \text{V}$, and $X = \text{P}, \text{As}, \text{Mo}, \text{W}, \text{S}$. (Fig. 1.11) [26]. This family is exemplified in $\text{Na}_{1+x}\text{Zr}_2\text{P}_{3-x}\text{Si}_x\text{O}_{12}$ ($0 \leq x \leq 3$). This system is a solid solution between $\text{NaZr}_2\text{P}_3\text{O}_{12}$ and $\text{Na}_4\text{Zr}_2\text{Si}_3\text{O}_{12}$. Within the range $x = 1.8\text{--}2.2$, the structure adopts the $C2/c$ space group and $R\bar{3}c$ otherwise. The room temperature resistivity ρ_{300} for the $x = 2$ member is $\leq 5 \Omega\text{cm}$, with an activation energy $E_A \approx 0.29 \text{ eV}$ [27]. Another example can be found in Sc-substituted NASICONs, in which the Sc for Zr substitution correlates with a corresponding Si for P adjustment to maintain the Na concentration [28].

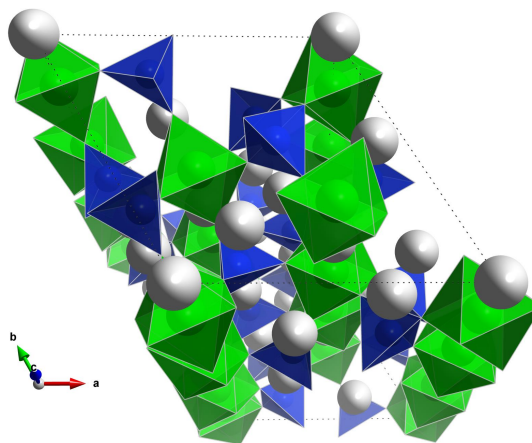


Figure 1.11: The NASICON structure, as viewed along the c axis, with unit cell outline shown in dotted lines. Na = white, ZrO_6 octahedra = green, SiO_4 tetrahedra = blue.

As mentioned, the pyrochlore structure can also be considered an adaptable framework structure; e.g., vacancies can be introduced into the A_2X' subarray while maintaining a stable B_2X_6 skeleton. An example of this is seen in AgSbO_3 , in which X' at the 8b site is missing [27]. Ionic conductivity can be observed in the $\text{KB}_x^{y+}\text{W}_{2-x}^{6+}\text{O}_6$ system ($B = \text{Al}, \text{Ti}, \text{Ta}$), with a σ_{300} of $5.2 \times 10^{-3} \Omega^{-1}\text{cm}^{-1}$ for $\text{KAl}_{0.33}\text{W}_{1.67}\text{O}_6$. The K^+ ions are occupied in its proper sites and polarization occurs in the B_2X_6 network [28].

1.2.2 Photocatalysis

Framework structures are also useful as photocatalytic materials; the quintessential photocatalyst is TiO_2 , found in many products, from paints to sunscreens. The photocatalytic activity is often linked to structural features, e.g., layers, tunnels,

distorted octahedra. For example, BaTi_4O_9 ($Pnmm$) contains pentagonal prism tunnels which serve as a concave nest for the uniform distribution of RuO_2 (Fig. 1.12) [29].

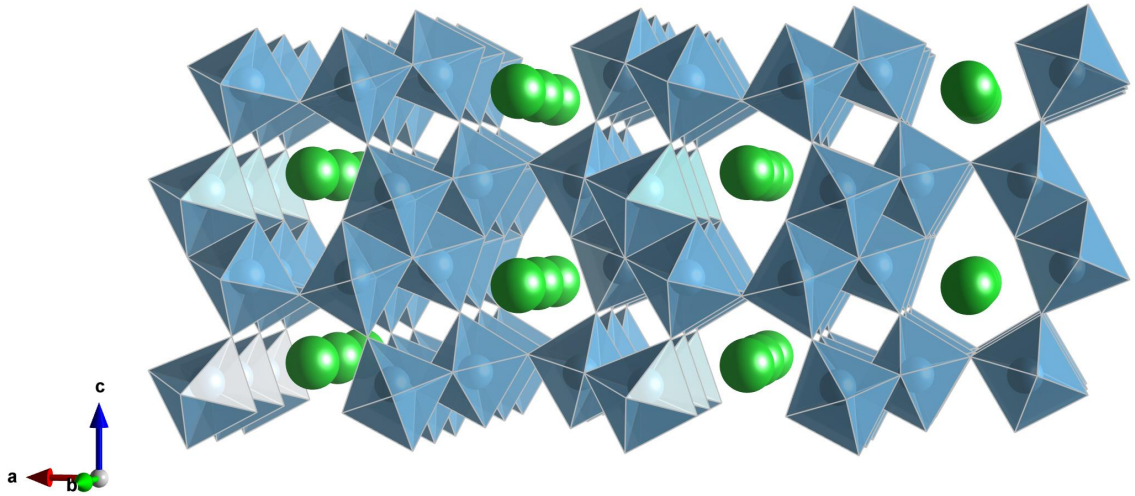


Figure 1.12: The BaTi_4O_9 structure, with tunnels viewable along the b axis. Ba = green, TiO_6 octahedra = blue.

Activity was shown to increase with decreasing band gaps E_g as approximated from transmission optical spectroscopy. In complex titanates (Fig. 1.13), the high activity is related to the density of the TiO_6 octahedra rather than tunnel size or shape; in the aforementioned β -gallia-rutile (BGR) intergrowth structure ($I4/m$), the tunnels are comprised of β -gallia blocks spaced apart by rutile blocks [17].

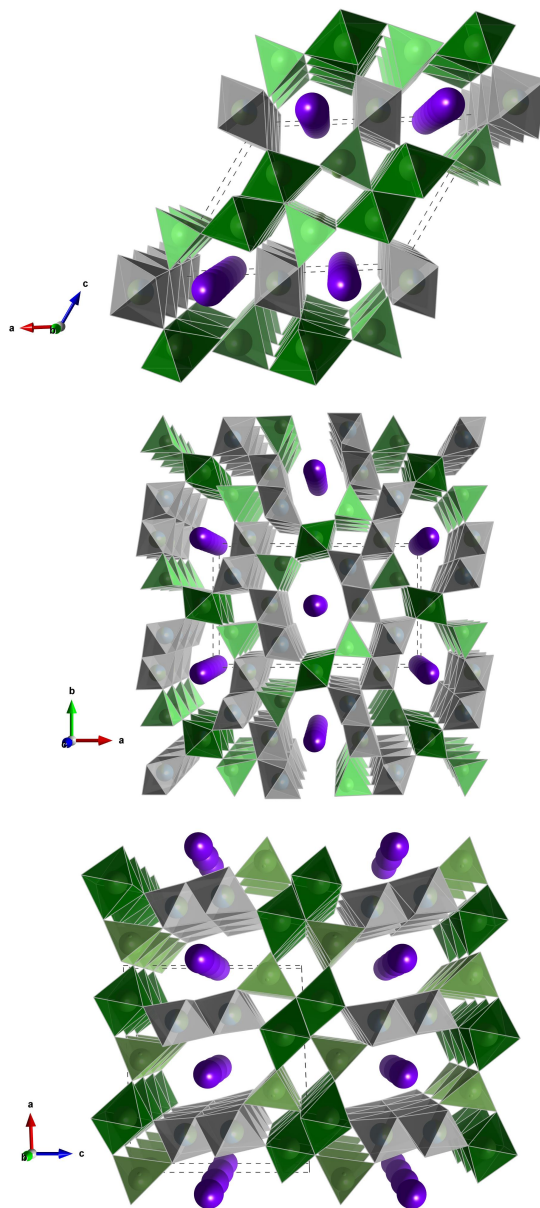


Figure 1.13: Examples of tunneled β -gallia rutile intergrowth titanates, with unit cell outlines shown in dashed lines. $\text{Na}_{0.7}\text{Ga}_{4.7}\text{Ti}_{0.3}\text{O}_8$ (top), $\text{Na}_{0.8}\text{Ga}_{4.8}\text{Ti}_{1.2}\text{O}_{10}$ (middle), $\text{Na}_{0.8}\text{Ga}_{4.8}\text{Ti}_{2.2}\text{O}_{12}$ (bottom). Na = purple, β -gallia blocks = green, rutile blocks = gray.

Pyrochlores can also exhibit high photocatalytic activity, e.g., CsTaWO_6 ($Fd\bar{3}m$) is shown to be promising for H_2 production [30]. It was shown that substitution of Nb for Ta in a 1:1 ratio insignificantly affects E_g , but activity changes drastically because of surface effects. In addition, substitution of Mo for W results in a conduction band minimum that is too positive for H_2 production; however, the valence band maximum is appropriate for O_2 evolution. This is an example of band gap engineering to coax new properties out of a material. Further details on this property can be found in Chapter 2.3.4.

1.2.3 Nonlinear Optics (NLO)

When designing advanced nonlinear optical materials, two major properties are involved: second-harmonic generation (SHG) and birefringence. Performance is expressed by a coefficient (χ^2) for SHG materials, and by the difference between refractive indices for birefringent materials [31]. Both of those properties can be correlated to crystal structure. Only non-centrosymmetric systems can produce SHG light, and non-cubic systems often exhibit birefringence [31]. These properties are exploited in laser technology to produce higher energy wavelengths, e.g., in green lasers, the output light (1064 nm) from $\text{Nd:Y}_3\text{Al}_5\text{O}_{12}$ (Nd:YAG, a Nd-doped garnet) is frequency-doubled by feeding it through a second-harmonic generator (such as LiB_3O_5 (LBO), Fig. 1.14) [32]. LBO lacks inversion symmetry ($Pna2_1$) and exhibits optical anisotropy.

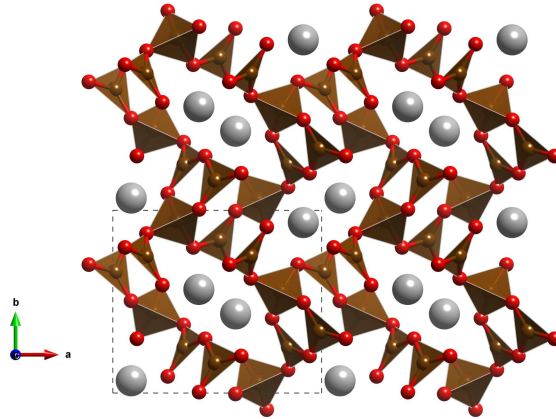


Figure 1.14: The LiB_3O_5 structure, with unit cell outlines shown in dashed lines. Li = gray, BO_4 tetrahedra and BO_3 trigonal planes = brown, O = red

Another framework that exhibits birefringence and a decent χ^2 is $\text{KBe}_2\text{BO}_3\text{F}_2$ (KBBF, $R32$), which contains an infinite planar network of $\text{Be}_3\text{B}_3\text{O}_6$ orthogonal to the c axis [33]. Cosubstitution of $\text{Sr}^{2+}/\text{O}^{2-}$ for K^+/F^- yields $\text{Sr}_2\text{Be}_2\text{B}_2\text{O}_7$ (SBBO, $P\bar{6}c2$), which was promising for SHG in the deep-UV wavelengths [34]. Difficulties in crystal growth, as well as the toxicity of Be, have led to several efforts to synthesize alternative analogs within this framework. One such example is $\text{K}_3\text{Ba}_3\text{Li}_2\text{Al}_4\text{B}_6\text{O}_{20}\text{F}$ ($P\bar{6}2c$), in which $\text{Li}^+/\text{Al}^{3+}$ is substituted for 2Be^{2+} and Ba^{2+} is added into the K^+ sites. (Fig. 1.15) [35].

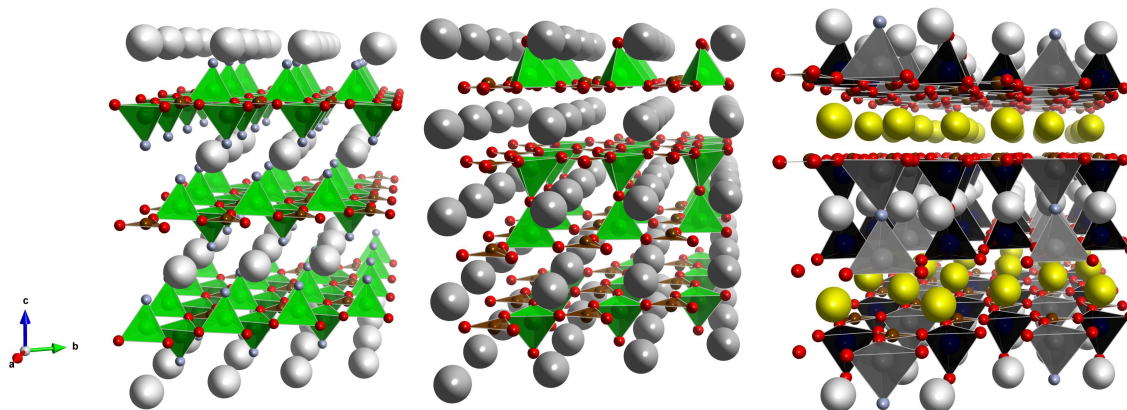


Figure 1.15: The KBBF (left), SBBO (middle), and $\text{K}_3\text{Ba}_3\text{Li}_2\text{Al}_4\text{B}_6\text{O}_{20}\text{F}$ (right) structures. K = white, Sr = gray, Ba = yellow, BeO_4 tetrahedra = green, BO_3 trigonal planes = brown, LiO_4 tetrahedra = dark gray, AlO_4 tetrahedra = black, O = red, F = pale blue.

1.2.4 Luminescence

Luminescent materials can be categorized by the excitation source, and may further be subdivided by mechanism, e.g., photoluminescence (light) can be described by either fluorescence ($\leq 10^{-8}$ s decay time) or phosphorescence (longer decay time) [4]. Phosphor materials in particular have been widely studied for their display applications, spawning a field of LED research. These materials generally consist of a host material (typically oxides) doped with activators (typically metal cations) that prolong the decay time by acting as impurities. Apatites ($3\text{Ca}_3(\text{PO}_4)_2 \cdot \text{Ca}(\text{Cl}, \text{F})_2$ ($P6_3/m$)) are one example of a host framework [4]. Another example is found in Eu^{2+} -doped minerals: gehlenite $\text{Ca}_2\text{Al}(\text{AlSiO}_7)$ ($P\bar{4}2_1m$) mixed with the Åkermanite $\text{Ca}_2\text{Mg}(\text{Si}_2\text{O}_7)$ ($P\bar{4}2_1m$) yields the melilite $\text{Ca}_2(\text{Al}_{1-x}\text{Mg}_x)(\text{Al}_{1-x}\text{Si}_{1+x})\text{O}_7$ ($P\bar{4}2_1m$)

via cosubstitution of $\text{Mg}^{2+}/\text{Si}^{4+}$ for $\text{Al}^{3+}/\text{Al}^{3+}$ (Fig. 1.16) [36]. The substitution in the tetrahedral site causes emission peak shifts from 513 to 538 nm as a result of crystal field perturbations. The same principle can also be applied to non-oxidic materials, like oxynitrides [37].

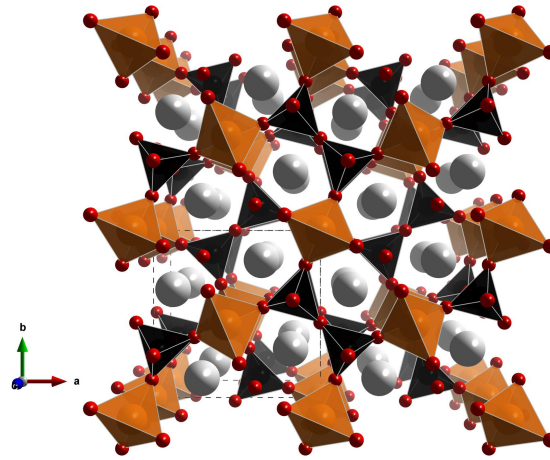


Figure 1.16: The Åkermanite structure, with unit cell outlines shown in dashed lines. Ca = white, MgO_4 tetrahedra = orange, SiO_4 tetrahedra = black, O = red.

1.2.5 Transparent Conducting Oxides (TCO)

Transparent conducting oxides are optically transparent while retaining metal-like conduction, and are used in various optoelectronic applications, from cell phone screens to modern television displays. The most studied compound is Sn-doped In_2O_3 ($Ia\bar{3}$), which has a conductivity of $\sim 10^3$ S/cm and is highly transparent when deposited as a thin film [38]. However, In-based compounds are cost-prohibitive, and further research is necessary to discover alternative materials with suitable transparency and

conductivity. One strategy involves solid solutions into the In_2O_3 structure to reduce the In content. For example, substituting Zn^{2+} for In^{3+} and charge balancing with O content can yield $\text{In}_{2-x}\text{Zn}_x\text{O}_{3-x/2}$. This can be extended further by substituting Sn^{4+} , yielding series like $\text{In}_{2-2x}\text{Sn}_x\text{Zn}_x\text{O}_3$ or $\text{In}_{2-x-y}\text{Sn}_x\text{Zn}_y\text{O}_{3-(y-x)/2}$ depending on the charge compensation mechanism [37, 38].

1.2.6 Photovoltaics (PV)

The modern world's growing need for sustainable energy sources has led to a diverse field of photovoltaics research, with organic chemists and biologists joining the forefront. Similar to photocatalysis, a PV cell involves a light-induced excitation of electrons from the valence to conduction bands. Unlike a photoreaction (in which an exciton migrates to the particle surface to initiate chemical reactions), a PV cell is integrated into a circuit, allowing current flow out of the system to power a device [39]. Currently, the industry standard is Si, packaged as modules in a series of thin films. Current research involves alternative materials that can utilize of a larger portion of the solar spectrum [40].

Therefore, an ideal PV cell material would have the following properties: E_g between 1.1 and 1.7 eV, direct band structure, non-toxic, readily available precursors, easy deposition conditions, high PV conversion efficiency, and long term stability [41]. One well-known structure type that has been explored for this property is the sphalerite ZnS ($F\bar{4}3m$), which can be transformed into the requisite CuInS_2 ($I\bar{4}2d$) via cosubstitution of $\text{Cu}^+/\text{In}^{3+}$ for 2Zn^{2+} . The observed symmetry reduction is due

to the ordering scheme, which splits the singular Zn site into two crystallographically distinct sites. This symmetry can be broken further to become the isostructural kesterite $\text{Cu}_2\text{ZnSnS}_4$ (CZTS, $I\bar{4}2m$) via $\text{Zn}^{2+}/\text{Sn}^{4+}$ for 2In^{3+} , which creates a total of three Zn sites, as Sn^{4+} exhibits a preference for one of the Zn sites (Fig. 1.17). Such compositional flexibility is manifest in the bandstructure, which could be engineered in the future to yield new phases with favorable photovoltaic capacity [42].

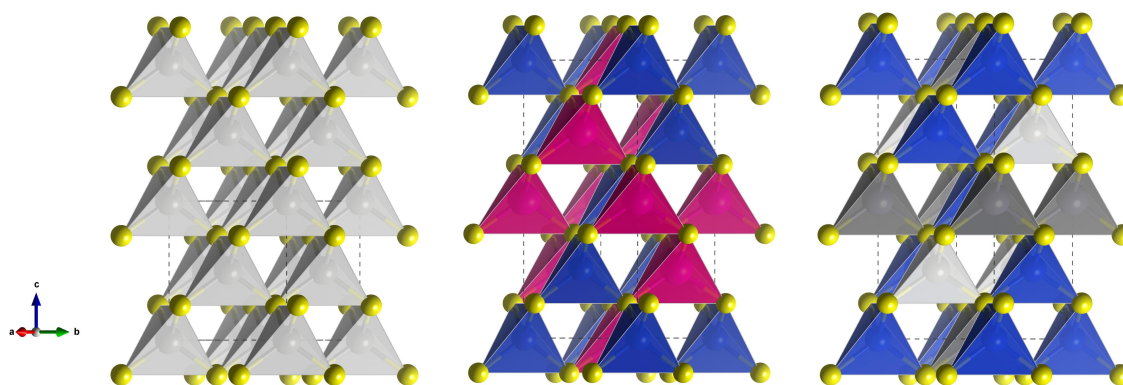


Figure 1.17: The sphalerite (left), roquesite (middle), and kesterite (right) structures, with unit cell outlines shown in dashed lines. Zn-centered tetrahedra = gray, Cu-centered tetrahedra = blue, In-centered tetrahedra = pink, Sn-centered tetrahedra = dark gray, S = yellow.

1.3 The Lyonsite Structure

Exploratory work in solid state chemistry has involved many structure types in the past century; while some structures are more ubiquitous in the literature, the understudied systems are no less worthy of investigation. In 2006, one of these lesser known families, the lyonsites, was given a thorough treatment in a seminal review [43],

and what follows here is a brief recapitulation of that work.

While the perovskite [24], pyrochlore [11, 44–46], and spinel [47] families have extensive histories, the lyonsite had its beginnings in the laboratory, being first synthesized in 1960 [48], and a general structure determination carried out in 1964 [49]. This compound, $\text{NaCo}_{2.31}(\text{MoO}_4)_3$ (*Pmcn*), was recognized as a new structure type. By 1970, two other compounds, $\text{Li}_3\text{Fe}(\text{MoO}_4)_3$ and $\text{Li}_2\text{Fe}_2(\text{MoO}_4)_3$ were discovered, and the structural similarity was noted, but no further elaboration was given [50]. Contrary to the typical trend of mineralogy inspiring chemistry, a natural lyonsite was not discovered until 1987, in which the iron-copper vanadate $\alpha\text{-Cu}_3\text{Fe}_4(\text{VO}_4)_6$ (*Pmcn*) was as a fumarolic sublimate at Izalco volcano in El Salvador; it was then named for mineralogist John B. Lyons [51].

1.3.1 Structural Description

The lyonsites can be described by a handful of general formulas, the most broad being $A_{16}M_{12}O_{48}$ (or $A_{16}(\text{MO}_4)_{12}$). The latter stoichiometry is shared in several other unrelated structures (e.g., fluorite derivatives [52] and cation-deficient perovskites [53, 54]). In many cases, as shown in this section, the stoichiometry is scaled down by a factor of 4 to yield $A_4M_3O_{12}$ (or $A_4(\text{MO}_4)_3$). Other common formula expressions also involve simple multipliers to clarify stoichiometric features or to facilitate ease of reading, e.g., scaling by 1.5 and introducing vacancies yields $\square_{1/6}A_{2.5}M_2O_8$.

This framework can be described by its structural motifs; a hexagonal tunnel comprised of zigzag sheets of edge-sharing AO_6 trigonal prisms and columns of edge-

sharing AO_6 octahedra gives the overall appearance of a "bracelet", while the inner wall of this tunnel is lined with isolated MO_4 tetrahedra in a "pinwheel" fashion, and passing through the center of the tunnel is an infinite chain of face-sharing AO_6 octahedra (Fig. 1.19). Via symmetry, this tunnel can then be tiled to yield a tessellation orthogonal to the primary viewing axis; in most cases, this is the a axis. While there are lyonsite-related minerals, these specific features are similar to only one other crystal system, even less studied than the lyonsite: the dumortierite structure (Fig. 1.18) [55, 56].

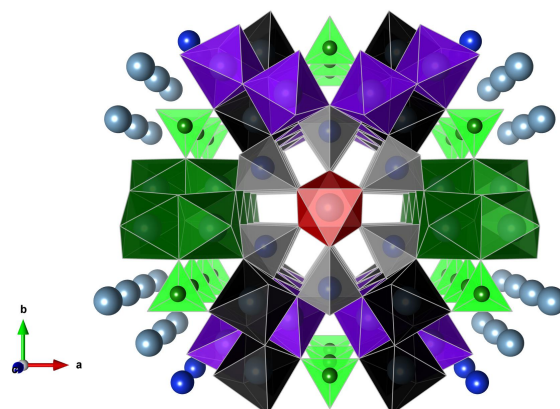


Figure 1.18: The primary tunnel motif of the $Al_7BO_3(SiO_4)_3O_3$ ($Pm\bar{c}n$) member of the dumortierite mineral family. AlO_6 face-sharing octahedra = red, AlO_6 edge-sharing octahedra = purple, black, AlO_6 face- and edge-sharing octahedra = dark green, SiO_4 tetrahedra = gray, BO_3 trigonal planes = green, Al = pale blue, Si = blue, B = green.

Typically, two cations occupy the A sites, the ionic radius range of which are empirically generalized to 0.46 to 1.02 Å [43]. The oxidation states of these cations can range between +1 and +5 [43]. The M site is limited to smaller, highly charged cations that prefer four-fold coordination [57, 58]. To date, this only includes V^{5+} , Mo^{6+} , and

W^{6+} [43]. The A sites are further distinguished by their polyhedral sharing schemes: A1 (face-shared octahedra), A2 (edge-shared octahedra), and A3 (edge-shared trigonal prisms) (Fig. 1.19). The M sites are also crystallographically distinct: M1 and M2. Each oxygen is bonded to two A atoms and one M atom. Overall, these features can be expressed in a descriptive formula as $AB_2C(M, M'O_4)_3$ [37].

The majority of these oxides crystallize in the $Pnma$ space group; however, the structural flexibility has led to the observation of several lyonsites crystallizing in subgroups of $Pnma$. This structural flexibility is also reflected in the ability to incorporate vacancies, \square ; these vacancies tend to localize in the face-sharing octahedral chain. Consequently, the bonded oxygens will displace towards the higher oxidation state M cation. Substitutions can therefore be made into any site exclusively or across all sites with vacancy compensation.

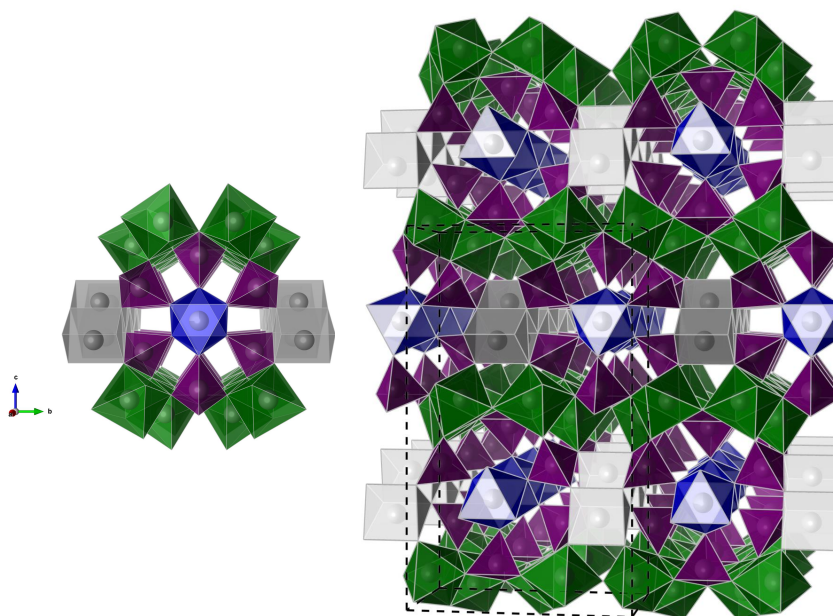


Figure 1.19: The lyonsite crystal structure as viewed along the a axis (A1 = blue, A2 = green, A3 = gray, M1, M2 = purple). Left: primary tunnel motif of the lyonsite. Right: representation of broader structure, with unit cell outline shown in dashed lines.

The trigonal prism environment is an unusual one, even in this structure; in most of the molybdate lyonsites discussed in the next section, the A3 site is fairly uniform; however, in Zn- and Cu-containing lyonsites, this site is highly distorted, with the cations pushed towards one of the square windows. They can be treated as distorted square pyramids ($\text{Cu}_{3.85}(\text{MoO}_4)_3$ [59], $(\text{Cu}, \text{Fe})_{3.63}(\text{MoO}_4)_3$ [60]) or square planes, in which one pair of $A\text{-O}$ bonds is significantly longer than the others, as in the case of $(\text{Cu}, \text{Mn})_{3.66}(\text{MoO}_4)_3$ [61], $(\text{Cu}, \text{Co})_{3.75}(\text{MoO}_4)_3$ [62], and $\text{Cu}_3\text{Fe}_4\text{V}_6\text{O}_{24}$ [51].

1.3.2 Molybdates

As mentioned, known lyonsites typically contain two cations in the *A* site, usually Li^+ , a transition metal (TM), and vacancies, the ratios and distribution of which are dictated primarily by charge separation. The molybdate members of this family show the most diversity in *A* site substitution [63]. After the discovery of $\text{Li}_3\text{Fe}(\text{MoO}_4)_3$ and $\text{Li}_2\text{Fe}_2(\text{MoO}_4)_3$, structural similarities were noted in an increasing number of compounds over the 1971–1987 period [43]. An empirical trend was observed: one *A* cation was an alkali metal ion (Li^+ , Na^+) and the other was of a flexible oxidation state. To maintain stoichiometry and charge neutrality, the possible *A* site combinations were found to be: $A_3^+A'^{3+}$ and $A_2^+A_2'^{2+}$. Some examples of such compounds include $\text{Li}_3\text{AlMo}_3\text{O}_{12}$ [64], $\text{Li}_3\text{ScMo}_3\text{O}_{12}$ [65], $\text{Li}_2\text{Cu}_2\text{Mo}_3\text{O}_{12}$ [66], $\text{Li}_2\text{Co}_2\text{Mo}_3\text{O}_{12}$ [67], $\text{Li}_2\text{Zn}_2\text{Mo}_3\text{O}_{12}$ [68], and $\text{Li}_2\text{Ni}_2\text{Mo}_3\text{O}_{12}$ [69, 70]. Introducing higher oxidation state cations or breaking this pattern necessitated the creation of vacancies (e.g., 6.25% of the *A* site in $\text{Li}_3\text{Ti}_{0.75}\text{Mo}_3\text{O}_{12}$ [71] is vacant), and/or a change in oxidation states, as in $\text{Cu}_{3.85}\text{Mo}_3\text{O}_{12}$ (in which Cu^+ is present, and 3.75% of the *A* site is vacant) [59]. One of the few lyonsites to exhibit cation and vacancy ordering in the A1 site is $\text{Li}_2\text{Zr}(\text{MoO}_4)_3$, in which the symmetry is reduced to $Pmn2_1$.

1.3.3 Vanadates

The mineral $\alpha\text{-Cu}_3\text{Fe}_4(\text{VO}_4)_6$ (*A* site vacancy: 12.5 %) was the first discovered vanadate variety. Attempts to replicate this in a laboratory setting had been unsuccessful, and resulted in a $\beta\text{-Cu}_3\text{Fe}_4(\text{VO}_4)_6$ phase. It was surmised that synthesis

of the α form was only possible at high pressures, mimicking that of the geological conditions for the mineral formation [72]. However, the ability of the structure type to incorporate vacancies allowed for off-stoichiometries, resulting in compounds like $\text{Cu}_4\text{Fe}_{3.33}(\text{VO}_4)_6$ (A site vacancy: 8.375%), $\text{Co}_4\text{Fe}_{3.33}(\text{VO}_4)_6$, $\text{Co}_{3.6}\text{Fe}_{3.6}(\text{VO}_4)_6$ (A site vacancy: 10 %), $\text{Cu}_{4.05}\text{Cr}_{3.3}(\text{VO}_4)_6$ (A site vacancy: 8.125 %), and $\text{Co}_5\text{Cr}_{2.667}(\text{VO}_4)_6$ (A site vacancy: 4.1625 %) [43]. It was determined that all these samples fall on the $A_{3+1.5x}A'_{4-x}(\text{VO}_4)_6$ phase line. It is clear at this point that a fully occupied model for vanadates cannot be charge balanced, and must inherently incorporate vacancies. For example, a more formal expression of $\alpha\text{-Cu}_3\text{Fe}_4(\text{VO}_4)_6$ would be $\square_2\text{Cu}_6\text{Fe}_8\text{V}_{12}\text{O}_{48}$.

1.3.4 Vanadomolybdates

The vanadomolybdates (in which past studies have often scaled down the stoichiometry by 1.5x for clarity [57, 73, 74]) are less studied than their previous counterparts. One such example is $\text{Mg}_{2.5}\text{VMoO}_8$, which was found to be catalytically active for hydrocarbon oxidation. Like the vanadate varieties, these lyonsites contain unavoidable vacancies, e.g., $\text{Mg}_{2.5}\text{VMoO}_8$ is rewritten as $\square\text{Mg}_{15}\text{V}_6\text{Mo}_6\text{O}_{48}$. Of note are two particular compounds, $\text{Zn}_{2.5}\text{VMoO}_8$ [75], white in color, crystallizing as $P2_12_12_1$, and $\text{Co}_{2.5}\text{VMoO}_8$ [74], which appears almost black, crystallizing as $Pnma$. They are two of the few known lyonsites in which only one cation (and corresponding vacancies) occupy the A site [57, 58, 73, 75]. Chapter 3 details an investigation into a solid solution between these two species and the resulting structural and physical properties. Until this work, the site preference for Zn^{2+} in this structure was unknown. In addition, the

other end member, $\text{Co}_{2.5}\text{VMoO}_8$, had been reported, but no physical properties had been explored [74]. Among the properties of the solid solution was its color, exhibiting varying shades of green.

Following the conclusions of that work, with this behavior in mind, it was worth experimentation to coax and tune other colors from this system of compounds. Chapter 4 therefore presents novel compositions and some physical properties of cationic substitutions into the white Zn-rich end member, namely with Mn, Ni, and Cu ions. A structural treatment of the end member $\text{Mn}_{2.5}\text{VMoO}_8$ was given in the literature [73], but no physical properties had been measured, so the possible color range was unknown. In addition, a fully substituted Ni lyonsite is not known to exist, and a fully substituted Cu lyonsite is demonstrated with Mo^{6+} as the M cation [59]. Substitutions with these two elements were therefore worthy of exploration, considering NiO/CuO are lower-cost precursors relative to CoO. In addition, Cu^{2+} is a Jahn-Teller active ion [21], which can sometimes create structural oddities [66, 76].

The hard solubility limits of the previous work prompted the work done in Chapter 5, which discusses the relationship between cationic substitution and vacancy concentration. In a previously studied work, a solid solution between was found between $\text{Li}_2\text{Mg}_2\text{Mo}_3\text{O}_{12}$ and the isostructural $\text{Mg}_{2.5}\text{VMoO}_8$, and was expressed as $\square_{0.25-\frac{1}{6}x}\text{Li}_{\frac{4}{3}x}\text{Mg}_{3.75-\frac{7}{6}x}\text{V}_{1.5-x}\text{Mo}_{1.5+x}\text{O}_{12}$ (in which the vacancy \square concentration varies as a function of charge neutrality and stoichiometric ratios of each cation) [77]. This vacancy tunability has been suggested for other lyonsite phases, but has not been explored. This behavior has also been demonstrated to be useful in catalysis and ionic conduction applications, e.g., the creation of cationic vacancies in the NASICON-like

lyonsite $(\text{Li, Na})_2\text{Fe}_2(\text{MoO}_4)_3$ facilitates Li-ion mobility [78]. To further explore this flexibility and to confirm the conclusions made in [43], a solid solution between the $\text{Li}_2\text{Co}_2(\text{MoO}_4)_3$ ($\square = 0$) and $\text{Co}_{2.5}\text{V}\text{MoO}_8$ ($\square_{0.25}\text{Co}_{3.75}\text{V}_{1.5}\text{Mo}_{1.5}\text{O}_{12}$) was synthesized, following the formula $\square_{0.25-\frac{1}{8}x}\text{Li}_x\text{Co}_{3.75-\frac{7}{8}x}\text{V}_{1.5-\frac{3}{4}x}\text{Mo}_{1.5+\frac{3}{4}x}\text{O}_{12}$.

1.3.5 Tungstates/Vanadotungstates

Prior to 2006, only two compounds of this variety were known, $\text{Li}_2\text{Mg}_2(\text{WO}_4)_3$ and $\text{Mg}_{2.5}\text{V}\text{WO}_8$ [79, 80]. Attempts to form $\text{Li}_2A'_2(\text{WO}_4)_3$ with anything other than Mg^{2+} have failed. Further investigation is therefore needed to understand the disparity in phase stability between Mo^{6+} - and W^{6+} - substituted lyonsites.

1.3.6 Physical Properties

Since their discovery, various lyonsite compounds have been proposed for direct functional applications. For example, $\text{Li}_2\text{Co}_2(\text{MoO}_4)_3$ can be considered to be a part of the NASICON (Na super ionic conductor) family, as it is constructed of a polyanionic framework with Li-occupied channels. This particular compound exhibits Li insertion/de-insertion at 4.9 V via oxidation of Co^{2+} to Co^{3+} , and at 1.5 V, de-insertion results in the reduction of Mo^{6+} to Mo^{5+} [26]. Similarly, $\text{Li}_2\text{Ni}_2(\text{MoO}_4)_3$ exhibits a reversible discharge capacity of ≈ 115 mAh/g [81].

Other examples include $\text{Li}_{2-x}\text{Mg}_{2+x}(\text{MoO}_4)_3$ ($0 \leq x \leq 0.3$) and $\text{Li}_3A'^{3+}(\text{MoO}_4)_3$ ($A'^{3+} = \text{Cr, Fe}$) [63]. While the framework is 3-dimensional the conduction pathway

is along the trigonal prismatic A3 site, which is exclusively occupied by Li. Because the conduction pathway is along the A3 site, it is possible that vacancies exist there in addition to the A1 site. The A3 site is preferable for ion migration due to the connectivity and window size ($\approx 3.95 \times 4.00 \text{\AA}$). AC impedance spectroscopy confirms that the conduction is 1-dimensional, with σ_{300} values of $\sim 10^{-7}$ S/cm for $\text{Li}_{2-x}\text{Mg}_{2+x}(\text{MoO}_4)_3$ and $\sim 10^{-6}$ S/cm for $\text{Li}_3A'^{3+}(\text{MoO}_4)_3$. For the former series, the low conductivity (as x increases) is attributed to the presence of +2 cations in the A3 site, which impedes the Li-ion mobility. For the latter series, the observed conductivity is superior to that of other 1D ionic conductors like LiAlSiO_4 and LiSbO_3 [63].

A similar example of this behavior exists with $\text{Li}_{3+x}\text{Fe}(\text{MoO}_4)_3$, in which insertion and de-insertion of Li is reversible via the reduction of Fe^{3+} [82]. Recently, the tungstate $\text{Li}_2\text{Mg}_2\text{W}_3\text{O}_{12}$ doped with Eu^{3+} was recently found to be a promising red phosphor for white light-emitting diodes [79]. Other compounds, like $\text{Li}_3\text{FeMo}_3\text{O}_{12}$, $\text{Li}_2\text{Mg}_2\text{Mo}_3\text{O}_{12}$, and $\text{Li}_2A'_2\text{Mo}_3\text{O}_{12}$ ($A' = \text{Zn}, \text{Ca}$), exhibit favorable microwave dielectric quality factors [83–85]. Some of the mentioned lyonsites, such as $\text{Zn}_{2.5}\text{VMoO}_8$ and $\text{Li}_3\text{FeMo}_3\text{O}_{12}$ are also noted for their photocatalytic activity [86, 87].

1.4 Other Structure Types in this Dissertation

1.4.1 The Spinel Structure

The well-studied spinel structure takes the general formula AM_2X_4 , in which A (8a site; $1/8, 1/8, 1/8$) and M (16d site; $1/2, 1/2, 1/2$) are metal cations and X (32e site; x, x, x) is an anion, typically oxygen [4, 47]. As mentioned, the structure can be described from a close packing perspective: the X anions form a ccp lattice with $1/8$ of the tetrahedral voids filled by the A cations and $1/2$ of the octahedral voids filled by the M cations (Fig. 1.20).

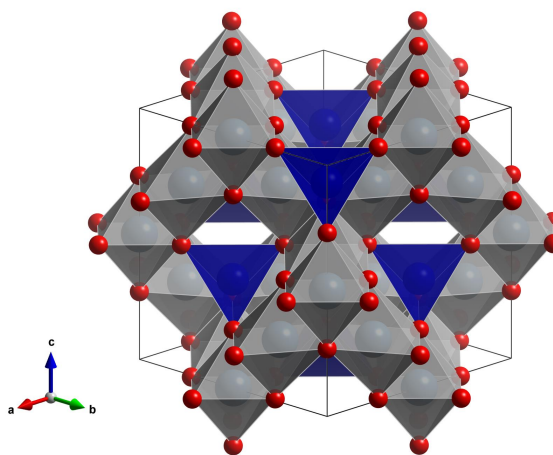


Figure 1.20: A unit cell representing the spinel structure (CoAl_2O_4 , $Fd\bar{3}m$). CoO_4 tetrahedra = blue, AlO_6 octahedra = gray, O = red.

Most spinels are rigid, adopting the cubic $Fd\bar{3}m$ space group; exceptions include displacement of X from its ideal position ($x = 1/4$), causing bond angle distortions away from 90° . Another exception involves tetragonal distortion due to Jahn-Teller effects at the A site, as with CuCr_2O_4 and NiCr_2O_4 [88–90]. Furthermore, the spinel

structure has an interesting subfeature; it can be described as a convolution of diamond (A site) and pyrochlore (M site) sublattices. The identity of the site occupants can cause geometric frustration, a useful situation for studying uncommon magnetic states [47, 91].

References

- [1] B. D. Cullity, S. R. Stock, Elements of X-Ray Diffraction, 3rd ed., Pearson, New Jersey, 2001.
- [2] E. Hahn, T., International Tables for Crystallography Volume A: Space-group symmetry, 5th ed., International Union of Crystallography, Chester, 2006.
- [3] R. Berthelot, W. Schmidt, S. Muir, J. Eilertsen, L. Etienne, A. W. Sleight, M. A. Subramanian, New layered compounds with honeycomb ordering: $\text{Li}_3\text{Ni}_2\text{BiO}_6$, $\text{Li}_3\text{NiM}'\text{BiO}_6$ ($M' = \text{Mg}, \text{Cu}, \text{Zn}$), and the delafossite $\text{Ag}_3\text{Ni}_2\text{BiO}_6$, Inorg. Chem. 51 (2012) 5377–5385. doi:10.1021/ic300351t.
- [4] A. R. West, Solid State Chemistry and its Applications, 2nd Edition, Student Edition, Wiley, Chichester, 2014.
- [5] Q. Wang, C. Liang, Y. Zheng, N. Ashburn, Y. J. Oh, F. Kong, C. Zhang, Y. Nie, J. Sun, K. He, Y. Ye, R. Chen, B. Shan, K. Cho, First principles study of the Mn-doping effect on the physical and chemical properties of mullite-family Al_2SiO_5 , Phys. Chem. Chem. Phys. 19 (2017) 24991–25001. doi:10.1039/C7CP04611A.
- [6] J. Li, S. Lorger, J. K. Stalick, A. W. Sleight, M. A. Subramanian, From serendipity to rational design: Tuning the blue trigonal bipyramidal Mn^{3+} chromophore to violet and purple through application of chemical pressure, Inorg. Chem. 55 (19) (2016) 9798–9804. doi:10.1021/acs.inorgchem.6b01639.
- [7] J. Li, E. A. Medina, J. K. Stalick, A. W. Sleight, M. A. Subramanian, Colored oxides with hibonite structure: A potential route to non-cobalt blue pigments, Prog. Solid State Chem. 44 (4) (2016) 107 – 122. doi:10.1016/j.progsolidstchem.2016.11.001.
- [8] E. A. Medina, J. Li, M. A. Subramanian, Colored oxides with hibonite structure ii:

- Structural and optical properties of $\text{CaAl}_{12}\text{O}_{19}$ -type pigments with chromophores based on Fe, Mn, Cr and Cu, *Prog. Solid State Chem.* 45-46 (2017) 9 – 29. doi:10.1016/j.progsolidstchem.2017.02.002.
- [9] M. D. Radin, A. Van der Ven, Stability of prismatic and octahedral coordination in layered oxides and sulfides intercalated with alkali and alkaline-earth metals, *Chem. Mater.* 28 (2016) 7898–7904. doi:10.1021/acs.chemmater.6b03454.
- [10] M. Avdeev, V. B. Nalbandyan, I. L. Shukaev, V. V. E. Kharton, *Solid State Electrochemistry I: Fundamentals, Materials and their Applications*, Wiley, 2009. doi:10.1002/9783527627868.
- [11] M. A. Subramanian, G. Aravamudan, G. V. Subba Rao, Oxide pyrochlores — A review, *Prog. Solid State Chem.* 15 (1983) 55–143. doi:10.1016/0079-6786(83)90001-8.
- [12] H. Mizoguchi, W. J. Marshall, A. P. Ramirez, A. W. Sleight, M. A. Subramanian, Partial charge ordering in the mixed-valent compound $(\text{Bi}_6\text{O}_5)\text{Rh}_8^{3+}\text{Rh}_4^{4+}\text{O}_{24}$, *J. Solid State Chem.* 180 (2007) 3463–3468. doi:10.1016/j.jssc.2007.09.031.
- [13] S. Yoshikado, T. Ohachi, I. Taniguchi, Frequency-independent ionic conductivity of hollandite type compounds, *Solid State Ionics* 10 (1983) 1305–1309.
- [14] R. N. De Guzman, A. Awaluddin, Y. F. Shen, Z. R. Tian, S. L. Suib, S. Ching, C. L. O’Young, Electrical-resistivity measurements on manganese oxides with layer and tunnel structures - birnessites, todorokites, and cryptomelanes, *Chem. Mater.* 7 (1995) 1286–1292.
- [15] L. Bursill, Structural relationships between β -gallia, rutile, hollandite, psilomelane, ramsdellite and gallium titanate type structures, *Acta Crystallogr.* B35 (1979) 530–538.
- [16] T. M. Tritt, M. A. Subramanian, Thermoelectric materials, phenomena, and applications: a bird’s eye view, *Mater. Res. Bull.* 31 (03) (2006) 188–198. doi:10.1557/mrs2006.44.
- [17] S. Sanford, S. T. Misture, D. D. Edwards, A comparison of the photocatalytic activity of six tunneled titanates, *J. Solid State Chem.* 200 (2013) 189–196. doi:10.1016/j.jssc.2012.12.036.
- [18] G. L. Miessler, P. J. Fischer, D. A. Tarr, *Inorganic Chemistry*, 5th Edition,

Pearson, 2013.

- [19] D. Abeysinghe, M. D. Smith, J. Yeon, T. T. Tran, R. Paria Sena, J. Hadermann, P. S. Halasyamani, H.-C. zur Loye, Crystal growth and structure analysis of $\text{Ce}_{18}\text{W}_{10}\text{O}_{57}$: A complex oxide containing tungsten in an unusual trigonal prismatic coordination environment, *Inorg. Chem.* 56 (5) (2017) 2566–2575. doi:10.1021/acs.inorgchem.6b02710.
- [20] R. Hoffmann, J. M. Howell, A. R. Rossi, Bicapped tetrahedral, trigonal prismatic, and octahedral alternatives in main and transition group six-coordination, *J. Am. Chem. Soc.* 98 (1976) 2484–2492. doi:10.1021/ja00425a016.
- [21] H. A. Jahn, E. Teller, Stability of polyatomic molecules in degenerate electronic states: I—orbital degeneracy, *Proc. R. Soc. London A* 161 (1937) 220–235. doi:10.1098/rspa.1937.0142.
- [22] D. A. Egger, A. M. Rappe, L. Kronik, Hybrid organic–inorganic perovskites on the move, *Acc. Chem. Res.* 49 (3) (2016) 573–581. doi:10.1021/acs.accounts.5b00540.
- [23] H.-S. Kim, S. H. Im, N.-G. Park, Organolead halide perovskite: New horizons in solar cell research, *J. Phys. Chem. C* 118 (2014) 5615–5625. doi:10.1021/jp409025w.
- [24] S. Vasala, M. Karppinen, $\text{A}_2\text{B}'\text{B}''\text{O}_6$ perovskites : A review, *Prog. Solid State Chem.* 43 (2015) 1–36. doi:10.1016/j.progsolidstchem.2014.08.001.
- [25] D. A. Tompsett, M. S. Islam, Surfaces of rutile MnO_2 are electronically conducting, whereas the bulk material is insulating, *J. Phys. Chem. C* 118 (2014) 25009–25015. doi:10.1021/jp507189n.
- [26] S. Prabaharan, S. Ramesh, M. Michael, K. Begam, Characterization of soft-combustion-derived NASICON-type $\text{Li}_2\text{Co}_2(\text{MoO}_4)_3$ for lithium batteries, *Mater. Chem. Phys.* 87 (2-3) (2004) 318–326. doi:10.1016/j.matchemphys.2004.05.041.
- [27] J. Goodenough, H. Hong, J. Kafalas, Fast Na^+ -ion transport in skeleton structures, *Mater. Res. Bull.* 11 (2) (1976) 203–220. doi:10.1016/0025-5408(76)90077-5.
- [28] M. Subramanian, P. Rudolf, A. Clearfield, The preparation, structure, and conductivity of scandium-substituted NASICONs, *J. Solid State Chem.* 60 (2)

- (1985) 172–181. doi:10.1016/0022-4596(85)90109-4.
- [29] M. Kaneko, I. Okura, *Photocatalysis: Science and Technology*, Springer, 2003.
- [30] L. Schwertmann, A. Grünert, A. Pougín, C. Sun, M. Wark, R. Marschall, Understanding the influence of lattice composition on the photocatalytic activity of defect-pyrochlore-structured semiconductor mixed oxides, *Adv. Funct. Mater.* 25 (2015) 905–912. doi:10.1002/adfm.201403092.
- [31] H. Zhang, M. Zhang, S. Pan, Z. Yang, Z. Wang, Q. Bian, X. Hou, H. Yu, F. Zhang, K. Wu, F. Yang, Q. Peng, Z. Xu, K. Chang, K. Poepplmeier, $\text{Na}_3\text{Ba}_2(\text{B}_3\text{O}_6)_2\text{F}$: Next generation of deep-ultraviolet birefringent materials, *Cryst. Growth Des.* 15 (2015) 523–529. doi:10.1021/cg5016912.
- [32] S. Lin, Z. Sun, B. Wu, C. Chen, The nonlinear optical characteristics of a LiB_3O_5 crystal, *J. Appl. Phys.* 67 (2) (1990) 634–638.
- [33] C. Chen, Y. Wang, Y. Xia, B. Wu, D. Tang, K. Wu, Z. Wenrong, L. Yu, L. Mei, New development of nonlinear optical crystals for the ultraviolet region with molecular engineering approach, *J. Appl. Phys.* 77 (6) (1995) 2268–2272.
- [34] C. Chen, Y. Wang, B. Wu, K. Wu, W. Zeng, L. Yu, Design and synthesis of an ultraviolet-transparent nonlinear optical crystal $\text{Sr}_2\text{Be}_2\text{B}_2\text{O}_7$, *Nature* 373 (1995) 322.
- [35] S. Zhao, L. Kang, Y. Shen, X. Wang, M. A. Asghar, Z. Lin, Y. Xu, S. Zeng, M. Hong, J. Luo, Designing a beryllium-free deep-ultraviolet nonlinear optical material without a structural instability problem, *J. Am. Chem. Soc.* 138 (9) (2016) 2961–2964. doi:10.1021/jacs.6b00436.
- [36] Z. Xia, C. Ma, M. S. Molokeev, Q. Liu, K. Rickert, K. R. Poepplmeier, Chemical unit cosubstitution and tuning of photoluminescence in the $\text{Ca}_2(\text{Al}_{1-x}\text{Mg}_x)(\text{Al}_{1-x}\text{Si}_{1+x})\text{O}_7:\text{Eu}^{2+}$ phosphor, *J. Am. Chem. Soc.* 137 (39) (2015) 12494–12497. doi:10.1021/jacs.5b08315.
- [37] Z. Xia, K. R. Poepplmeier, Chemistry-inspired adaptable framework structures, *Acc. Chem. Res.* 50 (5) (2017) 1222–1230. doi:10.1021/acs.accounts.7b00033.
- [38] G. B. Palmer, K. R. Poepplmeier, T. O. Mason, Conductivity and transparency of ZnO/SnO_2 -cosubstituted In_2O_3 , *Chem. Mater.* 9 (12) (1997) 3121–3126. doi:10.1021/cm9704037.

- [39] R. J. D. Tilley, *Understanding Solids: The Science of Materials*, 2nd ed., Wiley, 2013.
- [40] A. Goetzberger, C. Hebling, Photovoltaic materials, past, present, future, *Sol. Energy Mater. Sol. Cells* 62 (2000) 1–19. doi:10.1016/S0927-0248(99)00131-2.
- [41] A. Goetzberger, C. Hebling, H.-W. Schock, Photovoltaic materials, history, status and outlook, *Mater. Sci. Eng., R* 40 (2003) 1–46. doi:10.1016/S0927-796X(02)00092-X.
- [42] C. Wang, S. Chen, J.-H. Yang, L. Lang, H.-J. Xiang, X.-G. Gong, A. Walsh, S.-H. Wei, Design of $I_2-II-IV-VI_4$ semiconductors through element substitution: The thermodynamic stability limit and chemical trend, *Chem. Mater.* 26 (11) (2014) 3411–3417. doi:10.1021/cm500598x.
- [43] J. P. Smit, P. C. Stair, K. R. Poeppelmeier, The adaptable lyonsite structure, *Chem. Eur. J.* 12 (2006) 5944–5953. doi:10.1002/chem.200600294.
- [44] F. Jona, G. Shirane, R. Pepinsky, Dielectric, X-ray, and optical study of ferroelectric $Cd_2Nb_2O_7$ and related compounds, *Phys. Rev.* 98 (1955) 903–909. doi:10.1103/PhysRev.98.903.
- [45] R. Jin, J. He, S. McCall, C. S. Alexander, F. Drymiotis, D. Mandrus, Superconductivity in the correlated pyrochlore $Cd_2Re_2O_7$, *Phys. Rev. B* 64 (2001) 180503(R). doi:10.1103/PhysRevB.64.180503.
- [46] A. W. Sleight, New ternary oxides of mercury with the pyrochlore structure, *Inorg. Chem.* 7 (1968) 1704–1708. doi:10.1021/ic50067a003.
- [47] A. P. Ramirez, Colossal magnetoresistance, *J. Phys. Condens. Matter* 9 (1997) 8171–8199. doi:10.1088/0953-8984/9/39/005.
- [48] G. W. Smith, Crystal structure of orthorhombic cobalt molybdate, *Nat.* 188 (1960) 306–308. doi:10.1038/188306b0.
- [49] J. A. Ibers, G. W. Smith, Crystal structure of a sodium cobalt molybdate, *Act. Crystallogr.* 17 (1964) 190–197. doi:10.1107/S0365110X64000482.
- [50] R. F. Klevtsova, S. A. Magarill, Crystal structure of lithium-ferriferrous molybdates $Li_3Fe(MoO_4)_3$ and $Li_2Fe_2(MoO_4)_3$, *Kristallografiya* 15 (1970) 710–715.

- [51] J. M. Hughes, S. J. Starkey, M. L. Malinconico, L. L. Malinconico, Lyonsite, $\text{Cu}_3^{2+}\text{Fe}_4^{3+}(\text{VO}_4)_6^{3-}$, a new fumarolic sublimate from Izalco Volcano, El Salvador; descriptive mineralogy and crystal structure, *Am. Mineral.* 72 (1987) 1000–1005.
- [52] C. R. Stanek, C. Jiang, B. P. Uberuaga, K. E. Sickafus, A. R. Cleave, R. W. Grimes, Predicted structure and stability of $A_4B_3O_{12}$ δ -phase compositions, *Phys. Rev. B* 80 (2009) 174101. doi:10.1103/PhysRevB.80.174101.
- [53] L. Fang, H. Zhang, Q. Yu, H. Su, B. Wu, X. Cui, $\text{Sr}_3\text{LaNb}_3\text{O}_{12}$: A new low loss and temperature stable $A_4B_3O_{12}$ -type microwave dielectric ceramic, *J. Am. Ceram. Soc.* 92.
- [54] L. Fang, S.-S. Meng, H. Zhang, Z.-Q. Liu, $\text{Ba}_2\text{La}_2\text{TiNb}_2\text{O}_{12}$: A new microwave dielectric of $A_4B_3O_{12}$ -type cation-deficient perovskites, *Mater. Lett.* 60 (9) (2006) 1147 – 1150. doi:10.1016/j.matlet.2005.10.097.
- [55] R. J. Evans, L. A. Groat, Structure and topology of dumortierite and dumortierite-like materials, *Can. Mineral.* 50 (5) (2012) 1197–1231. doi:10.3749/canmin.50.5.1197.
- [56] A. Pieczka, R. J. Evans, E. S. Grew, L. A. Groat, C. Ma, G. R. Rossman, The dumortierite supergroup. I. A new nomenclature for the dumortierite and holtite groups, *Mineral. Mag.* 77 (2013) 2825–2839. doi:10.1180/minmag.2013.077.6.09.
- [57] X. Wang, J. D. Pless, D. A. Vander Griend, P. C. Stair, K. R. Poeppelmeier, Z. Hu, J. D. Jorgensen, Vanadium and molybdenum disorder in $\text{M}_{2.5}\text{VMoO}_8$ ($\text{M} = \text{Mg}, \text{Mn}, \text{and Zn}$) determined with neutron powder diffraction and phase formation studies of $\text{Mg}_{2.5+x}\text{V}_{1+2x}\text{Mo}_{1-2x}\text{O}_8$, *J. Alloys Compd.* 379 (2004) 87–94. doi:10.1016/j.jallcom.2004.02.015.
- [58] J. P. Smit, H. Kim, I. Saratovsky, K. B. Stark, G. Fitzgerald, G. W. Zajac, J. Gaillard, K. R. Poeppelmeier, P. C. Stair, A spectroscopic and computational investigation of the vanadomolybdate local structure in the lyonsite phase $\text{Mg}_{2.5}\text{VMoO}_8$, *Inorg. Chem.* 46 (2007) 6556–6564. doi:10.1021/ic7006815.
- [59] L. Katz, A. Kasenally, L. Kihlberg, The crystal structure of the reduced copper molybdate $\text{Cu}_{4-x}\text{Mo}_3\text{O}_{12}$ (x approx.= 0.15), *Acta Crystallogr., Sect. B: Struct. Sci* 27 (1971) 2071–2077. doi:10.1107/S0567740871005387.

- [60] O. Sedello, H. Müller-Buschbaum, Synthese und kristallstruktur von $(\text{Cu,Fe})_{3.63}\text{Mo}_3\text{O}_{12}$: Ein oxometallat mit eindimensional flächenverknüpften oktaederketten / Synthesis and crystal structure of $(\text{Cu,Fe})_{3.63}\text{Mo}_3\text{O}_{12}$: An oxometallate showing one-dimensional chains of face sharing octahedra, *Z. Naturforsch., B: Chem. Sci.* 51 (1996) 90–94. doi:10.1515/znb-1996-0117.
- [61] O. Sedello, H. Müller-Buschbaum, Zur kristallstruktur von $(\text{Cu,Mn})_{3.66}\text{Mo}_3\text{O}_{12}$ / On the crystal structure of $(\text{Cu,Mn})_{3.66}\text{Mo}_3\text{O}_{12}$, *Z. Naturforsch., B: Chem. Sci.* 51 (1996) 447–449. doi:10.1515/znb-1996-0325.
- [62] H. Szillat, H. Müller-Buschbaum, Zur kenntnis des oxocuprats $(\text{Cu,Co})_{3.75}\text{Mo}_3\text{O}_{12}$ / On the oxocuprate $(\text{Cu,Co})_{3.75}\text{Mo}_3\text{O}_{12}$, *Z. Naturforsch., B: Chem. Sci.* 50 (1995) 707–711. doi:10.1515/znb-1995-0503.
- [63] L. Sebastian, Y. Piffard, A. K. Shukla, F. Taulelle, J. Gopalakrishnan, Synthesis, structure and lithium-ion conductivity of $\text{Li}_{2-2x}\text{Mg}_{2+x}(\text{MoO}_4)_3$ and $\text{Li}_3\text{M}(\text{MoO}_4)_3$ ($\text{M}^{III} = \text{Cr, Fe}$), *J. Mater. Chem.* 13 (2003) 1797. doi:10.1039/b301189e.
- [64] D. E. Bugaris, H.-C. zur Loye, $\text{Li}_3\text{Al}(\text{MoO}_4)_3$, a lyonsite molybdate., *Acta Crystallogr., Sect. C: Cryst. Struct. Commun.* 68. doi:10.1107/S0108270112020513.
- [65] U. Kolitsch, E. Tillmanns, $\text{Li}_3\text{Sc}(\text{MoO}_4)_3$: substitutional disorder on three (Li,Sc) sites, *Acta Crystallogr., Sect. E: Struct. Rep. Online* 59 (2003) i55–i58. doi:10.1107/S1600536803004872.
- [66] M. Wiesmann, M. Geselle, H. Weitzel, H. Fueß, Crystal structure of lithium copper molybdate, $\text{Li}_2\text{Cu}_2(\text{MoO}_4)_3$, *Z. Kristallogr.* 209 (1994) 615. doi:10.1524/zkri.1994.209.7.615.
- [67] M. Wiesmann, I. Svoboda, H. Weitzel, H. Fuess, Crystal structure of lithium cobalt molybdate, $\text{Li}_2\text{Co}_2(\text{MoO}_4)_3$, *Z. Kristallogr.* 210 (1995) 1995. doi:10.1524/zkri.1995.210.7.525.
- [68] L. Xue, Y. Wang, P. Lv, D. Chen, Z. Lin, J. Liang, F. Huang, Z. Xie, Growth, structures, and properties of $\text{Li}_2\text{Zn}_2(\text{MoO}_4)_3$ and Co-doped $\text{Li}_2\text{Zn}_2(\text{MoO}_4)_3$, *Cryst. Growth Des.* 9 (2009) 914–920. doi:10.1021/cg800700h.
- [69] M. Ozima, S. Sato, T. Zoltai, The crystal structure of a lithium–nickel molybdate, $\text{Li}_2\text{Ni}_2\text{Mo}_3\text{O}_{12}$, and the systematics of the structure type, *Acta Crystallogr., Sect. B: Struct. Sci* 33 (1977) 2175–2181. doi:10.1107/S0567740877007973.

- [70] B. M. Wanklyn, F. R. Wondre, W. Davison, Flux growth of crystals of some magnetic oxide materials: $\text{Mn}_7\text{SiO}_{12}$, CuO , MCr_2O_4 , MTiO_3 , Ni_2NbBO_6 , MMoO_4 and $\text{Li}_2\text{M}_2(\text{MoO}_4)_3$, ($\text{M} = \text{Mn}, \text{Co}, \text{Ni}$), *J. Mater. Sci.* 11 (1976) 1607–1614. doi:10.1007/BF00737516.
- [71] J. P. Smit, T. M. McDonald, K. R. Poeppelmeier, $\text{Li}_3\text{Ti}_{0.75}(\text{MoO}_4)_3$: A lyonsite-type oxide, *Solid State Sci.* 10 (2008) 396–400.
- [72] M. Lafontaine, J. Grenéche, Y. Laligant, G. Férey, $\beta\text{-Cu}_3\text{Fe}_4(\text{VO}_4)_6$: Structural study and relationships; physical properties, *J. Solid State Chem.* 1–10doi: 10.1006/jssc.1994.1001.
- [73] X. Wang, K. R. Heier, C. L. Stern, K. R. Poeppelmeier, Crystal growth and structure of $\text{Mn}_{2.47}\text{V}_{0.94}\text{Mo}_{1.06}\text{O}_8$, *J. Alloys Compd.* 267 (1998) 79–85. doi: 10.1016/S0925-8388(97)00574-4.
- [74] M. Kurzawa, M. Bosacka, P. Jakubus, The structure and selected properties of $\text{Co}_{2.5}\text{VMoO}_8$, *J. Mater. Sci.* 38 (2003) 3137–3142. doi:10.1023/A:1024785415727.
- [75] X. Wang, K. R. Heier, C. L. Stern, K. R. Poeppelmeier, Crystal structure of $\text{Zn}_{3.77}\text{V}_{1.54}\text{Mo}_{1.46}\text{O}_{12}$ containing ZnO_6 trigonal prisms, *J. Alloys Compd.* 255 (1997) 190–194. doi:10.1016/S0925-8388(96)02812-5.
- [76] A. A. Belik, A. P. Malakho, K. V. Pokholok, B. I. Lazoryak, Phase formation in $\text{Cu}_{3+1.5x}\text{R}_{4-x}(\text{VO}_4)_6$ ($\text{R} = \text{Fe}$ and Cr) systems: crystal structure of $\text{Cu}_{2.5}\text{Fe}_{4.333}(\text{VO}_4)_6$, $\text{Cu}_4\text{Fe}_{3.333}(\text{VO}_4)_6$, and $\text{Cu}_{4.05}\text{Cr}_{3.3}(\text{VO}_4)_6$, *J. Solid State Chem.* 156 (2001) 339–348. doi:10.1006/jssc.2000.9004.
- [77] J. P. Smit, H.-S. Kim, J. D. Pless, P. C. Stair, K. R. Poeppelmeier, Probing the vanadyl and molybdenyl bonds in complex vanadomolybdate structures., *Inorg. Chem.* 45 (2) (2006) 521–8. doi:10.1021/ic051741+.
- [78] J. W. Heo, J. Hyung, S.-T. Hong, Unveiling the intercalation mechanism in $\text{Fe}_2(\text{MoO}_4)_3$ as an electrode material for Na-ion batteries by structural determination, *Inorg. Chem.* 57 (2018) 11901–11908. doi:10.1021/acs.inorgchem.8b01244.
- [79] Z. Mu, E. Song, D. Zhu, J. Feng, Y. Yang, Red phosphor $\text{Li}_2\text{Mg}_2(\text{WO}_4)_3$: Eu^{3+} with lyonsite structure for near ultraviolet light-emitting diodes, *Displays* 43

- (2016) 18–22. doi:10.1016/j.displa.2016.04.001.
- [80] J. D. Pless, H.-S. Kim, J. P. Smit, X. Wang, P. C. Stair, K. R. Poeppelmeier, Structure of $\text{Mg}_{2.56}\text{V}_{1.12}\text{W}_{0.88}\text{O}_8$ and vibrational raman spectra of $\text{Mg}_{2.5}\text{VWO}_8$ and $\text{Mg}_{2.5}\text{VMoO}_8$, *Inorg. Chem.* 45 (2006) 514–520. doi:10.1021/ic051740h.
- [81] S. Prabaharan, A. Fauzi, M. Michael, K. Begam, New NASICON-type $\text{Li}_2\text{Ni}_2(\text{MoO}_4)_3$ as a positive electrode material for rechargeable lithium batteries, *Solid State Ionics* 171 (3-4) (2004) 157–165. doi:10.1016/j.ssi.2004.05.001.
- [82] M. Alvarez-Vega, U. Amador, M. E. Arroyo-de Dompablo, Electrochemical study of $\text{Li}_3\text{Fe}(\text{MoO}_4)_3$ as positive electrode in lithium cells, *J. Electrochem. Soc.* 152 (2005) A1306–A1311. doi:10.1149/1.1925069.
- [83] Q. Liao, Y. Wang, F. Jiang, D. Guo, Ultra-low fire glass-free $\text{Li}_3\text{FeMo}_3\text{O}_{12}$ microwave dielectric ceramics, *J. Am. Ceram. Soc.* 97 (2014) 2394–2396. doi:10.1111/jace.13073.
- [84] D. Zhou, C. A. Randall, L. Pang, H. Wang, X. Wu, J. Guo, G. Zhang, L. Shui, X. Yao, Microwave dielectric properties of $\text{Li}_2(\text{M}^{2+})_2\text{Mo}_3\text{O}_{12}$ and $\text{Li}_3(\text{M}^{3+})\text{Mo}_3\text{O}_{12}$ ($\text{M} = \text{Zn}, \text{Ca}, \text{Al}, \text{and In}$) lyonsite-related-type ceramics with ultra-low sintering temperatures, *J. Am. Ceram. Soc.* 94 (2011) 802–805. doi:10.1111/j.1551-2916.2010.04148.x.
- [85] J. Zhang, R. Zuo, Synthesis and microwave dielectric properties of $\text{Li}_2\text{Mg}_2(\text{WO}_4)_3$ ceramics, *Mater. Lett.* 158 (2015) 92–94. doi:10.1016/j.matchemphys.2009.08.037.
- [86] D. Wang, Z. Zou, J. Ye, A novel series of photocatalysts $\text{M}_{2.5}\text{VMoO}_8$ ($\text{M} = \text{Mg}, \text{Zn}$) for O_2 evolution under visible light irradiation, *Catal. Today* 93-95 (2004) 891–894. doi:10.1016/j.cattod.2004.06.090.
- [87] K. Gourai, A. El Bouari, B. Belhorma, L. Bih, Adsorption of methylene blue on the $\text{Li}_3\text{Fe}_{1-x}\text{Cr}_x(\text{MoO}_4)_3$ ($x=0,0.5,1$) lyonsite phases, *Am. J. Chem.* 6 (2016) 47–54. doi:10.5923/j.chemistry.20160602.04.
- [88] W. A. Dollase, H. S. C. O’Neill, The spinels CuCr_2O_4 and CuRh_2O_4 , *Acta Crystallogr., Sect. C: Cryst. Struct. Commun.* 53 657–659. doi:10.1107/S0108270197000486.
- [89] M. Tovar, R. Torabi, C. Welker, F. Fleischer, Structural and magnetic properties

of Cu-Ni-Cr spinel oxides, *Physica B* 385 (2006) 196–198. doi:10.1016/j.physb.2006.05.181.

- [90] G. Ueno, S. Sato, Y. Kino, The low-temperature tetragonal phase of NiCr_2O_4 , *Acta Crystallogr., Sect. C: Cryst. Struct. Commun.* 55 (1999) 1963–1966. doi:10.1107/S0108270199011713.
- [91] J. E. Greedan, Geometrically frustrated magnetic materials, *J. Mater. Chem.* 11 (2001) 37–53. doi:10.1039/B003682J.

Chapter 2: Synthesis and Characterization Methods

The relevance of any proposed structure-property relationship hinges on data quality. Advancements in data analysis techniques are rendered ineffectual when applied to poorly resolved data. The application of sound experimental practices is therefore integral to any scientific endeavor. In the following sections, an overview of the experimental methods specific to the subsequent chapters is detailed.

2.1 Preparation of Bulk Oxides

2.1.1 *Ceramic Method*

The historic method for synthesizing powdered oxides goes by several names, mainly: the ceramic method, conventional solid state synthesis, and "shake-and-bake". Powdered starting reagents (not necessarily in oxide form) are intimately mixed with a mortar and pestle or ball mill, pressed into pastilles, pellets, or bars, and heated in a furnace (400–1700 °C) with intermittent grinding between heating cycles. The optimal duration and temperatures are dependent on various factors (including precursor properties, pastille size, sample quantity, and lattice enthalpies), and are determined through trial-and-error or through phase diagram consultation. Longer heating times do not necessarily encourage phase formation due to the growth of the new phase at the particle interfaces, resulting in a decrease in diffusion rates [1]. Because reactions

proceed slowly via ion diffusion at the particle interfaces, smaller starting particle sizes are desirable; in addition, intermittent grinding, pressing, and re-heating is crucial for the formation of new interfaces to guide the reaction (Fig. 2.1).

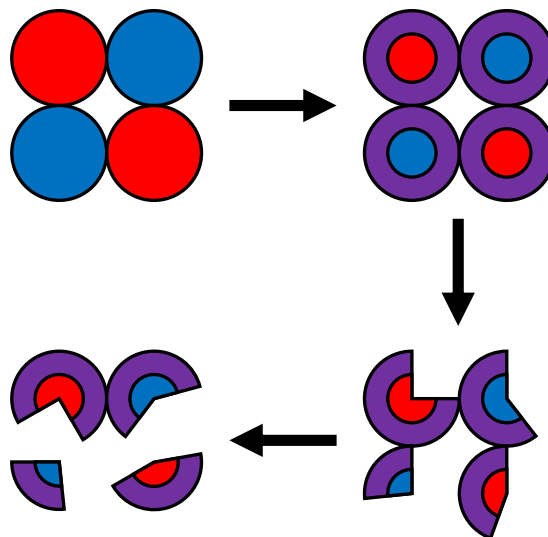


Figure 2.1: A representation of the ceramic method, in which precursors (red/blue) are mixed, forming the product phase at the interfaces through diffusion (purple). These particles are broken up to facilitate further reaction.

The choice of reaction vessel is dependent on the reactivity, volatility, and structure of the starting materials. Alumina (Al_2O_3), Au, and Pt are common reaction vessels, each with advantages/disadvantages. Alumina is highly inert and is suitable for most oxide samples; however, precursors that contain Cu^{2+} , Co^{2+} , or Ni^{2+} risk leeching into the crucible, which not only contaminates the vessel, but also reduces the stoichiometric quantity needed for reaction. In these cases, Au trays are a viable alternative, being more inert; however, the melting point is relatively low (1064 °C), and Au is inappropriate for phases that form above that temperature [2]. In such cases, Pt

(melting point: 1768 °C) can be used; however, Pt readily reacts with alkali metal ions at elevated temperatures [2]. Other factors to consider include pressure and environment. While these reactions are typically carried out in air, such conditions may not be advisable for non-oxide compounds or target compounds with unusual oxidation states. In these cases, a tube furnace may be employed, with oxidative/reductive/inert gas flowing over the sample, or heating the sample in a vacuum evacuated silica tube. Awareness of parameters like these and judicious usage of reaction vessels, temperatures, atmospheres, and duration can be the deciding factor in complete phase formation.

2.1.2 Citrate Gel Method

One of the primary drawbacks to the ceramic method is that it is dependent on the particulate mixing quality. Poor mixing can result in increased reaction trials, durations, and temperatures before phase purity is achieved. In addition, the physical act of grinding can only create so many new particle interfaces. Therefore, in contrast to the ceramic method, the citrate gel method (a type of Pechini process, and a subset of sol-gel synthesis) can be employed to achieve atomic-level mixing, resulting in quicker reactions at lower temperatures, and smaller particle sizes [1, 3]. In this method, stoichiometric quantities of water-soluble precursors (metal nitrates, carbonates, or hydroxides) are combined in a reaction vessel (e.g., beaker) with deionized water. Care must be taken during the weighing process, as some precursors may be very hygroscopic (or even deliquescent). The solution is then heated and stirred, and

citric acid added in a 2:1 molar ratio. This step is particularly advantageous for multi-cationic systems, as the acid acts as a cross-linking agent, chelating reactive metal cations, and thereby preventing unwanted binary oxide formation. The pH of the resulting solution was then adjusted to 7 using aqueous NH_4OH , and the solution was further heated at 250 °C for 2 h until a dark brown amorphous dry polymer "gel" was observed. Intermittent stirring was done with a glass rod to release any trapped NO_x or CO_x , as they can corrode the inside of the muffle furnaces. The final gel was then calcined at the synthesis temperature in air for 6–12 h. This process yields homogeneously dispersed cations, but due to the smaller particle sizes, may require longer duration diffraction experiments to achieve sufficient intensity. Results from this synthesis route can be found in Appendix B.1

2.2 Structural Characterization

2.2.1 *Scattering Techniques*

A brief discussion of scattering techniques is warranted to provide context for the following sections. Among the modern analytical techniques, the most appropriate for powdered samples is irradiation, i.e. a particle beam of wavelength λ and incident angle θ interacting with a material. Upon irradiation, the momentum transfer (or scattering vector) Q is given by $Q = 4\pi \sin \theta / \lambda$ (or $Q = 2\pi / d$); plotting diffraction patterns in Q can be useful when comparing between radiation sources with varying wavelength, e.g., direct comparison between a high-resolution X-ray source against a

lab diffractometer [4]. The wavelength of this beam must be on the order of 0.01–100 Å to glean useful atomic-level information; the suitable radiation types are therefore electrons, X-rays, and neutrons.

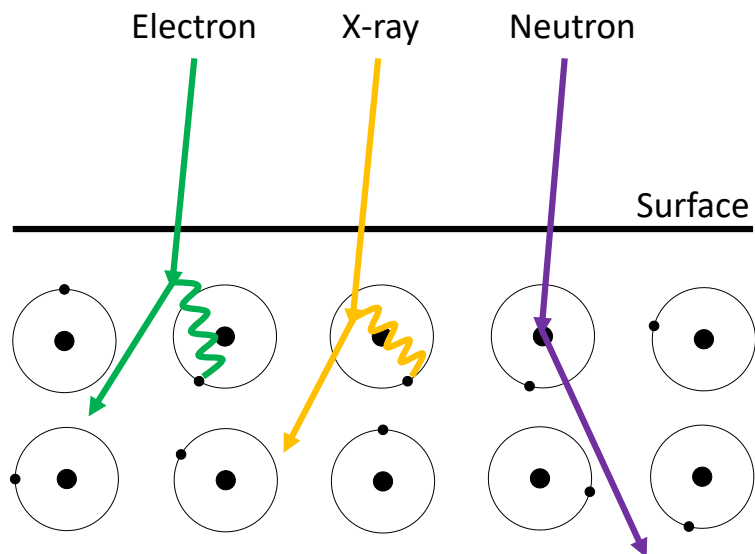


Figure 2.2: A comparison between the scattering behaviors of electrons, X-rays, and neutrons impinging on a sample surface

Electron scattering ($\approx 0.2 \text{ \AA}$) occurs via electrostatic repulsion with the electron cloud, and is sensitive to distortions, ordering, and defects; however, the penetration depth is shallow, and is therefore only viable for surface characterization (Fig. 2.2) [5]. X-ray scattering also interacts with the electron cloud; the lack of charge allows for further penetration, and is therefore appropriate for bulk ceramic samples. The scattering power scales linearly with atomic number Z (which can be disadvantageous when studying a material with both light and heavy atoms), and can vary as a function of $\sin \theta / \lambda$; scattering therefore weakens as the incident angle or wavelength increases.

Neutron scattering is unaffected by the Coulombic barrier of the electron cloud, and has even greater penetration power, interacting with the nucleus [5]. In addition, neutron scattering has no Z dependence, and is therefore suitable for analysis of samples with light atoms, such as H or O. However, some elements are highly absorbing (e.g., Cd, Gd, Ir) of neutrons [4-6]. These advantages/disadvantages must be considered when designing a scattering experiment.

2.2.2 X-ray Diffraction

2.2.2.1 In-House Diffractometers

One of the most ubiquitous methods of analyzing solid samples is powder X-ray diffraction (XRD or PXRD). From a bird's eye view, every setup requires an X-ray source tube, a sample stage, and a detector (Fig. 2.3). A high applied voltage (>10 kV) accelerates a beam of electrons from a heated tungsten filament towards an anode (metal targets include Cu, Mo, Co, Fe, Cr, W, and Ag); as the incident electrons ionize some of the anode's core electrons, relaxation from an outer orbital ejects X-rays [4]. The continuous (Bremsstrahlung) spectrum of white radiation from the impact is filtered out, and the characteristic short wavelength X-rays (K_α) are directed through focusing optics (monochromators and slits) and a Be window towards the sample [4].

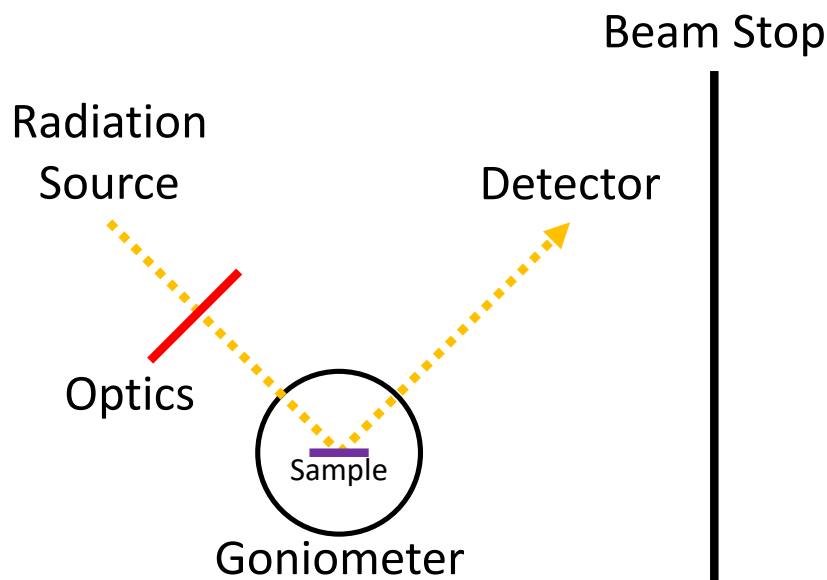


Figure 2.3: Basic schematic of an X-ray diffraction experiment.

For a crystalline sample, the atoms occupy points in various geometric planes (Miller Indices) with interplanar spacing d (Fig. 2.4). Incoming X-rays can only diffract in a detectable manner if they are in phase (constructive interference), as defined by Bragg's law (Eq. 2.1) [7]. The Bragg condition for various planes is accessed at different values of θ and a powder pattern displays the intensity as a function of 2θ . These Miller planes (defined by hkl) can be related to d -spacing via structure-dependent formulas to yield the unit cell dimensions a , b , and c ; for example, the relation used for the orthorhombic crystal system is given by Eq. 2.2 [3, 4].

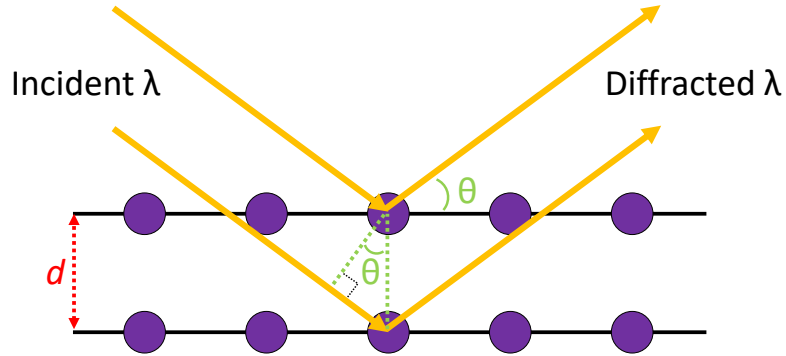


Figure 2.4: A representation of the conditions required for Bragg diffraction.

$$n\lambda = 2d \sin \theta \quad (2.1)$$

$$\frac{1}{d^2} = \frac{h^2}{a^2} + \frac{k^2}{b^2} + \frac{l^2}{c^2} \quad (2.2)$$

2.2.2.2 Synchrotron Radiation

Modern advances in diffraction technology has allowed for more sophisticated scattering experiments; one such example is synchrotron radiation sources. While the general principle remains the same as described above, the X-ray generation method differs. Electrons are generated by an electron gun at a particle accelerator (such as the Advanced Photon Source at Argonne National Laboratory), and accelerated in a booster ring, and then transferred to a storage ring [8]. Bending magnets, wigglers or undulators, and monochromators are then used to separate desired wavelengths for sample irradiation. Compared to benchtop diffractometers, advantages of this method

include higher resolution, faster acquisition time, and superior counting statistics.

2.2.3 Neutron Diffraction

In contrast to X-rays, neutrons are produced either through fission (at a reactor source) or through spallation (in which a metal target is bombarded by proton beam pulses, releasing pulses of neutrons) [9]. Unlike benchtop XRD (in which 2θ is varied), the polychromatic incident beam of various neutron wavelengths is directed (along path L) towards the sample, and the time-of-flight (TOF) t detection occurs at fixed 2θ positions [9]. In addition, neutron diffraction yields higher intensities at lower d -spacing, complementing the structural information obtained from an XRD experiment. Because the neutron flux is lower than that of XRD experiments, larger sample sizes and longer experiment durations are required to generate diffraction patterns with usable intensities.

The TOF (and in extension, wavelength) can be related to the d -spacing via a combination of the de Broglie equation and Bragg's law, in which h is the Planck constant and m_n is the neutron mass (Eq. 2.3) [9]. Neutrons produced at a spallation source have a higher incident flux than that of a reactor source, allowing for higher overall diffraction intensities; conversely, while the lower flux of a reactor source necessitates larger sample sizes and/or longer irradiation times, higher resolution data can be obtained [5]. The nature of these differences must be considered in both

experiment design and data analysis.

$$\lambda = \frac{ht}{m_n} L = 2d \sin \theta \quad (2.3)$$

2.2.4 Diffraction Instrumentation

In this dissertation, each of the above radiation sources were used to varying degrees. All XRD patterns were collected from a Rigaku MiniFlex II, over a 10–70 °2 θ range, using Cu K $_{\alpha 1}$ /K $_{\alpha 2}$ radiation (1.54 Å) and a graphite monochromator (to filter the accompanying K $_{\beta}$ wavelength) on the diffracted beam [10]. The MiniFlex II operates at a fixed tube voltage of 30 kV and a fixed output current of 15 mA. Fast scan measurements (2 θ variation >2°/min) were conducted for phase identification; structural refinements for unit cell parameter analysis necessitate decreasing the 2 θ increment and increasing the time at each increment. The data quality obtained on the MiniFlex II is sufficient for big picture analysis (symmetry, unit cell parameters, crystallite size, lattice strain), but is not adequate for detailed analysis (atomic positions, displacement parameters, and occupancies). To obtain higher quality data, samples were sent via mail-in programs to Argonne National Laboratory (11-BM, Advanced Photon Source), Oak Ridge National Laboratory (POWGEN, BL-11A, Spallation Neutron Source), and the National Institute of Standards and Technology (NIST) (BT-1, Center for Neutron Research).

At 11-BM, samples were ground with amorphous silica gel to account for absorption. The resulting mixtures were packed into Kapton capillary tubes (0.8 mm diameter),

mounted, and data were collected at room temperature over a 2θ range of 34° , with data points collected every $0.001^\circ 2\theta$ and a scan speed of $0.01^\circ/\text{s}$ [8]. At POWGEN, ≈ 5 g samples were loaded into V cans (10 mm diameter), and data were collected at room temperature over a d -spacing range of $\approx 0.1\text{--}8 \text{ \AA}$ [9]. The spallation source was a Hg target, and detection coverage was over a 2θ range of $20\text{--}170^\circ$. At BT-1, ≈ 10 g samples were loaded into V cans (15.6 mm diameter, 50 mm length), data were collected at room temperature over a 2θ range of $3\text{--}167^\circ$, and a Cu (311) monochromator was employed to yield an incident wavelength of $1.5403(2) \text{ \AA}$ [6]. Collimation of $15'$ of arc was used before the monochromator, $20'$ before the sample, and $7'$ before the detectors.

2.2.5 *Structure Modeling*

Once the data are collected and normalized, structure modeling can begin. Raw data from benchtop XRD were analyzed using the MDI Jade program with access to the International Center for Diffraction Data (ICDD) database; this program was utilized for phase identification and confirmation of phase purity. Following this is the laborious task of structure refinement, in which an intensity function (Eq. 2.5) is modeled against the data. This process is iterative, and was conducted using the least-squares analysis program GSAS with the EXPGUI interface [11, 12]. The two whole-pattern fitting techniques used were the Le Bail (structure-free) and Rietveld methods.

In the absence of a detailed structural model, the Le Bail method can be a

useful step, as it refines the hkl peak positions for a given space group to calculate the background intensity, unit cell parameters, and profile parameters, and assigns arbitrary peak intensities [13]. The intensity is simulated by fitting the profile of the peak shape (often a mixture of Gaussian and Lorentzian), adjusting it through instrumental effects, particle size, and structural strain. The Rietveld method is more comprehensive, incorporating atomic positions, atomic displacement parameters (ADPs), and site occupancies into the intensity calculations [14]. The overall goal of the Rietveld method is to minimize a residual function given by:

$$\Delta = \sum w_i (I_i(\text{obs}) - I_i(\text{calc}))^2 \quad (2.4)$$

in which w_i is the weight given to an observable. To obtain $I_i(\text{calc})$, the calculated Bragg intensity I at a given 2θ point i is expressed as a summation of a multitude of factors,

$$I_i(2\theta) = \sum_{j=i}^{N \text{ phases}} S_j \sum_{hkl}^{N \text{ peaks}} L_{hkl} A_j P_{j,hkl} |F_{hkl}|^2 \Phi_{hkl}(2\theta_i - 2\theta_{hkl}) + bkg_i \quad (2.5)$$

in which S is the scale factor for each phase, L is the Lorentz-Polarization factor (e.g., instrumental geometry, sample positioning), A is the absorption factor, P is the texture (or preferred orientation), $|F|$ is a generalized structure factor (for brevity, this includes the atomic displacement parameter B or U and multiplicity), Φ is the profile shape function (e.g., instrumental broadening, microstructure), and bkg is the background function. Regarding the ADPs, different Rietveld programs will supply

those values as either B or U ; they are related by a simple conversion of $U = B/8\pi^2$ [4, 14]. The number of peaks, N *peaks*, is determined by the symmetry/space group of the phase. Each of these terms are themselves convolutions of parameters that can be refined, and it is these parameters that are coded into a given refinement software.

The metrics involved when determining the completion of a refinement are (in order of importance): visual assessment of the fit/difference curve, chemical sense, the value of the weighted-profile reliability factor (wR_p , Eq. 2.6), and the χ^2 (Eq. 2.8) value [15, 16]. The latter two values are dependent on the experimental conditions, and can therefore be misleading, which is apparent upon inspection of their derivation. The χ^2 value incorporates an expected R factor, a measure of data quality (Eq. 2.7), in which N is the number of observables, P is then number of refined parameters, and C is the number of constraints used.

$$wR_p = \sqrt{\frac{\Delta}{\sum w_i I_i(\text{obs})^2}} \times 100\% \quad (2.6)$$

$$R_{\text{exp}} = \sqrt{\frac{N - P - C}{\sum w_i I_i(\text{obs})^2}} \times 100\% \quad (2.7)$$

$$\chi^2 = \left(\frac{wR_p}{R_{\text{exp}}}\right)^2 = \left(\frac{\sum w_i (I_i(\text{obs}) - I_i(\text{calc}))^2}{\sum w_i I_i(\text{obs})^2}\right)^2 \quad (2.8)$$

2.3 Physical Property Characterization

2.3.1 *Magnetic Properties*

2.3.1.1 *Fundamentals*

Modern luxuries owe much of their functionality to magnetic materials, e.g., computer memory, medical equipment, transformers. At the most fundamental level, magnetism and magnetic moments are associated with individual electrons' spins and orbits. The most broad classifications of behaviors a material exhibits under an external applied magnetic field are diamagnetism ($\sim 10^{-6}$ emu/mol) and paramagnetism ($\sim 10^1$ emu/mol), corresponding to the absence or presence of unpaired electrons, respectively [17–19]. Diamagnets repel applied fields by generating their own field in the opposing direction, resulting in a small, temperature-independent magnetic moment. Paramagnets exhibit a temperature-dependent alignment with the applied field, thereby enhancing the magnetic flux density; higher temperatures work against said alignment, and thus magnetization increases as temperature decreases. Without an applied field, both diamagnets and paramagnets are considered non-magnetic. In some cases, the lower temperatures can cause spontaneous long-range ordering of electron spins. If the spins are aligned parallel to each other, this is termed ferromagnetic (and antiferromagnetic if the spins are aligned antiparallel to each other) (Fig. 2.5). These two phenomena occur below specific transition temperatures, in which the exchange energy J overrides the thermally-induced paramagnetism; the temperatures are notated T_C (Curie temperature) for ferromagnets and T_N (Néel

temperature) for antiferromagnets. Of course, these categories become more nuanced in materials with uncommon spin states; because the samples in this dissertation do not exhibit such behaviors, these phenomena will not be discussed.

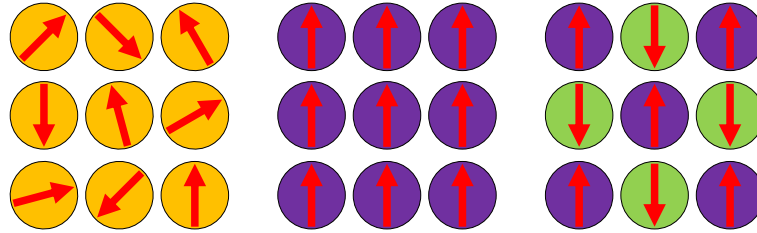


Figure 2.5: The broad categories of magnetic spin interactions: paramagnetism (left), ferromagnetism (middle), and antiferromagnetism (right).

2.3.1.2 Magnetism Instrumentation

The majority of the measurements performed in this dissertation were executed using a Quantum Design Physical Property Measurement System (PPMS), using the AC/DC Magnetometry System (ACMS) for DC magnetization (Fig. 2.6). Select samples were measured to confirm reproducibility results using a Quantum Design Magnetic Property Measurement System (MPMS) at University of California, Santa Cruz, in Dr. Arthur P. Ramirez' laboratory. The PPMS consists of a 9 T superconducting magnet in a He dewar with a sample T range of 1.9–400 K [20].



Figure 2.6: The Quantum Design Physical Property Measurement System (PPMS). The Model 6000 controller is housed in the white cabinet (left), while the sample chamber is housed in the He containment dewar (black, center). The cryopump (He level control via a second stage and condenser) is integrated into the dewar, and is connected to a compressor (not shown). Not shown: Scroll pump housing unit (temperature control), diaphragm pump housing unit (pressure control).

The ACMS coil set is connected in the main dewar chamber via a 12-pin connector at the base of the sample chamber. Samples are either loaded as sintered solids or as tightly packed powders in a polycarbonate straw; this is then attached to a sample rod, and loaded into the sample chamber. The sample is then located using a single point DC extraction to correct for sample displacement during measurement; while location via AC excitation is more accurate, location using the method employed for actual measurements is good experimental practice. A DC servo motor is used to vertically oscillate the sample through the coil set (Fig. 2.7). Faster oscillation speeds generally result in enhanced signal strength, and relates directly to measurement accuracy. An

applied field induces a magnetization that is detected by the coil set as an induced voltage. The amplitude of this voltage signal is correlated to the magnetic moment.



Figure 2.7: Sample preparation for ACMS: sample powders are packed into a straw (left), fitted to a sample rod (middle), and inserted through the DC servo motor (right).

When determining the measurement parameters, either zero-field-cooled (ZFC) or field-cooled (FC) options are available. If the ZFC option is chosen, then the sample is cooled to the desired temperature, the field is applied, and measurements are taken during the temperature sweep back to room temperature. For the FC option, the field is applied prior to cooling. For most materials, including compositions studied in this

thesis, data are collected in the 5–300 K range.

2.3.1.3 Data Analysis

A common model for analyzing the magnetic susceptibility χ of a material as a function of temperature is the Curie-Weiss Law (Eq: 2.9), in which C is the Curie constant (which can be used to provide the magnetic moment per formula unit μ_{eff} , T is the temperature in K, and θ_{W} is the Weiss constant (which provides information regarding the sum/strength of spin interactions) [17–19].

$$\chi_{\text{mol}} = \frac{C}{T - \theta_{\text{W}}} \quad (2.9)$$

The inverse of this relationship is particularly useful, as the linearity can be used to extract C from the slope and θ_{W} from the y -intercept. As such, this relation is only useful in paramagnetic regions at high temperatures, where the inverse susceptibility is most linear. It should also be noted that the Weiss constant can also indicate the short range interactions between adjacent atoms, as it is an empirically determined representation of the earlier-defined theoretical exchange energy J [18]. For a $\theta_{\text{W}} = 0$, paramagnetism is suggested. For $\theta_{\text{W}} \gg 0$, ferromagnetic interactions are indicated, and if $\theta_{\text{W}} \ll 0$, antiferromagnetic exchange is suggested. In later chapters, it will be observed that the Weiss temperature does not promise the presence of long range ordering. At times, additional interaction terms may be required to better model the system (Eq. 2.10), in which χ_0 can be attributed to any additional magnetic

interactions occurring in the sample. χ_0 may include terms such as χ_{dia} (diamagnetic susceptibility from core electrons) [21], χ_{VV} (Van Vleck term) [22], and/or χ_{Pauli} (Pauli paramagnets) [18, 23]. The Van Vleck term is useful when considering systems in which the total orbital momentum is equal to 0, while the Pauli paramagnetic factor is useful for metallic samples, in which only the itinerant electrons involved in electronic conduction are contributing to the magnetic behavior.

$$\chi_{\text{obs}} = \chi_{\text{para}} + \chi_0 \quad (2.10)$$

However, it is apparent from the Curie-Weiss law that χ_{mol} and C are not directly measured terms (θ_{W} is extracted as mentioned and is trivial); therefore, they need to be related to a physical quantity to be meaningful. Relating the molar susceptibility to the experimental magnetization can be done through a classical approach (Eq. 2.11), in which I is the experimental magnetization and H is applied field strength.

$$\chi_{\text{mol}} = \frac{I}{H \cdot \text{mol}_{\text{magnetic ion}}} \quad (2.11)$$

Relating the susceptibility to the magnetic moment, though, can be done through a quantum mechanical approach, via the Langevin expression (Eq. 2.12), in which N_{A} is the Avogadro constant, μ_{eff} is the effective magnetic moment, k is the Boltzmann constant ($1.381 \times 10^{-23} \text{ m}^2\text{kgs}^{-2}\text{K}^{-1}$), and T is temperature in K [3, 23].

$$\chi_{\text{mol}} = \frac{N_{\text{A}}\mu_{\text{eff}}^2}{3kT} \quad (2.12)$$

Combining the Langevin expression algebraically with the Curie law ($\chi = C/T$) allows for a physical relationship to be established between the Curie constant and the effective moment (Eq. 2.13); the quantity 2.84 is a simplification of the constants via $\sqrt{3k/N_A}$.

$$\mu_{\text{eff}} = 2.84\sqrt{C} \mu_{\text{B}} \quad (2.13)$$

At this point, a comparison between the μ_{eff} value and a theoretical, expected value can be used to determine the number of unpaired electrons in the system. The expected μ_{th} value can be calculated through the total spin S (only for $3d$ elements) (Eq. 2.14) [18, 19].

$$\mu_{\text{th}} = 2\sqrt{S(S+1)} \mu_{\text{B}} \quad (2.14)$$

Systems containing $4d$ and $5d$ elements must include the orbital angular momentum L (Eq. 2.15), and systems with spin-orbit coupling, i.e. $5d$ elements and lanthanides, must incorporate J , in which g_J is the gyromagnetic ratio (Eq. 2.16) [18, 23].

$$\mu_{\text{th}} = \sqrt{4S(S+1) + L(L+1)} \mu_{\text{B}} \quad (2.15)$$

$$\mu_{\text{th}} = g_J \sqrt{J(J+1)} \mu_{\text{B}} \quad (2.16)$$

The units of the magnetic moments are in Bohr magnetons ($\mu_{\text{B}} = 9.274 \times 10^{-24}$ J/T) [18, 23]. When more than one magnetic ion is present in a sample, the total magnetic moment consists of the stoichiometric (molar) contribution of the present elements and their number of unpaired electrons. For a hypothetical compound A_xM_y with magnetic ions A and M , the theoretical moment per formula unit can be obtained

in this manner. This concept is relevant for Appendix A, in which the theoretical moments are compared to those determined from magnetic susceptibility experiments.

$$\mu_{\text{total}} = \sqrt{x \times \mu_{A,\text{th}}^2 + y \times \mu_{M,\text{th}}^2} \quad (2.17)$$

2.3.1.4 Modeling Considerations

In some systems containing $3d$ elements, the contribution from L is unquenched [18, 23]. The rotation of electrons about a nucleus is equivalent to a current, which results in a magnetic field. This is the source of the interaction of the orbital momentum with the magnetic field. In a free ion, the d orbitals are degenerate, but not identical; partial quenching from the d_{z^2} is therefore inherent. Orbitals that are able to interchange into an identical and degenerate orbital (via rotation) contribute to the moment, i.e the t_{2g} in an octahedral field. The e_g orbitals do not contribute because they are not identical. The caveat to this phenomenon is that electrons cannot, by rotation, be placed into an orbital that is already occupied by an electron of the same spin. Thus, the t_{2g} does not always contribute to the moment. This means that d^1 , d^2 , d^6 , and d^7 configurations should exhibit unquenched angular momentum contributions (Fig. 2.8).

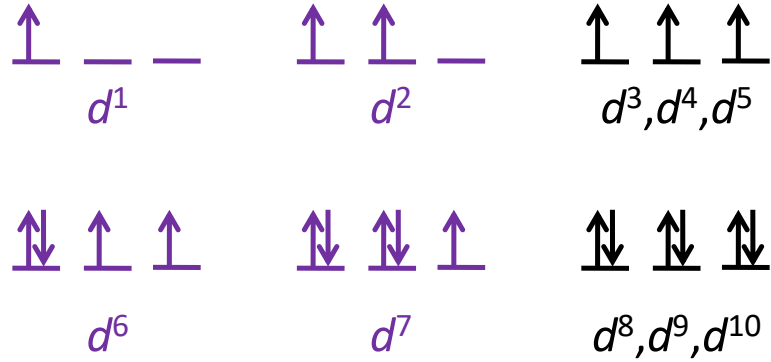


Figure 2.8: Electronic configurations for the t_{2g} orbitals. Highlighted in purple are the spin states that are expected to have an unquenched orbital angular momentum contribution.

2.3.2 Optical Properties

At first glance, the color of a material seems insignificant; in fact, the color can aid in determining the electronic interactions within a material. The most common sources of color in a material are: $d-d$ intra-atomic excitations, charge transfer excitations (metal-metal, anion-metal), color centers, intra-band excitations (metals), and valence to conduction band transitions (semiconductors) [24]. The mechanisms relevant to this dissertation are $d-d$ and charge transfer transitions. For $d-d$ transitions, differing ligand environments and spin states determine the color (e.g., Cr^{3+} in a Al_2O_3 host is responsible for the color of ruby) [24]. For metal-to-metal charge transfer (MMCT) transitions, the coordination environment and oxidation states determine the observed color (e.g., transitions from Fe^{2+} to Ti^{4+} in a Al_2O_3 host is responsible for the color of sapphire) [24]. Typically, ligand-to-metal charge transfer transitions occur in the

UV wavelength range; however, d^0 metals in high oxidation states are electronegative enough to shift the transition range into the visible region (e.g., in PbCrO_4 , transitions between the O $2p$ ligands and the tetrahedrally coordinated Cr^{6+} result in a yellow color [25]).

Experimentally, analysis involves incident light cast upon a solid; this light interacts in a variety of ways (including specular reflection, absorption, and transmission). The phenomenon relevant to the powder samples in this dissertation is diffuse reflection, in which light is reflected in all directions from scattering centers beneath a surface as a result of surface morphology and randomly oriented crystallites. Diffuse reflectance measurements were performed via two setups, each measuring a different portion of the electromagnetic spectrum. For the UV-visible wavelength range, experiments were conducted in Dr. David McIntyre's laboratory in the OSU Physics Department; deuterium and halogen light sources were directed to the sample through a Y-shaped bifurcated optical fiber assembly, which collected the diffuse reflectance and carried it to an Ocean Optics HR-4000 spectrometer (Fig. 2.9) [26]. While specular reflection can distort the band shapes and relative intensities in a diffuse reflectance spectrum, this effect can be minimized through proper sample preparation. The samples were scanned from 250–900 nm and normalized using a standard MgO or BaSO_4 sample as a white reference. For the visible-NIR region, data were collected up to 2500 nm on a Jasco V-670 spectrophotometer fitted with an integrating sphere in Dr. Chih-hung Chang's laboratory in the OSU Chemical Engineering Department (Fig. 2.10).

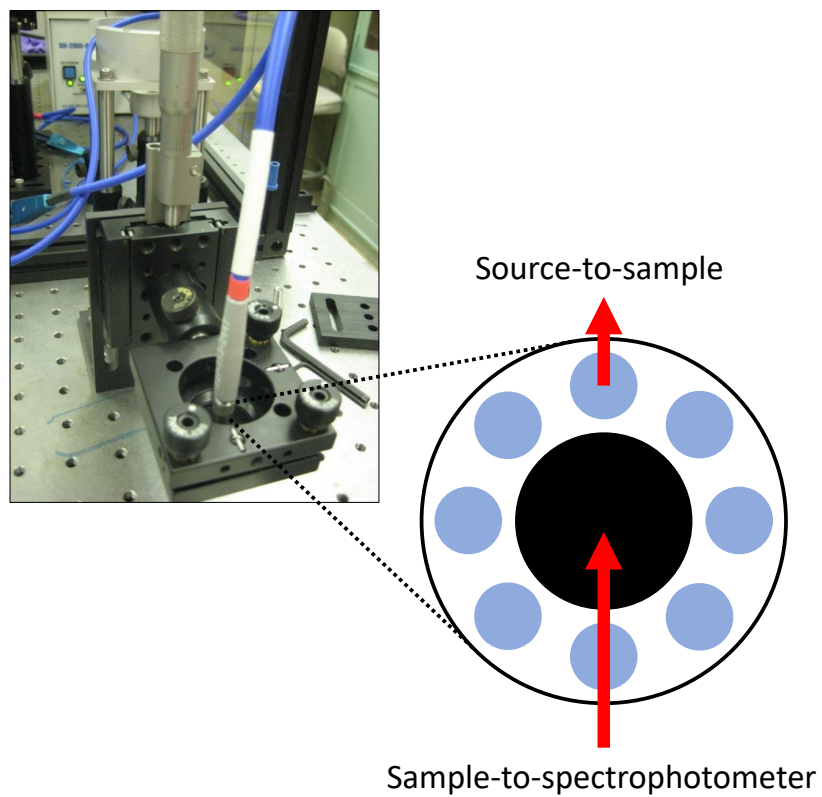


Figure 2.9: Schematic of the internal cross-section of the bifurcated optical fiber and the pathways for incident and reflected light.

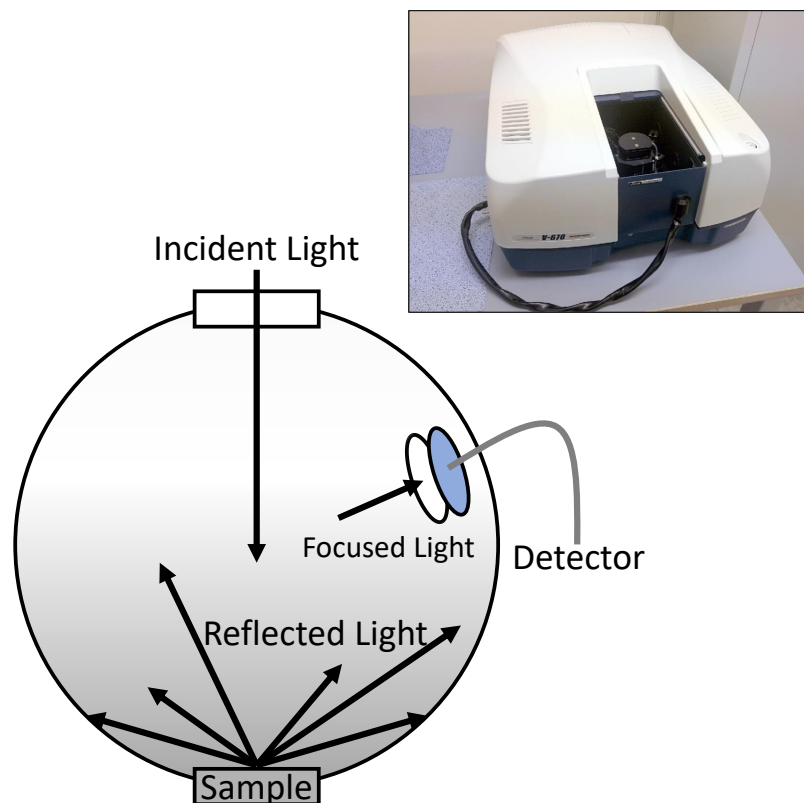


Figure 2.10: Schematic of the integrating sphere for a Jasco V-670 spectrophotometer and the pathways for incident and reflected light.

Naturally, there are advantages/disadvantages to both the fiber optic and integrating sphere attachments. The integrating sphere method is slower (on the order of minutes per collection), collects only diffuse reflection (specular reflection is directed out the incident port), but offers greater absolute intensities than the fiber optic method. In contrast, the bifurcated fiber optic method is faster (<1 sec.), collects both specular and diffuse reflection, but offers lower absolute intensities. Therefore, the fiber optic method is ideal for samples exhibiting large diffuse reflection (i.e., bulk

powders), while the integrating sphere method is ideal for samples with large specular reflection (e.g., bulk powders, thin films, and single crystals).

The intensity of the collected light (excluding specular reflection) is related to the intensity via Lambert's cosine law, $I = I_0 \cos \theta$, in which I is the observed intensity, I_0 is the incident intensity, and θ is the angle between the incident beam and the path of radiant emission [27]. This collected data are then converted to pseudo-absorbance using the Kubelka-Munk relation (Eq. 2.18), in which R is the reflectance intensity for the sample collected from the instrument; this method was initially designed to analyze the optics of paint layers [27]. While there is some contention regarding which conversion method is most scientifically appropriate, the Kubelka-Munk relation is the most ubiquitous for powder samples. Plotting the data as a function of wavelength (nm) yields a characteristic pattern that is dependent on the electron configuration.

$$F(R) = \frac{(1 - R)^2}{2R} \quad (2.18)$$

Plotting the data against energy (eV) allows for a qualitative approximation of the band gap energy E_g by extrapolating the linear portion of the absorption onset to the x -axis. Caution must be exercised, though, as this method is reliable so long as there are no convoluted/competing color mechanisms that overlap with the sharp absorbance drop-off associated with the band gap energy. For more accurate determination of the optical band gap energy, the Tauc method is more robust, and is detailed in Chapter 5.4.3.

2.3.3 Dielectric Properties

Dielectric materials are commonly used in the electronics industry (e.g., substrates, capacitors). Because they are insulators, they form islands of charge rather than allow electronic conduction. When a voltage differential is applied to a dielectric material, displacement and charge separation occurs, and is termed polarization (this is lost when the voltage is removed) [28]. Naturally, there are classes of dielectric materials that behave differently in response to an applied electric field (e.g., ferroelectrics retain this charge upon removal of the voltage); because the samples in this dissertation do not exhibit such behaviors, these phenomena will not be discussed. There are four contributions to the polarization: electronic, ionic, dipolar, and space charge [3, 28, 29]. Electronic polarization occurs when nucleus shifts towards the applied field, and the electron cloud shifts opposite the field. Ionic and dipolar polarization are the result of similar phenomena, but in relation to ions or dipoles in a solid, respectively. Lastly, space charge polarization occurs when there is a larger charge migration that occurs through the material.

Experimentally, the degree of polarization is determined from a parallel plate capacitor setup (Fig. 2.11). A well-sintered cylindrical pellet is placed between two parallel capacitor plates, a differential voltage V is applied across the sample, and a polarization of the static charge in the material should then be observed. Capacitance data were collected on an HP 4284 LCR meter at fixed frequencies of 1, 10, 100, 500, 1000 kHz, and in a temperature range of 30–200 °C. To form the parallel plate capacitor, electrodes were formed on the surfaces of the samples using Ag paint in

n-butyl acetate. For each sample, the Ag paint was cured at ≈ 120 °C for several hours. Before an experiment, an open (air) and short (Cu pastille) correction was performed to normalize the instrument to the approximate sample thickness.

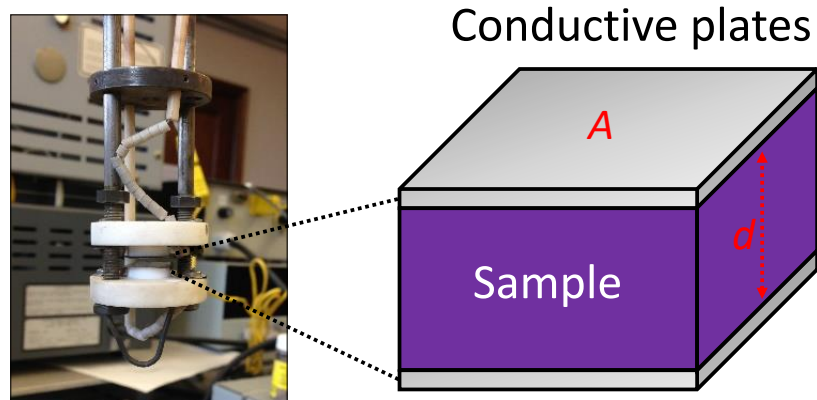


Figure 2.11: In-house parallel plate capacitor setup, with schematic of an idealized setup

When assessing the ability to store charge relative to a vacuum, two metrics are used: the dielectric constant κ and the loss tangent $\tan\delta$; these values allow for direct comparison between different dielectric materials [28]. The dielectric constant is the polarizability (the degree to which a material polarizes or the amount of charge displacement that occurs) of the sample, and the loss tangent will be discussed later in this section. First, the capacitance of free space C_0 and the capacitance of the sample C_s are measured,

$$C_0 = \frac{\varepsilon_0 A}{d} \quad (2.19)$$

in which ε_0 is the permittivity of free space (8.854×10^{-12} Fm⁻¹), A is the area of the plates, and d is the inter-plate distance, which is equivalent to the sample thickness.

The dielectric constant, also referred to as the relative permittivity ε_r , can then be determined from the relationship between the two capacitance values (Eq. 2.20).

$$\kappa = \varepsilon_r = \frac{C_s}{C_0} \quad (2.20)$$

The magnitude of κ depends on factors like crystal structure, defects, temperature, and frequency. The dielectric constant is composed of two terms:

$$\varepsilon_r = \varepsilon'_r - i\varepsilon''_r \quad (2.21)$$

in which ε'_r is the polarizability, and ε''_r is the loss. In an ideal dielectric, the current I outstrips the voltage V by 90° [3, 29]. In non-ideal dielectrics, ionic motion and electronic conductivity cause this angle to decrease by δ (Fig. 2.12). The loss tangent therefore represents the phase lag that leads to electrical energy loss, and this energy is either lost/absorbed in the material as heat.

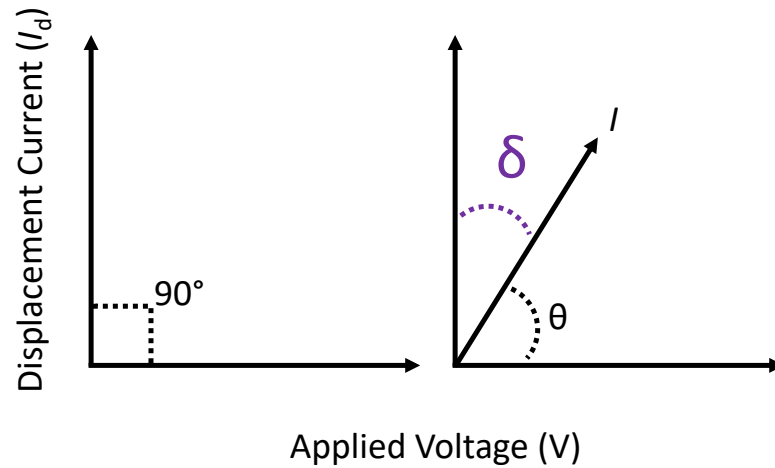


Figure 2.12: Capacitor phasor diagram, showing the phase angles between an ideal capacitor and a capacitor containing a lossy dielectric.

$$\tan \delta = \frac{\epsilon_r''}{\epsilon_r'} \quad (2.22)$$

The dielectric constant of a material can also be compared to that of a "theoretical" value; this is done via the Clausius-Mossotti relation, in which the atomic polarizability is related to the relative permittivity,

$$\frac{\kappa - \epsilon_0}{\kappa + 2\epsilon_0} \cdot \frac{M}{d} = \frac{4\pi N_A \alpha}{3} \quad (2.23)$$

in which M is the molar mass, d is the density, and α is the empirically derived atomic polarizability [3, 28]. This is relevant to Chapter 5.4.4, and data from these experiments can be found there.

2.3.4 *Photocatalytic Activity*

The conversion of light into chemical energy is a powerful process in nature; from plants (photosynthesis) to animals (vitamin D production), photochemistry is critical in producing essential chemicals needed for survival. Photochemistry can also be destructive, degrading paints/inks/dyes and plastics. In some cases, this photodegradation occurs slowly, and necessitates a photocatalyst. Photocatalytic activity is therefore a material property that converts light into chemical energy, which is then used to catalyze a reaction. These reactions occur when a material is irradiated with light of an energy that is slightly greater than that of its optical band gap. An electron is excited into the conduction band, generating a bound electron-hole pair called an exciton [30]. This quasiparticle migrates to an active site on the bulk surface, where redox reactions occur with adsorbed molecules (Fig. 2.13).

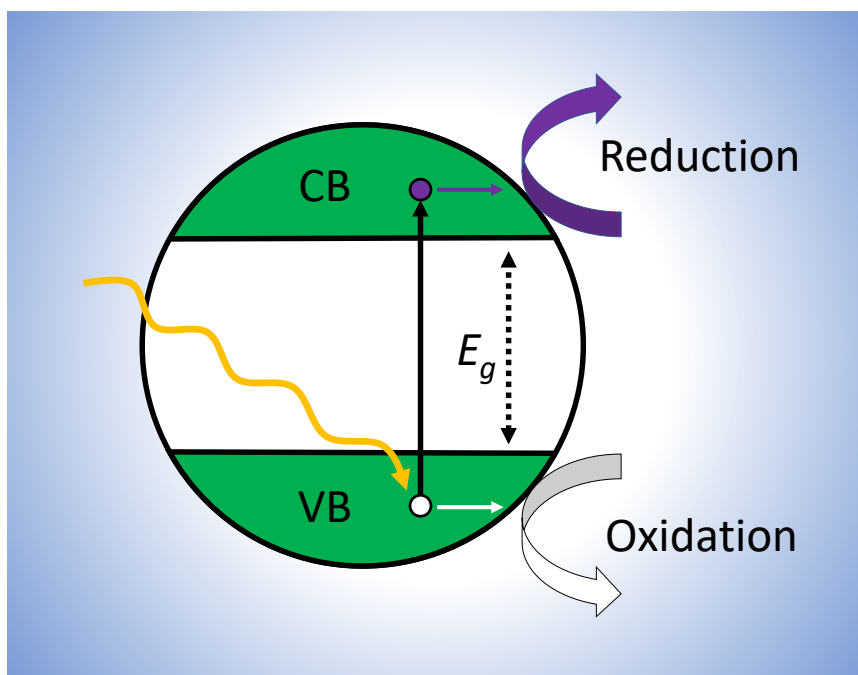


Figure 2.13: The general photocatalysis mechanism. A particle (green/white) suspended in solution (blue background) is irradiated with an incident light (yellow) with an energy $E > E_g$, forming an exciton, which migrates to the surface, causing single-electron reduction/oxidation reactions with adsorbed molecules. For water splitting, the reduction reaction is $\text{O}_2 + e^- \longrightarrow \text{O}_2^\bullet$ and the oxidation reaction is $\text{H}_2\text{O} + h^+ \longrightarrow \text{OH}^\bullet + \text{H}^+$.

In ideal future scenarios, an inorganic solid heterogeneous photocatalyst could be used to degrade harmful organic compounds via illumination from solar or lamp-produced light. Other applications include water splitting to generate H_2 fuels, surface sterilization, and air purification [31]. While there has been significant research and advancement in using TiO_2 as a photocatalyst, the band gap is large enough (3.2 eV) to only be effective in the UV region of light sources. As discussed, a large portion of ambient solar light is in the visible and IR regions, necessitating

the development of a photocatalyst that can be active in those wavelengths. When designing a photocatalytic material, several controllable properties include: band gap, carrier transport efficiencies/mechanism, surface area (directly related to particle size), and chemical stability. One way to achieve a narrower band gap semiconductor is to lower the conduction band minimum; as discussed in Chapter 1.2 and 1.3.6, vanadate/vanadomolybdate tunneled structures are shown to exhibit photocatalytic activity. This is posited to be the result of the V 3*d* band being energetically lower than that of the other cations in the structure [32]. Particle size can be controlled by synthetic methods (solution-based synthesis or ball milling).

Analysis of photocatalytic activity was performed via a lab-made reactor setup in conjunction with UV-vis spectroscopy (Fig. 2.14). A powdered sample (≈ 0.0200 g) is suspended in a 100 mL target solution (2.0×10^{-5} M) in a quartz roundbottom flask with an optically flat side. This flask was placed on a stir plate and enclosed in a dark box with an opening for illumination. Under constant stirring, illumination was provided from a 300 W Xe arc lamp; the intensity is regulated with a power supply (held constant at 155 mW at the reactor face) and energy meter to ensure all samples receive the same illuminance. Sample aliquots (≈ 2 mL) are withdrawn every 10–15 min. for 2 h, followed by centrifugation at 8000 rpm for 8 min. The supernatant is then analyzed with an Ocean Optics ISS-UV-Vis spectrophotometer to determine the maximum absorbance of methylene blue (MB). Options for gas flow and light filters are included in this setup. For this dissertation, the target solution was methylene blue, as the degradation of this dye molecule is well-documented and exhibits strong absorbance in the UV-vis region [33, 34]. The primary experimental aspects that

can be controlled include: concentration of the material, concentration of the target solution, incident light intensity, pH, and temperature. As a standard, a sample of Degussa P25 TiO₂ was analyzed under the full procedure. All powder samples were then evaporated and analyzed with X-ray diffraction to determine the retention of phase purity.

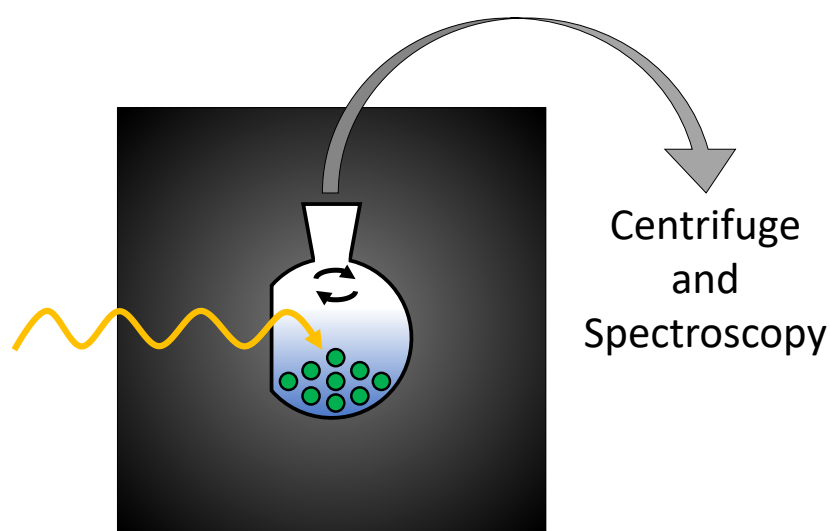


Figure 2.14: Schematic of a reactor setup for photocatalysis experiments. Powder samples (green) are suspended in solution with the degradation target and irradiated with incident light (yellow), all housed in a dark box. Aliquots are centrifuged and decanted, and degradation is monitored with a spectrophotometer.

Two variables must be accounted for prior to making any claims of photocatalytic efficacy: dye degradation from photolysis, and dye loss from sample-specific adsorption. To account for auto-degradation from photolysis, a full experiment was conducted on MB without a sample. To account for adsorption, a full experiment was conducted on MB with the sample, but without irradiation. It is important that the sample

mass is the same as that of the irradiated experiment. The photolysis and adsorption corrections were applied to each data point, and the overall degradation of MB was calculated. Data from these experiments can be found in Appendix B.2 and B.3.

References

- [1] S. A. Corr, R. Seshadri, 4.01 - Synthetic Methodologies, in: *Comprehensive Inorganic Chemistry II (Second Edition)*, Elsevier, Amsterdam, 2013, pp. 1–15. doi:10.1016/B978-0-08-097774-4.00401-0.
- [2] J. E. Rumble, *CRC Handbook of Chemistry and Physics*, CRC Press, 2018.
- [3] A. R. West, *Solid State Chemistry and its Applications*, 2nd Edition, Student Edition, Wiley, Chichester, 2014.
- [4] B. D. Cullity, S. R. Stock, *Elements of X-Ray Diffraction*, 3rd ed., Pearson, New Jersey, 2001.
- [5] D. S. Sivia, *Elementary Scattering Theory: For X-ray and Neutron Users*, Oxford University Press, 2011.
- [6] V. F. Sears, Neutron scattering lengths and cross sections, *Neutron News* 3 (1992) 26–37. doi:10.1080/10448639208218770.
- [7] W. H. Bragg, W. L. Bragg, The reflection of X-rays by crystals, *Proc. R. Soc. London, Ser. A* 88 (605) (1913) 428–438.
- [8] J. Wang, B. H. Toby, P. L. Lee, L. Ribaud, S. M. Antao, C. Kurtz, M. Ramanathan, R. B. Von Dreele, M. A. Beno, A dedicated powder diffraction beamline at the advanced photon source: Commissioning and early operational results, *Rev. Sci. Instrum.* 79 (8) (2008) 085105. doi:10.1063/1.2969260.
- [9] A. Huq, J. P. Hodges, O. Gourdon, L. Heroux, Powgen: A third-generation high-resolution high-throughput powder diffraction instrument at the Spallation Neutron Source, *Z. Kristallogr. Proc.* 1 (2011) 127–135. doi:10.1524/zkpr.2011.0019.
- [10] Rigaku Corporation, *X-Ray Diffractometer MiniFlex II Instruction Manual*, 2nd ed. (2006).

- [11] A. C. Larson, R. B. Von Dreele, General Structure Analysis System (GSAS), Tech. rep., Los Alamos National Laboratory Report LAUR 86-748 (2000).
- [12] B. H. Toby, EXPGUI , a graphical user interface for GSAS, *J. Appl. Crystallogr.* 34 (2001) 210–213. doi:10.1107/S0021889801002242.
- [13] A. Le Bail, Whole powder pattern decomposition methods and applications: A retrospection, *Powder Diffr.* 20 (2005) 316–326. doi:10.1154/1.2135315.
- [14] H. M. Rietveld, A profile refinement method for nuclear and magnetic structures, *J. Appl. Crystallogr.* 2 (1969) 65–71. doi:10.1107/S0021889869006558.
- [15] B. H. Toby, R factors in rietveld analysis: How good is good enough?, *Powder Diffr.* 21 (1) (2006) 67–70. doi:10.1154/1.2179804.
- [16] L. B. McCusker, R. B. Von Dreele, D. E. Cox, D. Louër, P. Scardi, Rietveld refinement guidelines, *J. Appl. Crystallogr.* 32 (1) (1999) 36–50. doi:10.1107/S0021889898009856.
- [17] J. B. Goodenough, *Magnetism and the Chemical Bond*, Wiley, New York, 1963.
- [18] A. F. Orchard, *Magnetochemistry*, Oxford University Press, 2003.
- [19] D. Jiles, *Introduction to Magnetism and Magnetic Materials*, 3rd ed., CRC Press, 2015.
- [20] Quantum Design, *Physical Property Measurement System Hardware and Operations Manual*, 2nd ed. (1999).
- [21] G. A. Bain, J. F. Berry, Diamagnetic corrections and Pascal’s constants, *J. Chem. Ed.* 85 (4) (2008) 532. doi:10.1021/ed085p532.
- [22] J. Van Vleck, Valence strength and the magnetism of complex salts, *J. Chem. Phys.* 3 (12) (1935) 807–813.
- [23] C. Kittel, *Introduction to Solid State Physics*, 8th ed., Wiley, 2012.
- [24] K. Nassau, The origins of colour in minerals, *Am. Mineral.* 63 (3) (1978) 219.
- [25] K. Adachi, Y. Tainosho, Characterization of heavy metal particles embedded in tire dust, *Environ. Int.* 30 (2004) 1009–1017. doi:10.1016/j.envint.2004.04.004.

- [26] J. Russell, Measurement of optical bandgap energies of semiconductors, Master's thesis, Oregon State University (2011).
- [27] P. Kubelka, F. Munk, An article on optics of paint layers, *Z. Tech. Phys.* 12 (1931) 593–601.
- [28] W. D. Kingery, H. K. Bowen, D. R. Uhlmann, *Introduction to Ceramics*, 2nd Edition, Wiley, New York, 1976.
- [29] R. J. D. Tilley, *Understanding Solids: The Science of Materials*, 2nd ed., Wiley, 2013.
- [30] M. Kaneko, I. Okura, *Photocatalysis: Science and Technology*, Springer, 2003.
- [31] S. Sanford, S. T. Mixture, D. D. Edwards, A comparison of the photocatalytic activity of six tunneled titanates, *J. Solid State Chem.* 200 (2013) 189–196. doi:10.1016/j.jssc.2012.12.036.
- [32] D. Wang, Z. Zou, J. Ye, A novel series of photocatalysts $M_{2.5}VMoO_8$ ($M = Mg, Zn$) for O_2 evolution under visible light irradiation, *Catal. Today* 93-95 (2004) 891–894. doi:10.1016/j.cattod.2004.06.090.
- [33] P. T. Hang, G. W. Brindley, Methylene blue absorption by clay minerals. determination of surface areas and cation exchange capacities (clay-organic studies XVIII), *Clays Clay Miner.* 18 (1970) 203–212. doi:10.1346/CCMN.1970.0180404.
- [34] A. Houas, H. Lachheb, M. Ksibi, E. Elaloui, C. Guillard, J.-M. Herrmann, Photocatalytic degradation pathway of methylene blue in water, *Appl. Catal., B* 31 (2001) 145–157. doi:10.1016/S0926-3373(00)00276-9.

Chapter 3: Structural investigation and selected properties of $\text{Zn}_{2.5-x}\text{Co}_x\text{VMoO}_8$ lyonsites

3.1 Abstract

The lyonsites are an underexplored crystal structure type; with precedent for compositional flexibility, this family of compounds has potential uses as inexpensive functional materials. This work examines cationic substitutions into $\text{Zn}_{2.5-x}\text{Co}_x\text{VMoO}_8$ and the subsequent effect on the Zn site preference. All samples were annealed between 700 and 1000 °C, resulting in green-colored pastilles. Powder X-ray diffraction (PXRD) and neutron powder diffraction (NPD) confirmed the solid solution range to be $0 \leq x \leq 2.5$, with all members isostructural with the parent compound. Magnetic susceptibility measurements indicated Curie-Weiss behavior in the high T region, confirming the presence of Co^{2+} . Diffuse reflectance measurements are also presented to explain the color mechanisms of this series.

Publications based on this chapter:

- [1] J. N. Tang, J. Li, M. A. Subramanian, Structural investigation and selected properties of $\text{Zn}_{2.5-x}\text{Co}_x\text{VMoO}_8$ lyonsites, *J. Solid State Chem.* 266 (2018) 155–160. doi:10.1016/j.jssc.2018.07.007.

3.2 Introduction/Motivation

Exploratory work in solid state chemistry has involved many structure types in the past century; while some structures are more ubiquitous in the literature, the understudied systems are no less worthy of investigation. In 2006, one of these lesser known families, the lyonsites, was given a thorough treatment in a seminal review [1], and what follows here is a brief recapitulation of that work. While the perovskite [2], pyrochlore [3], and spinel [4] families have extensive histories, the lyonsite had its beginnings in the laboratory, being first synthesized in 1960 [5], and a general structure determination carried out in 1964 [6]. Contrary to the typical trend of mineralogy inspiring chemistry, a natural lyonsite was not discovered until 1987, in which the iron-copper vanadate was found in El Salvador [7]. Since then, various lyonsite compounds have found potential uses as optical filters [8], photocatalytic materials [9, 10], and microwave dielectrics [11–13].

The lyonsites take the general formula $A_4M_3O_{12}$; other common formula expressions involve simple multipliers to clarify stoichiometric features or to facilitate ease of reading, such as is the case of $A_{2.5}M_2O_8$. The connectivity within this oxygen framework consists of face- and edge-shared AO_6 polyhedra, the vertices of each polyhedron connected to isolated MO_4 tetrahedra. Typically, two cations occupy the A sites, the ionic radius range of which are empirically generalized to 0.46 to 1.02 Å [1]. The oxidation states of these cations can range between +1 and +5 [1]. The M site is limited to smaller, highly charged cations that prefer four-fold coordination [14, 15]. The A sites are further distinguished by polyhedral sharing: A1 (face-shared

octahedra), A2 (edge-shared octahedra), and A3 (edge-shared trigonal prisms) (Fig. 3.1).

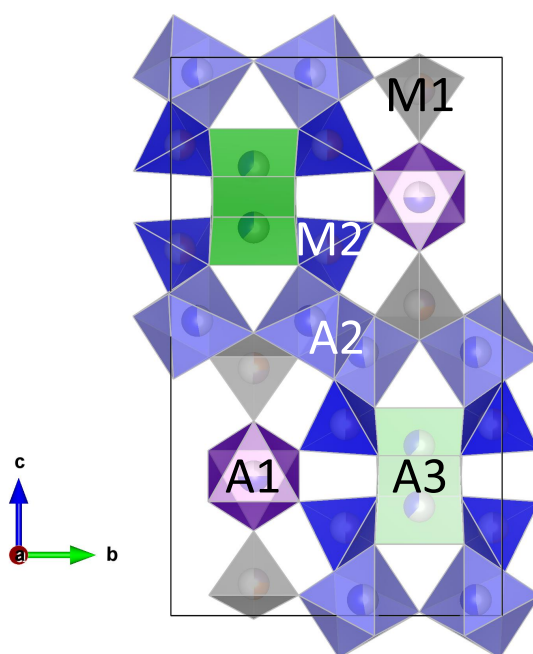


Figure 3.1: Lyonsite crystal structure (A1 = purple, A2 = blue, A3 = green, M1 = gray, M2 = navy).

Known lyonsites typically contain two cations in the *A* site, usually Li^+ , a transition metal (TM), and vacancies, the ratios and distribution of which are dictated primarily by charge separation [16–20]. The related compound $\text{Zn}_{2.5}\text{VMoO}_8$ is one of the few known lyonsites in which only one cation (and corresponding vacancies) occupy the *A* site [14, 15, 21, 22]. Currently, the site preference for Zn^{2+} in this structure is unknown. This study therefore explores the structural behavior when the *A* site undergoes isovalent substitution with Co^{2+} . Conventionally, Co^{2+} -containing oxides are blue in color, such as in the case of CoAl_2O_4 (spinel structure) [23]. The coloration

is due to $d-d$ transitions in the Co-containing tetrahedral site; in addition, the geometric arrangement of the Co^{2+} ions allows for atypical magnetic behaviors. The other end member, $\text{Co}_{2.5}\text{VMoO}_8$, has been reported, but no physical properties have been explored [24]. Thus, this work will also detail some physical properties of the solid solution.

3.3 Experimental

Stoichiometric ratios of ZnO (Aldrich, 99.9%), CoCO_3 (Sigma-Aldrich, 46-48% as Co), V_2O_5 (Cerac, 99.9%), and MoO_3 (Sigma-Aldrich, 99.5%) were ground in an agate mortar, pressed into cylindrical pellets, and decarbonated at 500 °C for 6 h prior to annealing. All samples were annealed between 700 and 1000 °C.

X-ray diffraction data were collected using a benchtop Rigaku MiniFlex II diffractometer using Cu K_α and a graphite monochromator. Le Bail refinements were performed with KCl as an internal standard. A sample at the midpoint of the solid solution was loaded in a 6 mm vanadium sample can, and room temperature time-of-flight (TOF) neutron powder diffraction data were obtained from Oak Ridge National Laboratory, on the BL-11A POWGEN beamline. Subsequent Rietveld analysis was performed via the General Structure Analysis System (GSAS) software with the EXPGUI interface [25].

Zero-field-cooled (ZFC) DC magnetization experiments were conducted using a Quantum Design PPMS, from 5–300 K, and a Quantum Design SQUID MPMS. Determination of the effective magnetic moments (in Bohr magnetons, μ_B) were done

by fitting the inverse susceptibility curves to the reciprocal of the Curie-Weiss Law (Eq. 3.1),

$$\frac{1}{\chi_{\text{mol}}} = \frac{T - \theta}{C}, \quad (3.1)$$

extracting the Curie constant C , and subsequent conversion to magnetic moment via $\mu_{\text{eff}} = 2.84\sqrt{C}$. UV-Vis diffuse reflectance data were obtained using an Ocean Optics HR-4000 spectrophotometer, with an MgO reference. The data, R , were then converted to absorbance units A via the Kubelka-Munk relationship (Eq. 3.2). Vis-NIR reflectance data were collected via a Jasco V-670 spectrophotometer (out to 2500 nm).

$$A = \frac{(1 - R)^2}{2R} \quad (3.2)$$

3.4 Results/Discussion

3.4.1 *Crystal Structure*

A full solid solution was found to exist along the $0 \leq x \leq 2.5$ range. However, due to the similarity in Shannon radii (Zn^{2+} : 0.74 Å and Co^{2+} : 0.745 Å)[26], lattice shifts are difficult to notice upon visual inspection of the XRD patterns (Fig. 3.2). The a and b parameter are shown to be relatively constant, while the c parameter (and in extension, the unit cell volume) decreases (from 17.63 Å to 17.52 Å) with increasing Co content (Fig. 3.3). The decrease along the c axis is counterintuitive, considering the Shannon radius for Co^{2+} is larger than that of Zn^{2+} . Initially, this atypical behavior was attributed to the unknown ionic radii of Co^{2+} and Zn^{2+} in

the trigonal prismatic site. This lack of reliable radii data for the TP site is due to the small number of known compounds exhibiting this coordination environment. Therefore, it is conjectured that if the Co^{2+} radius is smaller than that of Zn^{2+} in that coordination environment, it is conceivable that the unit cell would shrink. Radius determination is difficult, though, due to the asymmetric nature of the trigonal prism in this structure.

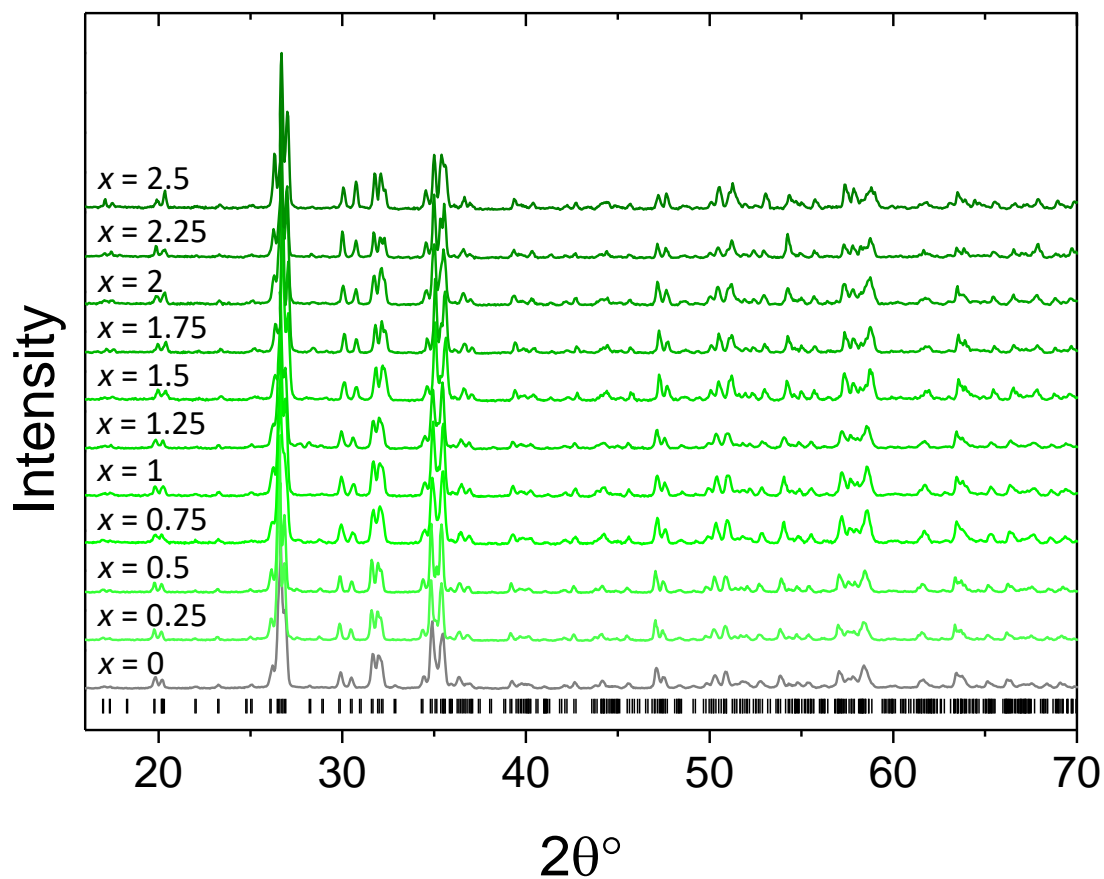


Figure 3.2: Powder X-ray diffraction patterns for $\text{Zn}_{2.5-x}\text{Co}_x\text{VMoO}_8$.

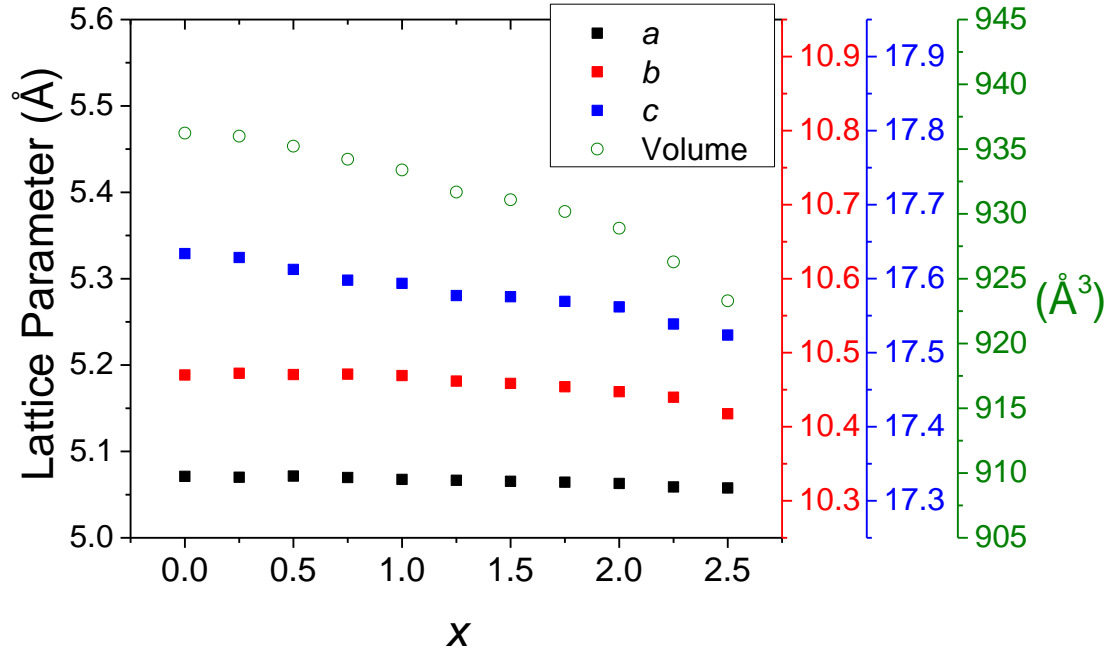


Figure 3.3: Lattice parameters for $\text{Zn}_{2.5-x}\text{Co}_x\text{VMoO}_8$. The ranges for the a , b , and c parameters are set to the same size (0.6 Å) for direct comparisons.

TOF neutron diffraction analysis was conducted on the $x = 1.25$ composition. The Rietveld refinement yielded a refined formula of $\text{Zn}_{1.20}\text{Co}_{1.30}\text{V}_{0.98}\text{Mo}_{1.02}\text{O}_8$ (or if adhering to the $A_4M_3O_{12}$ formula, $\square_{0.25}\text{Zn}_{1.80}\text{Co}_{1.95}\text{V}_{1.47}\text{Mo}_{1.53}\text{O}_{12}$), correlating well to the nominal composition (Fig. 3.4). Due to the presence of unavoidable vacancies in this system, several considerations had to be made. As a starting point, Zn, Co, and a vacancy, \square , were equally distributed across the three A sites, and V and Mo across the M sites. Vacancies were refined to localize on the A1 site, which consists of face-sharing octahedra. Localization along this chain of octahedra makes intuitive and chemical sense, as vacancies would stabilize the cationic repulsion that would result from the close proximity of Zn^{2+} and Co^{2+} . This behavior is also corroborated from

prior work on vanadomolybdate lyonsites [1, 21, 22].

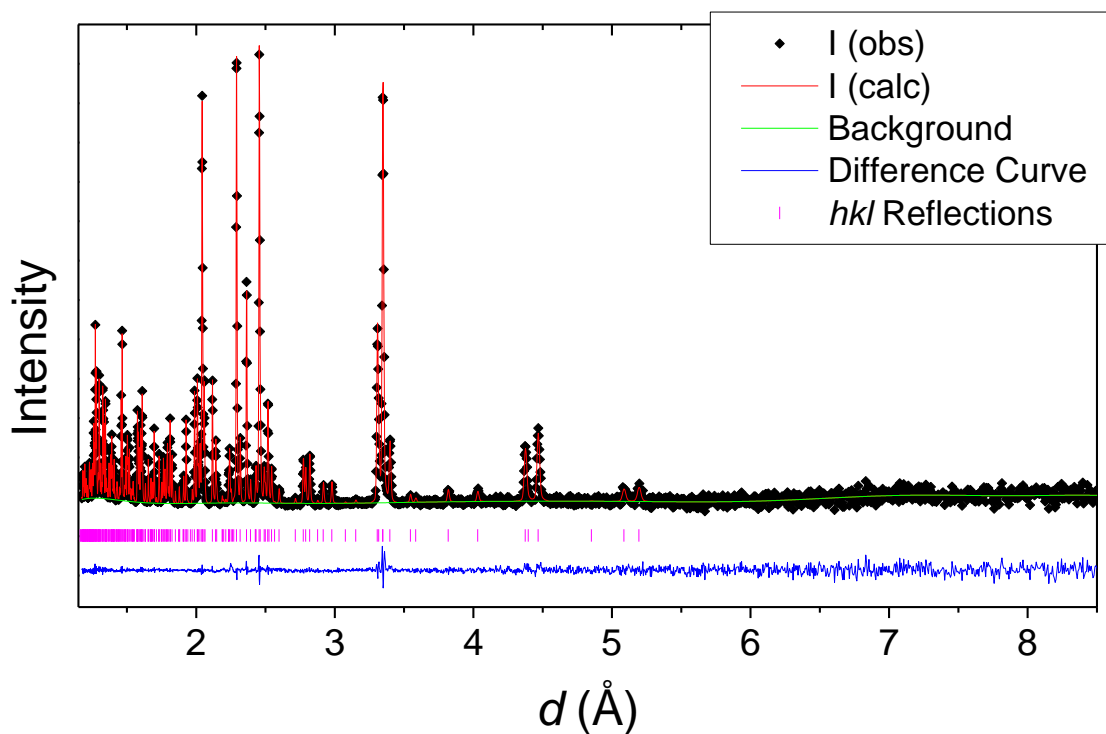


Figure 3.4: TOF neutron diffraction pattern for $\text{Zn}_{1.25}\text{Co}_{1.25}\text{VMoO}_8$. Display includes calculated intensities (red), difference curve (blue), and allowed reflections for $Pnma$ (magenta).

The O sites were determined to be fully occupied from the lack of impurity phases in the X-ray analysis, and subsequent refinement was performed with these sites' occupancies fixed at 1. The face-sharing octahedral site A1 extends through the center of the tunnel structure, and is occupied by an approximate ratio of 2:1:1 for $\text{Co}^{2+}:\text{Zn}^{2+}:\square$. The edge-sharing octahedral site A2 is evenly mixed between Co^{2+} and Zn^{2+} (Table 3.1). The central cations in these octahedra are displaced from the ideal centers, as expected from the geometric arrangement (face- and edge-sharing)

of these polyhedra. Edge-shared octahedra between unit cells are connected to each other in a staggered fashion, resulting in sheets extending along the tunnel. The trigonal prismatic site, A3, shows a 3:2 Zn^{2+} to Co^{2+} preference. Like the A2 site, the polyhedral distortions within each prism is accommodated between unit cells by staggering, forming zig-zag columns. V^{5+} and Mo^{6+} each occupy the isolated tetrahedral sites M1 and M2 in equal amounts. While V^{5+} is a poor scatterer in neutron diffraction, it shares sites with Mo^{6+} ; this situation allows Mo^{6+} to be incrementally refined against a manually-adjusted V^{5+} to a total occupancy of 1.

Table 3.1: Unit cell coordinates, occupancies, and displacement parameters for $\text{Zn}_{1.25}\text{Co}_{1.25}\text{VMoO}_8$ ($Pnma$). $a = 5.0497(1)$ Å, $b = 10.389(1)$ Å, $c = 17.497(1)$ Å, $V = 918.00(5)$ Å³. Reliability parameters $\chi^2 = 2.85$, $wR_p = 2.27$ %. *Refined anisotropic U values can be found in the available CIF file (CSD no. 434587).

Atom	Site	x	y	z	Occ.	$U_{\text{iso}}(\text{Å}^2)$
Zn/Co (A1)	4c	0.3945(1)	1/4	0.2515(4)	0.24(2)/0.51(2)	0.042(5)
Zn/Co (A2)	8d	0.7509(6)	0.0796(2)	0.5279(1)	0.47(1)/0.53(1)	0.010(1)
Zn/Co (A3)	4c	0.7506(7)	1/4	0.6953(2)	0.60(2)/0.40(2)	0.009(2)
V/Mo (M1)	4c	0.2166(9)	1/4	0.4430(2)	0.48/0.52(1)	0.004(3)
V/Mo (M2)	8d	0.7174(6)	-0.0278(2)	0.3432(2)	0.50/0.50(1)	0.004(2)
O1	4c	0.1424(6)	1/4	0.3478(1)	1.0	*
O2	4c	-0.0619(6)	1/4	0.5070(1)	1.0	*
O3	8d	0.4155(4)	0.1149(2)	0.4635(1)	1.0	*
O4	8d	0.4362(5)	-0.1147(2)	0.3719(1)	1.0	*
O5	8d	0.9237(4)	-0.1262(1)	0.2864(1)	1.0	*
O6	8d	0.6485(4)	0.1127(1)	0.2959(1)	1.0	*
O7	8d	0.9141(4)	0.0071(2)	0.4239(1)	1.0	*

Upon cursory inspection, these MO_4 tetrahedra are geometrically uniform relative to the A sites. However, the M1–O1 bonds that are oriented towards the A1 site are notably shorter than those toward the A2 site (Fig. 3.5a, bolded). This behavior is also seen in the M2 site, in which the corresponding M2–O6 bond is also shorter than the M2–O bonds oriented towards the A2 and A3 sites (Fig. 3.5b, bolded). Because the vacancies were determined to localize to the A1 site, the O1 and O6 atoms are under-coordinated. These atoms therefore displace towards a higher oxidation state

cation (in this case, the V^{5+} and Mo^{6+} atoms on the M sites) to satisfy bond valence.

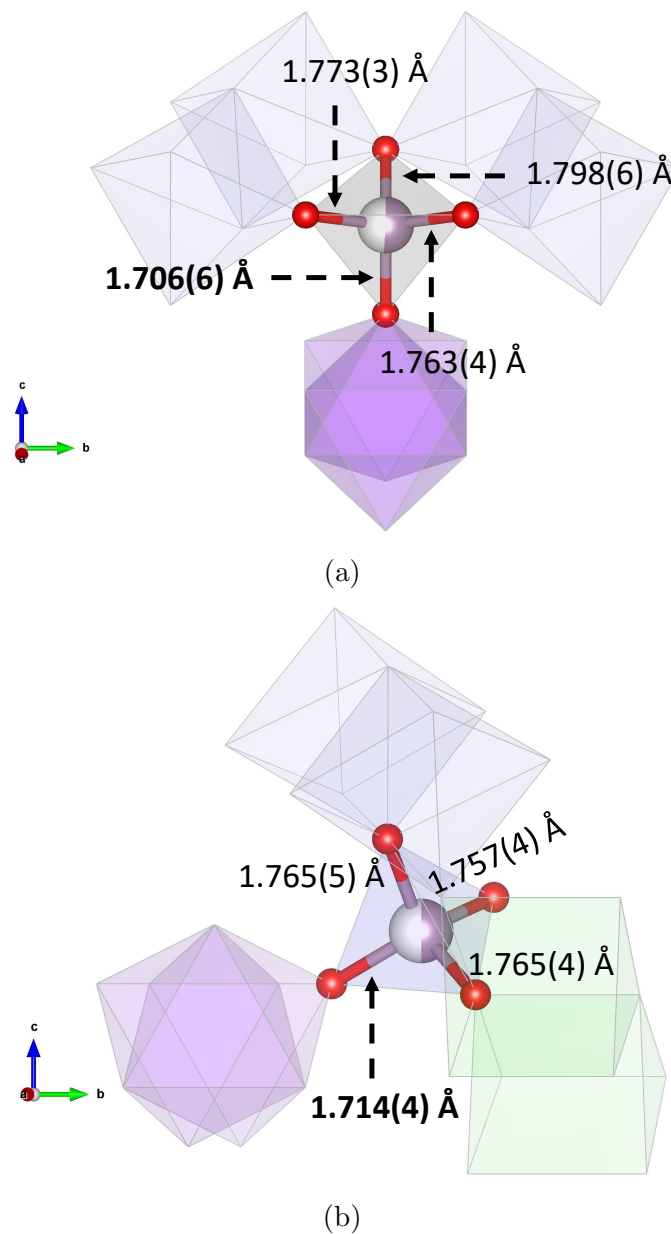


Figure 3.5: Fragments of the $Zn_{1.20}Co_{1.30}V_{0.98}Mo_{1.02}O_8$ unit cell, with the M1 (a) and M2 (b) sites' bond lengths labeled. Other structural features are provided for context. Atom colors: V = gray, Mo = purple, O = red.

Ordinarily, the vanadomolybdate lyonsites tend to crystallize as $Pnma$. However, prior work from Wang et al. on the structure of a Zn-rich end member (equivalent to $x = 0$ in this work) reported the compound to crystallize in the $P2_12_12_1$ space group [21], a non-centrosymmetric subgroup of $Pnma$. The trigonal prism site in that work was highly distorted, which propagated to a structure-wide distortion. Conversely, Kurzawa et al. demonstrated that the Co-rich end member ($x = 2.5$) is isotypic to $x = 0$, but its space group retains the centrosymmetric $Pnma$ [24]. This work's lattice parameter values correlate well to literature values (Fig. 3.6).

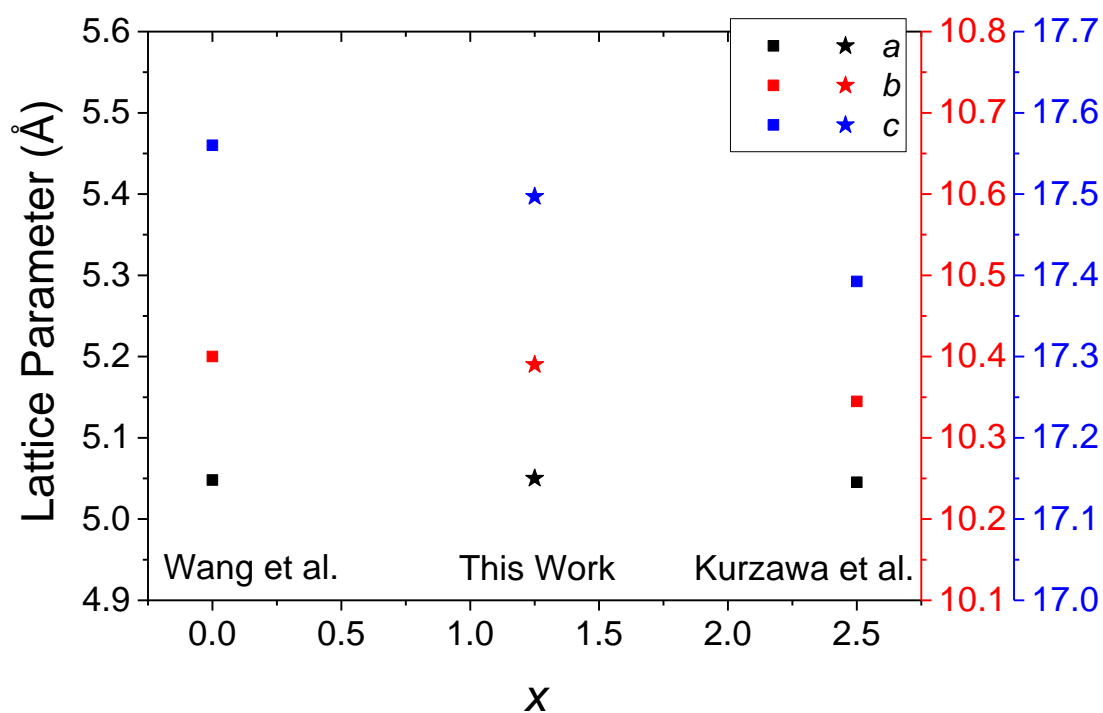


Figure 3.6: Lattice parameter comparisons for $Zn_{2.5-x}Co_xVMoO_8$ against literature values [21, 24].

Specifically, Wang et al. demonstrated that upon examination of the A3 site, the distortion in the trigonal prism leads to a 2_1 screw axis, from what would have been an a glide [21]. Due to the high degree of polyhedral connectivity, this distortion extends throughout the structure, causing the symmetry to reduce to $P2_12_12_1$. In this work, the presence of Co^{2+} in that site has increased its regularity, thereby increasing its symmetry back to $Pnma$ (Fig. 3.7). This is posited to be the result of the greater ionicity of Co–O bonds compared to Zn–O bonds; the covalency of Zn–O bonds imply bond directionality, and therefore decreased flexibility. The introduction of Co^{2+} thereby allows for the restoration of centrosymmetry, even in small quantities. This was especially observed during Le Bail lattice refinements, in which even the $x = 0.25$ member could be modeled to the $Pnma$ space group.

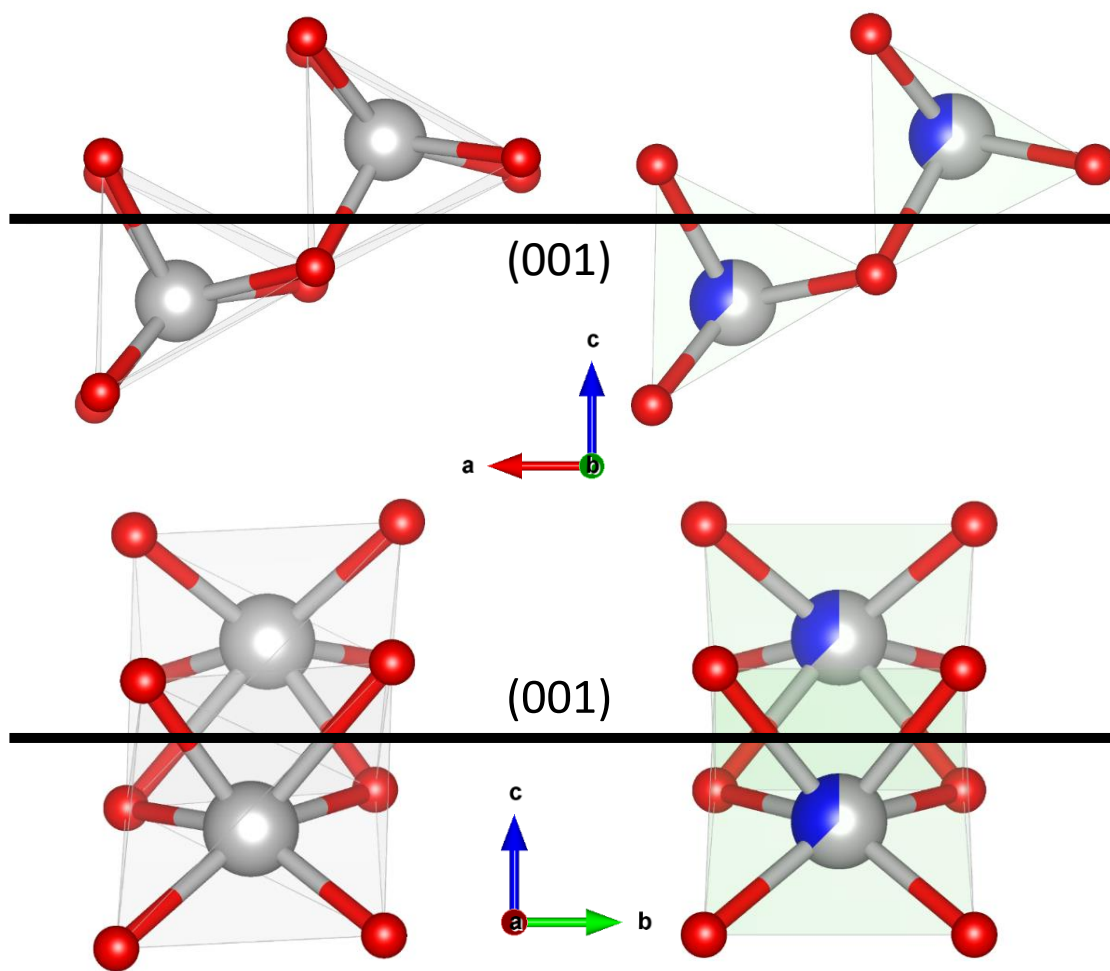


Figure 3.7: A3 site symmetry comparisons between Wang et al. [21] (left) and this work (right). Black line indicates (001) plane. Top row: projection viewed along the b axis, bottom row: along the a axis. Atom colors: Zn = gray, Co = blue, O = red.

The trend observed in the a and b cell edges can be demonstrated by comparing the dimensions of the A1 site (Fig. 3.8a). However, this alone provides little insight regarding the symmetry change. The cell edge reduction seen along the b and c directions can be visualized in the A1 and A3 site bond angles (Fig. 3.8b). Here,

there is a notable increase in polyhedral symmetry with the introduction of Co. The observed lattice contraction is therefore due to compositionally controlled bond angles, counter to the conventional radius difference rationale, as Zn^{2+} and Co^{2+} are practically identical in size.

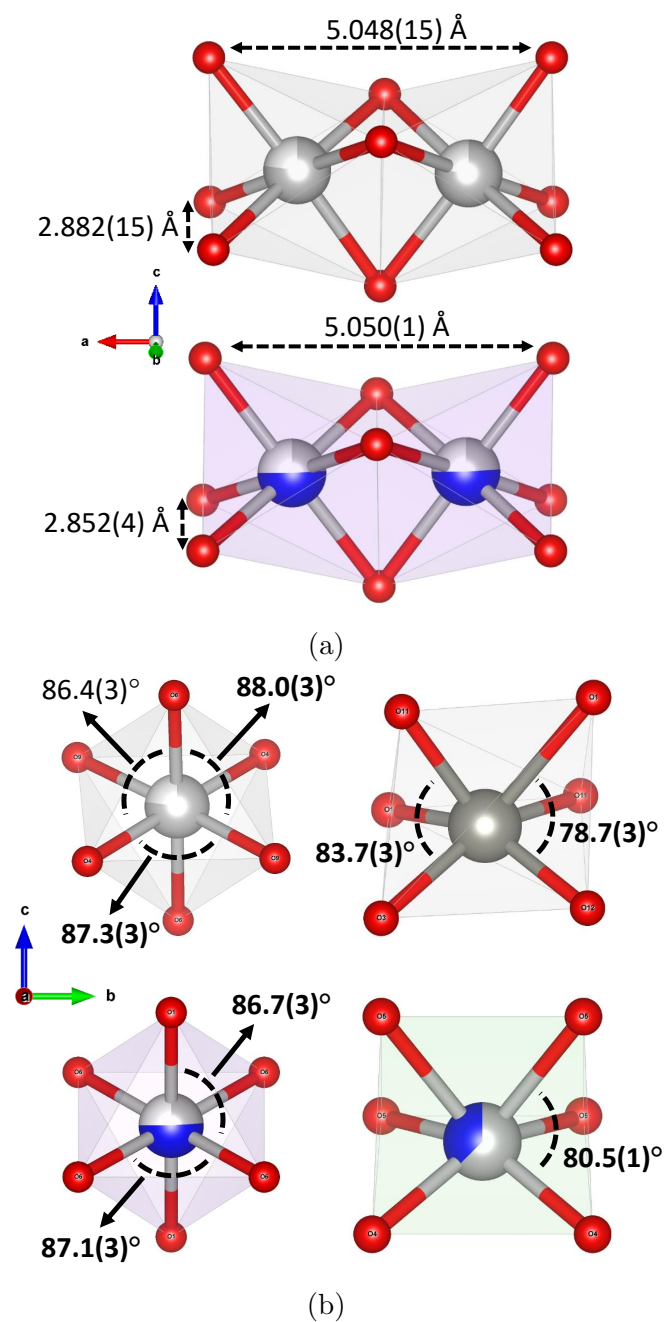


Figure 3.8: Isolated polyhedra for $\text{Zn}_{1.20}\text{Co}_{1.30}\text{V}_{0.98}\text{Mo}_{1.02}\text{O}_8$, labeled with (a) select A1 interatomic distances, and (b) A1(left)/A3(right) bond angles. Top row: Wang et al. [21], bottom row: this work. Atom colors: Zn = dark gray, Co = blue, \square = light gray, O = red.

Considering the geometric irregularity of these polyhedra, it is useful to quantify the polyhedral distortions. While this can be quantified in several ways, this work will focus on two methods. First, calculating the quadratic elongation parameter λ (Eq. 3.3, in which n = number of bonds, l_o = idealized bond length (taken by summing radii), l_i = bond length) yields whether or not a polyhedron is distorted relative to a polyhedron of identical volume [27]. Deviation away from a value of 1 indicates distortion. When calculated for all three sites across $x = 0, 1.25,$ and $2.5,$ it is apparent that the A1 and A2 site remain regular, while A3 expands with decreasing $x,$ which corresponds to decreasing Co content (Table 3.2a).

$$\lambda = \frac{1}{n} \sum_{i=1}^n \left(\frac{l_i}{l_o} \right)^2 \quad (3.3)$$

Second, calculating the bond length distortion parameter Δ (Eq. 3.4) will quantify the degree to which the polyhedron is distorted, in which higher deviation from a value of 0 indicates higher amounts of distortion [28].

$$\Delta = \frac{1}{n} \sum_{i=1}^n \left(\frac{l_i - l_o}{l_o} \right)^2 \quad (3.4)$$

The values shown in Table 3.2b indicate that with decreasing x values, the A1 and A3 site become more distorted, corresponding to a decrease in Co content. It should be noted that the tabulated values are all scalar quantities, and therefore can only be interpreted relative to each other, as is especially the case with the A3 site. Mathematically, the octahedra and trigonal prisms are treated equally, since they both represent six-fold coordination environments. Because of the framework nature of this

structure, the A1 and A3 sites' distortions correspond to the A2 site counter-distorting to compensate.

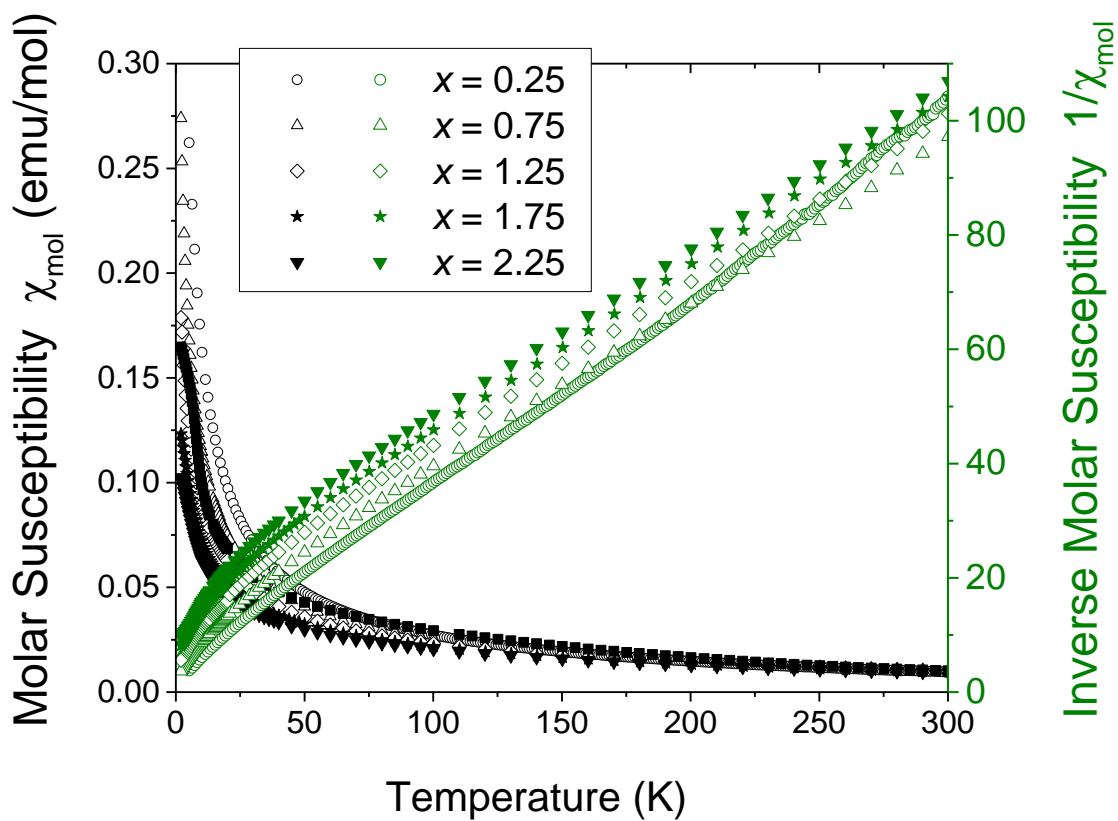
Table 3.2: Polyhedral distortion parameters: (a) quadratic elongation and (b) bond length distortion ($\times 10^3$). n = number of bonds, l_o = idealized bond length (taken by summing radii), l_i = bond length.

x	λ_{A1}	λ_{A2}	λ_{A3}	x	Δ_{A1}	Δ_{A2}	Δ_{A3}
0	1.00	1.00	1.10	0	0.66	0.74	9.32
1.25	0.99	0.99	1.03	1.25	0.25	0.79	1.37
2.5	1.01	1.01	0.99	2.5	0.14	1.67	0.99
$\lambda = \frac{1}{n} \sum_{i=1}^n \left(\frac{l_i}{l_o}\right)^2$ [27]				$\Delta = \frac{1}{n} \sum_{i=1}^n \left(\frac{l_i - l_o}{l_o}\right)^2$ [28]			
(a)				(b)			

3.4.2 Magnetic Properties

Magnetic susceptibility measurements reveal that all samples in this series are paramagnetic, and exhibit Curie-Weiss behavior in the high T region (150–300 K) (Fig. 3.9a). The spin-only effective moment value (μ_S) for a high-spin d^7 ion ($S = 3/2$) is calculated to be $3.87 \mu_B$. However, these samples exhibit magnetic moments that are closer to that of Co^{3+} ($S = 2$), $4.89 \mu_B$ (Table 3.9b). This observation would not make chemical sense, as the presence of Co^{3+} would require either charge balancing in the chemical formula, or the presence of diffraction peaks associated with a corresponding impurity phase. The more likely scenario is that the orbital angular momentum is unquenched, leading to a higher effective moment (μ_{S+L}), as is the case for other

compounds containing a high-spin d^6 or d^7 ion [29]. For Co^{2+} , this corresponds to a theoretical moment of $5.21 \mu_{\text{B}}$ (via $\mu_{\text{S+L}} = \sqrt{4S(S+1) + L(L+1)} \mu_{\text{B}}$), with a commonly observed range of $4.3\text{--}5.2 \mu_{\text{B}}$. For Co^{3+} , the moment would be $5.50 \mu_{\text{B}}$, with a commonly observed range of $5.0\text{--}5.6 \mu_{\text{B}}$. In addition, the demonstrated polyhedral irregularities must be considered; the local environment for Co^{2+} is tetragonally distorted, and the μ_{eff} should therefore reflect this symmetry. Earlier works have modeled the consequences of this symmetry [30], and the effective moments reported here agree well with those discussions. The +2 oxidation state is thereby confirmed for Co in the structure, as the μ_{eff} values match well to the $\mu_{\text{S+L}}$ values in both ideal and tetragonally distorted local symmetries.



(a)

x	θ_W	$\mu_{\text{eff}}(\mu_B)$
0.25	8.5	4.77
0.75	-37.2	5.30
1.25	-49.0	5.26
1.75	-54.2	5.23
2.25	-66.6	5.26

(b)

Figure 3.9: Magnetic susceptibility plots for $\text{Zn}_{2.5-x}\text{Co}_x\text{VMoO}_8$ and corresponding effective moments.

3.4.3 Optical Properties

The presence of Co^{2+} in all three A sites leads to two possible crystal field splitting schemes, shown in Figure 3.10a. In both of these coordination environments, there are spin-allowed $d-d$ transitions that should occur. The diffuse reflectance spectra exhibit two transitions. The lower energy peak can be attributed to the $d-d$ excitation in the Co^{2+} sites (at 600 nm), and the higher energy peak to a ligand-to-metal charge transfer band (LMCT) (Fig. 3.10c). The transition at 600 nm scales with Co content, with increasing absorbance as x value increases. Because V and Mo are in their highest oxidation states, the LMCT band can be assigned to the transition between the O $2p$ ligands and the empty d orbitals of the M site central atoms. The coexistence of both transitions give rise to the observed green color (Fig. 3.10b). In the case of the $x = 0$ member, the A cation is only Zn^{2+} , in which no $d-d$ transitions are possible. The only major transition is the higher energy LMCT band, and the observed color is therefore white. The sharp drop-off in absorbance at 350 nm allows for a rough band gap estimate of 3.16 eV, done via extrapolation to the horizontal axis, followed by conversion to photon energy. In the visible region of the Vis-NIR spectra, the decreasing reflectance in the visible region corresponds well to the darker shades of green as Co content increases. The NIR reflectance of the Zn end member is functionally 100%; however, the introduction of Co into the structure has a moderately negative effect on this reflectance (Fig. 3.10d). Similar behavior can also be observed in other common Co^{2+} compounds, such as the CoAl_2O_4 spinel [23].

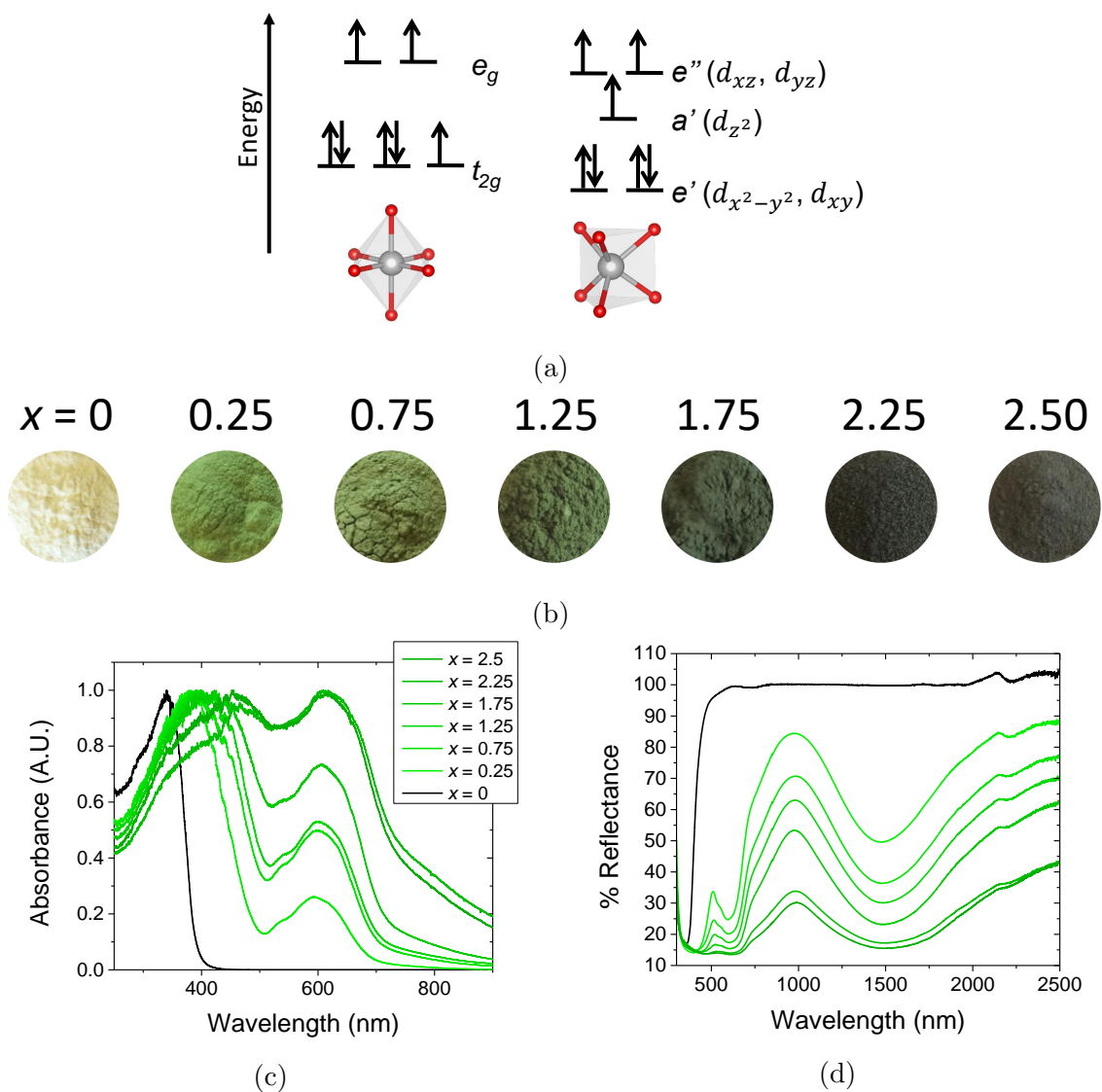


Figure 3.10: Optical properties for $\text{Zn}_{2.5-x}\text{Co}_x\text{VMoO}_8$. Displayed are (a) Crystal field splitting diagrams for ideal octahedra and trigonal prisms, (b) powder pictures from $x = 0$ (left) to $x = 2.5$ (right), (c) UV-vis diffuse reflectance spectra, and (d) vis-NIR diffuse reflectance spectra, following the same legend scheme as (c).

3.5 Conclusions

The $\text{Zn}_{2.5-x}\text{Co}_x\text{VMoO}_8$ lyonsites were successfully synthesized for the full range of $x = 0\text{--}2.5$. All non-parent members exhibited varying shades of green colors. Structural analysis via XRD and TOF NPD revealed that the introduction of Co^{2+} into the A sites increases the ionicity of the corresponding bonds, which increases polyhedral uniformity. This leads to a change from the lower symmetry $P2_12_12_1$ to the higher symmetry $Pnma$. All samples were shown to exhibit Curie-Weiss behavior, thereby confirming the presence of Co in the +2 oxidation state. The observed green colors are the result of the coexistence of LMCT in the M sites and $d\text{-}d$ transitions in the A sites.

3.6 Supporting Information

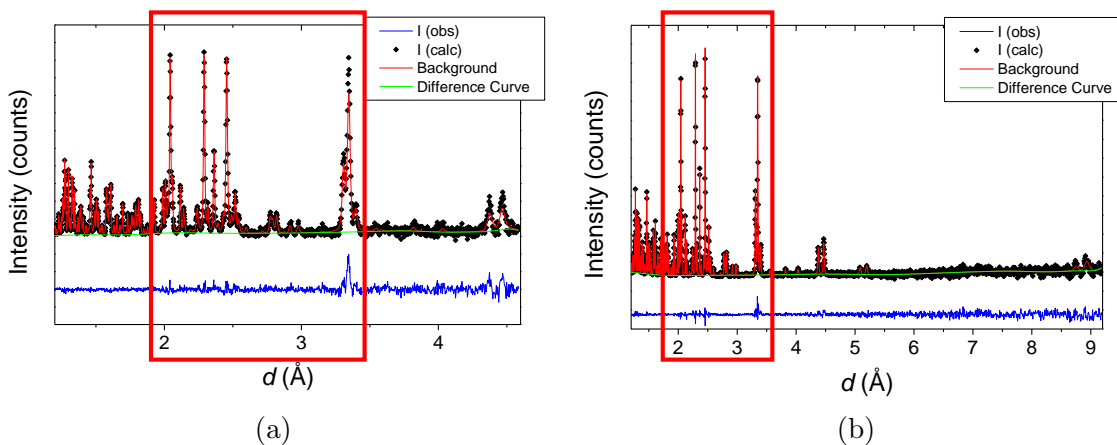


Figure 3.11: Powder neutron diffraction analysis for the nominal $\text{Zn}_{1.25}\text{Co}_{1.25}\text{VMO}_8$ between Banks 2 (a) and 4 (b) from POWGEN. Overlapping d -spacing regions are boxed in red to indicate intensity mismatch between banks. Bank 2 was omitted from further refinement due to the lower data quality.

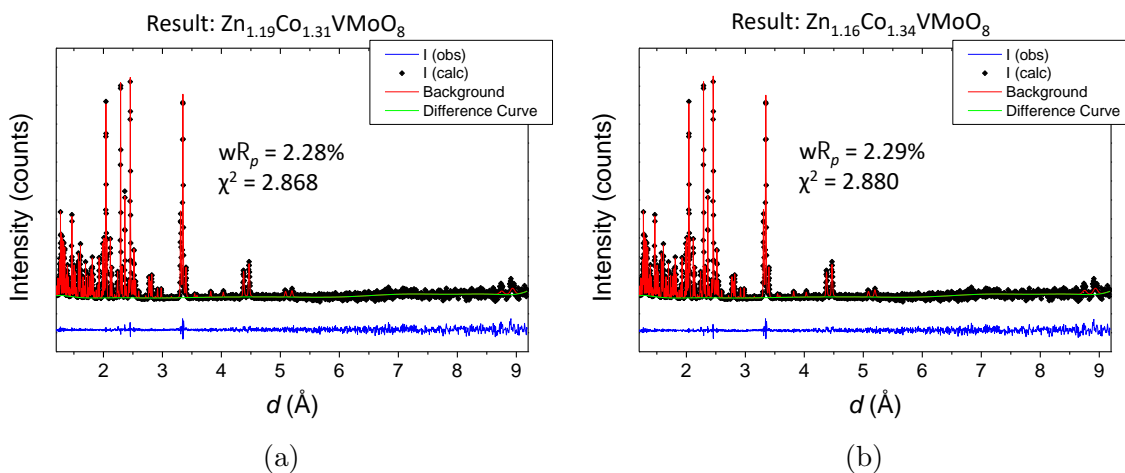


Figure 3.12: A site vacancy localization simulations on the A2 (a) and A3 (b) sites for the nominal $\text{Zn}_{1.25}\text{Co}_{1.25}\text{VMO}_8$.

Table 3.3: Summary of *A* site vacancy simulations for the nominal $\text{Zn}_{1.25}\text{Co}_{1.25}\text{VMoO}_8$ as obtained from neutron diffraction analysis. *Values deemed unreasonable, thereby invalidating that simulation

\square site	χ^2	wR_p	U_{iso} (\AA^2)	O4 U_{33}	Refined formula
A1	2.85	2.27	.042(5)	0.0008(16)	$\text{Zn}_{1.20}\text{Co}_{1.30}\text{V}_{0.98}\text{Mo}_{1.02}\text{O}_8$
A2	2.87	2.28	.042(4)	0.0001(16)*	$\text{Zn}_{1.19}\text{Co}_{1.31}\text{VMoO}_8$
A3	2.88	2.29	.042(4)	0.0008(16)	$\text{Zn}_{1.16}\text{Co}_{1.34}\text{VMoO}_8^*$
A1&A2	2.82	2.27	.041(4)	0.0003(14)*	$\text{Zn}_{1.19}\text{Co}_{1.31}\text{VMoO}_8^*$

Table 3.4: Summary of *M*–O site bond lengths (\AA) under different vacancy simulations for the nominal $\text{Zn}_{1.25}\text{Co}_{1.25}\text{VMoO}_8$ as obtained from neutron diffraction analysis. *Values indicate O displacement towards *M* cation.

\square site	M1–O1*	M1–O2	M1–O3	M2–O4	M2–O5	M2–O6*	M2–O7
A1	1.700(4)	1.781(4)	1.773(3)	1.762(3)	1.764(3)	1.709(3)	1.768(3)
A2	1.707(6)	1.799(6)	1.763(4)	1.757(4)	1.766(4)	1.714(4)	1.764(5)
A3	1.705(6)	1.802(6)	1.763(4)	1.758(4)	1.768(4)	1.713(4)	1.762(5)

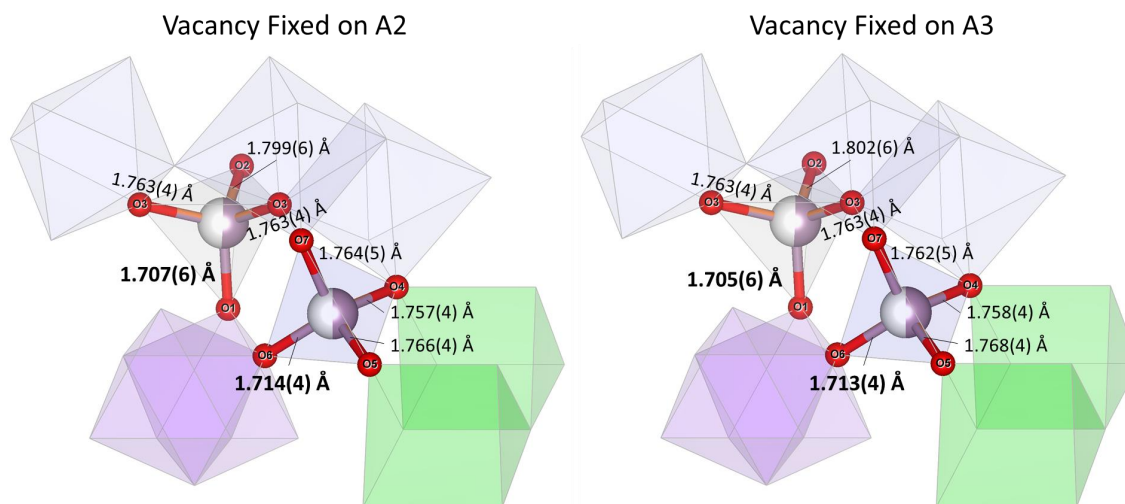


Figure 3.13: Visual representation of the M site under different vacancy simulations for the nominal $\text{Zn}_{1.25}\text{Co}_{1.25}\text{VMoO}_8$ as obtained from neutron diffraction analysis. Shortened M -O bond lengths resulting from O displacement towards the M cation are bolded.

Table 3.5: Bond valence sums for the nominal $\text{Zn}_{1.25}\text{Co}_{1.25}\text{VMoO}_8$ as obtained from neutron diffraction analysis.

Site	Site BVS
A1	1.57
A2	2.09
A3	1.88
M1	5.29
M2	5.36

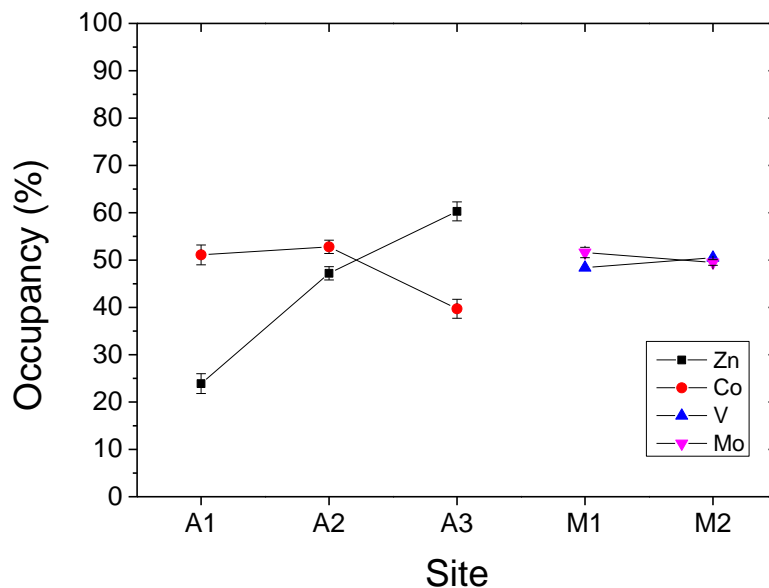


Figure 3.14: Site occupancy trends for the nominal $\text{Zn}_{1.25}\text{Co}_{1.25}\text{VMoO}_8$ as obtained from neutron diffraction analysis.

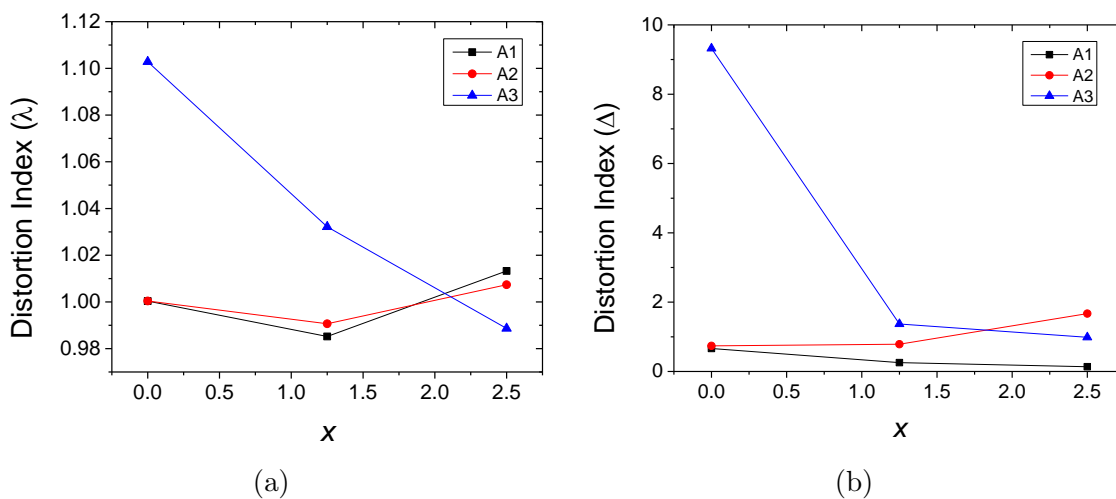


Figure 3.15: Combined A site polyhedral distortion comparison for the nominal $\text{Zn}_{1.25}\text{Co}_{1.25}\text{VMoO}_8$ as obtained from neutron diffraction analysis. Quadratic elongation (a) and bond length distortion (b) ($\times 10^3$).

References

- [1] J. P. Smit, P. C. Stair, K. R. Poeppelmeier, The adaptable lyonsite structure, *Chem. Eur. J.* 12 (2006) 5944–5953. doi:10.1002/chem.200600294.
- [2] S. Vasala, M. Karppinen, $A_2B'B''O_6$ perovskites : A review, *Prog. Solid State Chem.* 43 (2015) 1–36. doi:10.1016/j.progsolidstchem.2014.08.001.
- [3] M. A. Subramanian, G. Aravamudan, G. V. Subba Rao, Oxide pyrochlores — A review, *Prog. Solid State Chem.* 15 (1983) 55–143. doi:10.1016/0079-6786(83)90001-8.
- [4] A. P. Ramirez, Colossal magnetoresistance, *J. Phys. Condens. Matter* 9 (1997) 8171–8199. doi:10.1088/0953-8984/9/39/005.
- [5] G. W. Smith, Crystal structure of orthorhombic cobalt molybdate, *Nat.* 188 (1960) 306–308. doi:10.1038/188306b0.
- [6] J. A. Ibers, G. W. Smith, Crystal structure of a sodium cobalt molybdate, *Act. Crystallogr.* 17 (1964) 190–197. doi:10.1107/S0365110X64000482.
- [7] J. M. Hughes, S. J. Starkey, M. L. Malinconico, L. L. Malinconico, Lyonsite, $Cu_3^{2+}Fe_4^{3+}(VO_4)_6^{3-}$, a new fumarolic sublimate from Izalco Volcano, El Salvador; descriptive mineralogy and crystal structure, *Am. Mineral.* 72 (1987) 1000–1005.
- [8] Z. Mu, E. Song, D. Zhu, J. Feng, Y. Yang, Red phosphor $Li_2Mg_2(WO_4)_3 : Eu^{3+}$ with lyonsite structure for near ultraviolet light-emitting diodes, *Displays* 43 (2016) 18–22. doi:10.1016/j.displa.2016.04.001.
- [9] D. Wang, Z. Zou, J. Ye, A novel series of photocatalysts $M_{2.5}VMoO_8$ (M = Mg, Zn) for O_2 evolution under visible light irradiation, *Catal. Today* 93-95 (2004) 891–894. doi:10.1016/j.cattod.2004.06.090.
- [10] K. Gourai, A. El Bouari, B. Belhorma, L. Bih, Adsorption of methylene blue on the $Li_3Fe_{1-x}Cr_x(MoO_4)_3$ ($x=0,0.5,1$) lyonsite phases, *Am. J. Chem.* 6 (2016) 47–54. doi:10.5923/j.chemistry.20160602.04.
- [11] Q. Liao, Y. Wang, F. Jiang, D. Guo, Ultra-low fire glass-free $Li_3FeMo_3O_{12}$ microwave dielectric ceramics, *J. Am. Ceram. Soc.* 97 (2014) 2394–2396. doi:10.1111/jace.13073.

- [12] D. Zhou, C. A. Randall, L. Pang, H. Wang, X. Wu, J. Guo, G. Zhang, L. Shui, X. Yao, Microwave dielectric properties of $\text{Li}_2(\text{M}^{2+})_2\text{Mo}_3\text{O}_{12}$ and $\text{Li}_3(\text{M}^{3+})\text{Mo}_3\text{O}_{12}$ ($\text{M} = \text{Zn}, \text{Ca}, \text{Al}, \text{and In}$) lyonsite-related-type ceramics with ultra-low sintering temperatures, *J. Am. Ceram. Soc.* 94 (2011) 802–805. doi:10.1111/j.1551-2916.2010.04148.x.
- [13] J. Zhang, R. Zuo, Synthesis and microwave dielectric properties of $\text{Li}_2\text{Mg}_2(\text{WO}_4)_3$ ceramics, *Mater. Lett.* 158 (2015) 92–94. doi:10.1016/j.matchemphys.2009.08.037.
- [14] X. Wang, J. D. Pless, D. A. Vander Griend, P. C. Stair, K. R. Poeppelmeier, Z. Hu, J. D. Jorgensen, Vanadium and molybdenum disorder in $\text{M}_{2.5}\text{VMoO}_8$ ($\text{M} = \text{Mg}, \text{Mn}, \text{and Zn}$) determined with neutron powder diffraction and phase formation studies of $\text{Mg}_{2.5+x}\text{V}_{1+2x}\text{Mo}_{1-2x}\text{O}_8$, *J. Alloys Compd.* 379 (2004) 87–94. doi:10.1016/j.jallcom.2004.02.015.
- [15] J. P. Smit, H. Kim, I. Saratovsky, K. B. Stark, G. Fitzgerald, G. W. Zajac, J. Gaillard, K. R. Poeppelmeier, P. C. Stair, A spectroscopic and computational investigation of the vanadomolybdate local structure in the lyonsite phase $\text{Mg}_{2.5}\text{VMoO}_8$, *Inorg. Chem.* 46 (2007) 6556–6564. doi:10.1021/ic7006815.
- [16] J. P. Smit, T. M. McDonald, K. R. Poeppelmeier, $\text{Li}_3\text{Ti}_{0.75}(\text{MoO}_4)_3$: A lyonsite-type oxide, *Solid State Sci.* 10 (2008) 396–400.
- [17] D. E. Bugaris, H.-C. zur Loye, $\text{Li}_3\text{Al}(\text{MoO}_4)_3$, a lyonsite molybdate., *Acta Crystallogr., Sect. C: Cryst. Struct. Commun.* 68. doi:10.1107/S0108270112020513.
- [18] U. Kolitsch, E. Tillmanns, $\text{Li}_3\text{Sc}(\text{MoO}_4)_3$: substitutional disorder on three (Li,Sc) sites, *Acta Crystallogr., Sect. E: Struct. Rep. Online* 59 (2003) i55–i58. doi:10.1107/S1600536803004872.
- [19] M. Wiesmann, M. Geselle, H. Weitzel, H. Fueß, Crystal structure of lithium copper molybdate, $\text{Li}_2\text{Cu}_2(\text{MoO}_4)_3$, *Z. Kristallogr.* 209 (1994) 615. doi:10.1524/zkri.1994.209.7.615.
- [20] H. Bensaid, A. El Bouari, S. Benmokhtar, B. Manoun, L. Bih, P. Lazor, New molybdate $\text{Li}_2\text{Co}_{2-x}\text{Ni}_x(\text{MoO}_4)_3$ ($0 \leq x \leq 2$) materials with a lyonsite structure: X-ray diffraction and Raman spectroscopy studies, *J. Mol. Struct.* 1031 (2013) 152–159. doi:10.1016/j.molstruc.2012.06.060.

- [21] X. Wang, K. R. Heier, C. L. Stern, K. R. Poeppelmeier, Crystal structure of $\text{Zn}_{3.77}\text{V}_{1.54}\text{Mo}_{1.46}\text{O}_{12}$ containing ZnO_6 trigonal prisms, *J. Alloys Compd.* 255 (1997) 190–194. doi:10.1016/S0925-8388(96)02812-5.
- [22] X. Wang, K. R. Heier, C. L. Stern, K. R. Poeppelmeier, Crystal growth and structure of $\text{Mn}_{2.47}\text{V}_{0.94}\text{Mo}_{1.06}\text{O}_8$, *J. Alloys Compd.* 267 (1998) 79–85. doi:10.1016/S0925-8388(97)00574-4.
- [23] A. E. Smith, M. C. Comstock, M. A. Subramanian, Spectral properties of the UV absorbing and near-IR reflecting blue pigment, $\text{YIn}_{1-x}\text{Mn}_x\text{O}_3$, *Dyes Pigm.* 133 (2016) 214–221. doi:10.1016/j.dyepig.2016.05.029.
- [24] M. Kurzawa, M. Bosacka, P. Jakubus, The structure and selected properties of $\text{Co}_{2.5}\text{VMoO}_8$, *J. Mater. Sci.* 38 (2003) 3137–3142. doi:10.1023/A:1024785415727.
- [25] B. H. Toby, EXPGUI, a graphical user interface for GSAS, *J. Appl. Crystallogr.* 34 (2001) 210–213. doi:10.1107/S0021889801002242.
- [26] R. D. Shannon, Revised effective ionic radii and systematic studies of interatomic distances in halides and chalcogenides, *Acta Crystallogr., Sect. A: Found. Crystallogr.* 32 (1976) 751–767. doi:10.1107/S0567739476001551.
- [27] R. M. Hazen, R. T. Downs, C. T. Prewitt, Principles of comparative crystal chemistry, *Rev. Mineral. Geochem.* 41 (2000) 1–34. doi:10.2138/rmg.2000.41.1.
- [28] A. Ertl, J. M. Hughes, F. Pertlik, F. F. Foit, S. E. Wright, F. Brandstätter, B. Marler, Polyhedron distortions in tourmaline, *Can. Mineral.* 40 (2002) 153–162. doi:10.2113/gscanmin.40.1.153.
- [29] M. C. Viola, M. J. Martínez-Lope, J. A. Alonso, J. L. Martínez, J. M. De Paoli, S. Pagola, J. C. Pedregosa, M. T. Fernández-Díaz, R. E. Carbonio, Structure and magnetic properties of Sr_2CoWO_6 : an ordered double perovskite containing $\text{Co}^{2+}(\text{HS})$ with unquenched orbital magnetic moment, *Chem. Mater.* 15 (2003) 1655–1663. doi:10.1021/cm0208455.
- [30] F. E. Mabbs, D. J. Machin, *Magnetism and Transition Metal Complexes*, Chapman and Hall, London, 1973.

Chapter 4: Novel compositions and physical property comparisons for
 $(A, A')_{2.5}V\text{MoO}_8$ lyonsites ($A = \text{Zn}, A' = \text{Mn, Ni, Cu}$)

4.1 Abstract

This work details a comparative investigation within the system $\text{Zn}_{2.5-x}A'_x\text{VMoO}_8$ ($A'^{2+} = \text{Mn, Ni, Cu}$). Samples were prepared between 700 and 1000 °C, resulting in various colors. All three solid solutions were found to exhibit a miscibility gap before or at the midpoint, beyond which phase separation occurs. X-ray and neutron powder diffraction were used to elucidate the cause of these solubility limits and diffuse reflectance measurements reveal varying color mechanisms. All phase pure members of the solid solutions are found to be similar to the parent compound, and magnetic susceptibility measurements confirmed the +2 oxidation state for all substitutions, with tendency towards antiferromagnetic exchange as x increases.

Publications based on this chapter:

- [1] J. N. Tang, M. A. Subramanian, Novel compositions and physical property comparisons for $(A, A')_{2.5}\text{VMoO}_8$ lyonsites ($A = \text{Zn}$, $A' = \text{Mn, Ni, Cu}$), (Submitted).

4.2 Introduction/Motivation

The underexplored lyonsite structure follow the general formula $A_4M_3O_{12}$; in some cases, stoichiometries are scaled to highlight structural features, e.g., $\square_{1/6}A_{2.5}M_2O_8$. This framework is comprised of several structural motifs: face-sharing AO_6 octahedra, edge-sharing AO_6 octahedra, edge-sharing AO_6 trigonal prisms, and isolated MO_4 tetrahedra that are corner-sharing with the A site polyhedra (Fig. 4.1). The A sites are typically occupied by metal cations (with a wide range of oxidation states and ionic size) and/or vacancies [1]. The A sites are further distinguished by their polyhedral sharing schemes: A1 (face-shared octahedra), A2 (edge-shared octahedra), and A3 (edge-shared trigonal prisms). The M sites are typically occupied by small, highly charged cations; to date, this only includes V^{5+} , Mo^{6+} , and W^{6+} [1].

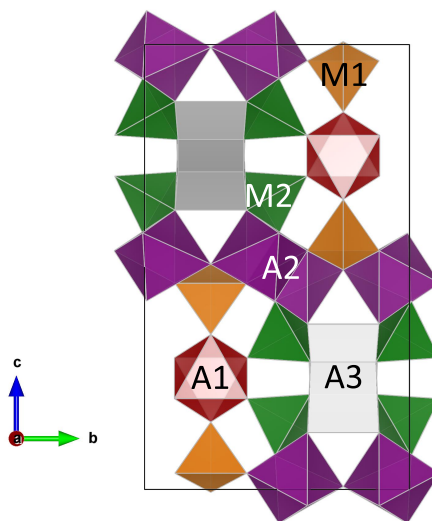


Figure 4.1: Lyonsite crystal structure (A1 = red, A2 = purple, A3 = gray, M1 = orange, M2 = green).

While the molybdate members of this family show the most diversity in *A* site substitution [2–10], the vanadomolybdates (in which past studies have often scaled down the stoichiometry by 1.5x for clarity [11–13]) are less studied. Of note are two particular compounds, $\text{Zn}_{2.5}\text{VMoO}_8$ [14], white in color, and $\text{Co}_{2.5}\text{VMoO}_8$ [12], which appears almost black. A recent investigation into the solid solution between these two species yielded an unexpected gradient of green colors [15]. The origin of these colors were determined to be the result of two coexisting transitions: interatomic ligand-to-metal charge transfer (LMCT) between O and *M* ions, and intra-atomic *d-d* excitations within the Co^{2+} ions. The Co-rich end member was therefore not truly black, but a very dark shade of green, as confirmed with diffuse reflectance measurements. With this behavior in mind, it is worth experimentation to coax and tune other colors from this system of compounds. This study therefore presents novel compositions and some physical properties of cationic substitutions into the white Zn-rich end member, namely with Mn, Ni, and Cu ions.

Mn-containing complexes can be particularly colorful, as Mn can adopt a range of oxidation states and reside in various coordination environments; $\text{Ba}_5\text{Mn}_{3-x}\text{M}_x\text{O}_{12}\text{Cl}$ ($M = \text{V}, \text{P}$), for example, are turquoise powders [16], while $\text{YIn}_{1-x}\text{Mn}_x\text{O}_3$ exhibits a brilliant, vivid blue color [17]. In the latter case, the color mechanism is due to *d-d* transitions in the Mn-occupied trigonal bipyramidal (TBP) site. In the context of the lyonsites, a structural treatment of the end member $\text{Mn}_{2.5}\text{VMoO}_8$ has been given [11], but no physical properties have been measured, so the possible color range is unknown. Ni^{2+} - and Cu^{2+} -containing compounds are typically green or blue (akin to Co^{2+} -containing compounds), as in the case of nickelate spinels [18, 19], Egyptian

Blue ($\text{CaCuSi}_4\text{O}_{10}$), or Han Blue ($\text{BaCuSi}_4\text{O}_{10}$) [20]. To date, a fully substituted Ni lyonsite is not known to exist, while a fully substituted Cu lyonsite is demonstrated with Mo^{6+} as the M cation [21]. Substitutions with these two elements are therefore worthy of exploration, considering NiO/CuO are lower-cost precursors relative to CoO. In addition, Cu^{2+} is a Jahn-Teller active ion [22], which can sometimes create structural oddities [4, 23].

4.3 Experimental

Stoichiometric ratios of ZnO (Aldrich, 99.9%), MnO (Johnson Matthey, 99.5%), NiO (Alfa Aesar, 99.998%), CuO (Aldrich, 99.99%), V_2O_5 (Cerac, 99.9%), and MoO_3 (Sigma-Aldrich, 99.5%) were ground in an agate mortar, pressed into cylindrical pellets, and annealed between 700 and 1000 °C in air.

X-ray diffraction data were collected using a benchtop Rigaku MiniFlex II diffractometer using Cu K_α radiation and a graphite monochromator. Le Bail refinements were performed with KCl as an internal standard. Select samples were loaded in vanadium sample cans, and room temperature neutron powder diffraction data were collected on the BL-11A POWGEN beamline at Oak Ridge National Laboratory and on the BT-1 beamline at the Center for Neutron Research at the National Institute of Standards and Technology. Subsequent Rietveld analysis was performed via the General Structure Analysis System (GSAS) software with the EXPGUI interface [24].

Zero-field-cooled (ZFC) DC magnetization experiments were performed using a Quantum Design PPMS, from 5–300 K, and a Quantum Design SQUID MPMS.

Oxidation states were confirmed by fitting the inverse magnetic susceptibility curves to the reciprocal of the Curie-Weiss Law ($1/\chi_{\text{mol}} = (T - \theta)/C$) and extracting effective magnetic moments (in Bohr magnetons, μ_{B}) via $\mu_{\text{eff}} = 2.84\sqrt{C}$. Diamagnetic corrections were applied during calculations of experimental μ_{B} . UV-Vis diffuse reflectance data were obtained using an Ocean Optics HR-4000 spectrophotometer, with an MgO reference. The data were then converted to pseudo-absorbance units via the Kubelka-Munk relationship, $A = (1 - R)^2/(2R)$ [25]. Vis-NIR reflectance data were collected via a Jasco V-670 spectrophotometer (out to 2500 nm).

4.4 Results/Discussion

4.4.1 *Crystal Structure*

Partial solid solutions were found to exist in different ranges for each substitution, and lattice parameter trends follow Vegard's law. For $A' = \text{Mn}^{2+}$, the phase purity range was $0 \leq x \leq 1.5$ (Fig. 4.2a). Because the samples were synthesized in ambient conditions, the miscibility gap is possibly due to the over-oxidation of Mn. A significant lattice expansion is reflected in the Shannon ionic radii differences (Zn^{2+} : 0.74 Å and Mn^{2+} : 0.83 Å, [26]) (Fig. 4.2b).

For $A' = \text{Ni}^{2+}$, solubility exists in the range $0 \leq x \leq 1.25$ (Fig. 4.3a). A lattice contraction is observed due to the smaller ionic radius of Ni^{2+} (0.69 Å) (Fig. 4.3b). Unlike the Mn substitution, a Ni-rich end member does not exist, yet the solubility limit is at the midpoint in the solid solution. Prior to detailed structure analysis, this

behavior was posited to be the result of site preference competition.

The $A' = \text{Cu}^{2+}$ solid solution exhibited the smallest range of phase pure compounds, $0 \leq x \leq 1$ (Fig. 4.4a). Like the Ni^{2+} substitution, a Cu-rich end member does not exist; difficulties in phase formation in the range $1 \leq x \leq 2.5$ is possibly due to Jahn-Teller distortion in the Cu sites. Because of the framework nature of this structure, it is likely that excessive geometric distortions caused by an abundance of Jahn-Teller active ions can lead to overall structural collapse. All cell parameters remain relatively constant, which is consistent with the similarity in ionic radii (Cu^{2+} : 0.73 Å) (Fig. 4.4b).

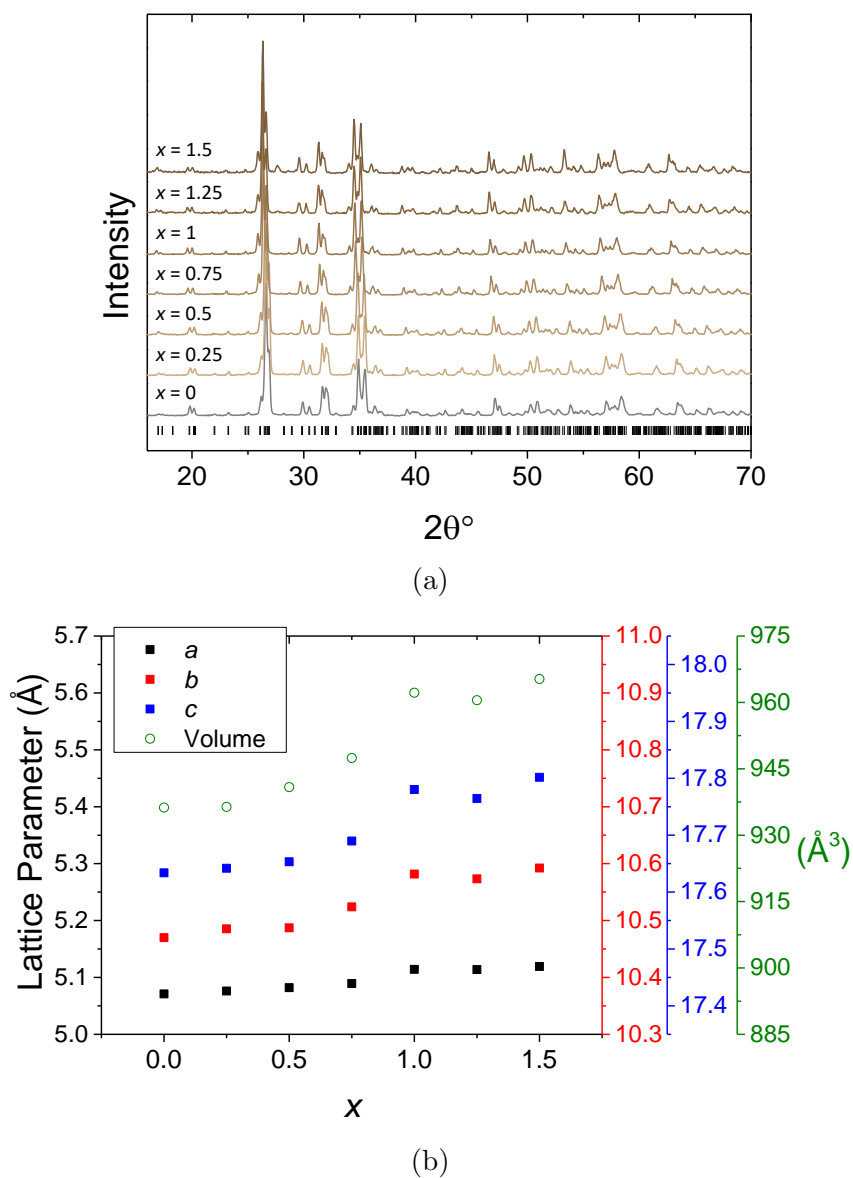


Figure 4.2: Powder X-ray diffraction pattern (a) and lattice parameters (b) for $\text{Zn}_{2.5-x}\text{A}'_x\text{VMoO}_8$, in which $\text{A}' = \text{Mn}^{2+}$. The ranges for the a , b , and c parameters are set to the same size (0.7 \AA) for direct comparisons.

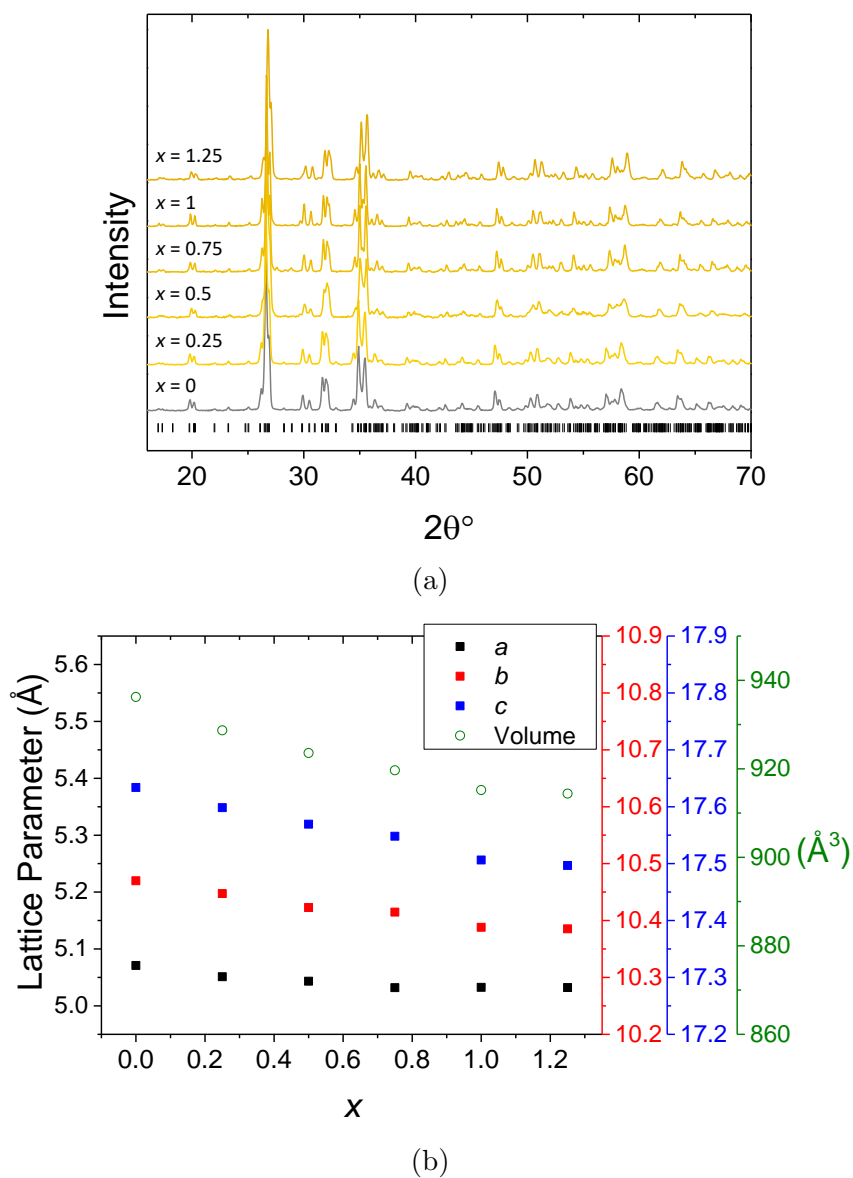


Figure 4.3: Powder X-ray diffraction pattern (a) and lattice parameters (b) for $\text{Zn}_{2.5-x}\text{A}'_x\text{VMoO}_8$, in which $A' = \text{Ni}^{2+}$. The ranges for the a , b , and c parameters are set to the same size (0.7 \AA) for direct comparisons.

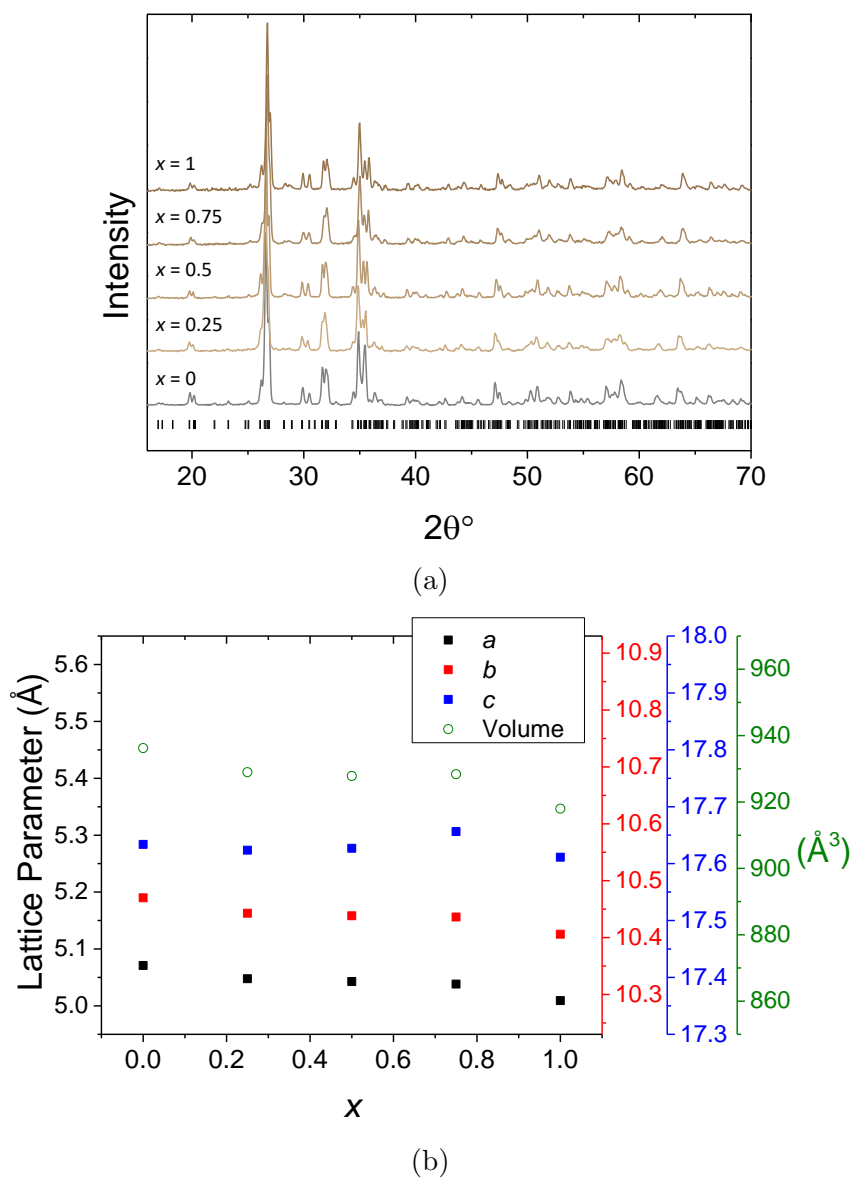
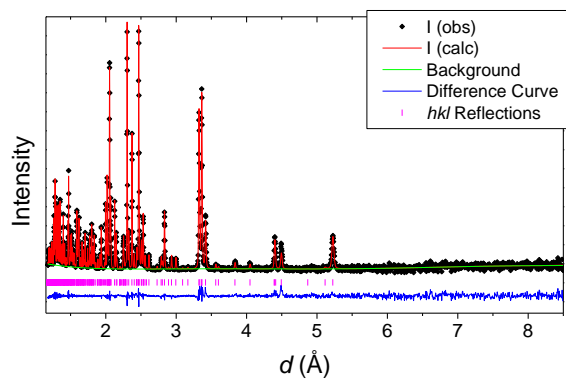
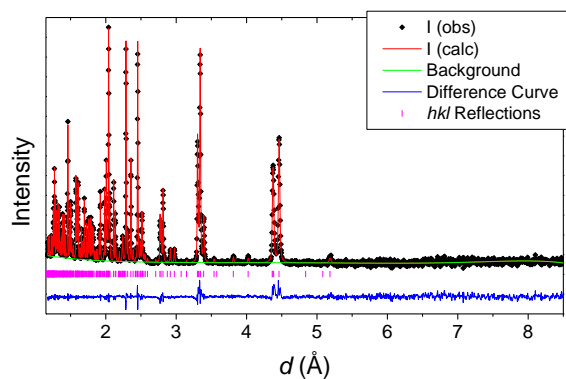


Figure 4.4: Powder X-ray diffraction pattern (a) and lattice parameters (b) for $\text{Zn}_{2.5-x}\text{A}'_x\text{VMoO}_8$, in which $\text{A}' = \text{Cu}^{2+}$. The ranges for the a , b , and c parameters are set to the same size (0.7 \AA) for direct comparisons.

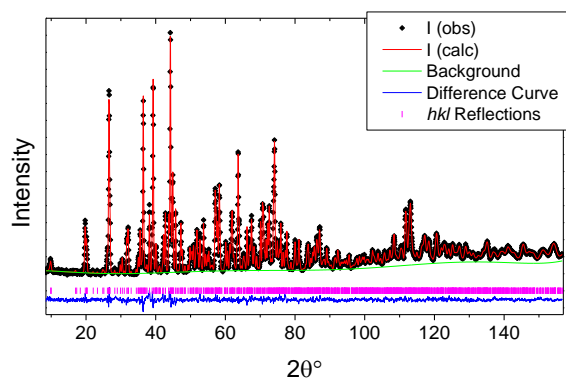
Neutron diffraction analysis was conducted on the nominal $x = 0.5$ member of each substitution (Fig. 4.5). Rietveld refinements for each sample yielded the formulas $\text{Zn}_{1.96}\text{Mn}_{0.54}\text{V}_{0.99}\text{Mo}_{1.01}\text{O}_8$, $\text{Zn}_{1.87}\text{Ni}_{0.62}\text{V}_{0.98}\text{Mo}_{1.02}\text{O}_8$, and $\text{Zn}_{1.98}\text{Cu}_{0.52}\text{V}_{0.99}\text{Mo}_{1.01}\text{O}_8$. Other works have demonstrated that the space group symmetry in the parent compound is demoted from $Pnma$ to $P2_12_12_1$; this is possible through a highly distorted A3 site, which extends through the connecting O atoms [14]. All samples here, though, are isostructural, crystallizing in the $Pnma$ space group, and unit cell parameter differences are reflective of the aforementioned ionic radii differences (Table 4.1). The initial structural model was taken from a previous work on $\text{Zn}_{2-x}\text{Co}_x\text{VMoO}_8$, in which centrosymmetry ($Pnma$) is restored when introducing a second cation into the A site [15]. Refinement of each site with independently varied concentrations yielded unreasonable stoichiometries in the A, A', and M sites compared to weighted precursors. As per the previous work, vacancies were therefore introduced into the A1 site, and Zn^{2+} and A' were distributed across the A1, A2, and A3 sites in the refinement strategy. O site occupancies converged to 1, and the tetrahedral M1 and M2 sites were determined to be fully occupied by V^{5+} and Mo^{6+} in functionally equal amounts (Tables 4.2,4.3,4.4). In other works, cation ordering in the M1 and M2 sites is possible, but was deemed unlikely [13]. Substitutions in this work exhibit similar behavior, as well as large atomic displacement parameters in the A1 site (Tables 4.2,4.3,4.4). This is expected, as adjacent cations in this face-sharing octahedral channel would exhibit repulsive forces due to proximity.



(a)



(b)



(c)

Figure 4.5: Neutron diffraction patterns for $\text{Zn}_2A'_{0.5}\text{VMoO}_8$, in which $A' = \text{Mn}^{2+}$ (a), Ni^{2+} (b), and Cu^{2+} (c). Display includes calculated intensities (red), difference curve (blue), and allowed reflections for $Pnma$ (magenta).

Table 4.1: Crystallographic information for $\text{Zn}_{2.5-x}\text{A}'_x\text{VMoO}_8$ ($x = 0.5$) ($Pnma$).

A'	Mn^{2+}	Ni^{2+}	Cu^{2+}
a (Å)	5.0677(5)	5.0353(1)	5.0193(1)
b (Å)	10.449(1)	10.370(1)	10.403(1)
c (Å)	17.600(2)	17.495(1)	17.597(1)
V (Å ³)	931.98(28)	913.58(7)	918.95(3)
wR_p (%)	3.05	3.45	3.59

Table 4.2: Unit cell coordinates, occupancies, and displacement parameters for the nominal $\text{Zn}_2\text{Mn}_{0.5}\text{VMoO}_8$. *Refined anisotropic U values can be found in the available CIF file (CCDC no. 1866822).

Atom	Site	x	y	z	Occ.	U_{iso} (Å ²)
Zn/Mn (A1)	4c	0.4153(15)	1/4	0.2504(4)	0.53(1)/0.21(1)	0.030(6)
Zn/Mn (A2)	8d	0.7519(5)	0.0811(2)	0.5276(1)	0.94(1)/0.05(1)	0.018(1)
Zn/Mn (A3)	4c	0.7454(27)	1/4	0.6901(8)	0.52(1)/0.47(1)	0.012(9)
V/Mo (M1)	4c	0.2223(12)	1/4	0.4438(3)	0.48/0.52(1)	0.014(4)
V/Mo (M2)	8d	0.7201(8)	-0.0249(3)	0.3444(2)	0.50/0.50(1)	0.009(2)
O1	4c	0.1421(6)	1/4	0.3500(2)	1.0	*
O2	4c	-0.0570(7)	1/4	0.5073(2)	1.0	*
O3	8d	0.4172(5)	0.1159(2)	0.4635(1)	1.0	*
O4	8d	0.4354(5)	-0.1131(2)	0.3722(1)	1.0	*
O5	8d	0.9188(4)	-0.1257(2)	0.2876(1)	1.0	*
O6	8d	0.6495(4)	0.1108(2)	0.2966(1)	1.0	*
O7	8d	0.9121(4)	0.0076(2)	0.4242(1)	1.0	*

Table 4.3: Unit cell coordinates, occupancies, and displacement parameters for the nominal $\text{Zn}_2\text{Ni}_{0.5}\text{VMoO}_8$. *Refined anisotropic U values can be found in the available CIF file (CCDC no. 1866823).

Atom	Site	x	y	z	Occ.	$U_{\text{iso}}(\text{\AA}^2)$
Zn/Ni (A1)	4c	0.4009(8)	1/4	0.2513(2)	0.41(2)/0.34(2)	0.065(3)
Zn/Ni (A2)	8d	0.7515(4)	0.0772(1)	0.5277(1)	0.71(1)/0.29(1)	0.015(1)
Zn/Ni (A3)	4c	0.7472(7)	1/4	0.6944(2)	0.97(1)/0.02(1)	0.021(2)
V/Mo (M1)	4c	0.2219(12)	1/4	0.4427(3)	0.49/0.51(1)	0.007(4)
V/Mo (M2)	8d	0.7229(9)	-0.0249(4)	0.3435(2)	0.49/0.50(1)	0.013(2)
O1	4c	0.1427(7)	1/4	0.3487(2)	1.0	*
O2	4c	-0.0591(7)	1/4	0.5062(2)	1.0	*
O3	8d	0.4170(5)	0.1151(3)	0.4637(1)	1.0	*
O4	8d	0.4348(5)	-0.1140(2)	0.3719(1)	1.0	*
O5	8d	0.9231(5)	-0.1267(2)	0.2873(1)	1.0	*
O6	8d	0.6494(5)	0.1130(2)	0.2961(1)	1.0	*
O7	8d	0.9135(5)	0.0076(2)	0.4238(1)	1.0	*

Table 4.4: Unit cell coordinates, occupancies, and displacement parameters for the nominal $\text{Zn}_2\text{Cu}_{0.5}\text{VMoO}_8$. *Refined anisotropic U values can be found in the available CIF file (CCDC no. 1866824).

Atom	Site	x	y	z	Occ.	$U_{\text{iso}}(\text{\AA}^2)$
Zn/Cu (A1)	4c	0.3947(13)	1/4	0.2529(4)	0.73(2)/0.01(2)	0.047(2)
Zn/Cu (A2)	8d	0.7488(6)	0.0797(2)	0.5283(1)	0.85(1)/0.14(1)	0.018(1)
Zn/Cu (A3)	4c	0.7678(9)	1/4	0.6840(2)	0.53(4)/0.47(4)	0.031(1)
V/Mo (M1)	4c	0.2156(13)	1/4	0.4427(3)	0.50/0.49(1)	0.004(2)
V/Mo (M2)	8d	0.7158(9)	-0.0273(4)	0.3421(2)	0.48/0.51(1)	0.011(1)
O1	4c	0.1419(8)	1/4	0.3493(2)	1.0	*
O2	4c	-0.0580(8)	1/4	0.5069(2)	1.0	*
O3	8d	0.4169(6)	0.1153(2)	0.4636(1)	1.0	*
O4	8d	0.4337(5)	-0.1171(2)	0.3723(1)	1.0	*
O5	8d	0.9375(6)	-0.1253(2)	0.2892(1)	1.0	*
O6	8d	0.6537(4)	0.1109(2)	0.2961(1)	1.0	*
O7	8d	0.9106(6)	0.0064(2)	0.4247(1)	1.0	*

The earlier suppositions regarding solubility limits are explored here and given credence through neutron analysis. The site preference differences between substitutions are tabulated (Table 4.5) and displayed (Fig. 4.6) to facilitate this discussion. For $A' = \text{Mn}^{2+}$, occupation in the A3 trigonal prism environment is preferred, and unexpectedly followed by the A1 face-sharing octahedral site. As Mn^{2+} concentration increases, the A2 site is therefore likely the overflow site (Fig. 4.6a). In addition, there is no appreciable crystal field stabilization energy (CFSE) for these d^5 cations in

any of the available six-fold coordination environments. Therefore, the miscibility gap in this series is the result of over-oxidation of the substituted cation when synthesized at ambient conditions.

The $A' = \text{Ni}^{2+}$ sample, however, presents a different scenario. Here, the face- and edge-sharing environments (A1 and A2, respectively) are strongly preferred over the trigonal prism environment (Fig. 4.6b). This behavior is due to the CFSE of Ni^{2+} being empirically greater for the octahedral environment than the trigonal prism environment [27]. It is therefore likely that as x increases and once the A1 and A2 sites are filled, the A3 site cannot act as a stable overflow site for Ni^{2+} , causing phase separation. The miscibility gap in this series is therefore inferred to be the result of CFSE restrictions on site occupancy.

For $A' = \text{Cu}^{2+}$, the A3 site is most preferred, followed by the A2 and A1 sites. This behavior is likely due to each site's respective ability to tolerate Jahn-Teller distortions without collapsing the entire structure. The trigonal prism environment has the largest cavity size and affords the most flexibility in the structure. The A3 site in several other Cu-substituted lyonsites are distorted without compromising phase purity, to the point of being treated as distorted square pyramids ($\text{Cu}_{3.85}(\text{MoO}_4)_3$ [21], $(\text{Cu}, \text{Fe})_{3.63}(\text{MoO}_4)_3$ [28]) or square planes (in which one pair of A–O bonds is significantly longer than the others, as in the case of $(\text{Cu}, \text{Mn})_{3.66}(\text{MoO}_4)_3$ [29], $(\text{Cu}, \text{Co})_{3.75}(\text{MoO}_4)_3$ [30], and $\text{Cu}_3\text{Fe}_4\text{V}_6\text{O}_{24}$ [31]). Unlike the A3 site, though, the A1 site is a face-sharing octahedral chain that also contains vacancies; this site is the least likely to undergo geometric distortions (Fig. 4.6c). Therefore, if x increases to the point where the Jahn-Teller active Cu^{2+} ion must overflow into the A1 site, the

inability of that site to distort would lead to phase separation. Hence, the observed miscibility gap in this series is posited to be the result of Jahn-Teller distortion restrictions on site occupancy.

Table 4.5: *A* site occupancy comparisons for $\text{Zn}_{2.5-x}\text{A}'_x\text{VMoO}_8$ ($x = 0.5$) ($Pnma$) as obtained from neutron diffraction analysis.

Site	Mn^{2+}	Ni^{2+}	Cu^{2+}
A1 (%)	21.5(8)	33.8(21)	1.9(26)
A2 (%)	5.9(5)	28.8(12)	14.7(15)
A3 (%)	47.1(8)	2.5(19)	47.5(39)

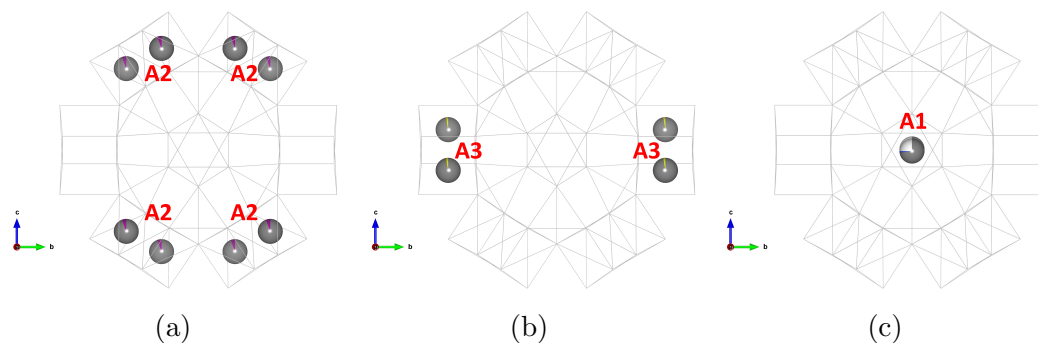
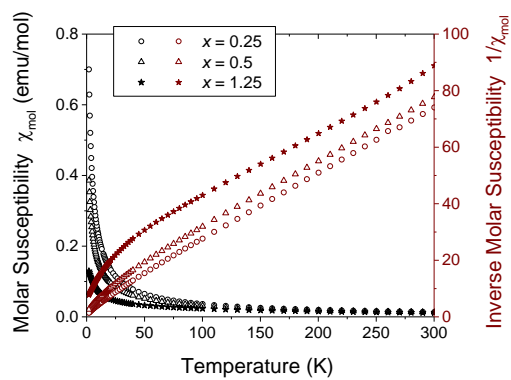


Figure 4.6: *A* site occupancy comparisons for $\text{Zn}_{2.5-x}\text{A}'_x\text{VMoO}_8$ ($x = 0.5$), in which $A' = \text{Mn}^{2+}$ (a), Ni^{2+} (b), and Cu^{2+} (c). Display includes overall polyhedral framework as viewed along the *a* axis (faded gray) and least-occupied sites (labeled). Atom colors: Zn = dark gray, Mn = purple, Ni = yellow, Cu = blue, \square = white.

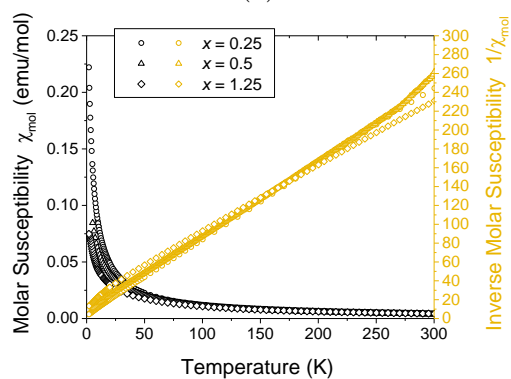
4.4.2 Magnetic Properties

Magnetic susceptibility measurements reveal that all substitutions are paramagnetic and exhibit Curie-Weiss behavior in the high temperature region (150–300 K) (Fig.

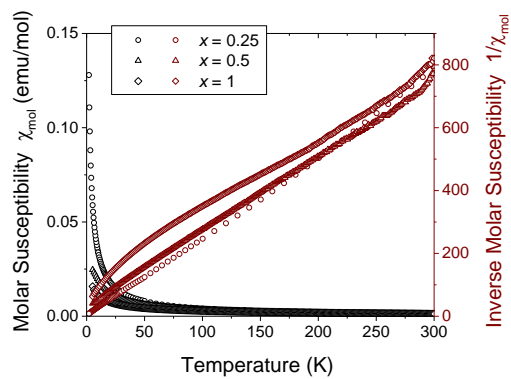
4.7). Extracted magnetic moments (μ_{eff}) are tabulated in Table 4.6. For $A' = \text{Mn}^{2+}$, the effective magnetic moment values match closely to the spin-only value for a high-spin (HS) d^5 ion ($5.92 \mu_{\text{B}}$). For $A' = \text{Ni}^{2+}$, while the spin-only value for a HS d^8 ion is $2.83 \mu_{\text{B}}$, the experimental μ_{eff} values fall within the range of commonly observed values ($2.9\text{--}3.9 \mu_{\text{B}}$). For $A' = \text{Cu}^{2+}$, the spin-only value for d^8 ions is $1.73 \mu_{\text{B}}$, and the experimental μ_{eff} values fall within the expected values ($1.9\text{--}2.1 \mu_{\text{B}}$), with the exception being $x = 0.25$. Unlike the $x = 0.25$ members of the other two substitutions, the d^9 configuration has only one unpaired electron, which can be diluted in concentrations as small as this. For all samples, the Weiss constants θ_{W} are variable with both substitution and concentration, becoming more negative as x increases; this hints at a tendency towards antiferromagnetic exchange between magnetic moments.



(a)



(b)



(c)

Figure 4.7: Magnetic susceptibility plots for $\text{Zn}_{2.5-x}A'_x\text{VMoO}_8$, in which $A' = \text{Mn}^{2+}$ (a), Ni^{2+} (b), and Cu^{2+} (c).

Table 4.6: Effective magnetic moments for $\text{Zn}_{2.5-x}\text{A}'_x\text{VMoO}_8$.

A'	x	θ_{W}	$\mu_{\text{eff}}(\mu_{\text{B}})$
Mn^{2+}	0.25	-19.3	5.89
	0.5	-40.7	5.95
	1.25	-90.1	5.99
Ni^{2+}	0.25	-5.1	3.17
	0.5	-5.6	3.15
	1.25	-40.4	3.45
Cu^{2+}	0.25	25.4	1.68
	0.5	-23.1	1.88
	1	-49.0	1.90

4.4.3 Optical Properties

All samples exhibit a predominant ligand-to-metal charge transfer (LMCT) transition in the 300–500 nm range, arising between the O 2*p* orbitals and the empty *d* orbitals from the *M* site cations in their highest oxidation states (Fig. 4.8). The spin state of the Mn^{2+} ion (d^5) implies a lack of spin-allowed transitions, which is reflected in the weak absorbance past 500 nm (Fig. 4.8a). This broad absorbance in the visible range yields varying shades of brown colors (Fig. 4.8b). The Ni^{2+} ions (d^8) are expected to have spin-allowed transitions, which are indicated by the *d-d* excitations in the 700–900 nm range (Fig. 4.8c). The coexistence of both transitions produces a notable yellow color (Fig. 4.8d). Lastly, the electronic configuration of

the Cu^{2+} ions (d^9) allows for one spin allowed transition, which is indicated by the broad $d-d$ absorption band in the 650–900 nm range (Fig. 4.8e). The coexistence of both transitions over such a broad range in the visible wavelengths produces a brown color (Fig. 4.8f). Typically, absorption bands are assigned to specific $d-d$ excitations. However, when cations are distributed over multiple structurally similar environments, absorption bands can become convoluted and superimposed, leading to the observed broadening. This phenomenon is exacerbated when the next-nearest-neighbor distribution (in this case, the M sites) is also variable; assignment therefore becomes impractical.

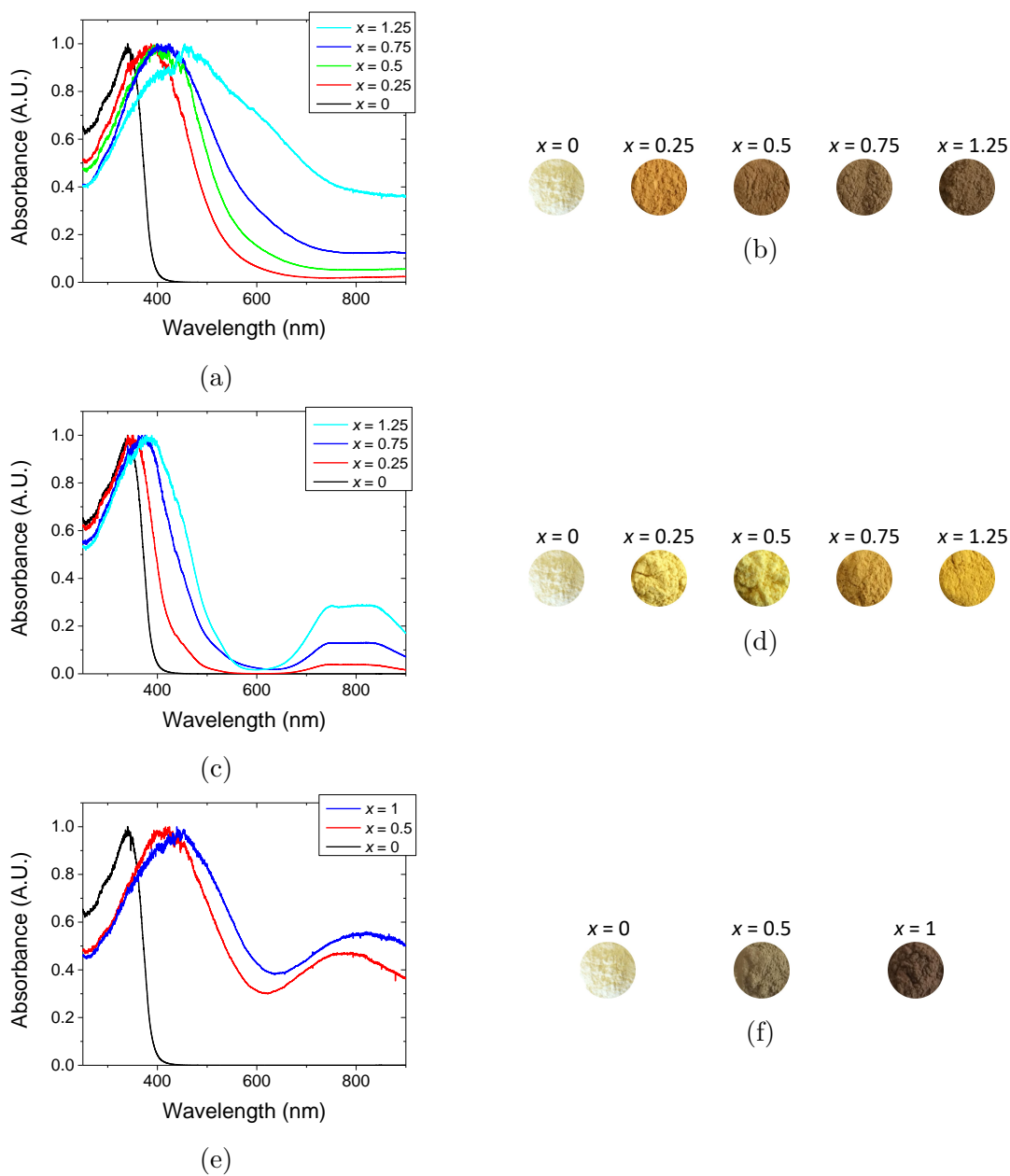
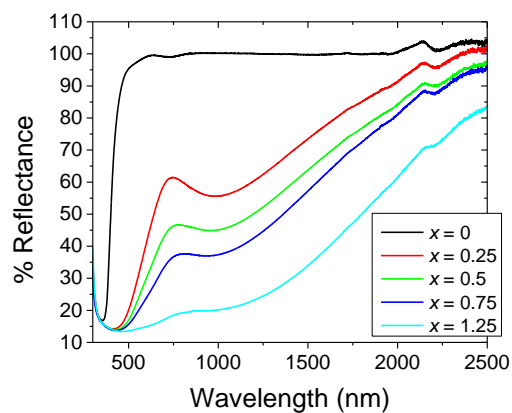
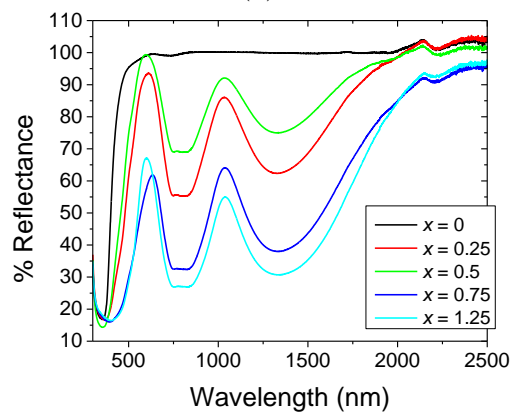


Figure 4.8: UV-vis diffuse reflectance spectra and powder pictures for $\text{Zn}_{2.5-x}\text{A}'_x\text{VMoO}_8$, in which $\text{A}' = \text{Mn}^{2+}$ (a,b), Ni^{2+} (c,d), and Cu^{2+} (e,f).

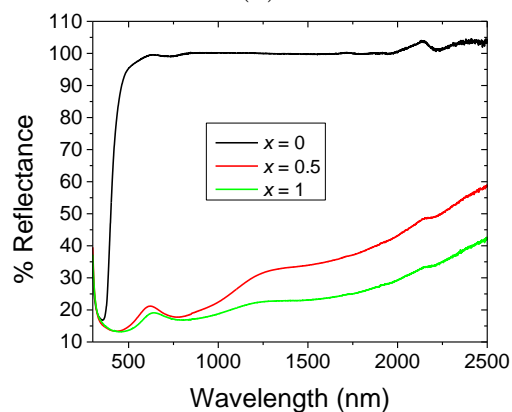
In $A' = \text{Mn}^{2+}$, decreasing reflectance in the visible region in the NIR spectra correspond to darker shades of brown, and samples with low Mn content exhibit moderate NIR reflectance (Fig. 4.9a). For $A' = \text{Ni}^{2+}$, high reflectance in the 500–700 nm range in the NIR spectra correspond to the observed shades of yellow, and the NIR reflectance decreases with increased Ni^{2+} substitution (Fig. 4.9b). The moderate reflectance in the post-1000 nm range is comparable to the behavior of Co^{2+} -containing oxides, such as CoAl_2O_4 [32]. In $A' = \text{Cu}^{2+}$, low reflectance in the 500–700 nm range in the NIR spectra correspond to the observed shades of brown, and the NIR reflectance decreases with increased Cu^{2+} content. Weak reflectance is observed in the post-1000 nm range, though a gradual increase can be observed as the measurement tracks towards the mid-infrared range (Fig. 4.9c).



(a)



(b)



(c)

Figure 4.9: Vis-NIR diffuse reflectance spectra for $\text{Zn}_{2.5-x}A'_x\text{VMoO}_8$, in which $A' = \text{Mn}^{2+}$ (a), Ni^{2+} (b), and Cu^{2+} (c).

4.5 Conclusions

Partial solid solutions were synthesized for $(A, A')_{2.5}\text{VMoO}_8$ lyonsites. Solubility limits exist at various points for each substitution for differing chemical reasons. For $A' = \text{Mn}^{2+}$, the over-oxidation of Mn occurs at the ambient synthesis environment; a full solid solution likely exists under slightly reducing conditions. This substitution exhibits absorption bands that cover enough of the visible spectrum to yield brown colors. For $A' = \text{Ni}^{2+}$, unfavorable crystal field stabilization energies in the trigonal prismatic site prevent a full solid solution from forming. The combination of spin-allowed transitions and a strong LMCT band result in yellow colors; this series may be a potential inorganic replacement candidate for PbCrO_4 pigments formerly used in road markings [33]. For $A' = \text{Cu}^{2+}$, Jahn-Teller effects cause phase separation past a certain dopant concentration, and a broad $d-d$ transition yields brown colors. The observed colors are contrary to those commonly observed in compounds containing these TM ions due to electronic configuration and multiple coordination environments.

4.6 Supporting Information

CCDC 1866822, 1866823, and 1866824 (for $\text{Zn}_2\text{Mn}_{0.5}\text{VMoO}_8$, $\text{Zn}_2\text{Ni}_{0.5}\text{VMoO}_8$, and $\text{Zn}_2\text{Cu}_{0.5}\text{VMoO}_8$, respectively) contains the supplementary crystallographic data for this paper. The data can be obtained free of charge from The Cambridge Crystallographic Data Centre via www.ccdc.cam.ac.uk/structures.

Table 4.7: Bond valence sums for the nominal $\text{Zn}_2\text{Mn}_{0.5}\text{VMoO}_8$ (a), $\text{Zn}_2\text{Ni}_{0.5}\text{VMoO}_8$ (b), and $\text{Zn}_2\text{Cu}_{0.5}\text{VMoO}_8$ (c) as obtained from neutron diffraction analysis.

(a)		(b)		(c)	
Site	Site BVS	Site	Site BVS	Site	Site BVS
A1	1.59	A1	1.55	A1	1.53
A2	2.09	A2	2.09	A2	2.11
A3	2.02	A3	1.92	A3	1.97
M1	5.42	M1	5.46	M1	5.40
M2	5.47	M2	5.47	M2	5.36

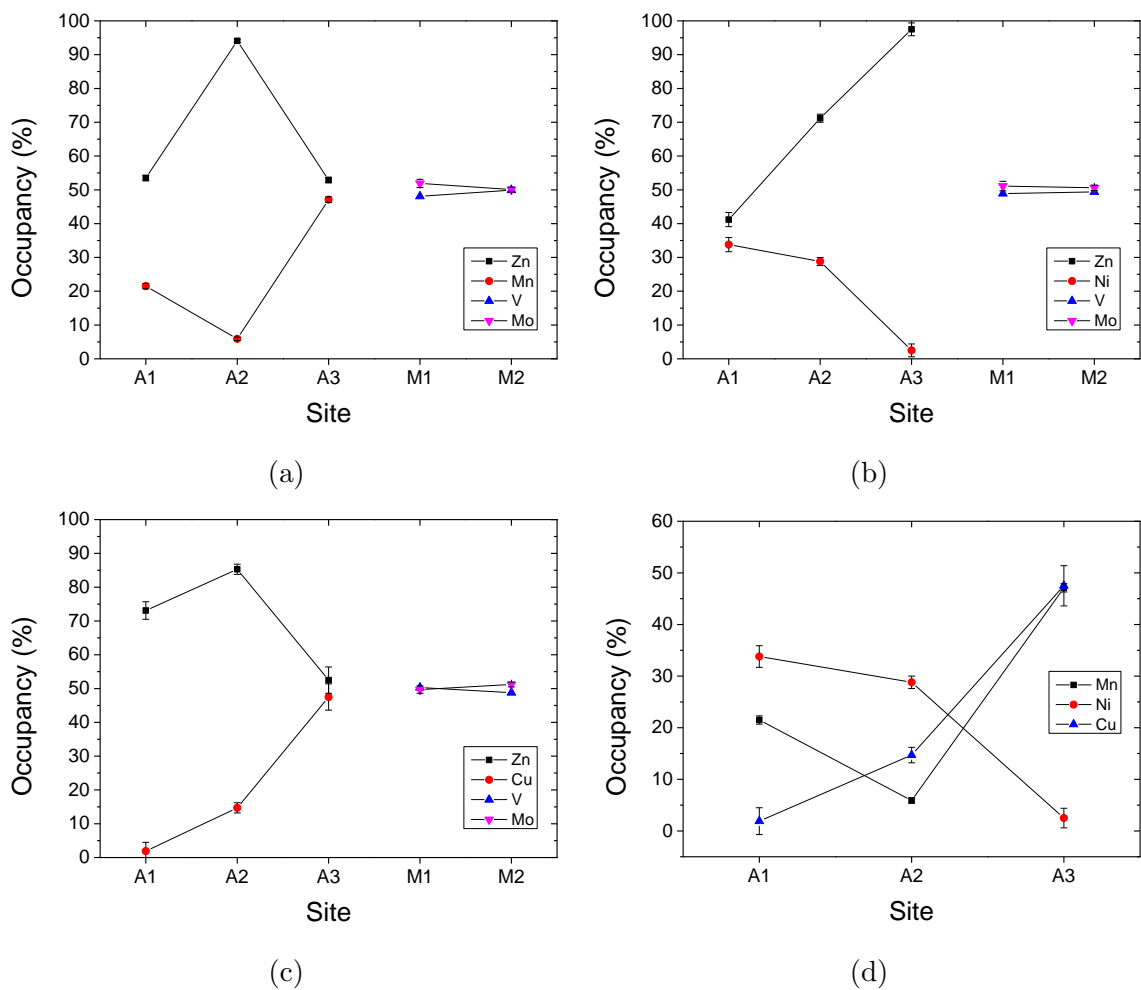


Figure 4.10: Site occupancy trends for the nominal $\text{Zn}_2\text{Mn}_{0.5}\text{VMoO}_8$ (a), $\text{Zn}_2\text{Ni}_{0.5}\text{VMoO}_8$ (b), $\text{Zn}_2\text{Cu}_{0.5}\text{VMoO}_8$ (c), and a combined A site occupancy comparison for each substituted cation (d) as obtained from neutron diffraction analysis.

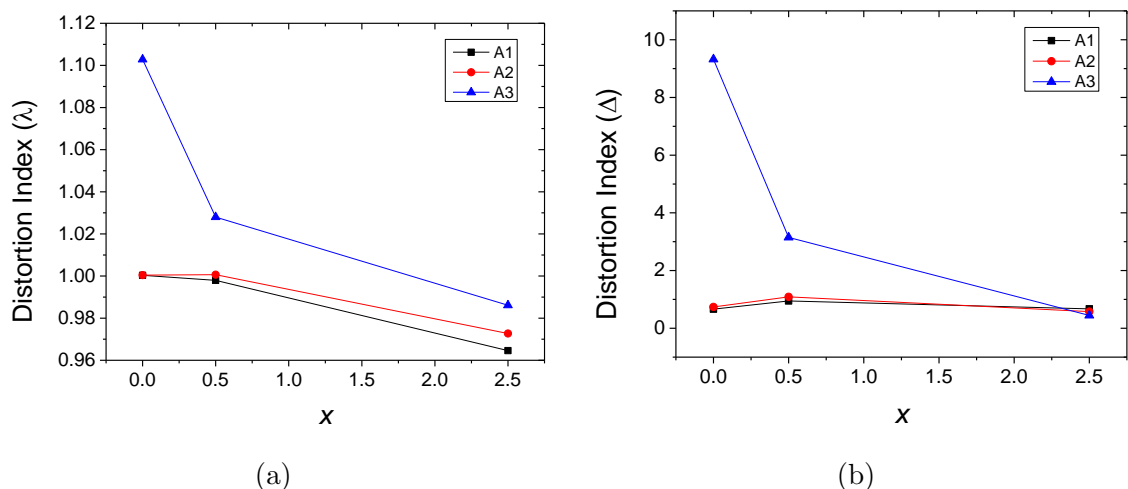


Figure 4.11: A site polyhedral distortion parameters for $A' = \text{Mn}^{2+}$. Quadratic elongation (a): $\lambda = \frac{1}{n} \sum_{i=1}^n \left(\frac{l_i}{l_o}\right)^2$ [34] and bond length distortion (b): $\Delta = \frac{1}{n} \sum_{i=1}^n \left(\frac{l_i - l_o}{l_o}\right)^2$ [35] ($\times 10^3$). n = number of bonds, l_o = idealized bond length (taken by summing radii), l_i = bond length.

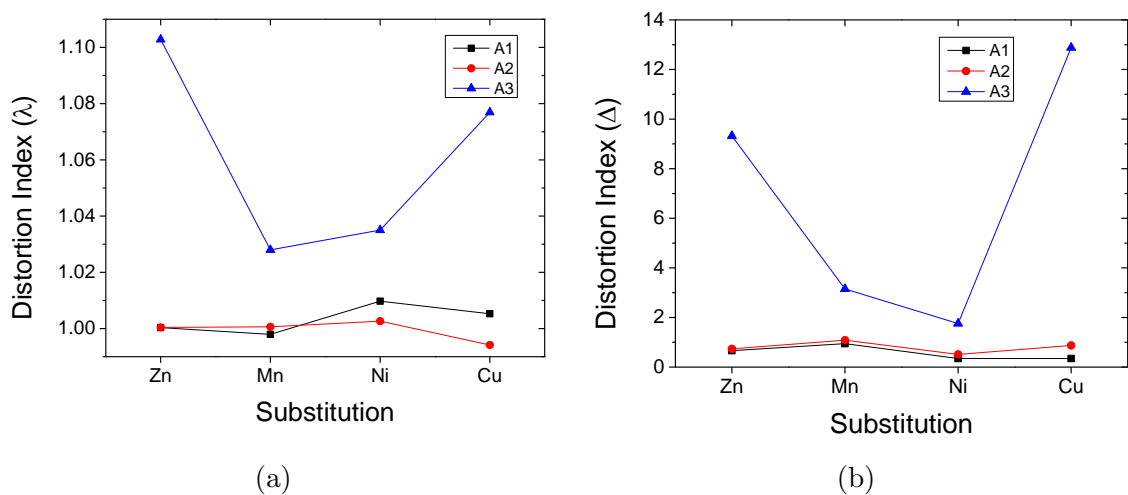


Figure 4.12: Combined A site polyhedral distortion comparison for each substituted cation. Quadratic elongation (a) and bond length distortion (b) ($\times 10^3$).

References

- [1] J. P. Smit, P. C. Stair, K. R. Poeppelmeier, The adaptable lyonsite structure, *Chem. Eur. J.* 12 (2006) 5944–5953. doi:10.1002/chem.200600294.
- [2] J. A. Ibers, G. W. Smith, Crystal structure of a sodium cobalt molybdate, *Acta Crystallogr.* 17 (1964) 190–197. doi:10.1107/S0365110X64000482.
- [3] D. E. Bugaris, H.-C. zur Loye, $\text{Li}_3\text{Al}(\text{MoO}_4)_3$, a lyonsite molybdate., *Acta Crystallogr., Sect. C: Cryst. Struct. Commun.* 68. doi:10.1107/S0108270112020513.
- [4] M. Wiesmann, M. Geselle, H. Weitzel, H. Fueß, Crystal structure of lithium copper molybdate, $\text{Li}_2\text{Cu}_2(\text{MoO}_4)_3$, *Z. Kristallogr.* 209 (1994) 615. doi:10.1524/zkri.1994.209.7.615.
- [5] M. Wiesmann, I. Svoboda, H. Weitzel, H. Fuess, Crystal structure of lithium cobalt molybdate, $\text{Li}_2\text{Co}_2(\text{MoO}_4)_3$, *Z. Kristallogr.* 210 (1995) 1995. doi:10.1524/zkri.1995.210.7.525.
- [6] L. Xue, Y. Wang, P. Lv, D. Chen, Z. Lin, J. Liang, F. Huang, Z. Xie, Growth, structures, and properties of $\text{Li}_2\text{Zn}_2(\text{MoO}_4)_3$ and Co-doped $\text{Li}_2\text{Zn}_2(\text{MoO}_4)_3$, *Cryst. Growth Des.* 9 (2009) 914–920. doi:10.1021/cg800700h.
- [7] J. P. Smit, T. M. McDonald, K. R. Poeppelmeier, $\text{Li}_3\text{Ti}_{0.75}(\text{MoO}_4)_3$: A lyonsite-type oxide, *Solid State Sci.* 10 (2008) 396–400.
- [8] M. Ozima, S. Sato, T. Zoltai, The crystal structure of a lithium–nickel molybdate, $\text{Li}_2\text{Ni}_2\text{Mo}_3\text{O}_{12}$, and the systematics of the structure type, *Acta Crystallogr., Sect. B: Struct. Sci* 33 (1977) 2175–2181. doi:10.1107/S0567740877007973.
- [9] U. Kolitsch, E. Tillmanns, $\text{Li}_3\text{Sc}(\text{MoO}_4)_3$: substitutional disorder on three (Li,Sc) sites, *Acta Crystallogr., Sect. E: Struct. Rep. Online* 59 (2003) i55–i58. doi:10.1107/S1600536803004872.
- [10] L. Sebastian, Y. Piffard, A. K. Shukla, F. Taulelle, J. Gopalakrishnan, Synthesis, structure and lithium-ion conductivity of $\text{Li}_{2-2x}\text{Mg}_{2+x}(\text{MoO}_4)_3$ and $\text{Li}_3\text{M}(\text{MoO}_4)_3$ ($\text{M}^{III} = \text{Cr}, \text{Fe}$), *J. Mater. Chem.* 13 (2003) 1797. doi:10.1039/b301189e.
- [11] X. Wang, K. R. Heier, C. L. Stern, K. R. Poeppelmeier, Crystal growth and structure of $\text{Mn}_{2.47}\text{V}_{0.94}\text{Mo}_{1.06}\text{O}_8$, *J. Alloys Compd.* 267 (1998) 79–85. doi:10.1016/S0925-8388(97)00574-4.

- [12] M. Kurzawa, M. Bosacka, P. Jakubus, The structure and selected properties of $\text{Co}_{2.5}\text{VMoO}_8$, *J. Mater. Sci.* 38 (2003) 3137–3142. doi:10.1023/A:1024785415727.
- [13] X. Wang, J. D. Pless, D. A. Vander Griend, P. C. Stair, K. R. Poeppelmeier, Z. Hu, J. D. Jorgensen, Vanadium and molybdenum disorder in $\text{M}_{2.5}\text{VMoO}_8$ (M = Mg, Mn, and Zn) determined with neutron powder diffraction and phase formation studies of $\text{Mg}_{2.5+x}\text{V}_{1+2x}\text{Mo}_{1-2x}\text{O}_8$, *J. Alloys Compd.* 379 (2004) 87–94. doi:10.1016/j.jallcom.2004.02.015.
- [14] X. Wang, K. R. Heier, C. L. Stern, K. R. Poeppelmeier, Crystal structure of $\text{Zn}_{3.77}\text{V}_{1.54}\text{Mo}_{1.46}\text{O}_{12}$ containing ZnO_6 trigonal prisms, *J. Alloys Compd.* 255 (1997) 190–194. doi:10.1016/S0925-8388(96)02812-5.
- [15] J. N. Tang, J. Li, M. A. Subramanian, Structural investigation and selected properties of $\text{Zn}_{2.5-x}\text{Co}_x\text{VMoO}_8$ lyonsites, *J. Solid State Chem.* 266 (2018) 155–160. doi:10.1016/j.jssc.2018.07.007.
- [16] E. A. Medina, J. Li, J. K. Stalick, M. A. Subramanian, Intense turquoise colors of apatite-type compounds with Mn^{5+} in tetrahedral coordination., *Solid State Sci.* 52 (2016) 97–105. doi:10.1016/j.solidstatesciences.2015.12.001.
- [17] A. E. Smith, H. Mizoguchi, K. Delaney, N. A. Spaldin, A. W. Sleight, M. A. Subramanian, Mn^{3+} in trigonal bipyramidal coordination: A new blue chromophore, *J. Am. Chem. Soc.* 131 (2009) 17084–17086. doi:10.1021/ja9080666.
- [18] G. Lorenzi, G. Baldi, F. Di Benedetto, V. Faso, P. Lattanzi, M. Romanelli, Spectroscopic study of a Ni-bearing gahnite pigment, *J. Eur. Ceram. Soc.* 26 (2006) 317–321. doi:10.1016/j.jeurceramsoc.2004.10.027.
- [19] M. Gaudon, L. C. Robertson, E. Lataste, M. Duttine, M. Ménétrier, A. Demourgues, Cobalt and nickel aluminate spinels: Blue and cyan pigments, *Ceram. Int.* 40 (2014) 5201–5207. doi:10.1016/j.ceramint.2013.10.081.
- [20] P. García-Fernández, M. Moreno, J. A. Aramburu, Origin of the anomalous color of Egyptian and Han blue historical pigments: going beyond the complex approximation in ligand field theory, *J. Chem. Educ.* 93 (2016) 111–117. doi:10.1021/acs.jchemed.5b00288.
- [21] L. Katz, A. Kasenally, L. Kihlberg, The crystal structure of the reduced copper

- molybdate $\text{Cu}_{4-x}\text{Mo}_3\text{O}_{12}$ (x approx.= 0.15), *Acta Crystallogr., Sect. B: Struct. Sci* 27 (1971) 2071–2077. doi:10.1107/S0567740871005387.
- [22] H. A. Jahn, E. Teller, Stability of polyatomic molecules in degenerate electronic states: I—orbital degeneracy, *Proc. R. Soc. London A* 161 (1937) 220–235. doi:10.1098/rspa.1937.0142.
- [23] A. A. Belik, A. P. Malakho, K. V. Pokholok, B. I. Lazoryak, Phase formation in $\text{Cu}_{3+1.5x}\text{R}_{4-x}(\text{VO}_4)_6$ ($R = \text{Fe}$ and Cr) systems: crystal structure of $\text{Cu}_{2.5}\text{Fe}_{4.333}(\text{VO}_4)_6$, $\text{Cu}_4\text{Fe}_{3.333}(\text{VO}_4)_6$, and $\text{Cu}_{4.05}\text{Cr}_{3.3}(\text{VO}_4)_6$, *J. Solid State Chem.* 156 (2001) 339–348. doi:10.1006/jssc.2000.9004.
- [24] B. H. Toby, EXPGUI, a graphical user interface for GSAS, *J. Appl. Crystallogr.* 34 (2001) 210–213. doi:10.1107/S0021889801002242.
- [25] P. Kubelka, F. Munk, An article on optics of paint layers, *Z. Tech. Phys.* 12 (1931) 593–601.
- [26] R. D. Shannon, Revised effective ionic radii and systematic studies of interatomic distances in halides and chalcogenides, *Acta Crystallogr., Sect. A: Found. Crystallogr.* 32 (1976) 751–767. doi:10.1107/S0567739476001551.
- [27] R. Hoffmann, J. M. Howell, A. R. Rossi, Bicapped tetrahedral, trigonal prismatic, and octahedral alternatives in main and transition group six-coordination, *J. Am. Chem. Soc.* 98 (1976) 2484–2492. doi:10.1021/ja00425a016.
- [28] O. Sedello, H. Müller-Buschbaum, Synthese und kristallstruktur von $(\text{Cu,Fe})_{3.63}\text{Mo}_3\text{O}_{12}$: Ein oxometallat mit eindimensional flächenverknüpften oktaederketten / Synthesis and crystal structure of $(\text{Cu,Fe})_{3.63}\text{Mo}_3\text{O}_{12}$: An oxometallate showing one-dimensional chains of face sharing octahedra, *Z. Naturforsch., B: Chem. Sci.* 51 (1996) 90–94. doi:10.1515/znb-1996-0117.
- [29] O. Sedello, H. Müller-Buschbaum, Zur kristallstruktur von $(\text{Cu,Mn})_{3.66}\text{Mo}_3\text{O}_{12}$ / On the crystal structure of $(\text{Cu,Mn})_{3.66}\text{Mo}_3\text{O}_{12}$, *Z. Naturforsch., B: Chem. Sci.* 51 (1996) 447–449. doi:10.1515/znb-1996-0325.
- [30] H. Szillat, H. Müller-Buschbaum, Zur kenntnis des oxocuprats $(\text{Cu,Co})_{3.75}\text{Mo}_3\text{O}_{12}$ / On the oxocuprate $(\text{Cu,Co})_{3.75}\text{Mo}_3\text{O}_{12}$, *Z. Naturforsch., B: Chem. Sci.* 50 (1995) 707–711. doi:10.1515/znb-1995-0503.
- [31] J. M. Hughes, S. J. Starkey, M. L. Malinconico, L. L. Malinconico, Lyonsite,

- $\text{Cu}_3^{2+}\text{Fe}_4^{3+}(\text{VO}_4)_6^{3-}$, a new fumarolic sublimate from Izalco Volcano, El Salvador; descriptive mineralogy and crystal structure, *Am. Mineral.* 72 (1987) 1000–1005.
- [32] A. E. Smith, M. C. Comstock, M. A. Subramanian, Spectral properties of the UV absorbing and near-IR reflecting blue pigment, $\text{YIn}_{1-x}\text{Mn}_x\text{O}_3$, *Dyes Pigm.* 133 (2016) 214–221. doi:10.1016/j.dyepig.2016.05.029.
- [33] K. Adachi, Y. Tainosho, Characterization of heavy metal particles embedded in tire dust, *Environ. Int.* 30 (2004) 1009–1017. doi:10.1016/j.envint.2004.04.004.
- [34] R. M. Hazen, R. T. Downs, C. T. Prewitt, Principles of comparative crystal chemistry, *Rev. Mineral. Geochem.* 41 (2000) 1–34. doi:10.2138/rmg.2000.41.1.
- [35] A. Ertl, J. M. Hughes, F. Pertlik, F. F. Foit, S. E. Wright, F. Brandstätter, B. Marler, Polyhedron distortions in tourmaline, *Can. Mineral.* 40 (2002) 153–162. doi:10.2113/gscanmin.40.1.153.

Chapter 5: Vacancy Tuning in Li,V-Substituted Lyonsites

5.1 Abstract

The lyonsite structure, characterized by the formula $A_4M_3O_{12}$, is a relatively understudied crystal structure. The structure is known to be compositionally flexible, able to incorporate vacancies into the A site. In the parent compound $\text{Co}_{3.75}\text{V}_{1.5}\text{Mo}_{1.5}\text{O}_{12}$, it is apparent that a stoichiometric vacancy of 0.25 is unavoidable, as a result of both coulombic repulsion and simple charge balance. This work focuses on the systematic elimination of said vacancies by introducing increasing Li content, with varying V content for charge balance. A full solid solution was found to exist with the formula $\square_{0.25-\frac{1}{8}x}\text{Li}_x\text{Co}_{3.75-\frac{7}{8}x}\text{V}_{1.5-\frac{3}{4}x}\text{Mo}_{1.5+\frac{3}{4}x}\text{O}_{12}$ ($0 \leq x \leq 2$), terminating at the known end member $\text{Li}_2\text{Co}_2\text{Mo}_3\text{O}_{12}$. Samples were synthesized using high temperature solid state reaction methods in air under ambient pressure. Lattice refinements on PXRD data confirmed the isostructural nature of the whole series. Structure-property relationships were also explored via magnetic susceptibility, optical, and dielectric measurements.

Publications based on this chapter:

J. N. Tang, D. M. Crook, M. A. Subramanian, Vacancy tuning in Li,V-substituted lyonsites, (*In Progress*).

5.2 Introduction/Motivation

Adaptable materials with tunable properties have long been of great importance to solid state chemistry, as evident by the functional materials that can arise from solid solutions. At times, the solid solution compositions may exhibit more interesting properties than the end members, e.g., the recently discovered YInMn Blue and $\text{BaPb}_{1-x}\text{Bi}_x\text{O}_3$ high T_c superconductor. In YInMn blue, the end member YInO_3 is a white ferroelectric, while YMnO_3 is a black ferromagnet. Oddly enough, the solid solution $\text{YIn}_{1-x}\text{Mn}_x\text{O}_3$ is a vivid blue, as a result of the Mn occupation in the trigonal bipyramidal (TBP) site [1]. In $\text{BaPb}_{1-x}\text{Bi}_x\text{O}_3$, the Pb-rich end member is metallic, while the Bi-rich compound is insulating [2].

Recent studies in the underexplored lyonsite structure family have demonstrated that tunability was possible in cation sites as well as vacancy concentrations [3]. The lyonsites take the general formula $A_{16}M_{12}O_{48}$ (or $A_{16}(\text{MO}_4)_{12}$). In many cases, the stoichiometry is scaled down to clarify compositional features, e.g., $\square_{1/6}A_{2.5}M_2O_8$. This framework structure can be described by its structural motifs; a hexagonal tunnel comprised of zigzag sheets of edge-sharing AO_6 trigonal prisms and columns of edge-sharing AO_6 octahedra gives the overall appearance of a "bracelet", while the inner wall of this tunnel is lined with isolated MO_4 tetrahedra in a "pinwheel" fashion, and passing through the center of the tunnel is an infinite chain of face-sharing AO_6 octahedra (Fig. 5.1) [4, 5]. The A sites are distinguished by their polyhedral sharing schemes: A1 (face-shared octahedra), A2 (edge-shared octahedra), and A3 (edge-shared trigonal prisms). The M sites are also crystallographically distinct: M1

and M2. Each oxygen is bonded to two A atoms and one M atom. Overall, these features can be expressed in a descriptive formula as $AB_2C(M, M'O_4)_3$ [6].

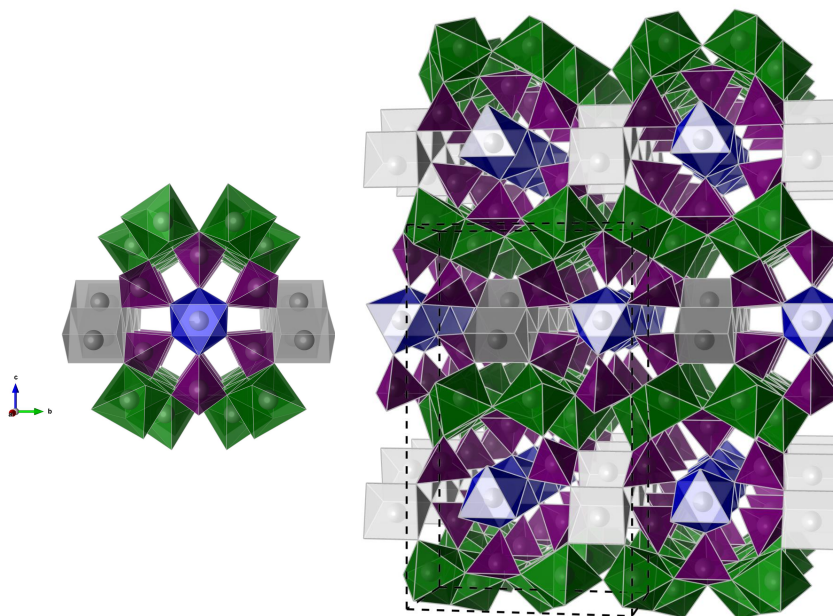


Figure 5.1: The lyonsite crystal structure as viewed along the a axis ($A1 = \text{blue}$, $A2 = \text{green}$, $A3 = \text{gray}$, $M1, M2 = \text{purple}$). Left: primary tunnel motif of the lyonsite. Right: representation of broader structure, with unit cell outline shown in dashed lines.

Since their discovery, various lyonsite compounds have been proposed for direct functional applications. For example, $\text{Li}_2\text{Co}_2(\text{MoO}_4)_3$ and $\text{Li}_2\text{Ni}_2(\text{MoO}_4)_3$ can be considered to be part of the NASICON (Na super ionic conductor) family, as it is constructed of a polyanionic framework with Li-occupied channels [7, 8]. Some compounds exhibiting ionic conductivity include $\text{Li}_{2-x}\text{Mg}_{2+x}(\text{MoO}_4)_3$ ($0 \leq x \leq 0.3$) and $\text{Li}_3A'^{3+}(\text{MoO}_4)_3$ ($A'^{3+} = \text{Cr, Fe}$) [9]. While the framework is 3-dimensional the conduction pathway is proposed to be along the trigonal prismatic $A3$ site (exclusively

occupied by Li), due to the window size ($\approx 3.95 \times 4.00 \text{ \AA}$). It is therefore possible that vacancies exist there, in addition to the A1 site. For the former series, low conductivity values were attributed to the presence of +2 cations in the A3 site, which impedes the Li-ion mobility; this phenomenon is not seen in the $\text{Li}_3\text{A}'^{3+}(\text{MoO}_4)_3$ series. A similar example of this behavior exists with $\text{Li}_{3+x}\text{Fe}(\text{MoO}_4)_3$, in which insertion and de-insertion of Li is reversible via the reduction of Fe^{3+} [10]. Recently, the tungstate $\text{Li}_2\text{Mg}_2\text{W}_3\text{O}_{12}$ doped with Eu^{3+} was recently found to be a promising red phosphor for white light-emitting diodes [11]. Other compounds, like $\text{Li}_3\text{FeMo}_3\text{O}_{12}$, $\text{Li}_2\text{Mg}_2\text{Mo}_3\text{O}_{12}$, and $\text{Li}_2\text{A}'_2\text{Mo}_3\text{O}_{12}$ ($\text{A}' = \text{Zn}, \text{Ca}$), exhibit favorable microwave dielectric quality factors [12–14]. Further still, compounds such as $\text{Zn}_{2.5}\text{VMoO}_8$ and $\text{Li}_3\text{FeMo}_3\text{O}_{12}$ are also noted for their photocatalytic activity [15, 16].

In one particular work, a solid solution was found between $\text{Li}_2\text{Mg}_2\text{Mo}_3\text{O}_{12}$ and the isostructural $\text{Mg}_{2.5}\text{VMoO}_8$, and was expressed as $\square_{0.25-\frac{1}{6}x}\text{Li}_{\frac{4}{3}x}\text{Mg}_{3.75-\frac{7}{6}x}\text{V}_{1.5-x}\text{Mo}_{1.5+x}\text{O}_{12}$ (in which the vacancy \square concentration varies as a function of charge neutrality and stoichiometric ratios of each cation) [17]. This vacancy tunability has been suggested for other lyonsite phases, but has not been explored. This behavior has also been demonstrated to be useful in catalysis and ionic conduction applications, e.g., the creation of cationic vacancies in the NASICON-like lyonsite $(\text{Li}, \text{Na})_2\text{Fe}_2(\text{MoO}_4)_3$ facilitates Li-ion mobility [18]. To further explore this flexibility and to confirm the conclusions made in [3], a solid solution between the $\text{Li}_2\text{Co}_2(\text{MoO}_4)_3$ ($\square = 0$) and $\text{Co}_{2.5}\text{VMoO}_8$ ($\square_{0.25}\text{Co}_{3.75}\text{V}_{1.5}\text{Mo}_{1.5}\text{O}_{12}$) is detailed in this work; the Co-containing lyonsites were chosen as an extension of a previous study [19], but this substitution scheme could easily be adapted and attempted for other A cations.

5.3 Experimental

Stoichiometric quantities of Li_2CO_3 (Sigma-Aldrich, 99.9%), CoCO_3 (Sigma-Aldrich, 46-48% as Co), V_2O_5 (Cerac, 99.9%), and MoO_3 (Sigma-Aldrich, 99.5%) were ground in an agate mortar, pressed into cylindrical pellets, and annealed between 600 and 975 °C in air.

X-ray diffraction data were collected using a benchtop Rigaku MiniFlex II diffractometer using Cu K_α radiation and a graphite monochromator. Le Bail refinements were performed with KCl as an internal standard. Select (≈ 10 g) samples were loaded in vanadium sample cans (15.6 mm diameter, 50 mm length), and room temperature neutron powder diffraction data were collected on the BT-1 beamline at the Center for Neutron Research at the National Institute of Standards and Technology. Measurement was conducted over a 2θ range of 3–167°, and a Cu (311) monochromator was employed to yield an incident wavelength of 1.5403(2) Å [20]. Collimation of 15' of arc was used before the monochromator, 20' before the sample, and 7' before the detectors. Small portions of each sample were also used to collect high-resolution synchrotron X-ray diffraction data on the 11-BM beamline at the Advanced Photon Source at Argonne National Laboratory. Samples were ground with amorphous silica gel to account for absorption. The resulting mixtures were packed into Kapton capillary tubes (0.8 mm diameter), mounted, and data were collected at room temperature over a 2θ range of 34°, with data points collected every 0.001 ° 2θ and a scan speed of 0.01°/s [21]. Subsequent Rietveld analysis was performed via the General Structure Analysis System (GSAS) software with the EXPGUI interface [22, 23].

Zero-field-cooled (ZFC) DC magnetization experiments were performed using a Quantum Design PPMS, from 5–300 K. Oxidation states were confirmed by fitting the inverse magnetic susceptibility curves to the reciprocal of the Curie-Weiss Law ($1/\chi_{\text{mol}} = (T - \theta)/C$) and extracting effective magnetic moments (in Bohr magnetons, μ_{B}) via $\mu_{\text{eff}} = 2.84\sqrt{C}$. Diamagnetic corrections were applied during calculations of experimental μ_{B} . Vis-NIR diffuse reflectance data were obtained using a Jasco V-670 spectrophotometer (out to 2500 nm) fitted with an integrating sphere. The data were then converted to pseudo-absorbance units via the Kubelka-Munk relationship, $F(R) = (1 - R)^2/(2R)$ [24], to generate corresponding Tauc plots.

Dielectric constant measurements were performed on an in-house parallel plate capacitor setup. Sintered pastilles of $>75\%$ density were painted with Ag paint, cured at ≈ 120 °C, placed between the Pt electrodes, and a differential voltage was applied. Capacitance data were then collected as a function of temperature and frequency on an HP 4284 LCR meter at fixed frequencies of 1, 10, 100, 500, and 1000 kHz over a temperature range of 30–200 °C.

5.4 Results/Discussion

5.4.1 Crystal Structure

A full solid solution was found to exist in the $0 \leq x \leq 2$ range (Fig. 5.2). The similarity in Shannon ionic radii between Li^+ (0.76 Å) and Co^{2+} (0.745 Å) should result in little (if any) change in cell parameters [25]. The difference between V^{5+}

(0.355 Å) and Mo^{6+} (0.41 Å), though, is significant, and causes a unit cell expansion (Fig. 5.3).

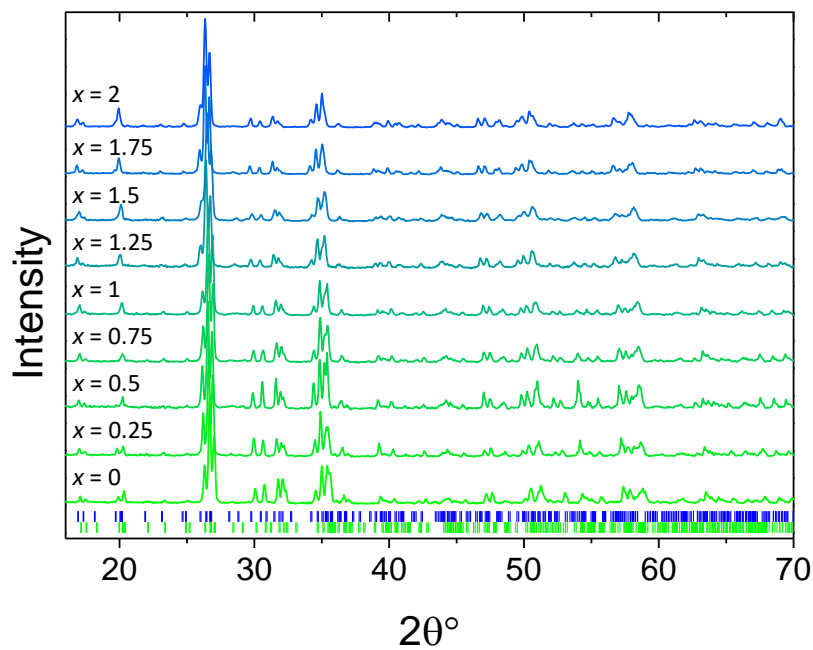


Figure 5.2: Powder X-ray diffraction patterns for $\square_{0.25-\frac{1}{8}x}\text{Li}_x\text{Co}_{3.75-\frac{7}{8}x}\text{V}_{1.5-\frac{3}{4}x}\text{Mo}_{1.5+\frac{3}{4}x}\text{O}_{12}$. hkl tick marks: $x = 0$ end member (green), $x = 2$ end member (blue).

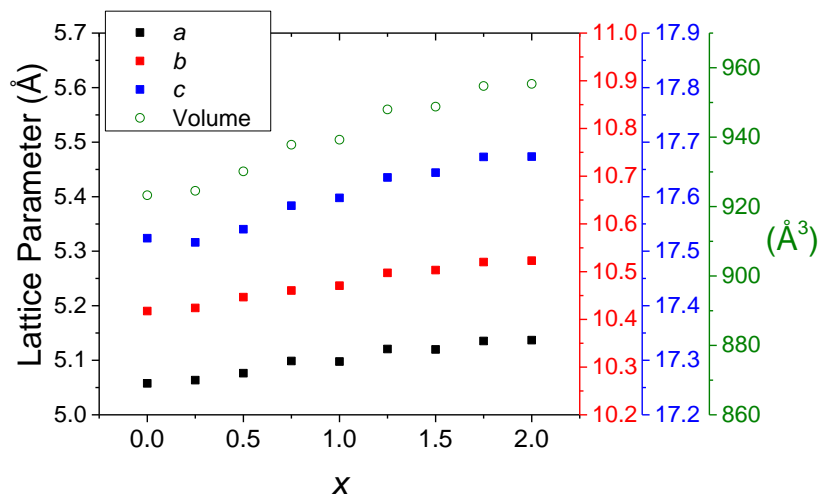


Figure 5.3: Lattice parameters for $\square_{0.25-\frac{1}{8}x}\text{Li}_x\text{Co}_{3.75-\frac{7}{8}x}\text{V}_{1.5-\frac{3}{4}x}\text{Mo}_{1.5+\frac{3}{4}x}\text{O}_{12}$. The ranges for the a , b , and c parameters are set to the same size (0.7 Å) for direct comparisons.

A related molybdate, $\text{Li}_{2-2x}\text{Zn}_{2+x}(\text{MoO}_4)_3$, which also exhibits vacancy flexibility, follows a similar substitution scheme to this work: $2\text{Li}^+ \longrightarrow \text{Zn}^{2+} + \square$ [26]. As Zn content increased, the vacancy concentration increased in the A1 site, alleviating the electrostatic repulsion between the ions in that face-sharing site. The anisotropic atomic displacement parameters (ADPs) also reflected that scenario, as the thermal ellipsoids elongate along the axis of the AO_6 chain. The overall result is an expansion in the (100) and contraction along the [100] due to vacancy-induced steric strain relief. This behavior likely occurs in $\square_{0.25-\frac{1}{8}x}\text{Li}_x\text{Co}_{3.75-\frac{7}{8}x}\text{V}_{1.5-\frac{3}{4}x}\text{Mo}_{1.5+\frac{3}{4}x}\text{O}_{12}$, but is indiscernable due to the aforementioned M site radii differences.

Constant-wavelength (CW) neutron diffraction analysis was performed for one member of this series ($x = 1.25$). The pattern indexes well to $Pnma$, and lattice

constants were consistent with that of benchtop diffraction analysis. The initial refinement strategy involved an equal distribution of atoms across their respective sites (Li, Co across the *A* sites, and V, Mo across the *M* sites). The vacancy concentration was localized to the A1 site, as per precedent. Chemical constraints were added for the A2, A3, M1, and M2 sites to a total occupancy of 1. Furthermore, chemical restraints were added to incorporate charge neutrality into the model, e.g., all Li occupancies adding up to the expected stoichiometry.

As the refinements proceeded, the ADPs tended to converge towards negative values, and thus the added restraints were given more weight. While the stoichiometry and ADPs were more reasonable, and the statistics were sufficient, the visual fit worsened. Overall, the Rietveld refinement is of low quality, even though the reliability statistics indicate otherwise ($wR_p = 7.35\%$, $\chi^2 = 5.436$) (Fig. 5.4). ADPs and site occupancy values are difficult to refine, due to the number of variables.

Refinement against a second data set was therefore necessary, and synchrotron X-ray diffraction analysis was conducted. While the data quality is high, the occupancies and ADPs are still highly correlated in a system like this, resulting in a poor refinement ($wR_p = 16.51\%$, $\chi^2 = 15.80$).

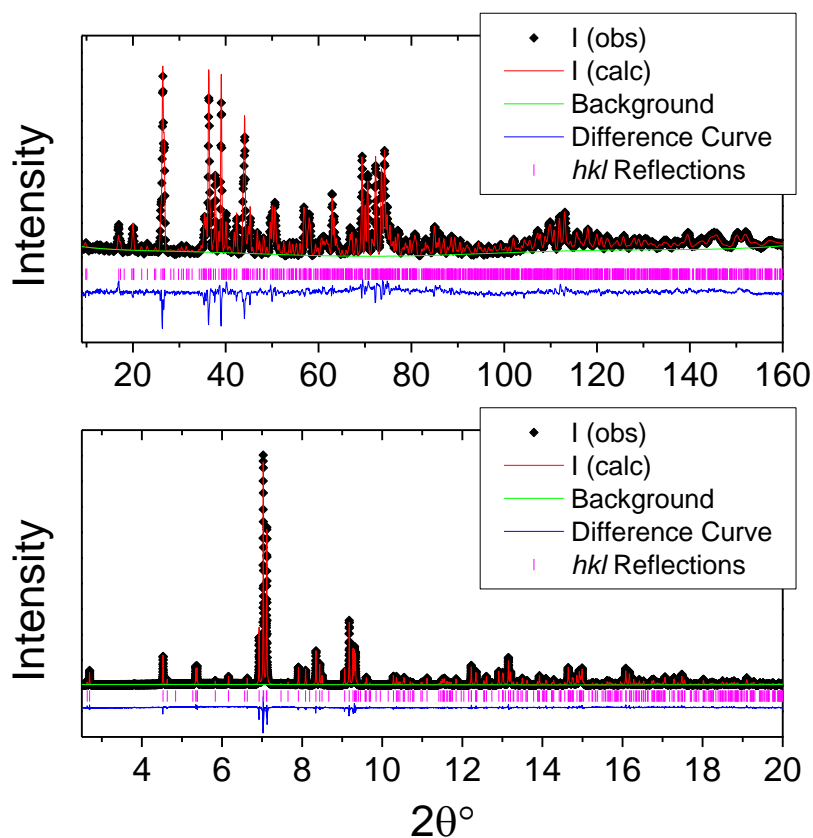


Figure 5.4: CW neutron diffraction pattern (top) and synchrotron X-ray diffraction pattern (bottom) for $\square_{0.25-\frac{1}{8}x}\text{Li}_x\text{Co}_{3.75-\frac{7}{8}x}\text{V}_{1.5-\frac{3}{4}x}\text{Mo}_{1.5+\frac{3}{4}x}\text{O}_{12}$ at $x = 1.25$. Display includes calculated intensities (red), difference curve (blue), and allowed reflections for $Pnma$ (magenta).

5.4.2 Magnetic Properties

Magnetic susceptibility measurements indicate that all samples are paramagnetic, and exhibit Curie-Weiss behavior in the high temperature region ($\approx 150\text{--}300$ K) (Fig. 5.5). Though the Weiss constant is quite negative (Table 5.1), there is no indication of

long-range antiferromagnetic exchange between the Co^{2+} magnetic moments. In most $3d$ transition metal ions, the total magnetic moment is derived solely from the spin moment (e.g., the spin-only effective moment (μ_S) for a high-spin d^7 ion ($S = 3/2$) is $3.87 \mu_B$). Clearly, the observed values do not correlate well to the spin-only moment. In some cases (such as this), the net contribution from orbital angular momentum is nonzero, leading to a higher effective moment. The magnetic moment is therefore expressed as a function of both S and L , i.e., μ_{S+L} . For Co^{2+} , this corresponds to an expected moment of $5.21 \mu_B$ via $\mu_{S+L} = \sqrt{4S(S+1) + L(L+1)} \mu_B$ [27, 28]. The +2 oxidation state is thereby confirmed for Co in this series.

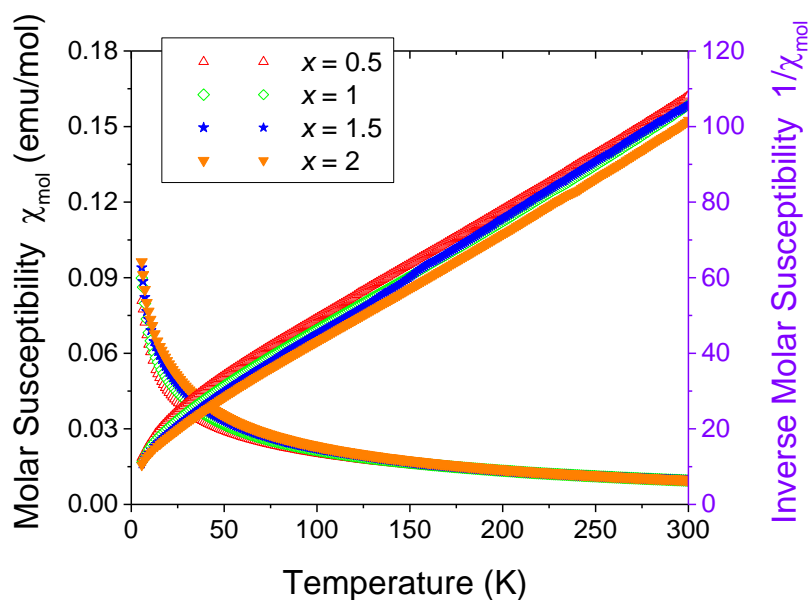


Figure 5.5: Magnetic susceptibility plots for $\square_{0.25-\frac{1}{8}x}\text{Li}_x\text{Co}_{3.75-\frac{7}{8}x}\text{V}_{1.5-\frac{3}{4}x}\text{Mo}_{1.5+\frac{3}{4}x}\text{O}_{12}$.

Table 5.1: Effective magnetic moments for $\square_{0.25-\frac{1}{8}x}\text{Li}_x\text{Co}_{3.75-\frac{7}{8}x}\text{V}_{1.5-\frac{3}{4}x}\text{Mo}_{1.5+\frac{3}{4}x}\text{O}_{12}$.

x	θ_{W}	$\mu_{\text{eff}}(\mu_{\text{B}})$	Modeling T
0	45.4	4.56	217–300K
0.5	-61.7	5.21	183–300K
1	-46.7	5.16	168–300K
1.5	-49.4	5.16	149–300K
2	-43.1	5.23	142–300K

5.4.3 Optical Properties

The \square -rich end member was reported to be very dark green in color [19], while the Li-rich end member is blue 5.6. Visually, the transition from dark green to blue is difficult to grasp, with the first hint of blue occurring at the $x = 1.5$ member. The diffuse reflectance spectra also show a dramatic drop in absorbance in the 500–650 nm range between $x = 2$ and $x = 1.5$, after which point, changes are not as marked (Fig. 5.7). These set of peaks correspond to the spin-allowed $d-d$ excitations from the Co^{2+} environments, but curiously, the absorbance drops as Co^{2+} content increases, which could signify a change in local geometry as the preferential occupation of Li^+ in the trigonal prismatic site becomes a less significant factor.

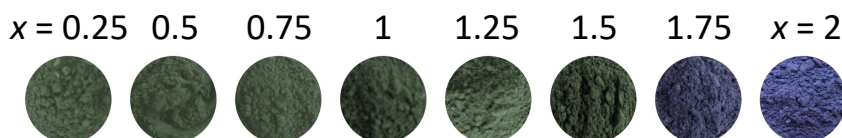


Figure 5.6: Powder pictures for $\square_{0.25-\frac{1}{8}x}\text{Li}_x\text{Co}_{3.75-\frac{7}{8}x}\text{V}_{1.5-\frac{3}{4}x}\text{Mo}_{1.5+\frac{3}{4}x}\text{O}_{12}$.

The higher energy peak is attributed to a ligand-to-metal charge transfer band (LMCT) from the O $2p$ to M cation's empty d orbitals. In addition, the LMCT band associated with the higher energy peaks in the 350–500 nm range shift gradually with x . These peaks shift toward lower energies, corresponding with the increase in V^{5+} content and decreasing Mo^{6+} content. The non-absorbing trough region corresponds to the observed green color. Furthermore, the complexity of the cation distributions over the various, structurally similar, coordination environments, makes specific transition assignments impractical. The NIR reflectance of the solid solution resembles that of other common Co^{2+} compounds, such as CoAl_2O_4 spinel [29], with moderately high reflectance, but with a dip around 1500 nm.

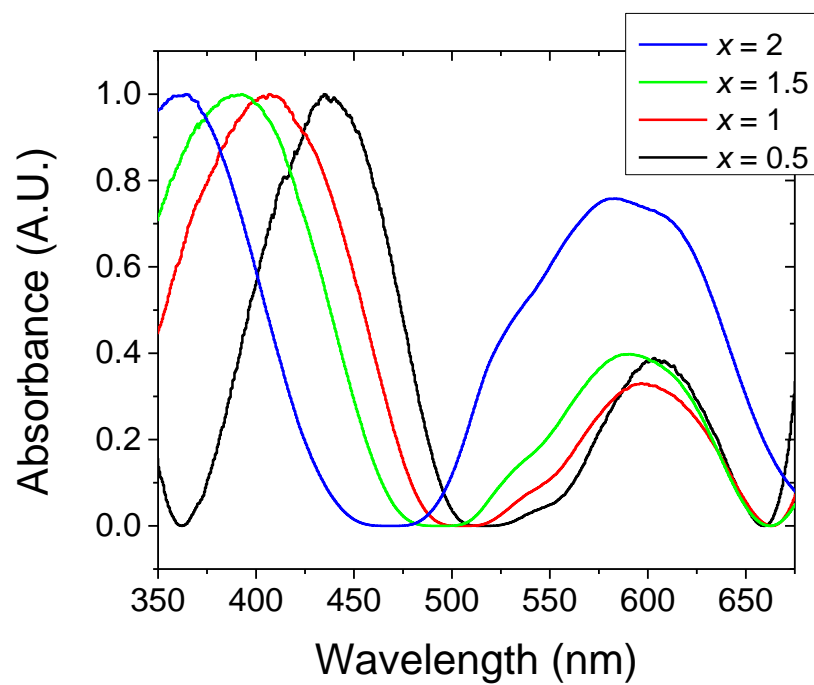


Figure 5.7: Visible wavelength diffuse reflectance spectra for $\square_{0.25-\frac{1}{8}x}\text{Li}_x\text{Co}_{3.75-\frac{7}{8}x}\text{V}_{1.5-\frac{3}{4}x}\text{Mo}_{1.5+\frac{3}{4}x}\text{O}_{12}$.

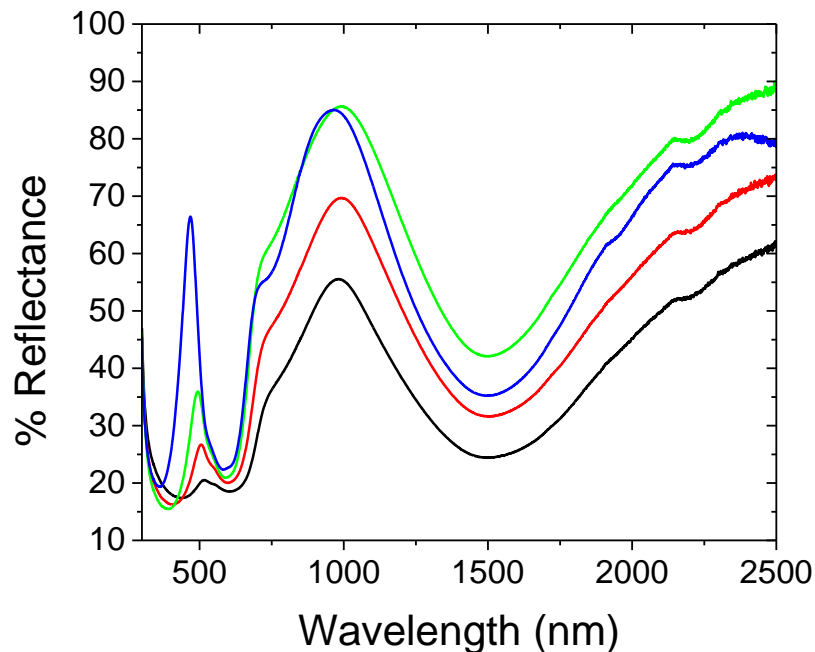


Figure 5.8: Vis-NIR diffuse reflectance spectra for $\square_{0.25-\frac{1}{8}x}\text{Li}_x\text{Co}_{3.75-\frac{7}{8}x}\text{V}_{1.5-\frac{3}{4}x}\text{Mo}_{1.5+\frac{3}{4}x}\text{O}_{12}$, following the same legend scheme as Fig. 5.7.

While direct assignment of electronic transitions is impractical in this series, it is possible to glean some information about the optical band gap E_g . While it is common to extrapolate a band gap from a direct Kubelka-Munk pseudo-absorbance conversion, the graphical representations of the plots during fitting may skew the results. This is often the case, as particle size and/or synthetic conditions directly influence the absorbance data [30]. Without corrective measures, the dispersion of extrapolated band gap values can be significant, e.g., the band gaps given for the standard Degussa P25 TiO_2 have been shown to vary even up to 0.24 eV [31].

It is therefore more accurate, however marginal, to use the Tauc method [32]. A McLean analysis is first applied to the pseudo-absorbance data to determine whether

the optical band gap is direct or indirect, and whether the transitions are allowed or forbidden [31]. Not performing this analysis may give a larger spread of values for the estimated band gaps. As mentioned, the Kubelka-Munk relation is given by

$$F(R) = \frac{\alpha}{s} = \frac{(1 - R)^2}{2R} \quad (5.1)$$

in which α is the absorption coefficient, R is the reflectance, and s is the scattering factor. It is clear from this relationship that s is wavelength-independent, and thus $F(R)$ is directly proportional to α . The McLean analysis incorporates this as

$$\alpha h\nu = k(h\nu - E_g)^{1/n} \quad (5.2)$$

in which h is the Planck constant, ν is the frequency, k is a proportional constant, E_g is the optical band gap, and n signifies the type of transition. A plot of $(F(R)h\nu)^n$ vs. $h\nu$ can reveal the transition type:

Table 5.2: Possible band-to-band absorption transitions for a given material.

n	Type	Selection
2	Direct	Allowed
2/3	Direct	Forbidden
1/2	Indirect	Allowed
1/3	Indirect	Forbidden

Direct transitions do not involve the absorption or emission of a phonon, while indirect transitions do; any and all of these transitions can occur in a semiconducting

material. The plot that exhibits the most linear drop-off at the absorption edge corresponds to the transition type, and is therefore the most appropriate model to use in E_g calculations. From Fig. 5.9, it is apparent that the $n = 2$ model satisfies this condition, and is a direct allowed band-to-band transition.

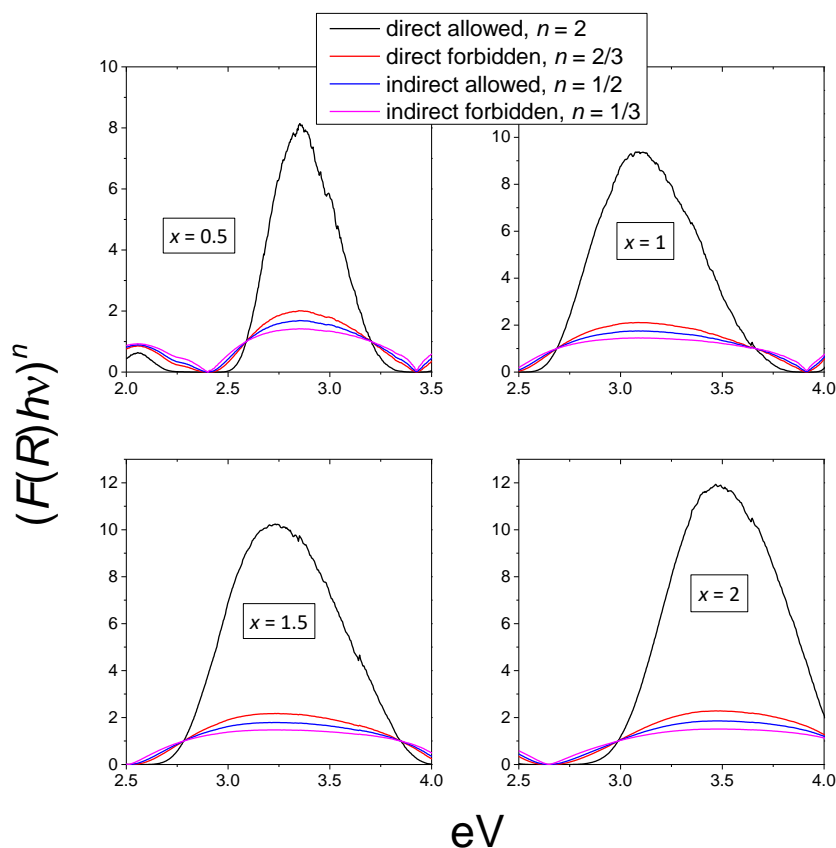


Figure 5.9: McLean analysis for $\square_{0.25-\frac{1}{8}x}\text{Li}_x\text{Co}_{3.75-\frac{7}{8}x}\text{V}_{1.5-\frac{3}{4}x}\text{Mo}_{1.5+\frac{3}{4}x}\text{O}_{12}$.

The substitution of n yields $F(R)h\nu = k(h\nu - E_g)^{1/2}$, and a Tauc plot of $(F(R)h\nu)^2$ vs. $h\nu$ can be generated. Subsequent determination of the inflection point at the absorbance onset is done via the first derivative of the Tauc plots (Fig. 5.10). A

tangent line can then be plotted and extrapolated to the x -axis. The x -intercepts are then taken to be the estimated band gaps (Table 5.3).

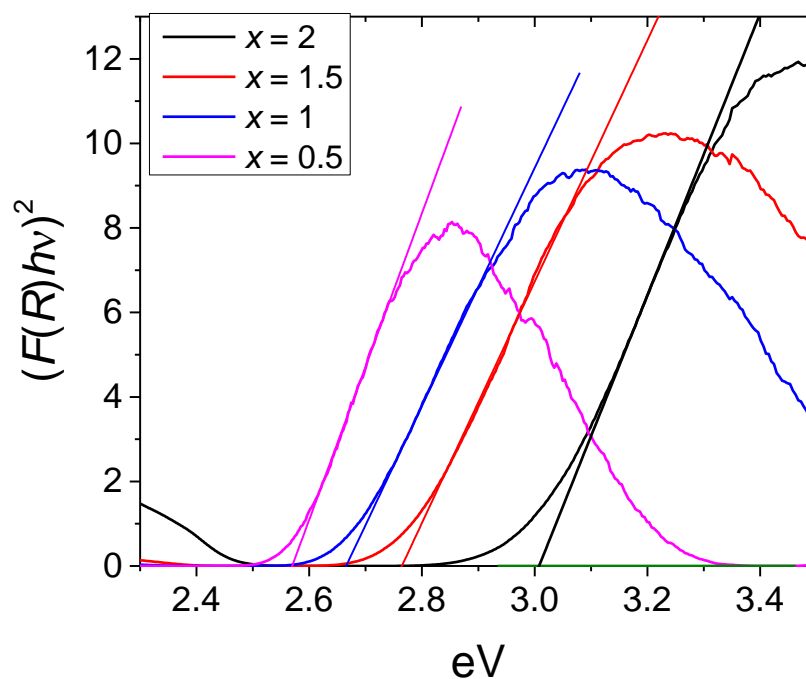


Figure 5.10: Tauc plots for $\square_{0.25-\frac{1}{8}x}\text{Li}_x\text{Co}_{3.75-\frac{7}{8}x}\text{V}_{1.5-\frac{3}{4}x}\text{Mo}_{1.5+\frac{3}{4}x}\text{O}_{12}$.

The optical band gaps are shown in Table 5.3. It is apparent that E_g is tunable, and increases with x , which corresponds to: decreasing \square concentrations, increasing Li^+ content, decreasing Co^{2+} content, decreasing V^{5+} content, and increasing Mo^{6+} content. The M site is likely the primary cause of this trend, as the energies at the absorption edges align with that of the O-to- M charge transfer excitations.

Table 5.3: Estimated optical band gaps for $\square_{0.25-\frac{1}{8}x}\text{Li}_x\text{Co}_{3.75-\frac{7}{8}x}\text{V}_{1.5-\frac{3}{4}x}\text{Mo}_{1.5+\frac{3}{4}x}\text{O}_{12}$.

x	E_g (eV)
0.5	2.57
1	2.66
1.5	2.76
2	3.00

5.4.4 Dielectric Properties

Dielectric constants were measured for the $x = 0$ and $x = 2$ members, as they have not been reported. The $x = 0$ compound exhibits both temperature and frequency dependence, increasing with both parameters as expected (Fig. 5.11). This compound is also very lossy, with high loss tangent values. At room temperature, κ is frequency-independent, and the experimental data correlate well to the polarizability values obtained from the Clausius-Mossotti relation [33, 34], with $\kappa_{\text{th}} = 9.47$ at 1 MHz, and $\kappa_{\text{exp}} = 10.04$. It must be noted that there is no established literature value for the atomic polarizability of Mo, and as such, it had to be approximated as 4.00, neighboring the Nb value of 3.97. The $x = 2$ compound exhibited little temperature and frequency dependence, and displayed high loss values, which hints at a conduction mechanism (Fig. 5.12). This sample also corresponds to a Li-rich compound, and the high loss could be due to ionic conduction along the A3 site. However, a more complete structural refinement would be required to fully understand the site preferences and

possible conduction pathways. The room temperature experimental permittivity (6.24 at 1 MHz) also agrees well with the polarizability obtained from the Clausius-Mossotti relation (9.25).

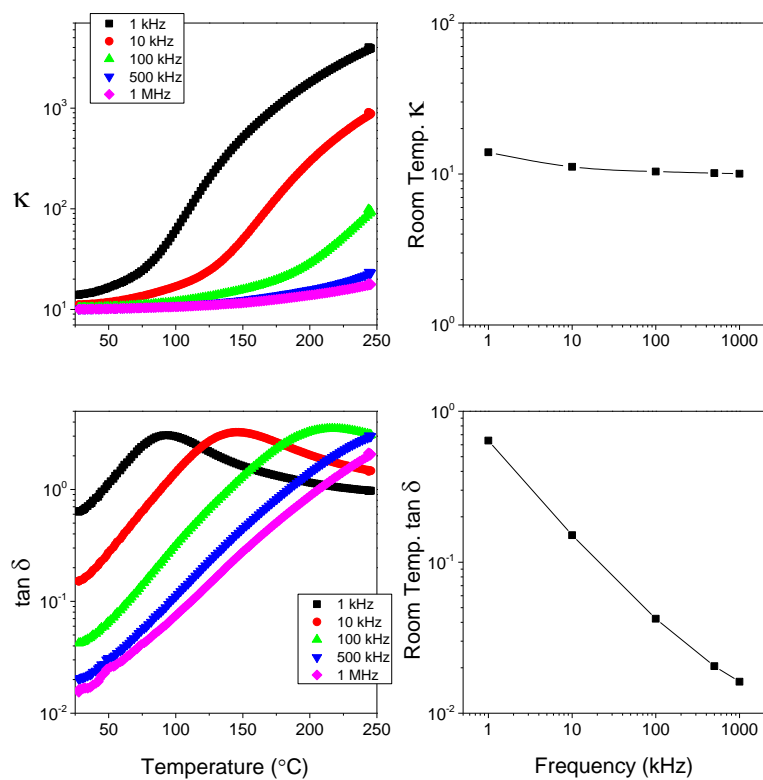


Figure 5.11: Dielectric constant and loss tangent plots for the $x = 0$ member of the $\square_{0.25-\frac{1}{8}x}\text{Li}_x\text{Co}_{3.75-\frac{7}{8}x}\text{V}_{1.5-\frac{3}{4}x}\text{Mo}_{1.5+\frac{3}{4}x}\text{O}_{12}$ solid solution.

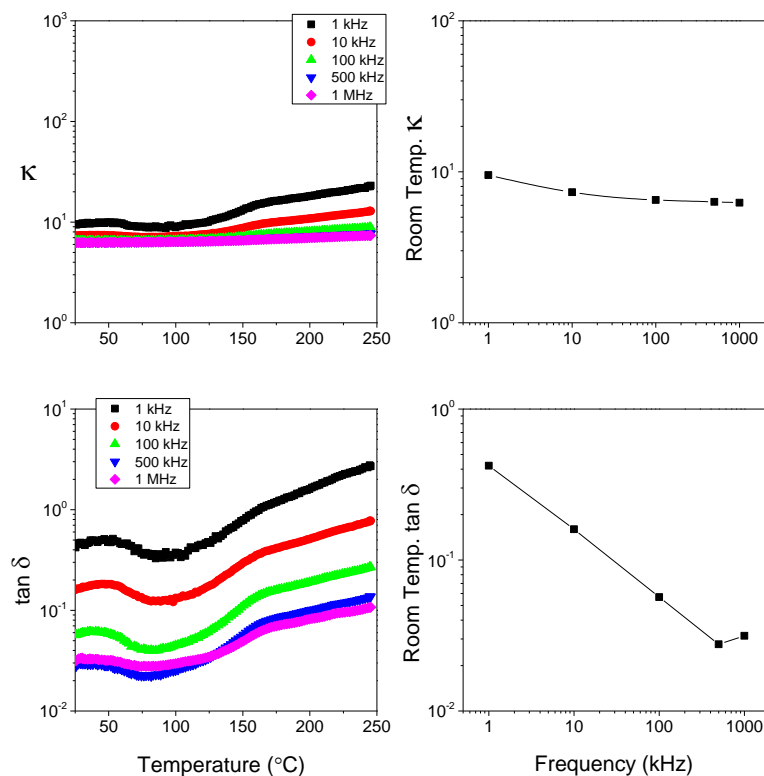


Figure 5.12: Dielectric constant and loss tangent plots for the $x = 2$ member of the $\square_{0.25-\frac{1}{8}x}\text{Li}_x\text{Co}_{3.75-\frac{7}{8}x}\text{V}_{1.5-\frac{3}{4}x}\text{Mo}_{1.5+\frac{3}{4}x}\text{O}_{12}$ solid solution.

5.5 Conclusions

A full solid solution was synthesized for $\square_{0.25-\frac{1}{8}x}\text{Li}_x\text{Co}_{3.75-\frac{7}{8}x}\text{V}_{1.5-\frac{3}{4}x}\text{Mo}_{1.5+\frac{3}{4}x}\text{O}_{12}$ lyonsites. All members exhibited varying shades of green/blue colors, and are isostructural, indexing to the $Pnma$ space group. Lattice refinements correlate well to the expected trends based on ionic radii. All samples exhibit Curie-Weiss behavior in the

high temperature region, and while the Weiss constant would indicate some tendency towards antiferromagnetic ordering, no indication of such exchanges were apparent. The excitations in the visible region correspond to the various cation environments. The tunable optical band gap is notable, and is correlated to the complex substitution scheme. The dielectric constants are low, and the measured compounds exhibit high loss. The temperature and frequency dependence are composition-dependent, and the high loss in the $x = 2$ end member is possibly due to thermally activated conduction. It is posited that future systematic studies in this family will yield similarly tunable behaviors.

References

- [1] A. E. Smith, H. Mizoguchi, K. Delaney, N. A. Spaldin, A. W. Sleight, M. A. Subramanian, Mn^{3+} in trigonal bipyramidal coordination: A new blue chromophore, *J. Am. Chem. Soc.* 131 (2009) 17084–17086. doi:10.1021/ja9080666.
- [2] A. W. Sleight, J. L. Gillson, P. E. Bierstedt, High-temperature superconductivity in the $\text{BaPb}_{1-x}\text{Bi}_x\text{O}_3$ systems, *Solid State Comm.* 17 (1) (1975) 27–28. doi:10.1016/0038-1098(75)90327-0.
- [3] J. P. Smit, P. C. Stair, K. R. Poeppelmeier, The adaptable lyonsite structure, *Chem. Eur. J.* 12 (2006) 5944–5953. doi:10.1002/chem.200600294.
- [4] R. J. Evans, L. A. Groat, Structure and topology of dumortierite and dumortierite-like materials, *Can. Mineral.* 50 (5) (2012) 1197–1231. doi:10.3749/canmin.50.5.1197.
- [5] A. Pieczka, R. J. Evans, E. S. Grew, L. A. Groat, C. Ma, G. R. Rossman, The dumortierite supergroup. I. A new nomenclature for the dumortierite and holtite groups, *Mineral. Mag.* 77 (2013) 2825–2839. doi:10.1180/minmag.2013.077.6.09.
- [6] Z. Xia, K. R. Poeppelmeier, Chemistry-inspired adaptable framework structures,

- Acc. Chem. Res. 50 (5) (2017) 1222–1230. doi:10.1021/acs.accounts.7b00033.
- [7] S. Prabakaran, S. Ramesh, M. Michael, K. Begam, Characterization of soft-combustion-derived NASICON-type $\text{Li}_2\text{Co}_2(\text{MoO}_4)_3$ for lithium batteries, Mater. Chem. Phys. 87 (2-3) (2004) 318–326. doi:10.1016/j.matchemphys.2004.05.041.
- [8] S. Prabakaran, A. Fauzi, M. Michael, K. Begam, New NASICON-type $\text{Li}_2\text{Ni}_2(\text{MoO}_4)_3$ as a positive electrode material for rechargeable lithium batteries, Solid State Ionics 171 (3-4) (2004) 157–165. doi:10.1016/j.ssi.2004.05.001.
- [9] L. Sebastian, Y. Piffard, A. K. Shukla, F. Taulelle, J. Gopalakrishnan, Synthesis, structure and lithium-ion conductivity of $\text{Li}_{2-2x}\text{Mg}_{2+x}(\text{MoO}_4)_3$ and $\text{Li}_3\text{M}(\text{MoO}_4)_3$ ($\text{M}^{III} = \text{Cr}, \text{Fe}$), J. Mater. Chem. 13 (2003) 1797. doi:10.1039/b301189e.
- [10] M. Alvarez-Vega, U. Amador, M. E. Arroyo-de Dompablo, Electrochemical study of $\text{Li}_3\text{Fe}(\text{MoO}_4)_3$ as positive electrode in lithium cells, J. Electrochem. Soc. 152 (2005) A1306–A1311. doi:10.1149/1.1925069.
- [11] Z. Mu, E. Song, D. Zhu, J. Feng, Y. Yang, Red phosphor $\text{Li}_2\text{Mg}_2(\text{WO}_4)_3 : \text{Eu}^{3+}$ with lyonsite structure for near ultraviolet light-emitting diodes, Displays 43 (2016) 18–22. doi:10.1016/j.displa.2016.04.001.
- [12] Q. Liao, Y. Wang, F. Jiang, D. Guo, Ultra-low fire glass-free $\text{Li}_3\text{FeMo}_3\text{O}_{12}$ microwave dielectric ceramics, J. Am. Ceram. Soc. 97 (2014) 2394–2396. doi:10.1111/jace.13073.
- [13] D. Zhou, C. A. Randall, L. Pang, H. Wang, X. Wu, J. Guo, G. Zhang, L. Shui, X. Yao, Microwave dielectric properties of $\text{Li}_2(\text{M}^{2+})_2\text{Mo}_3\text{O}_{12}$ and $\text{Li}_3(\text{M}^{3+})\text{Mo}_3\text{O}_{12}$ ($\text{M} = \text{Zn}, \text{Ca}, \text{Al}, \text{and In}$) lyonsite-related-type ceramics with ultra-low sintering temperatures, J. Am. Ceram. Soc. 94 (2011) 802–805. doi:10.1111/j.1551-2916.2010.04148.x.
- [14] J. Zhang, R. Zuo, Synthesis and microwave dielectric properties of $\text{Li}_2\text{Mg}_2(\text{WO}_4)_3$ ceramics, Mater. Lett. 158 (2015) 92–94. doi:10.1016/j.matchemphys.2009.08.037.
- [15] D. Wang, Z. Zou, J. Ye, A novel series of photocatalysts $\text{M}_{2.5}\text{VMoO}_8$ ($\text{M} = \text{Mg}, \text{Zn}$) for O_2 evolution under visible light irradiation, Catal. Today 93-95 (2004) 891–894. doi:10.1016/j.cattod.2004.06.090.

- [16] K. Gourai, A. El Bouari, B. Belhorma, L. Bih, Adsorption of methylene blue on the $\text{Li}_3\text{Fe}_{1-x}\text{Cr}_x(\text{MoO}_4)_3$ ($x=0,0.5,1$) lyonsite phases, *Am. J. Chem.* 6 (2016) 47–54. doi:10.5923/j.chemistry.20160602.04.
- [17] J. P. Smit, H.-S. Kim, J. D. Pless, P. C. Stair, K. R. Poeppelmeier, Probing the vanadyl and molybdenyl bonds in complex vanadomolybdate structures., *Inorg. Chem.* 45 (2) (2006) 521–8. doi:10.1021/ic051741+.
- [18] J. W. Heo, J. Hyoung, S.-T. Hong, Unveiling the intercalation mechanism in $\text{Fe}_2(\text{MoO}_4)_3$ as an electrode material for Na-ion batteries by structural determination, *Inorg. Chem.* 57 (2018) 11901–11908. doi:10.1021/acs.inorgchem.8b01244.
- [19] J. N. Tang, J. Li, M. A. Subramanian, Structural investigation and selected properties of $\text{Zn}_{2.5-x}\text{Co}_x\text{VMoO}_8$ lyonsites, *J. Solid State Chem.* 266 (2018) 155–160. doi:10.1016/j.jssc.2018.07.007.
- [20] V. F. Sears, Neutron scattering lengths and cross sections, *Neutron News* 3 (1992) 26–37. doi:10.1080/10448639208218770.
- [21] J. Wang, B. H. Toby, P. L. Lee, L. Ribaud, S. M. Antao, C. Kurtz, M. Ramanathan, R. B. Von Dreele, M. A. Beno, A dedicated powder diffraction beamline at the advanced photon source: Commissioning and early operational results, *Rev. Sci. Instrum.* 79 (8) (2008) 085105. doi:10.1063/1.2969260.
- [22] B. H. Toby, EXPGUI, a graphical user interface for GSAS, *J. Appl. Crystallogr.* 34 (2001) 210–213. doi:10.1107/S0021889801002242.
- [23] A. C. Larson, R. B. Von Dreele, General Structure Analysis System (GSAS), Tech. rep., Los Alamos National Laboratory Report LAUR 86-748 (2000).
- [24] P. Kubelka, F. Munk, An article on optics of paint layers, *Z. Tech. Phys.* 12 (1931) 593–601.
- [25] R. D. Shannon, Revised effective ionic radii and systematic studies of interatomic distances in halides and chalcogenides, *Acta Crystallogr., Sect. A: Found. Crystallogr.* 32 (1976) 751–767. doi:10.1107/S0567739476001551.
- [26] S. F. Solodovnikov, Z. A. Solodovnikova, E. S. Zolotova, L. I. Yudanova, T. Y. Kardash, A. A. Pavlyuk, V. A. Nadolinsky, Revised phase diagram of Li_2MoO_4 – ZnMoO_4 system, crystal structure and crystal growth of lithium zinc

- molybdate, *J. Solid State Chem.* 182 (7) (2009) 1935–1943. doi:10.1016/j.jssc.2009.04.036.
- [27] M. C. Viola, M. J. Martínez-Lope, J. A. Alonso, J. L. Martínez, J. M. De Paoli, S. Pagola, J. C. Pedregosa, M. T. Fernández-Díaz, R. E. Carbonio, Structure and magnetic properties of Sr_2CoWO_6 : an ordered double perovskite containing $\text{Co}^{2+}(\text{HS})$ with unquenched orbital magnetic moment, *Chem. Mater.* 15 (2003) 1655–1663. doi:10.1021/cm0208455.
- [28] F. E. Mabbs, D. J. Machin, *Magnetism and Transition Metal Complexes*, Chapman and Hall, London, 1973.
- [29] A. E. Smith, M. C. Comstock, M. A. Subramanian, Spectral properties of the UV absorbing and near-IR reflecting blue pigment, $\text{YIn}_{1-x}\text{Mn}_x\text{O}_3$, *Dyes Pigm.* 133 (2016) 214–221. doi:10.1016/j.dyepig.2016.05.029.
- [30] R. Köferstein, L. Jäger, S. G. Ebbinghaus, Magnetic and optical investigations on LaFeO_3 powders with different particle sizes and corresponding ceramics, *Solid State Ionics* 249-250 (2013) 1–5. doi:10.1016/j.ssi.2013.07.001.
- [31] R. López, R. Gómez, Band-gap energy estimation from diffuse reflectance measurements on sol-gel and commercial TiO_2 : A comparative study, *J. Sol-Gel Sci. Technol.* 61 (1) (2012) 1–7. doi:10.1007/s10971-011-2582-9.
- [32] J. Tauc, R. Grigorovici, A. Vancu, Optical properties and electronic structure of amorphous germanium, *Physica Status Solidi B* 15 (2) (1966) 627–637. doi:10.1002/pssb.19660150224.
- [33] A. R. West, *Solid State Chemistry and its Applications*, 2nd Edition, Student Edition, Wiley, Chichester, 2014.
- [34] W. D. Kingery, H. K. Bowen, D. R. Uhlmann, *Introduction to Ceramics*, 2nd Edition, Wiley, New York, 1976.

General Conclusions and Future Work

This dissertation focused on understanding the physical properties of several vanadomolybdate members of the lyonsite family of compounds. The cations Li^+ , Co^{2+} , Mn^{2+} , Ni^{2+} , and Cu^{2+} were chosen to be substituted into the A site in order to complete a systematic study based on ionic size and electronic configuration differences. The solid solutions between appropriate end members have allowed for the structural parameters to be analyzed with respect to the interesting physical properties observed. These compositions were investigated using X-ray and neutron diffraction, in addition to magnetic, optical, and dielectric characterization methods.

In the $\text{Zn}_{2.5-x}\text{Co}_x\text{VMoO}_8$ system, for which a full solid solution exists, the combination of unusual cell parameter trends, as well as the green colors, prompted a detailed structural investigation. TOF neutron powder diffraction analysis revealed that the lattice parameter trend was due not to ionic radius, but due to compositionally controlled bond angles; furthermore, the introduction of Co^{2+} into the A3 site in a disordered manner contributed to the increase in symmetry from $P2_12_12_1$ to $Pnma$. The site preference for Zn^{2+} was elucidated, and the incorporation of Co^{2+} into every A site causes a decrease in polyhedral distortion across the entire structure. Magnetometry results confirmed the +2 oxidation state for Co for this series, and the magnetic moments correlate well to a spin state that exhibits an unquenched orbital angular momentum contribution. Diffuse reflection data clarified that two color

mechanisms were at work: LMCT in the M sites and $d-d$ transitions in the A sites.

In the comparative study of $(A, A')_{2.5}\text{VMoO}_8$ lyonsites, in which $A = \text{Zn}$ and $A' = \text{Mn, Ni, Cu}$ (all in the +2 oxidation state), each solid solution exhibited a miscibility gap, and detailed structural data were collected to understand this behavior. For $A' = \text{Mn}$, over-oxidation was found to be the limiting factor; as such, heating samples under an inert or slightly reducing atmosphere should yield the missing portion of the solid solution. For $A' = \text{Ni}$, unfavorable crystal field stabilization energies in the trigonal prismatic site prevent a full solid solution from forming. The combination of spin-allowed transitions and a strong LMCT band result in yellow colors; this series may be a potential inorganic replacement candidate for PbCrO_4 pigments formerly used in road markings. For $A' = \text{Cu}$, Jahn-Teller effects cause phase separation past a certain dopant concentration, and a broad $d-d$ transition yields brown colors. The observed colors are contrary to those commonly observed in compounds containing these TM ions due to electronic configuration and multiple coordination environments. The end members for both the Ni and Cu solid solutions are not known; alternative synthesis routes and differing stoichiometries might be viable routes towards new lyonsite compounds.

In the $\square_{0.25-\frac{1}{8}x}\text{Li}_x\text{Co}_{3.75-\frac{7}{8}x}\text{V}_{1.5-\frac{3}{4}x}\text{Mo}_{1.5+\frac{3}{4}x}\text{O}_{12}$ system, the vacancy concentrations were systematically varied as a function of Li content, and all cation sites were adjusting to preserve charge neutrality. A gradual shift from green to blue colors were observed as Li content increases. The magnetometry results confirmed the presence of Co^{2+} , with the same orbital angular momentum contribution as that of the first project. Like the other systems, this series was paramagnetic in the high temperature region. Like

the other systems, the Weiss constant indicated an antiferromagnetic tendency, though ordering was not apparent in the data due to site disorder. Tauc plots were used to determine the optical band gap, which falls within the lower wavelength visible region. This band gap was shown to be tunable, correlating to the complex substitution scheme. The dielectric constants were low, and the Li-rich end member exhibited extremely high loss tangents, hinting at a conduction pathway.

This particular family of compounds has proven to be highly interesting for its compositional flexibility, and future systematic studies could yield similarly tunable behaviors. Broadly speaking, tunable framework compounds like these continue to be an important class of materials, with applications ranging from environmental remediation, to catalysis and electronics. While there are several structure families that have stood in the research spotlight (and for good reason), other exotic crystal families are just as worthy of exploration. As history has proven time and again, exciting new properties are possible in the most unassuming of structures, from the disparate array of variable structure high T_c superconductors, to the vivid colors of advanced inorganic pigments like YInMn Blue. It is therefore in our best interest as scientists to continue casting a wide net and collaborate, lest solutions to contemporary technological challenges escape us entirely.

Bibliography

- [1] Abeysinghe, D., Smith, M. D., Yeon, J., Tran, T. T., Paria Sena, R., Hadermann, J., Halasyamani, P. S. and zur Loye, H.-C. [2017], ‘Crystal growth and structure analysis of $\text{Ce}_{18}\text{W}_{10}\text{O}_{57}$: A complex oxide containing tungsten in an unusual trigonal prismatic coordination environment’, *Inorg. Chem.* **56**(5), 2566–2575.
- [2] Adachi, K. and Tainosho, Y. [2004], ‘Characterization of heavy metal particles embedded in tire dust’, *Environ. Int.* **30**, 1009–1017.
- [3] Alvarez-Vega, M., Amador, U. and Arroyo-de Dompablo, M. E. [2005], ‘Electrochemical study of $\text{Li}_3\text{Fe}(\text{MoO}_4)_3$ as positive electrode in lithium cells’, *J. Electrochem. Soc.* **152**, A1306–A1311.
- [4] Arita, R., Kuroki, K., Held, K., Lukoyanov, A. V., Skornyakov, S. and Anisimov, V. I. [2008], ‘Origin of large thermopower in LiRh_2O_4 : Calculation of the seebeck coefficient by the combination of local density approximation and dynamical mean-field theory’, *Phys. Rev. B* **78**, 115121.
- [5] Avdeev, M., Nalbandyan, V. B., Shukaev, I. L. and Kharton, V. V. E. [2009], *Solid State Electrochemistry I: Fundamentals, Materials and their Applications*, Wiley.
- [6] Bain, G. A. and Berry, J. F. [2008], ‘Diamagnetic corrections and Pascal’s constants’, *J. Chem. Ed.* **85**(4), 532.
- [7] Belik, A. A., Malakho, A. P., Pokholok, K. V. and Lazoryak, B. I. [2001], ‘Phase formation in $\text{Cu}_{3+1.5x}\text{R}_{4-x}(\text{VO}_4)_6$ ($R = \text{Fe}$ and Cr) systems: crystal structure of $\text{Cu}_{2.5}\text{Fe}_{4.333}(\text{VO}_4)_6$, $\text{Cu}_4\text{Fe}_{3.333}(\text{VO}_4)_6$, and $\text{Cu}_{4.05}\text{Cr}_{3.3}(\text{VO}_4)_6$ ’, *J. Solid State Chem.* **156**, 339–348.
- [8] Bensaïd, H., El Bouari, A., Benmokhtar, S., Manoun, B., Bih, L. and Lazor, P. [2013], ‘New molybdate $\text{Li}_2\text{Co}_{2-x}\text{Ni}_x(\text{MoO}_4)_3$ ($0 \leq x \leq 2$) materials with a lyonsite structure: X-ray diffraction and Raman spectroscopy studies’, *J. Mol. Struct.* **1031**, 152–159.
- [9] Berthelot, R., Schmidt, W., Muir, S., Eilertsen, J., Etienne, L., Sleight, A. W. and Subramanian, M. A. [2012], ‘New layered compounds with honeycomb ordering: $\text{Li}_3\text{Ni}_2\text{BiO}_6$, $\text{Li}_3\text{NiM}'\text{BiO}_6$ ($M' = \text{Mg}, \text{Cu}, \text{Zn}$), and the delafossite $\text{Ag}_3\text{Ni}_2\text{BiO}_6$ ’, *Inorg. Chem.* **51**, 5377–5385.

- [10] Bragg, W. H. and Bragg, W. L. [1913], ‘The reflection of X-rays by crystals’, *Proc. R. Soc. London, Ser. A* **88**(605), 428–438.
- [11] Bugaris, D. E. and zur Loye, H.-C. [2012], ‘ $\text{Li}_3\text{Al}(\text{MoO}_4)_3$, a lyonsite molybdate.’, *Acta Crystallogr., Sect. C: Cryst. Struct. Commun.* **68**.
- [12] Bursill, L. [1979], ‘Structural relationships between β -gallia, rutile, hollandite, psilomelane, ramsdellite and gallium titanate type structures’, *Acta Crystallogr.* **B35**, 530–538.
- [13] Chen, C., Wang, Y., Wu, B., Wu, K., Zeng, W. and Yu, L. [1995], ‘Design and synthesis of an ultraviolet-transparent nonlinear optical crystal $\text{Sr}_2\text{Be}_2\text{B}_2\text{O}_7$ ’, *Nature* **373**, 322.
- [14] Chen, C., Wang, Y., Xia, Y., Wu, B., Tang, D., Wu, K., Wenrong, Z., Yu, L. and Mei, L. [1995], ‘New development of nonlinear optical crystals for the ultraviolet region with molecular engineering approach’, *J. Appl. Phys.* **77**(6), 2268–2272.
- [15] Corr, S. A. and Seshadri, R. [2013], 4.01 - Synthetic Methodologies, in ‘Comprehensive Inorganic Chemistry II (Second Edition)’, Elsevier, Amsterdam, pp. 1–15.
- [16] Cullity, B. D. and Stock, S. R. [2001], *Elements of X-Ray Diffraction, 3rd ed.*, Pearson, New Jersey.
- [17] De Guzman, R. N., Awaluddin, A., Shen, Y. F., Tian, Z. R., Suib, S. L., Ching, S. and O’Young, C. L. [1995], ‘Electrical-resistivity measurements on manganese oxides with layer and tunnel structures - birnessites, todorokites, and cryptomelanes’, *Chem. Mater.* **7**, 1286–1292.
- [18] Dollase, W. A. and O’Neill, H. S. C. [n.d.], ‘The spinels CuCr_2O_4 and CuRh_2O_4 ’, *Acta Crystallogr., Sect. C: Cryst. Struct. Commun.* **53**, 657–659.
- [19] Egger, D. A., Rappe, A. M. and Kronik, L. [2016], ‘Hybrid organic–inorganic perovskites on the move’, *Acc. Chem. Res.* **49**(3), 573–581.
- [20] Ertl, A., Hughes, J. M., Pertlik, F., Foit, F. F., Wright, S. E., Brandstätter, F. and Marler, B. [2002], ‘Polyhedron distortions in tourmaline’, *Can. Mineral.* **40**, 153–162.
- [21] Evans, R. J. and Groat, L. A. [2012], ‘Structure and topology of dumortierite and dumortierite-like materials’, *Can. Mineral.* **50**(5), 1197–1231.

- [22] Fang, L., Meng, S.-S., Zhang, H. and Liu, Z.-Q. [2006], ‘Ba₂La₂TiNb₂O₁₂: A new microwave dielectric of A₄B₃O₁₂-type cation-deficient perovskites’, *Mater. Lett.* **60**(9), 1147 – 1150.
- [23] Fang, L., Zhang, H., Yu, Q., Su, H., Wu, B. and Cui, X. [2009], ‘Sr₃LaNb₃O₁₂: A new low loss and temperature stable A₄B₃O₁₂-type microwave dielectric ceramic’, *J. Am. Ceram. Soc.* **92**.
- [24] García-Fernández, P., Moreno, M. and Aramburu, J. A. [2016], ‘Origin of the anomalous color of Egyptian and Han blue historical pigments: going beyond the complex approximation in ligand field theory’, *J. Chem. Educ.* **93**, 111–117.
- [25] Gaudon, M., Robertson, L. C., Lataste, E., Duttine, M., Ménétrier, M. and Demourgues, A. [2014], ‘Cobalt and nickel aluminate spinels: Blue and cyan pigments’, *Ceram. Int.* **40**, 5201–5207.
- [26] Goetzberger, A. and Hebling, C. [2000], ‘Photovoltaic materials, past, present, future’, *Sol. Energy Mater. Sol. Cells* **62**, 1–19.
- [27] Goetzberger, A., Hebling, C. and Schock, H.-W. [2003], ‘Photovoltaic materials, history, status and outlook’, *Mater. Sci. Eng., R* **40**, 1–46.
- [28] Goodenough, J. B. [1963], *Magnetism and the Chemical Bond*, Wiley, New York.
- [29] Goodenough, J., Hong, H. and Kafalas, J. [1976], ‘Fast Na⁺-ion transport in skeleton structures’, *Mater. Res. Bull.* **11**(2), 203–220.
- [30] Gourai, K., El Bouari, A., Belhorma, B. and Bih, L. [2016], ‘Adsorption of methylene blue on the Li₃Fe_{1-x}Cr_x(MoO₄)₃ (x=0,0.5,1) lyonsite phases’, *Am. J. Chem.* **6**, 47–54.
- [31] Greedan, J. E. [2001], ‘Geometrically frustrated magnetic materials’, *J. Mater. Chem.* **11**, 37–53.
- [32] Hahn, T., E. [2006], *International Tables for Crystallography Volume A: Space-group symmetry, 5th ed.*, International Union of Crystallography, Chester.
- [33] Hang, P. T. and Brindley, G. W. [1970], ‘Methylene blue absorption by clay minerals. determination of surface areas and cation exchange capacities (clay-organic studies XVIII)’, *Clays Clay Miner.* **18**, 203–212.

- [34] Hazen, R. M., Downs, R. T. and Prewitt, C. T. [2000], ‘Principles of comparative crystal chemistry’, *Rev. Mineral. Geochem.* **41**, 1–34.
- [35] Heo, J. W., Hyung, J. and Hong, S.-T. [2018], ‘Unveiling the intercalation mechanism in $\text{Fe}_2(\text{MoO}_4)_3$ as an electrode material for Na-ion batteries by structural determination’, *Inorg. Chem.* **57**, 11901–11908.
- [36] Hoffmann, R., Howell, J. M. and Rossi, A. R. [1976], ‘Bicapped tetrahedral, trigonal prismatic, and octahedral alternatives in main and transition group six-coordination’, *J. Am. Chem. Soc.* **98**, 2484–2492.
- [37] Houas, A., Lachheb, H., Ksibi, M., Elaloui, E., Guillard, C. and Herrmann, J.-M. [2001], ‘Photocatalytic degradation pathway of methylene blue in water’, *Appl. Catal., B* **31**, 145–157.
- [38] Hughes, J. M., Starkey, S. J., Malinconico, M. L. and Malinconico, L. L. [1987], ‘Lyonsite, $\text{Cu}_3^{2+}\text{Fe}_4^{3+}(\text{VO}_4)_6^{3-}$, a new fumarolic sublimate from Izalco Volcano, El Salvador; descriptive mineralogy and crystal structure’, *Am. Mineral.* **72**, 1000–1005.
- [39] Huq, A., Hodges, J. P., Gourdon, O. and Heroux, L. [2011], ‘Powgen: A third-generation high-resolution high-throughput powder diffraction instrument at the Spallation Neutron Source’, *Z. Kristallogr. Proc.* **1**, 127–135.
- [40] Ibers, J. A. and Smith, G. W. [1964], ‘Crystal structure of a sodium cobalt molybdate’, *Act. Crystallogr.* **17**, 190–197.
- [41] Jahn, H. A. and Teller, E. [1937], ‘Stability of polyatomic molecules in degenerate electronic states: I–orbital degeneracy’, *Proc. R. Soc. London A* **161**, 220–235.
- [42] Jiles, D. [2015], *Introduction to Magnetism and Magnetic Materials*, 3rd ed., CRC Press.
- [43] Jin, R., He, J., McCall, S., Alexander, C. S., Drymiotis, F. and Mandrus, D. [2001], ‘Superconductivity in the correlated pyrochlore $\text{Cd}_2\text{Re}_2\text{O}_7$ ’, *Phys. Rev. B* **64**, 180503(R).
- [44] Jona, F., Shirane, G. and Pepinsky, R. [1955], ‘Dielectric, X-ray, and optical study of ferroelectric $\text{Cd}_2\text{Nb}_2\text{O}_7$ and related compounds’, *Phys. Rev.* **98**, 903–909.
- [45] Kaneko, M. and Okura, I. [2003], *Photocatalysis: Science and Technology*,

Springer.

- [46] Katz, L., Kasenally, A. and Kihlberg, L. [1971], ‘The crystal structure of the reduced copper molybdate $\text{Cu}_{4-x}\text{Mo}_3\text{O}_{12}$ (x approx.= 0.15)’, *Acta Crystallogr., Sect. B: Struct. Sci* **27**, 2071–2077.
- [47] Kim, H.-S., Im, S. H. and Park, N.-G. [2014], ‘Organolead halide perovskite: New horizons in solar cell research’, *J. Phys. Chem. C* **118**, 5615–5625.
- [48] Kingery, W. D., Bowen, H. K. and Uhlmann, D. R. [1976], *Introduction to Ceramics, 2nd Edition*, Wiley, New York.
- [49] Kittel, C. [2012], *Introduction to Solid State Physics, 8th ed.*, Wiley.
- [50] Klevtsova, R. F. and Magarill, S. A. [1970], ‘Crystal structure of lithium-ferriferrous molybdates $\text{Li}_3\text{Fe}(\text{MoO}_4)_3$ and $\text{Li}_2\text{Fe}_2(\text{MoO}_4)_3$ ’, *Kristallografiya* **15**, 710–715.
- [51] Knox, K. R., Abeykoon, A. M. M., Zheng, H., Yin, W.-G., Tselvik, A. M., Mitchell, J. F., Billinge, S. J. L. and Bozin, E. S. [2013], ‘Local structural evidence for strong electronic correlations in spinel LiRh_2O_4 ’, *Phys. Rev. B* **88**, 174114.
- [52] Köferstein, R., Jäger, L. and Ebbinghaus, S. G. [2013], ‘Magnetic and optical investigations on LaFeO_3 powders with different particle sizes and corresponding ceramics’, *Solid State Ionics* **249-250**, 1–5.
- [53] Kolitsch, U. and Tillmanns, E. [2003], ‘ $\text{Li}_3\text{Sc}(\text{MoO}_4)_3$: substitutional disorder on three (Li,Sc) sites’, *Acta Crystallogr., Sect. E: Struct. Rep. Online* **59**, i55–i58.
- [54] Kubelka, P. and Munk, F. [1931], ‘An article on optics of paint layers’, *Z. Tech. Phys.* **12**, 593–601.
- [55] Kurzawa, M., Bosacka, M. and Jakubus, P. [2003], ‘The structure and selected properties of $\text{Co}_{2.5}\text{VMoO}_8$ ’, *J. Mater. Sci.* **38**, 3137–3142.
- [56] Lafontaine, M., Grenéche, J., Laligant, Y. and Férey, G. [n.d.], ‘ $\beta\text{-Cu}_3\text{Fe}_4(\text{VO}_4)_6$: Structural study and relationships; physical properties’, *J. Solid State Chem.* pp. 1–10.
- [57] Larson, A. C. and Von Dreele, R. B. [2000], General Structure Analysis System (GSAS), Technical report, Los Alamos National Laboratory Report LAUR 86-748.

- [58] Le Bail, A. [2005], ‘Whole powder pattern decomposition methods and applications: A retrospection’, *Powder Diffr.* **20**, 316–326.
- [59] Li, J., Lorger, S., Stalick, J. K., Sleight, A. W. and Subramanian, M. A. [2016], ‘From serendipity to rational design: Tuning the blue trigonal bipyramidal Mn^{3+} chromophore to violet and purple through application of chemical pressure’, *Inorg. Chem.* **55**(19), 9798–9804.
- [60] Li, J., Medina, E. A., Stalick, J. K., Sleight, A. W. and Subramanian, M. A. [2016], ‘Colored oxides with hibonite structure: A potential route to non-cobalt blue pigments’, *Prog. Solid State Chem.* **44**(4), 107 – 122.
- [61] Liao, Q., Wang, Y., Jiang, F. and Guo, D. [2014], ‘Ultra-low fire glass-free $\text{Li}_3\text{FeMo}_3\text{O}_{12}$ microwave dielectric ceramics’, *J. Am. Ceram. Soc.* **97**, 2394–2396.
- [62] Lin, S., Sun, Z., Wu, B. and Chen, C. [1990], ‘The nonlinear optical characteristics of a LiB_3O_5 crystal’, *J. Appl. Phys.* **67**(2), 634–638.
- [63] López, R. and Gómez, R. [2012], ‘Band-gap energy estimation from diffuse reflectance measurements on sol-gel and commercial TiO_2 : A comparative study’, *J. Sol-Gel Sci. Technol.* **61**(1), 1–7.
- [64] Lorenzi, G., Baldi, G., Di Benedetto, F., Faso, V., Lattanzi, P. and Romanelli, M. [2006], ‘Spectroscopic study of a Ni-bearing gahnite pigment’, *J. Eur. Ceram. Soc.* **26**, 317–321.
- [65] Mabbs, F. E. and Machin, D. J. [1973], *Magnetism and Transition Metal Complexes*, Chapman and Hall, London.
- [66] Masquelier, C., Tabuchi, M., Ado, K., Kanno, R., Kobayashi, Y., Maki, Y., Nakamura, O. and Goodenough, J. B. [1996], ‘Chemical and magnetic characterization of spinel materials in the LiMn_2O_4 - $\text{Li}_2\text{Mn}_4\text{O}_9$ - $\text{Li}_4\text{Mn}_5\text{O}_{12}$ system’, *J. Solid State Chem.* **123**(2), 255 – 266.
- [67] McCusker, L. B., Von Dreele, R. B., Cox, D. E., Louër, D. and Scardi, P. [1999], ‘Rietveld refinement guidelines’, *J. Appl. Crystallogr.* **32**(1), 36–50.
- [68] Medina, E. A., Li, J., Stalick, J. K. and Subramanian, M. A. [2016], ‘Intense turquoise colors of apatite-type compounds with Mn^{5+} in tetrahedral coordination.’, *Solid State Sci.* **52**, 97–105.

- [69] Medina, E. A., Li, J. and Subramanian, M. A. [2017], ‘Colored oxides with hibonite structure ii: Structural and optical properties of $\text{CaAl}_{12}\text{O}_{19}$ -type pigments with chromophores based on Fe, Mn, Cr and Cu’, *Prog. Solid State Chem.* **45-46**, 9 – 29.
- [70] Miessler, G. L., Fischer, P. J. and Tarr, D. A. [2013], *Inorganic Chemistry, 5th Edition*, Pearson.
- [71] Mizoguchi, H., Marshall, W. J., Ramirez, A. P., Sleight, A. W. and Subramanian, M. A. [2007], ‘Partial charge ordering in the mixed-valent compound $(\text{Bi}_6\text{O}_5)\text{Rh}_8^{3+}\text{Rh}_4^{4+}\text{O}_{24}$ ’, *J. Solid State Chem.* **180**, 3463–3468.
- [72] Mu, Z., Song, E., Zhu, D., Feng, J. and Yang, Y. [2016], ‘Red phosphor $\text{Li}_2\text{Mg}_2(\text{WO}_4)_3 : \text{Eu}^{3+}$ with lyonsite structure for near ultraviolet light-emitting diodes’, *Displays* **43**, 18–22.
- [73] Nassau, K. [1978], ‘The origins of colour in minerals’, *Am. Mineral.* **63**(3), 219.
- [74] Okamoto, Y., Niitaka, S., Uchida, M., Waki, T., Takigawa, M., Nakatsu, Y., Sekiyama, A., Suga, S., Arita, R. and Takagi, H. [2008], ‘Band jahn-teller instability and formation of valence bond solid in a mixed-valent spinel oxide LiRh_2O_4 ’, *Phys. Rev. Lett.* **101**, 086404.
- [75] Orchard, A. F. [2003], *Magnetochemistry*, Oxford University Press.
- [76] Ozima, M., Sato, S. and Zoltai, T. [1977], ‘The crystal structure of a lithium–nickel molybdate, $\text{Li}_2\text{Ni}_2\text{Mo}_3\text{O}_{12}$, and the systematics of the structure type’, *Acta Crystallogr., Sect. B: Struct. Sci* **33**, 2175–2181.
- [77] Palmer, G. B., Poepelmeier, K. R. and Mason, T. O. [1997], ‘Conductivity and transparency of ZnO/SnO_2 -cosubstituted In_2O_3 ’, *Chem. Mater.* **9**(12), 3121–3126.
- [78] Pieczka, A., Evans, R. J., Grew, E. S., Groat, L. A., Ma, C. and Rossman, G. R. [2013], ‘The dumortierite supergroup. I. A new nomenclature for the dumortierite and holtite groups’, *Mineral. Mag.* **77**, 2825–2839.
- [79] Pless, J. D., Kim, H.-S., Smit, J. P., Wang, X., Stair, P. C. and Poepelmeier, K. R. [2006], ‘Structure of $\text{Mg}_{2.56}\text{V}_{1.12}\text{W}_{0.88}\text{O}_8$ and vibrational raman spectra of $\text{Mg}_{2.5}\text{VVO}_8$ and $\text{Mg}_{2.5}\text{VMoO}_8$.’, *Inorg. Chem.* **45**, 514–520.
- [80] Prabakaran, S., Fauzi, A., Michael, M. and Begam, K. [2004], ‘New NASICON-

- type $\text{Li}_2\text{Ni}_2(\text{MoO}_4)_3$ as a positive electrode material for rechargeable lithium batteries’, *Solid State Ionics* **171**(3-4), 157–165.
- [81] Prabakaran, S., Ramesh, S., Michael, M. and Begam, K. [2004], ‘Characterization of soft-combustion-derived NASICON-type $\text{Li}_2\text{Co}_2(\text{MoO}_4)_3$ for lithium batteries’, *Mater. Chem. Phys.* **87**(2-3), 318–326.
- [82] Qua [1999], *Physical Property Measurement System Hardware and Operations Manual, 2nd ed.*
- [83] Radin, M. D. and Van der Ven, A. [2016], ‘Stability of prismatic and octahedral coordination in layered oxides and sulfides intercalated with alkali and alkaline-earth metals’, *Chem. Mater.* **28**, 7898–7904.
- [84] Ramirez, A. P. [1997], ‘Colossal magnetoresistance’, *J. Phys. Condens. Matter* **9**, 8171–8199.
- [85] Rietveld, H. M. [1969], ‘A profile refinement method for nuclear and magnetic structures’, *J. Appl. Crystallogr.* **2**, 65–71.
- [86] Rig [2006], *X-Ray Diffractometer MiniFlex II Instruction Manual, 2nd ed.*
- [87] Rumble, J. E. [2018], *CRC Handbook of Chemistry and Physics*, CRC Press.
- [88] Russell, J. [2011], Measurement of optical bandgap energies of semiconductors, Master’s thesis, Oregon State University.
- [89] Sanford, S., Misture, S. T. and Edwards, D. D. [2013], ‘A comparison of the photocatalytic activity of six tunneled titanates’, *J. Solid State Chem.* **200**, 189–196.
- [90] Schwertmann, L., Grünert, A., Pougin, A., Sun, C., Wark, M. and Marschall, R. [2015], ‘Understanding the influence of lattice composition on the photocatalytic activity of defect-pyrochlore-structured semiconductor mixed oxides’, *Adv. Funct. Mater.* **25**, 905–912.
- [91] Sears, V. F. [1992], ‘Neutron scattering lengths and cross sections’, *Neutron News* **3**, 26–37.
- [92] Sebastian, L., Piffard, Y., Shukla, A. K., Taulelle, F. and Gopalakrishnan, J. [2003], ‘Synthesis, structure and lithium-ion conductivity of $\text{Li}_{2-2x}\text{Mg}_{2+x}(\text{MoO}_4)_3$

and $\text{Li}_3\text{M}(\text{MoO}_4)_3$ ($M^{\text{III}} = \text{Cr, Fe}$), *J. Mater. Chem.* **13**, 1797.

- [93] Sedello, O. and Müller-Buschbaum, H. [1996a], ‘Synthese und kristallstruktur von $(\text{Cu,Fe})_{3.63}\text{Mo}_3\text{O}_{12}$: Ein oxometallat mit eindimensional flächenverknüpften oktaederketten / Synthesis and crystal structure of $(\text{Cu,Fe})_{3.63}\text{Mo}_3\text{O}_{12}$: An oxometallate showing one-dimensional chains of face sharing octahedra’, *Z. Naturforsch., B: Chem. Sci.* **51**, 90–94.
- [94] Sedello, O. and Müller-Buschbaum, H. [1996b], ‘Zur kristallstruktur von $(\text{Cu,Mn})_{3.66}\text{Mo}_3\text{O}_{12}$ / On the crystal structure of $(\text{Cu,Mn})_{3.66}\text{Mo}_3\text{O}_{12}$ ’, *Z. Naturforsch., B: Chem. Sci.* **51**, 447–449.
- [95] Shannon, R. D. [1976], ‘Revised effective ionic radii and systematic studies of interatomic distances in halides and chalcogenides’, *Acta Crystallogr., Sect. A: Found. Crystallogr.* **32**, 751–767.
- [96] Sivia, D. S. [2011], *Elementary Scattering Theory: For X-ray and Neutron Users*, Oxford University Press.
- [97] Sleight, A. W. [1968], ‘New ternary oxides of mercury with the pyrochlore structure’, *Inorg. Chem.* **7**, 1704–1708.
- [98] Sleight, A. W., Gillson, J. L. and Bierstedt, P. E. [1975], ‘High-temperature superconductivity in the $\text{BaPb}_{1-x}\text{Bi}_x\text{O}_3$ systems’, *Solid State Comm.* **17**(1), 27–28.
- [99] Smit, J. P., Kim, H.-S., Pless, J. D., Stair, P. C. and Poeppelmeier, K. R. [2006], ‘Probing the vanadyl and molybdenyl bonds in complex vanadomolybdate structures.’, *Inorg. Chem.* **45**(2), 521–8.
- [100] Smit, J. P., Kim, H., Saratovsky, I., Stark, K. B., Fitzgerald, G., Zajac, G. W., Gaillard, J., Poeppelmeier, K. R. and Stair, P. C. [2007], ‘A spectroscopic and computational investigation of the vanadomolybdate local structure in the lyonsite phase $\text{Mg}_{2.5}\text{VMoO}_8$ ’, *Inorg. Chem.* **46**, 6556–6564.
- [101] Smit, J. P., McDonald, T. M. and Poeppelmeier, K. R. [2008], ‘ $\text{Li}_3\text{Ti}_{0.75}(\text{MoO}_4)_3$: A lyonsite-type oxide’, *Solid State Sci.* **10**, 396–400.
- [102] Smit, J. P., Stair, P. C. and Poeppelmeier, K. R. [2006], ‘The adaptable lyonsite structure’, *Chem. Eur. J.* **12**, 5944–5953.

- [103] Smith, A. E., Comstock, M. C. and Subramanian, M. A. [2016], ‘Spectral properties of the UV absorbing and near-IR reflecting blue pigment, $\text{YIn}_{1-x}\text{Mn}_x\text{O}_3$ ’, *Dyes Pigm.* **133**, 214–221.
- [104] Smith, A. E., Mizoguchi, H., Delaney, K., Spaldin, N. A., Sleight, A. W. and Subramanian, M. A. [2009], ‘ Mn^{3+} in trigonal bipyramidal coordination: A new blue chromophore’, *J. Am. Chem. Soc.* **131**, 17084–17086.
- [105] Smith, G. W. [1960], ‘Crystal structure of orthorhombic cobalt molybdate’, *Nat.* **188**, 306–308.
- [106] Solodovnikov, S. F., Solodovnikova, Z. A., Zolotova, E. S., Yudanova, L. I., Kardash, T. Y., Pavlyuk, A. A. and Nadolinny, V. A. [2009], ‘Revised phase diagram of Li_2MoO_4 – ZnMoO_4 system, crystal structure and crystal growth of lithium zinc molybdate’, *J. Solid State Chem.* **182**(7), 1935–1943.
- [107] Stanek, C. R., Jiang, C., Uberuaga, B. P., Sickafus, K. E., Cleave, A. R. and Grimes, R. W. [2009], ‘Predicted structure and stability of $A_4B_3O_{12}$ δ -phase compositions’, *Phys. Rev. B* **80**, 174101.
- [108] Subramanian, M. A., Aravamudan, G. and Subba Rao, G. V. [1983], ‘Oxide pyrochlores — A review’, *Prog. Solid State Chem.* **15**, 55–143.
- [109] Subramanian, M., Rudolf, P. and Clearfield, A. [1985], ‘The preparation, structure, and conductivity of scandium-substituted NASICONs’, *J. Solid State Chem.* **60**(2), 172–181.
- [110] Szillat, H. and Müller-Buschbaum, H. [1995], ‘Zur kenntnis des oxocuprats $(\text{Cu},\text{Co})_{3.75}\text{Mo}_3\text{O}_{12}$ / On the oxocuprate $(\text{Cu},\text{Co})_{3.75}\text{Mo}_3\text{O}_{12}$ ’, *Z. Naturforsch., B: Chem. Sci.* **50**, 707–711.
- [111] Tang, J. N., Li, J. and Subramanian, M. A. [2018], ‘Structural investigation and selected properties of $\text{Zn}_{2.5-x}\text{Co}_x\text{VMoO}_8$ lyonsites’, *J. Solid State Chem.* **266**, 155–160.
- [112] Tauc, J., Grigorovici, R. and Vancu, A. [1966], ‘Optical properties and electronic structure of amorphous germanium’, *Physica Status Solidi B* **15**(2), 627–637.
- [113] Thackeray, M., Johnson, P., de Picciotto, L., Bruce, P. and Goodenough, J. [1984], ‘Electrochemical extraction of lithium from LiMn_2O_4 ’, *Mater. Res. Bull.* **19**(2), 179 – 187.

- [114] Tilley, R. J. D. [2013], *Understanding Solids: The Science of Materials, 2nd ed.*, Wiley.
- [115] Toby, B. H. [2001], 'EXPGUI , a graphical user interface for GSAS', *J. Appl. Crystallogr.* **34**, 210–213.
- [116] Toby, B. H. [2006], 'R factors in rietveld analysis: How good is good enough?', *Powder Diffr.* **21**(1), 67–70.
- [117] Tompsett, D. A. and Islam, M. S. [2014], 'Surfaces of rutile MnO₂ are electronically conducting, whereas the bulk material is insulating', *J. Phys. Chem. C* **118**, 25009–25015.
- [118] Tovar, M., Torabi, R., Welker, C. and Fleischer, F. [2006], 'Structural and magnetic properties of Cu-Ni-Cr spinel oxides', *Physica B* **385**, 196–198.
- [119] Tritt, T. M. and Subramanian, M. A. [2006], 'Thermoelectric materials, phenomena, and applications: a bird's eye view', *Mater. Res. Bull.* **31**(03), 188–198.
- [120] Ueno, G., Sato, S. and Kino, Y. [1999], 'The low-temperature tetragonal phase of NiCr₂O₄', *Acta Crystallogr., Sect. C: Cryst. Struct. Commun.* **55**, 1963–1966.
- [121] Van Vleck, J. [1935], 'Valence strength and the magnetism of complex salts', *J. Chem. Phys.* **3**(12), 807–813.
- [122] Vasala, S. and Karppinen, M. [2015], 'A₂B'B''O₆ perovskites : A review', *Prog. Solid State Chem.* **43**, 1–36.
- [123] Viola, M. C., Martínez-Lope, M. J., Alonso, J. A., Martínez, J. L., De Paoli, J. M., Pagola, S., Pedregosa, J. C., Fernández-Díaz, M. T. and Carbonio, R. E. [2003], 'Structure and magnetic properties of Sr₂CoWO₆: an ordered double perovskite containing Co²⁺(HS) with unquenched orbital magnetic moment', *Chem. Mater.* **15**, 1655–1663.
- [124] Wang, C., Chen, S., Yang, J.-H., Lang, L., Xiang, H.-J., Gong, X.-G., Walsh, A. and Wei, S.-H. [2014], 'Design of I₂-II-IV-VI₄ semiconductors through element substitution: The thermodynamic stability limit and chemical trend', *Chem. Mater.* **26**(11), 3411–3417.
- [125] Wang, D., Zou, Z. and Ye, J. [2004], 'A novel series of photocatalysts M_{2.5}VMoO₈ (M = Mg, Zn) for O₂ evolution under visible light irradiation', *Catal. Today*

93-95, 891–894.

- [126] Wang, J., Toby, B. H., Lee, P. L., Ribaud, L., Antao, S. M., Kurtz, C., Ramanathan, M., Von Dreele, R. B. and Beno, M. A. [2008], ‘A dedicated powder diffraction beamline at the advanced photon source: Commissioning and early operational results’, *Rev. Sci. Instrum.* **79**(8), 085105.
- [127] Wang, Q., Liang, C., Zheng, Y., Ashburn, N., Oh, Y. J., Kong, F., Zhang, C., Nie, Y., Sun, J., He, K., Ye, Y., Chen, R., Shan, B. and Cho, K. [2017], ‘First principles study of the Mn-doping effect on the physical and chemical properties of mullite-family Al_2SiO_5 ’, *Phys. Chem. Chem. Phys.* **19**, 24991–25001.
- [128] Wang, X., Heier, K. R., Stern, C. L. and Poeppelmeier, K. R. [1997], ‘Crystal structure of $\text{Zn}_{3.77}\text{V}_{1.54}\text{Mo}_{1.46}\text{O}_{12}$ containing ZnO_6 trigonal prisms’, *J. Alloys Compd.* **255**, 190–194.
- [129] Wang, X., Heier, K. R., Stern, C. L. and Poeppelmeier, K. R. [1998], ‘Crystal growth and structure of $\text{Mn}_{2.47}\text{V}_{0.94}\text{Mo}_{1.06}\text{O}_8$ ’, *J. Alloys Compd.* **267**, 79–85.
- [130] Wang, X., Pless, J. D., Vander Griend, D. A., Stair, P. C., Poeppelmeier, K. R., Hu, Z. and Jorgensen, J. D. [2004], ‘Vanadium and molybdenum disorder in $\text{M}_{2.5}\text{VMoO}_8$ (M = Mg, Mn, and Zn) determined with neutron powder diffraction and phase formation studies of $\text{Mg}_{2.5+x}\text{V}_{1+2x}\text{Mo}_{1-2x}\text{O}_8$ ’, *J. Alloys Compd.* **379**, 87–94.
- [131] Wanklyn, B. M., Wondre, F. R. and Davison, W. [1976], ‘Flux growth of crystals of some magnetic oxide materials: $\text{Mn}_7\text{SiO}_{12}$, CuO , MCr_2O_4 , MTiO_3 , Ni_2NbBO_6 , MMoO_4 and $\text{Li}_2\text{M}_2(\text{MoO}_4)_3$, (M = Mn, Co, Ni)’, *J. Mater. Sci.* **11**, 1607–1614.
- [132] West, A. R. [2014], *Solid State Chemistry and its Applications, 2nd Edition, Student Edition*, Wiley, Chichester.
- [133] Wiesmann, M., Geselle, M., Weitzel, H. and Fueß, H. [1994], ‘Crystal structure of lithium copper molybdate, $\text{Li}_2\text{Cu}_2(\text{MoO}_4)_3$ ’, *Z. Kristallogr.* **209**, 615.
- [134] Wiesmann, M., Svoboda, I., Weitzel, H. and Fuess, H. [1995], ‘Crystal structure of lithium cobalt molybdate, $\text{Li}_2\text{Co}_2(\text{MoO}_4)_3$ ’, *Z. Kristallogr.* **210**, 1995.
- [135] Xia, Z., Ma, C., Moloakeev, M. S., Liu, Q., Rickert, K. and Poeppelmeier, K. R. [2015], ‘Chemical unit cosubstitution and tuning of photoluminescence in the $\text{Ca}_2(\text{Al}_{1-x}\text{Mg}_x)(\text{Al}_{1-x}\text{Si}_{1+x})\text{O}_7:\text{Eu}^{2+}$ phosphor’, *J. Am. Chem. Soc.*

- 137**(39), 12494–12497.
- [136] Xia, Z. and Poeppelmeier, K. R. [2017], ‘Chemistry-inspired adaptable framework structures’, *Acc. Chem. Res.* **50**(5), 1222–1230.
- [137] Xue, L., Wang, Y., Lv, P., Chen, D., Lin, Z., Liang, J., Huang, F. and Xie, Z. [2009], ‘Growth, structures, and properties of $\text{Li}_2\text{Zn}_2(\text{MoO}_4)_3$ and Co-doped $\text{Li}_2\text{Zn}_2(\text{MoO}_4)_3$ ’, *Cryst. Growth Des.* **9**, 914–920.
- [138] Yoshikado, S., Ohachi, T. and Taniguchi, I. [1983], ‘Frequency-independent ionic conductivity of hollandite type compounds’, *Solid State Ionics* **10**, 1305–1309.
- [139] Zhang, H., Zhang, M., Pan, S., Yang, Z., Wang, Z., Bian, Q., Hou, X., Yu, H., Zhang, F., Wu, K., Yang, F., Peng, Q., Xu, Z., Chang, K. and Poeppelmeier, K. [2015], ‘ $\text{Na}_3\text{Ba}_2(\text{B}_3\text{O}_6)_2\text{F}$: Next generation of deep-ultraviolet birefringent materials’, *Cryst. Growth Des.* **15**, 523–529.
- [140] Zhang, J. and Zuo, R. [2015], ‘Synthesis and microwave dielectric properties of $\text{Li}_2\text{Mg}_2(\text{WO}_4)_3$ ceramics’, *Mater. Lett.* **158**, 92–94.
- [141] Zhao, S., Kang, L., Shen, Y., Wang, X., Asghar, M. A., Lin, Z., Xu, Y., Zeng, S., Hong, M. and Luo, J. [2016], ‘Designing a beryllium-free deep-ultraviolet nonlinear optical material without a structural instability problem’, *J. Am. Chem. Soc.* **138**(9), 2961–2964.
- [142] Zhou, D., Randall, C. A., Pang, L., Wang, H., Wu, X., Guo, J., Zhang, G., Shui, L. and Yao, X. [2011], ‘Microwave dielectric properties of $\text{Li}_2(\text{M}^{2+})_2\text{Mo}_3\text{O}_{12}$ and $\text{Li}_3(\text{M}^{3+})\text{Mo}_3\text{O}_{12}$ ($\text{M} = \text{Zn, Ca, Al, and In}$) lyonsite-related-type ceramics with ultra-low sintering temperatures’, *J. Am. Ceram. Soc.* **94**, 802–805.

APPENDICES

Appendix A: Structure-Property Relationships and Charge Distribution in $\text{LiMn}_{2-x}\text{Rh}_x\text{O}_4$ Spinels

A.1 Abstract

Four members of the spinel family $\text{LiMn}_{2-x}\text{Rh}_x\text{O}_4$ and their structures characterized using X-ray and neutron diffraction. All samples were prepared by standard solid state synthesis, and lattice refinements indicate a change in cell edges in accordance with Vegard's law. Electrical resistivity measurements have been performed, and the magnetic behavior of each spinel was also characterized through magnetic susceptibility measurements. Paramagnetic behavior was observed in the $\chi(T)$ data, and observed magnetic moments correlate well to expected values, resulting in the proposed formulas: $\text{LiMn}^{4+}\text{Rh}^{3+}\text{O}_4$ for $x = 1$ and $\text{LiMn}_{0.5}^{4+}\text{Rh}^{3+}\text{Rh}_{0.5}^{4+}\text{O}_4$ for $x = 1.5$. The oxidation state distribution analysis for the $x = 0.5$ is not as straightforward, and will require complementary analysis techniques to fully comprehend.

Publications based on this chapter:

J. N. Tang, S. Svadlenak, M. K. Wallace, M. A. Subramanian, Structure-property relationships and charge distribution in $\text{LiMn}_{2-x}\text{Rh}_x\text{O}_4$ spinels, (*In Progress*).

A.2 Introduction

The spinel family (AM_2X_4 , typically $Fd\bar{3}m$) is known to be structurally rigid, yet compositionally flexible. The structure can be described as ccp, with 1/2 of the octahedral voids and 1/8 of the tetrahedral voids filled. The geometric arrangement of the cation sites often lead to frustrated magnetic states, resulting in properties like spin glasses. While it is a rigid structure, there are reports of Jahn-Teller-induced distortions, as in $A^{2+}Rh^{3+}O_4$ ($A = Cu, Ni$) [1–3].

While Rh^{3+} is diamagnetic, it can also exist in the +4 oxidation state. One Rh-based spinel, $LiRh_2O_4$, was only discovered in the last 10 years, and was characterized as being a mixed-valence oxide. Magnetometry results have revealed that there exists a metal-insulator transition that is intimately tied to two temperature-dependent structural phase transitions (cubic to tetragonal at 230 K and tetragonal to orthorhombic at 170 K) [4]. In addition, a high Seebeck was observed at high temperatures (80 $\mu V/K$ at 800 K) and the origin of the thermopower was determined computationally to be the result of band instability, allowing for a high Seebeck in spite of the metallic nature of the compound [5]. To further understand this system, local structure analysis was done via atomic-pair distribution function (PDF), which determined that the compound is strongly correlated, indicated by the formation of Rh-Rh dimers in the pyrochlore sublattice [6].

The compositional flexibility also brings to mind the transition metal with the most number of observed oxidation states: Mn. Alas, Mn-based spinels have been extensively studied in recent years as a Li-ion battery cathode material. A stoichiometric analog

to the mentioned Rh-based spinel, LiMn_2O_4 , is demonstrated to be capable of delithiation (up to 60%) without compromising the MnO_4 network [7]. Furthermore, magnetic investigations reveal that the variable Mn oxidation state (as a function of $\text{Li}_{1-x}\text{Mn}_{2-x}$) allows for a tunable antiferromagnetic ($\text{Mn}^{3.5+}$) to ferromagnetic (Mn^{4+}) state, as indicated by a crossover of the Weiss constant from highly negative to positive ($\theta_{\text{W}} = -266 \rightarrow 40$ K) [8].

Because both Mn and Rh can be variable in oxidation state, the potential functional properties of a solid solution between these two spinels are of great interest; this work therefore aims to explore the structure-property relationships of the $\text{LiMn}_{2-x}\text{Rh}_x\text{O}_4$ solid solution.

A.3 Experimental

Stoichiometric quantities of Li_2CO_3 (99.9%, Sigma-Aldrich), MnO (99.5%, Johnson Matthey), and Rh_2O_3 (99.8%, Sigma-Aldrich) were ground in an agate mortar, pressed into pastilles, calcined at 500 °C, and annealed at 950 °C for 12 h in air at ambient pressures.

Powder X-ray diffraction data were collected in the 10–60 2θ range on a benchtop Rigaku MiniFlex II diffractometer using Cu K_α radiation and a graphite monochromator. Select (≈ 5 g) samples were portioned for room temperature neutron powder diffraction analysis on the BT-1 beamline at the Center for Neutron Research at the National Institute of Standards and Technology. Measurement was conducted over a 2θ range of 3–167°, and a Cu (311) monochromator was employed yield an

incident wavelength of 1.5403(2) Å [9]. Collimation of 15' of arc was used before the monochromator, 20' before the sample, and 7' before the detectors. Subsequent Rietveld analysis was performed via the General Structure Analysis System (GSAS) software with the EXPGUI interface [10, 11].

The electrical conductivity σ and Seebeck coefficients S of sintered bar-shaped samples were characterized between 300–600 K on an ULVAC ZEM-3 under He atmosphere.

Zero-field-cooled (ZFC) DC magnetometry was conducted via a Quantum Design PPMS and a Quantum Design SQUID MPMS between 5–300 K. Oxidation state distribution analysis was performed by fitting the inverse susceptibility plots to the reciprocal Curie-Weiss Law and extracting effective moments. A more detailed discussion of this analysis can be found in the Results section.

A.4 Results/Discussion

A.4.1 *Crystal Structure*

Phase pure polycrystalline samples were obtained for all except the $x = 2$ member, as it is already known and characterized. Powder X-ray diffraction analysis confirm that all samples are phase pure and isostructural to the parents, crystallizing in the cubic $Fd\bar{3}m$ space group (Fig. A.1).

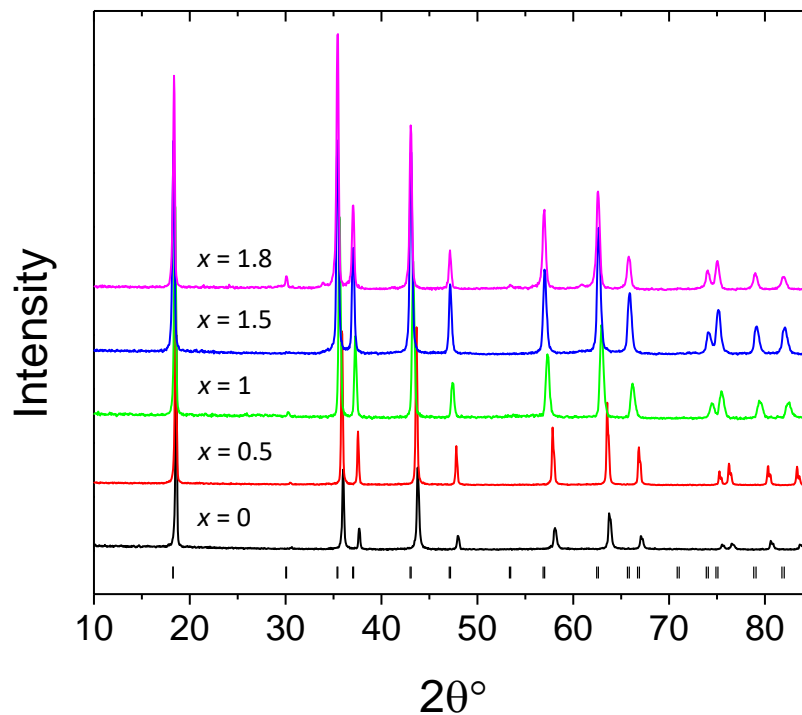


Figure A.1: Powder X-ray diffraction patterns for $\text{LiMn}_{2-x}\text{Rh}_x\text{O}_4$. hkl tick marks (black) are shown for allowed reflections for $Fd\bar{3}m$.

Lattice refinements indicate a unit cell expansion with increasing Rh content, corresponding well to the difference in Shannon ionic radii in the substituted site (Fig. A.2). In this system, both Mn and Rh should occupy the mixed M site, and can adopt either the +3 and/or +4 oxidation states. Mn^{3+} , Mn^{4+} , Rh^{3+} , and Rh^{4+} have ionic radii of 0.645, 0.530, 0.665, and 0.60 Å, respectively [12]. Therefore, a lattice expansion is expected.

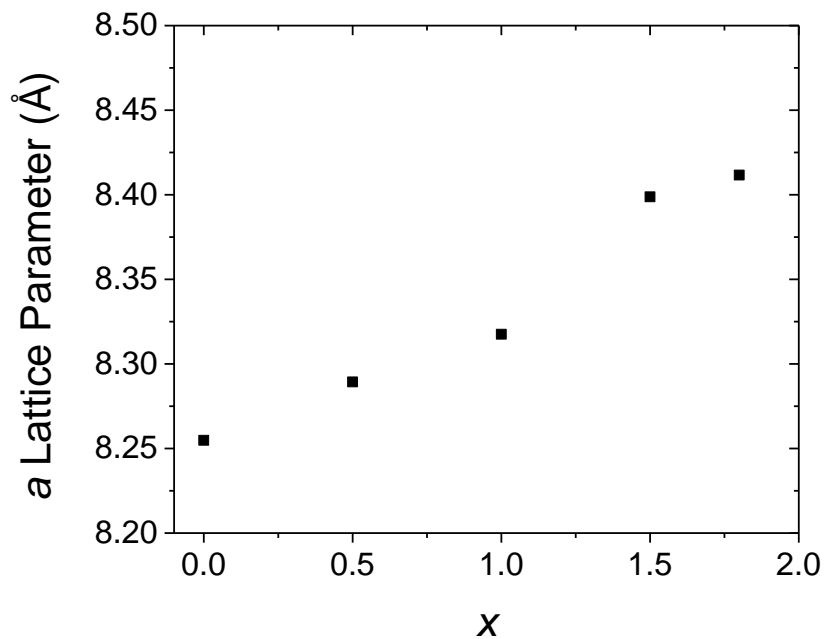


Figure A.2: *a* lattice parameter for $\text{LiMn}_{2-x}\text{Rh}_x\text{O}_4$.

The short scattering length of Li compared to heavier elements indicate that the X-ray diffraction data are not sufficient to determine the distribution of the Mn and Rh ions, as well the overall stoichiometry. The neutron scattering length contrast between Li, Mn, and Rh (-1.9, -3.73, and 5.88 fm, respectively) [9] are sufficient to warrant neutron diffraction data. The data were collected, but structural refinements are still in progress at the time of writing, and no detailed conclusions can yet be made.

A.4.2 Magnetic Properties

Magnetic susceptibility data were collected to determine the Mn and Rh oxidation states (Fig. A.3) for three samples: $x = 0.5, 1, 1.5$. All samples obey the Curie-Weiss law in the high temperature region. Because the magnetic moment is highly correlated to the cation oxidation states, it was possible to deduce the oxidation state distribution of Mn and Rh for $x = 1$ and $x = 1.5$. A discussion of this analysis follows.

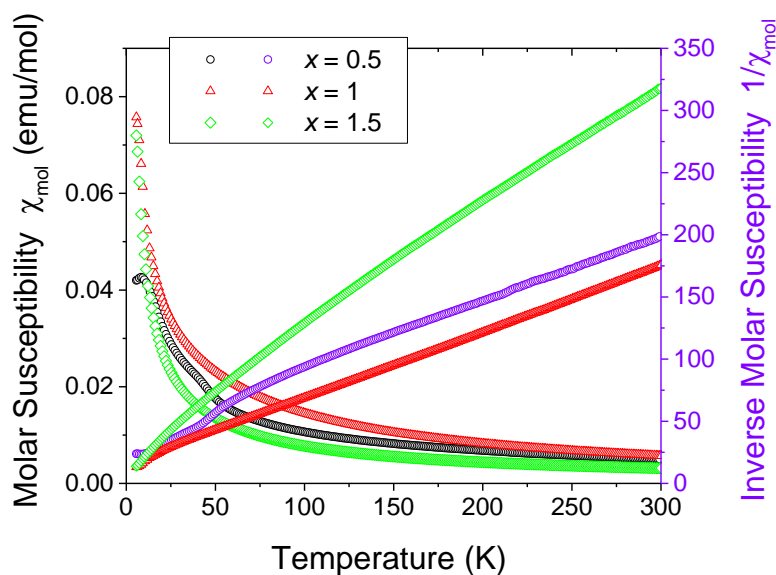


Figure A.3: Magnetic susceptibility plots for $\text{LiMn}_{2-x}\text{Rh}_x\text{O}_4$.

When more than one magnetic ion is present in a sample, the total magnetic moment consists of the stoichiometric (molar) contribution of the present elements and their number of unpaired electrons. For a hypothetical compound A_xM_y with

magnetic ions A and M , the theoretical moment per formula unit can be obtained via

$$\mu_{\text{total}} = \sqrt{x \times \mu_{A,\text{th}}^2 + y \times \mu_{M,\text{th}}^2} \quad (\text{A.1})$$

Some considerations must be made for the modeling conditions. Ideally, the high temperature region is highly linear, with fitting typically done in the 150–300 K range. In some cases, linearity is broken, and the lower bound for fitting must be shifted higher. In addition, the extracted μ_{eff} is highly dependent on the *a priori* oxidation state assumptions. Thus, the experimental μ_{eff} value can vary widely depending on those two factors.

In this series, the possible oxidation states and their respective electron configurations are given (Fig. A.4), with the presumption that they occupy the octahedral site. It is apparent that all but Rh^{3+} are magnetically active, and can contribute to the observed moment. From Eq. A.1, a variety of scenarios can be simulated (Table A.1). Naturally, these are not the only possible permutations; to preserve charge neutrality, though, the scenarios presented are the most chemically intuitive.

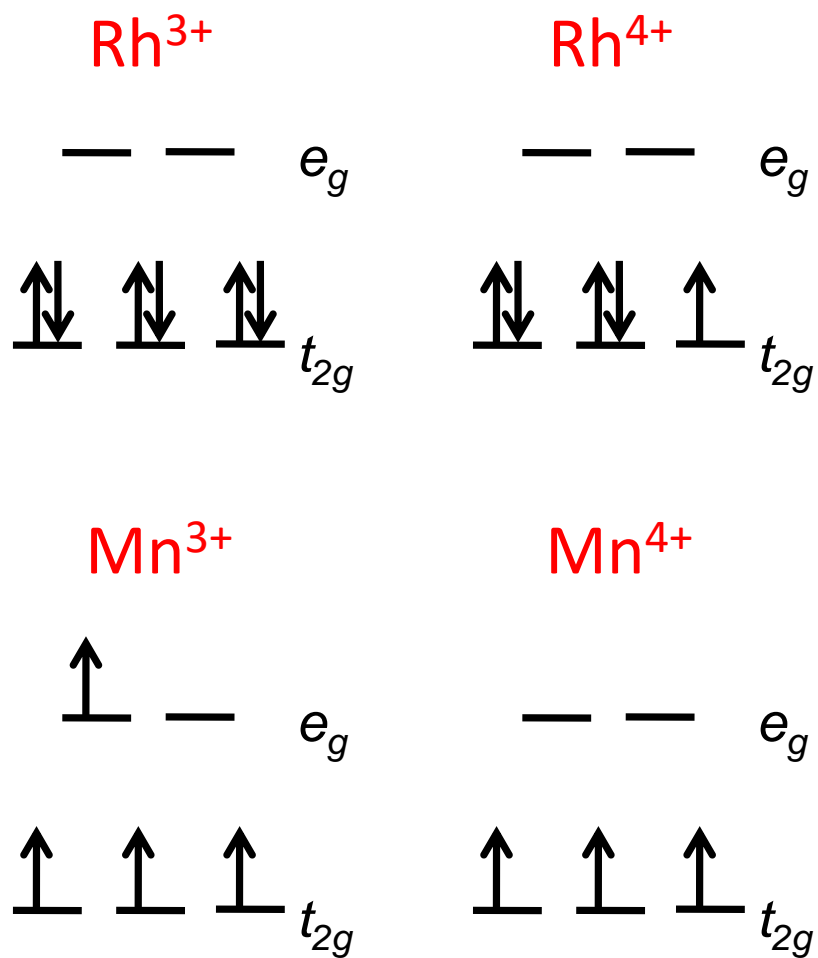


Figure A.4: Crystal field splitting diagrams and possible spin states for $\text{LiMn}_{2-x}\text{Rh}_x\text{O}_4$.

Table A.1: Possible oxidation state and stoichiometries for $\text{LiMn}_{2-x}\text{Rh}_x\text{O}_4$.

x	Rh^{3+}	Rh^{4+}	Mn^{3+}	Mn^{4+}	μ_{th}
0.5	0.5	0	0.5	1	5.19
–	0	0.5	1	0.5	5.74
–	0.25	0.25	0.75	0.75	5.48
1	1	0	0	1	3.87
–	0	1	1	0	5.20
1.5	1.5	0	0	0.5	2.74
–	0	1.5	0.5	0	4.06
–	1	0.5	0	0.5	3.00

Table A.2: Effective magnetic moments and modeling conditions for $\text{LiMn}_{2-x}\text{Rh}_x\text{O}_4$.

x	θ_{W}	$\mu_{\text{eff}} (\mu_{\text{B}})$	$\mu_{\text{th}} (\mu_{\text{B}})$	Model Formula	Model Range
0.5	-85.3	3.95	5.19	$\text{LiMn}_{0.5}^{3+}\text{Mn}^{4+}\text{Rh}_{0.5}^{3+}\text{O}_4$	115–300K
	-86.5	3.43	5.74	$\text{LiMn}_1^{3+}\text{Mn}_{0.5}^{4+}\text{Rh}_{0.5}^{4+}\text{O}_4$	115–300K
	4.24	3.86	5.74	$\text{LiMn}_1^{3+}\text{Mn}_{0.5}^{4+}\text{Rh}_{0.5}^{4+}\text{O}_4$	241–300K
1	-25.8	3.87	3.87	$\text{LiMn}^{4+}\text{Rh}^{3+}\text{O}_4$	151–300K
	-28.7	2.76	5.20	$\text{LiMn}^{3+}\text{Rh}^{4+}\text{O}_4$	142–300K
1.5	-49.2	4.17	2.74	$\text{LiMn}_{0.5}^{4+}\text{Rh}_{1.5}^{3+}\text{O}_4$	193–300K
	-61.4	2.16	4.06	$\text{LiMn}_{0.5}^{3+}\text{Rh}_{1.5}^{4+}\text{O}_4$	218–300K
	-52.6	2.98	3.00	$\text{LiMn}_{0.5}^{4+}\text{Rh}^{3+}\text{Rh}_{0.5}^{4+}\text{O}_4$	192–300K

As seen in Table A.2, oxidation states can be assigned with good agreement for $x = 1$ and $x = 1.5$. Regardless of simulation, the Weiss constants indicate a propensity towards antiferromagnetic ordering. At very low temperatures (≈ 8 K), there is an indication of an antiferromagnetic transition for $x = 0.5$. The charge distribution analysis was not resolved for the $x = 0.5$ member. Attempts to model the data against other permutations (not shown) was intractable, with charge neutrality as a restrictive parameter. Determination of the cation distribution and oxygen occupancies via neutron diffraction analysis will therefore shed light on the cause of the μ_{eff} value discrepancy.

A.5 Conclusions

A full solid solution was shown to exist in the $\text{LiMn}_{2-x}\text{Rh}_x\text{O}_4$ series. All samples are isostructural, indexing to the $Fd\bar{3}m$ space group. Lattice refinements reveal a cell expansion, corresponding to the larger ionic radius of Rh^{3+} and Rh^{4+} . All samples exhibit Curie-Weiss behavior in the high temperature region, and the $x = 0.5$ member displays an antiferromagnetic transition at ≈ 8 K. The charge distributions were determined for $x = 1$ and $x = 1.5$, expressed as the formulas $\text{LiMn}^{4+}\text{Rh}^{3+}\text{O}_4$ and $\text{LiMn}_{0.5}^{4+}\text{Rh}^{3+}\text{Rh}_{0.5}^{4+}\text{O}_4$, respectively.

Bibliography

- [1] W. A. Dollase, H. S. C. O'Neill, The spinels CuCr_2O_4 and CuRh_2O_4 , *Acta Crystallogr., Sect. C: Cryst. Struct. Commun.* 53 657–659. doi:10.1107/S0108270197000486.

- [2] M. Tovar, R. Torabi, C. Welker, F. Fleischer, Structural and magnetic properties of Cu-Ni-Cr spinel oxides, *Physica B* 385 (2006) 196–198. doi:10.1016/j.physb.2006.05.181.
- [3] G. Ueno, S. Sato, Y. Kino, The low-temperature tetragonal phase of NiCr_2O_4 , *Acta Crystallogr., Sect. C: Cryst. Struct. Commun.* 55 (1999) 1963–1966. doi:10.1107/S0108270199011713.
- [4] Y. Okamoto, S. Niitaka, M. Uchida, T. Waki, M. Takigawa, Y. Nakatsu, A. Sekiyama, S. Suga, R. Arita, H. Takagi, Band jahn-teller instability and formation of valence bond solid in a mixed-valent spinel oxide LiRh_2O_4 , *Phys. Rev. Lett.* 101 (2008) 086404. doi:10.1103/PhysRevLett.101.086404.
- [5] R. Arita, K. Kuroki, K. Held, A. V. Lukoyanov, S. Skornyakov, V. I. Anisimov, Origin of large thermopower in LiRh_2O_4 : Calculation of the seebeck coefficient by the combination of local density approximation and dynamical mean-field theory, *Phys. Rev. B* 78 (2008) 115121. doi:10.1103/PhysRevB.78.115121.
- [6] K. R. Knox, A. M. M. Abeykoon, H. Zheng, W.-G. Yin, A. M. Tselvik, J. F. Mitchell, S. J. L. Billinge, E. S. Bozin, Local structural evidence for strong electronic correlations in spinel LiRh_2O_4 , *Phys. Rev. B* 88 (2013) 174114. doi:10.1103/PhysRevB.88.174114.
- [7] M. Thackeray, P. Johnson, L. de Picciotto, P. Bruce, J. Goodenough, Electrochemical extraction of lithium from LiMn_2O_4 , *Mater. Res. Bull.* 19 (2) (1984) 179 – 187. doi:10.1016/0025-5408(84)90088-6.
- [8] C. Masquelier, M. Tabuchi, K. Ado, R. Kanno, Y. Kobayashi, Y. Maki, O. Nakamura, J. B. Goodenough, Chemical and magnetic characterization of spinel materials in the LiMn_2O_4 - $\text{Li}_2\text{Mn}_4\text{O}_9$ - $\text{Li}_4\text{Mn}_5\text{O}_{12}$ system, *J. Solid State Chem.* 123 (2) (1996) 255 – 266. doi:10.1006/jssc.1996.0176.
- [9] V. F. Sears, Neutron scattering lengths and cross sections, *Neutron News* 3 (1992) 26–37. doi:10.1080/10448639208218770.
- [10] B. H. Toby, EXPGUI, a graphical user interface for GSAS, *J. Appl. Crystallogr.* 34 (2001) 210–213. doi:10.1107/S0021889801002242.
- [11] A. C. Larson, R. B. Von Dreele, General Structure Analysis System (GSAS), Tech. rep., Los Alamos National Laboratory Report LAUR 86-748 (2000).

- [12] R. D. Shannon, Revised effective ionic radii and systematic studies of interatomic distances in halides and chalcogenides, *Acta Crystallogr., Sect. A: Found. Crystallogr.* 32 (1976) 751–767. doi:10.1107/S0567739476001551.

Appendix B: Alternate Synthesis and Photocatalytic Activity for Select Lyonsite-Type Oxides

In the following sections, supplemental results on select lyonsites will be discussed.

B.1 Citrate Gel Method: An Alternative Synthesis Route

As mentioned in Chapter 2.1.2, a drawback of the ceramic method is the dependence on particle mixing quality. During the course of research detailed in Chapter 4, some samples of $A' = \text{Ni}$ were difficult to form by the ceramic method. Those samples were repeatedly heated 800 °C until phase purity was achieved. As a side experiment, the citrate gel method [1, 2] was employed for $\text{Zn}_2\text{Ni}_{0.5}\text{VMoO}_8$ to attempt phase formation at lower temperatures and reduce reaction times.

Stoichiometric quantities of $\text{Zn}(\text{NO}_3)_2 \cdot 6 \text{H}_2\text{O}$, $\text{Ni}(\text{NO}_3)_2 \cdot 6 \text{H}_2\text{O}$, NH_4VO_3 , $(\text{NH}_4)_6\text{Mo}_7\text{O}_{24} \cdot 4 \text{H}_2\text{O}$ were combined in a beaker with deionized water. In particular, $\text{Ni}(\text{NO}_3)_2 \cdot 6 \text{H}_2\text{O}$ is deliquescent, so speed was critical during the weighting process. The solution was heated and stirred, while adding citric acid in a 2:1 molar ratio, to allow for cross-linking of metal cations to the citrate. The pH was then adjusted to 7 with NH_4OH . The solution was heated at 250 °C for 2 h until a dark brown, amorphous, dry polymer "gel" was observed. Intermittent stirring was done with a glass rod to release any trapped NO_x or CO_x , as they can corrode the inside of the

muffle furnaces. The final gel was then calcined at at 600 °C in air for 6–12 h.

This process yields homogeneously dispersed cations, but due to the smaller particle sizes, requires longer duration diffraction experiments to achieve intensities appropriate for detailed structural refinements. A comparison between the two methods for this compound is shown in Fig. B.1. The results were positive, with phase purity achieved in 1/3 the time, and at 200 °C below that of the ceramic method. The observed peak broadening (especially apparent at high 2θ) is unavoidable, as the particle sizes are small enough to cause broadening of the diffracted Bragg peaks. The powder sample was still yellow in color, but was also paler than that of the ceramic method, which could be due to the refractive index changes as a result of particle size.

As of right now, the only known routes to synthesis of lyonsite powder samples are the ceramic method and soft combustion methods; in addition, it is posited that high-pressure synthesis can be utilized to form the original mineral phase [3], which has not been successfully synthesized at ambient pressures. The success of this experiment may indicate this method as a viable low-temperature synthesis route for other lyonsite compounds.

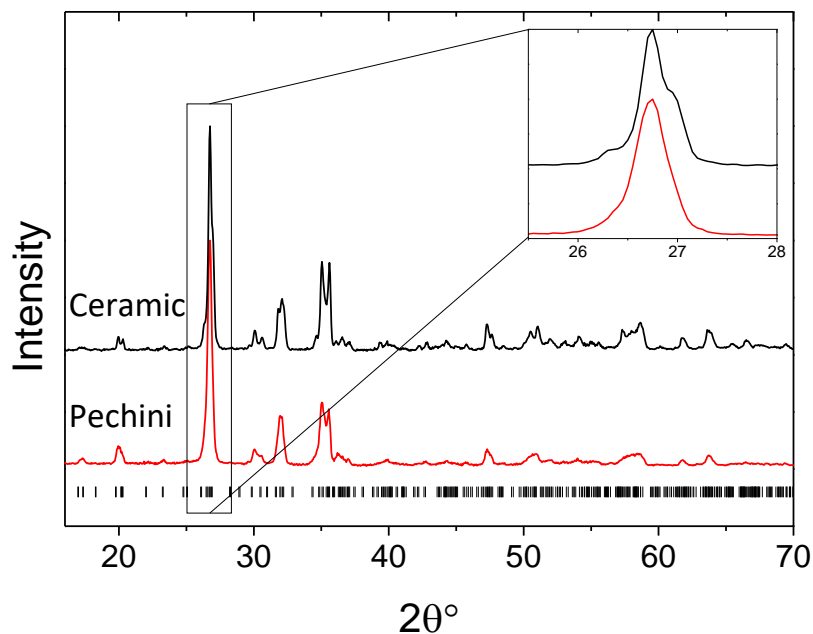


Figure B.1: Powder X-ray diffraction patterns for $\text{Zn}_2\text{Ni}_{0.5}\text{VMoO}_8$. hkl tick marks (black) are shown for allowed reflections for $Pnma$. Inset figure displays the peak broadening associated with the smaller particle size (resulting from the citrate gel method).

B.2 Photocatalytic Activity of $\text{Zn}_{2-x}\text{A}_x\text{VMoO}_8$ and $\text{Li}_3\text{CrMo}_3\text{O}_{12}$

As mentioned in Chapter 2.3.4, photocatalysis is an attractive physical property, as it can be used to degrade harmful organic compounds. In these experiments, methylene blue (MB) was used as a model compound, and standardization was performed with samples of Degussa P25 TiO_2 .

An entire experiment with only MB in the reaction vessel was performed as a control (Fig. B.2). Plotting the absorbance values at λ_{max} against time t reveals

the degradation of MB without the influence of a photocatalyst (Fig. B.3). In these experiments, λ_{\max} was determined to be roughly 665 nm. Over several trials, the average degradation was determined to be $11.5 \pm 0.7\%$ over 2 h. This agrees well to established literature values [4], and this value was applied as a subtractive photolysis correction to all future degradation values. An adsorption correction was not applied to any of the experiments, as this value is typically quite small for powders synthesized by the ceramic method.

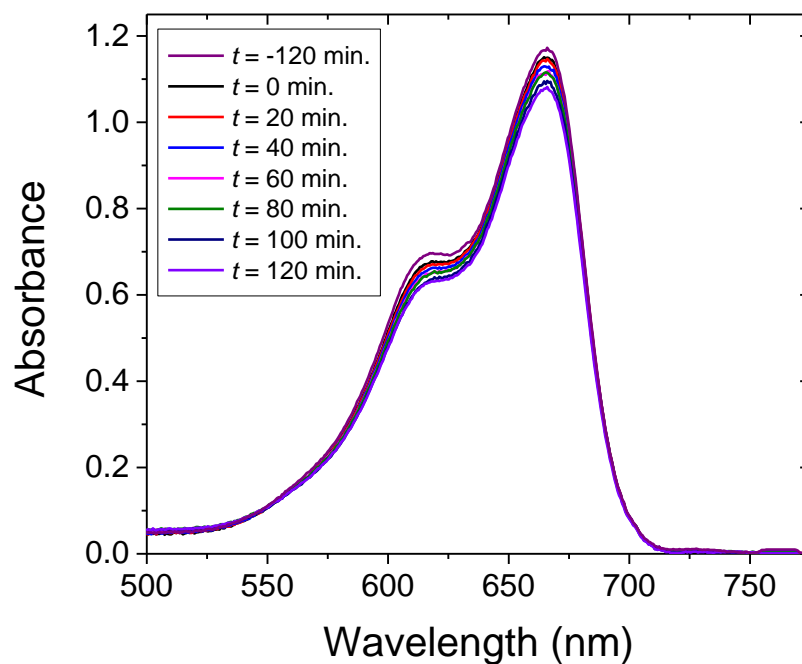


Figure B.2: UV-vis absorbance spectra for MB after 2 h irradiation time (truncated for λ_{\max}).

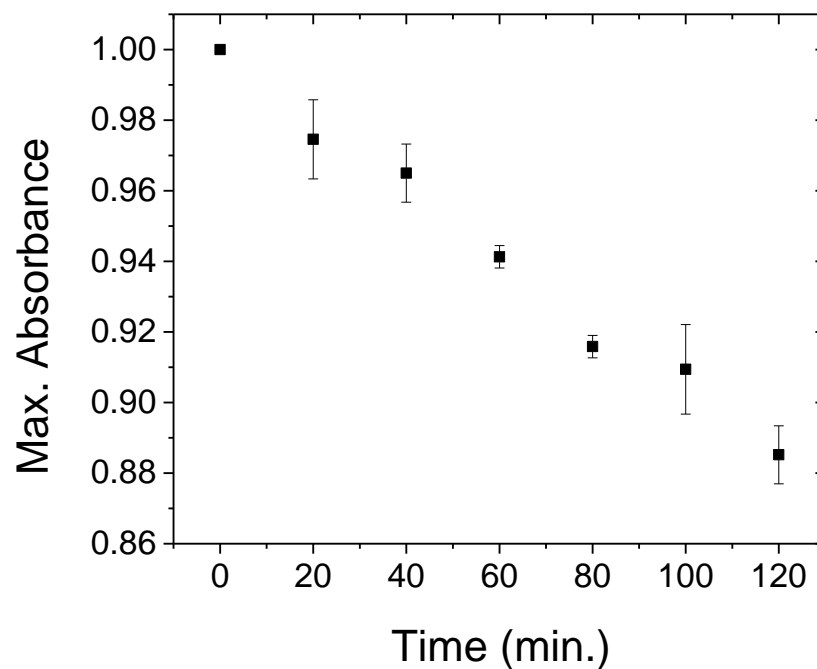


Figure B.3: Average degradation plot for MB over 2 h irradiation time.

The next control experiment involved adding the well-known TiO_2 photocatalyst to the solution of MB; this was done to ensure that the experimental setup was robust and that reproducibility could be achieved. Under ideal conditions, at 155 mW irradiation for 2 h, a 2.0×10^{-5} M solution of MB should completely degrade in the presence of TiO_2 . In this control experiment, the solution of MB had degraded by 97.9 %, confirming the validity of the setup (Fig. B.4).

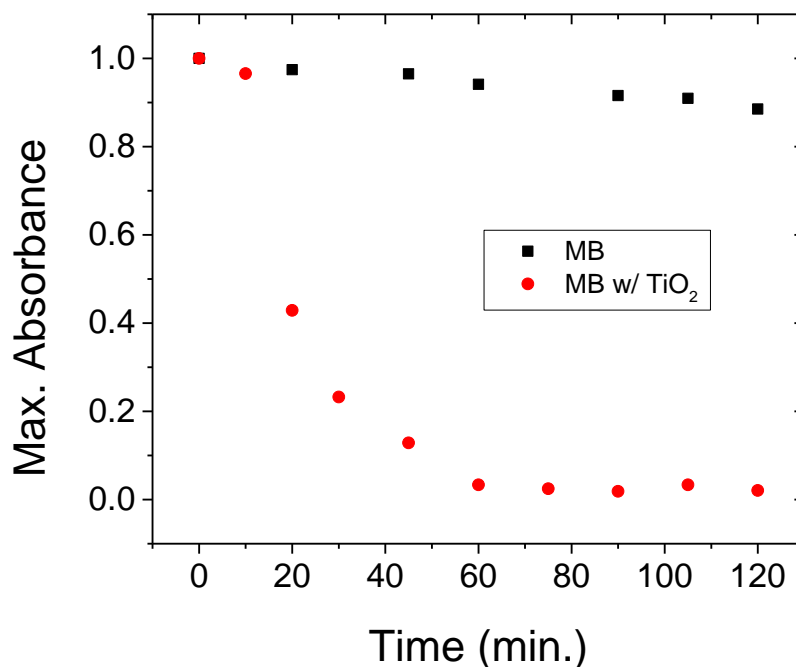


Figure B.4: Degradation plot comparison for MB-only (black) and MB loaded with TiO₂ (red) over 2 h irradiation time.

Powders of Zn₂Cu_{0.5}VMoO₈ and Zn₂Ni_{0.5}VMoO₈ were prepared by solid state reaction, as detailed in Chapter 4. Experiments were performed for both samples (Fig. B.5,B.6). X-ray diffraction analysis was performed before and after photocatalysis experiments to check for retention of phase purity.

Both samples displayed little to no photocatalytic activity, which was surprising, given the Zn-rich parent compound's known photocatalytic activity for O₂ evolution under visible light [5]. Considering that the optical band gap of a material decreases with increasing particle size, it is possible that the hand-ground powders formed by the ceramic method are inappropriate for this experiment, as the decreased band gap energy could promote exciton recombination before reaction can occur.

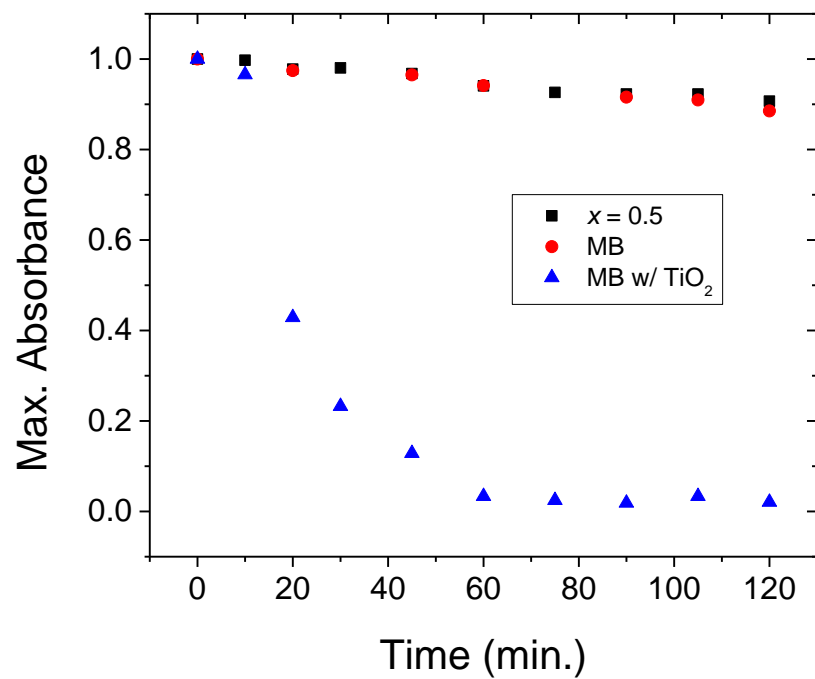


Figure B.5: Degradation plot comparison for $\text{Zn}_2\text{Cu}_{0.5}\text{VMoO}_8$ (black), MB-only (red), and MB loaded with TiO_2 (blue) over 2 h irradiation time.

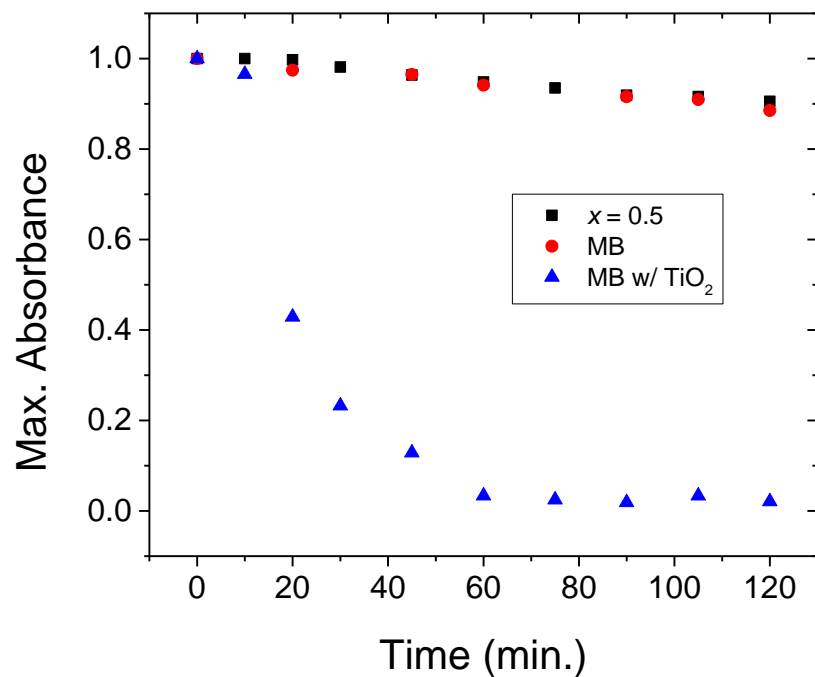


Figure B.6: Degradation plot comparison for $\text{Zn}_{12}\text{Ni}_{0.5}\text{VMoO}_8$ (black), MB-only (red), and MB loaded with TiO_2 (blue) over 2 h irradiation time.

A side experiment was attempted on the known molybdate $\text{Li}_3\text{CrMo}_3\text{O}_{12}$, as the solid solution $\text{Li}_3\text{Fe}_{1-x}\text{Cr}_x(\text{MoO}_4)_3$ was shown to adsorb MB well [6], but no photocatalytic activity was reported. The bandstructure for this compound also differs from the previous two samples, as the bottom of the conduction band is not influenced by the presence of V. The post-correction degradation is determined to be 5%.

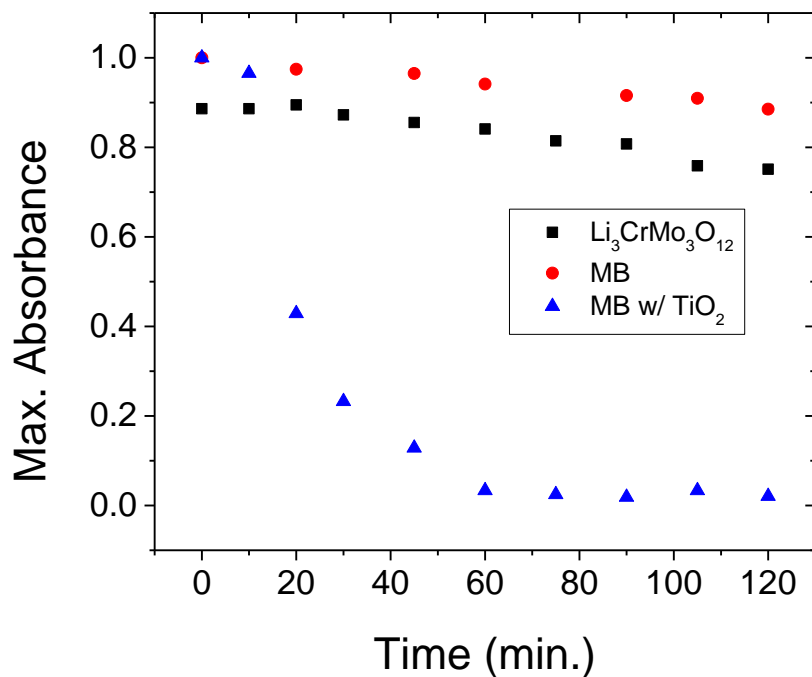


Figure B.7: Degradation plot comparison for $\text{Li}_3\text{CrMo}_3\text{O}_{12}$ (black), MB-only (red), and MB loaded with TiO_2 (blue) over 2 h irradiation time.

B.3 Reactivity of $\text{Li}_3\text{Ti}_{0.75}\text{Mo}_3\text{O}_{12}$ with Methylene Blue

With the previous results in mind, another side experiment was performed, in which the recently synthesized molybdate $\text{Li}_3\text{Ti}_{0.75}(\text{MoO}_4)_3$ was subjected to testing. The choice of compound was made because complex titanates have a history of being photocatalytically active [4], and this is the only Ti-substituted lyonsite with published detailed structural information [7]. The sample was subjected to the same experimental design, and the MB absorbance results were startling (Fig. B.8).

The absorbance at λ_{max} (664.69 nm) drops precipitously, even before irradiation.

Corresponding to this trend is a similar trend around 300 nm, and an opposite trend around 231.36 nm. The degradation plot was compared to TiO_2 (Fig. B.9), but the behavior was markedly different. For TiO_2 , adsorption was a minimal factor in the 2 h prior to irradiation, and upon irradiation, the degradation of MB is exponential. In contrast, MB loaded with $\text{Li}_3\text{Ti}_{0.75}(\text{MoO}_4)_3$ exhibited minimal degradation upon irradiation. If anything, the degradation occurred primarily in the dark, which suggests a non-photo-initiated reaction. The drop in absorbance corresponds to an increase in the 231.36 nm peak. Comparatively, the degradation of MB loaded with TiO_2 is known to be proportionate; the behavior of this sample, though, suggests that intermediate products were formed, and incomplete degradation occurred. These less-conjugated aromatic metabolites are likely responsible for the absorbance increase at 231.36 nm.

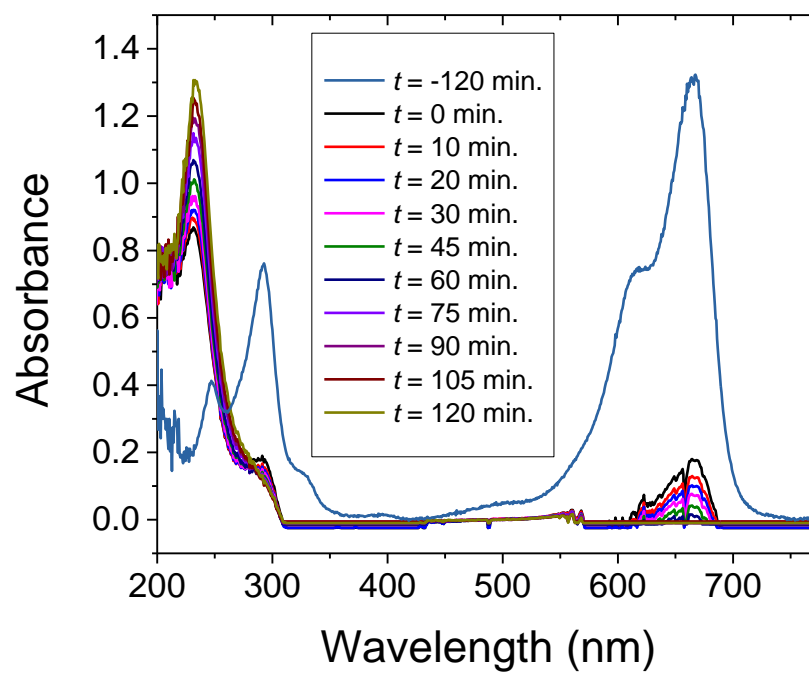


Figure B.8: UV-vis absorbance spectra for MB loaded with $\text{Li}_3\text{Ti}_{0.75}\text{Mo}_3\text{O}_{12}$ after 2 h irradiation time. Also shown is the initial absorbance taken prior to the 2 h dark phase (labeled as $t = -120$ min.).

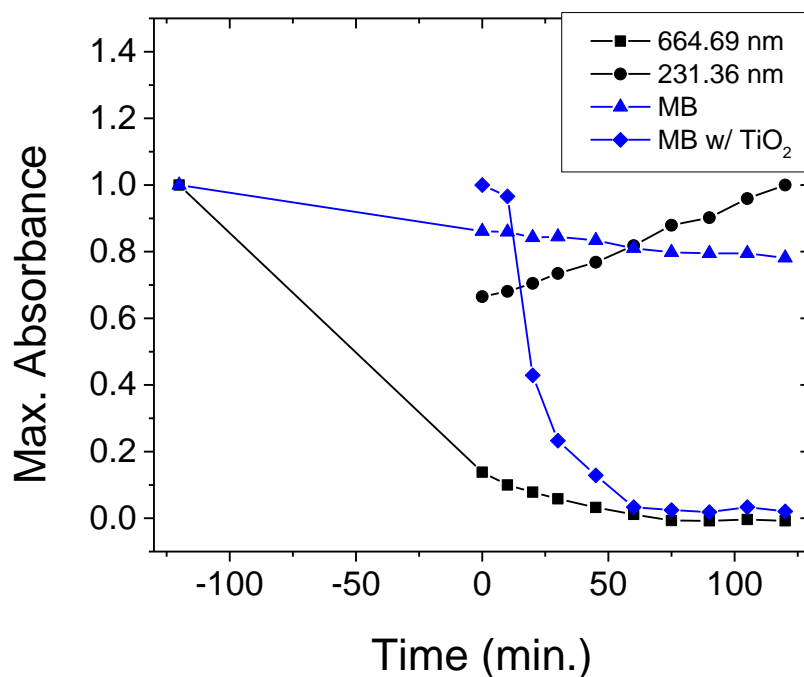


Figure B.9: .Degradation plot comparison for MB-only (blue triangles), MB loaded with TiO₂ (blue diamonds), and MB loaded with Li₃Ti_{0.75}Mo₃O₁₂ measured at two wavelengths, over 2 h irradiation time. Also shown is the initial absorbance taken prior to the 2 h dark phase (labeled as $x = -120$ min.).

The powder diffraction data collected before the experiment confirmed phase purity (Fig. B.10); however, the post-experiment XRD pattern revealed a complete degradation of the sample as well. An amorphous, multiphase mixture resulted, suggesting that this compound does not act as a photocatalyst, but participates as a reactant. The cause of this behavior is unknown at the time of writing.

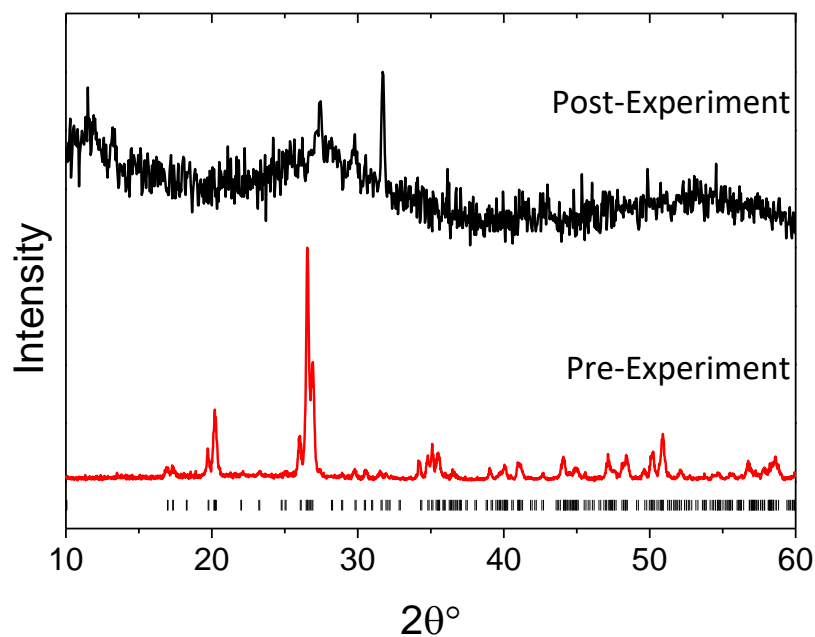


Figure B.10: Powder X-ray diffraction patterns for $\text{Li}_3\text{Ti}_{0.75}\text{Mo}_3\text{O}_{12}$. hkl tick marks (black) are shown for allowed reflections for $Pnma$.

B.4 Conclusions

An alternative low-temperature synthesis method was shown to be applicable for lyonsite oxides. The photocatalytic activity is highly dependent on the composition, suggesting that the tunneled nature of the crystal structure has no inherent effect. The differing activities correspond to compositional differences. Bandstructure calculations would be integral to a more complete understanding of this behavior. Because particle size and surface area also impact activity, adsorption analyses would also be valuable.

Bibliography

- [1] S. A. Corr, R. Seshadri, 4.01 - Synthetic Methodologies, in: *Comprehensive Inorganic Chemistry II (Second Edition)*, Elsevier, Amsterdam, 2013, pp. 1–15. doi:10.1016/B978-0-08-097774-4.00401-0.
- [2] A. R. West, *Solid State Chemistry and its Applications*, 2nd Edition, Student Edition, Wiley, Chichester, 2014.
- [3] J. P. Smit, P. C. Stair, K. R. Poeppelmeier, The adaptable lyonsite structure, *Chem. Eur. J.* 12 (2006) 5944–5953. doi:10.1002/chem.200600294.
- [4] M. Kaneko, I. Okura, *Photocatalysis: Science and Technology*, Springer, 2003.
- [5] X. Wang, K. R. Heier, C. L. Stern, K. R. Poeppelmeier, Crystal structure of $\text{Zn}_{3.77}\text{V}_{1.54}\text{Mo}_{1.46}\text{O}_{12}$ containing ZnO_6 trigonal prisms, *J. Alloys Compd.* 255 (1997) 190–194. doi:10.1016/S0925-8388(96)02812-5.
- [6] K. Gourai, A. El Bouari, B. Belhorma, L. Bih, Adsorption of methylene blue on the $\text{Li}_3\text{Fe}_{1-x}\text{Cr}_x(\text{MoO}_4)_3$ ($x=0,0.5,1$) lyonsite phases, *Am. J. Chem.* 6 (2016) 47–54. doi:10.5923/j.chemistry.20160602.04.
- [7] J. P. Smit, T. M. McDonald, K. R. Poeppelmeier, $\text{Li}_3\text{Ti}_{0.75}(\text{MoO}_4)_3$: A lyonsite-type oxide, *Solid State Sci.* 10 (2008) 396–400.

Appendix C: A Rudimentary Standalone Dielectric Density Calculator

C.1 Overview

As discussed in Chapter 2.3.3 and 5.4.4, dielectric constant measurements require well-sintered samples (>75 %), as air pockets can contribute to loss. This percentage is a ratio of the physical, experimental density to a theoretical density, which assumes 100 % density. The physical density is determined by the experimenter, using an appropriate method (balance and calipers, pycnometry, Archimedes method). The theoretical bulk crystal density is determined by the standard density equation, adjusted to the scale of a unit cell [1],

$$\rho = \frac{Z \times \text{MW}}{V \times N} \quad (\text{C.1})$$

in which Z is the number of atoms in the unit cell, MW is the molecular weight, N is the Avogadro constant, and V is the unit cell volume [2], expressed as

$$V = abc\sqrt{1 - \cos^2 \alpha - \cos^2 \beta - \cos^2 \gamma + 2 \cos \alpha \cos \beta \cos \gamma} \quad (\text{C.2})$$

This calculation, while simple, can be laborious and error-prone when done by hand, especially for multiple samples. The goal, then, was to quicken calculations by providing a simple standalone executable that accepts basic information and outputs

the density ratio. This project was successful, and the tool was christened "TangCalc".

C.2 Development Details

The general idea for this calculator is shown (Fig. C.1). Ideally, the program accepts a handful of parameters that are obtained from lattice refinements and sample dimensions. It should be able to parse chemical formulas, so a dictionary of the elements and their respective atomic masses was required. To simplify the code and increase future flexibility, all mathematical functions were collected into a module to be called upon by the main script or future scripts that may require them.

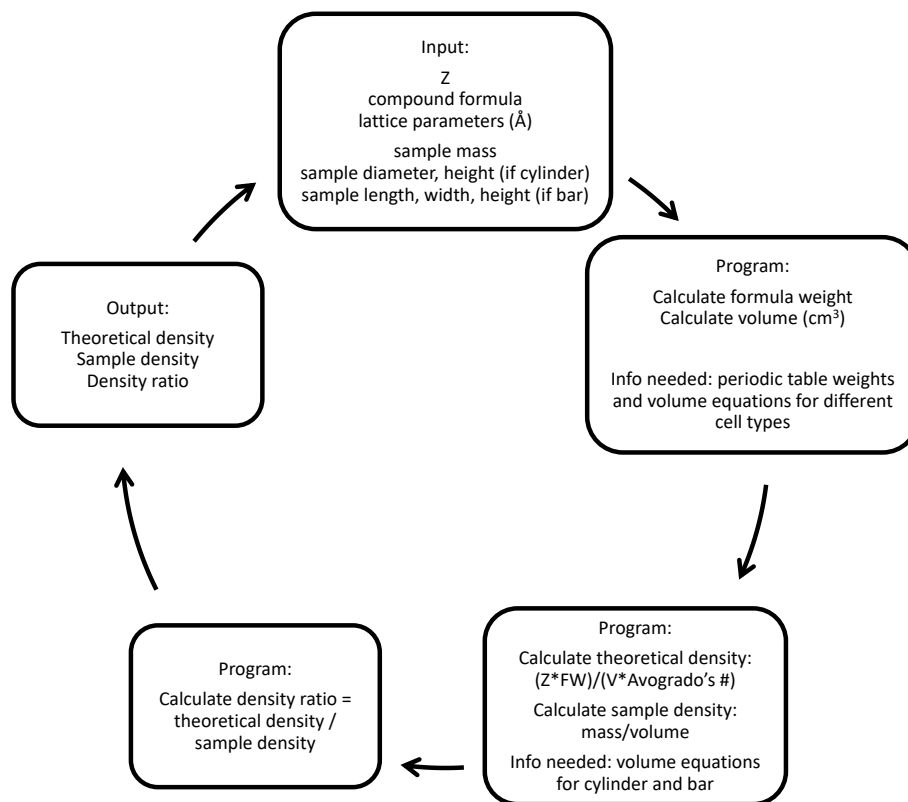


Figure C.1: General workflow for the proposed program.

The code itself was written in Python, and was wrapped in an EasyGUI-based interface. The Python script was then converted into a Windows executable via py2exe.

To increase the robustness of the script, several challenges had to be addressed, including the program's ability to: accept non-integer stoichiometries (as is common in solid state chemistry), calculate cell volumes with absurd angles (due to the volume equation containing trigonometric functions), and calculate divisions over absurd denominators and not consider it a division by 0.

These issues were all resolved with test cases and subsequent modifications to the script. A general flowchart of the running program is displayed (Fig. C.2). After the calculation is complete, the user is prompted to either do another calculation (which will lead to step 1 again) or exit the program. The final results window displays the formula weight, theoretical and experimental densities, and the density ratio. The entered parameters are also logged in the background window, along with a congratulatory message to encourage the researcher.

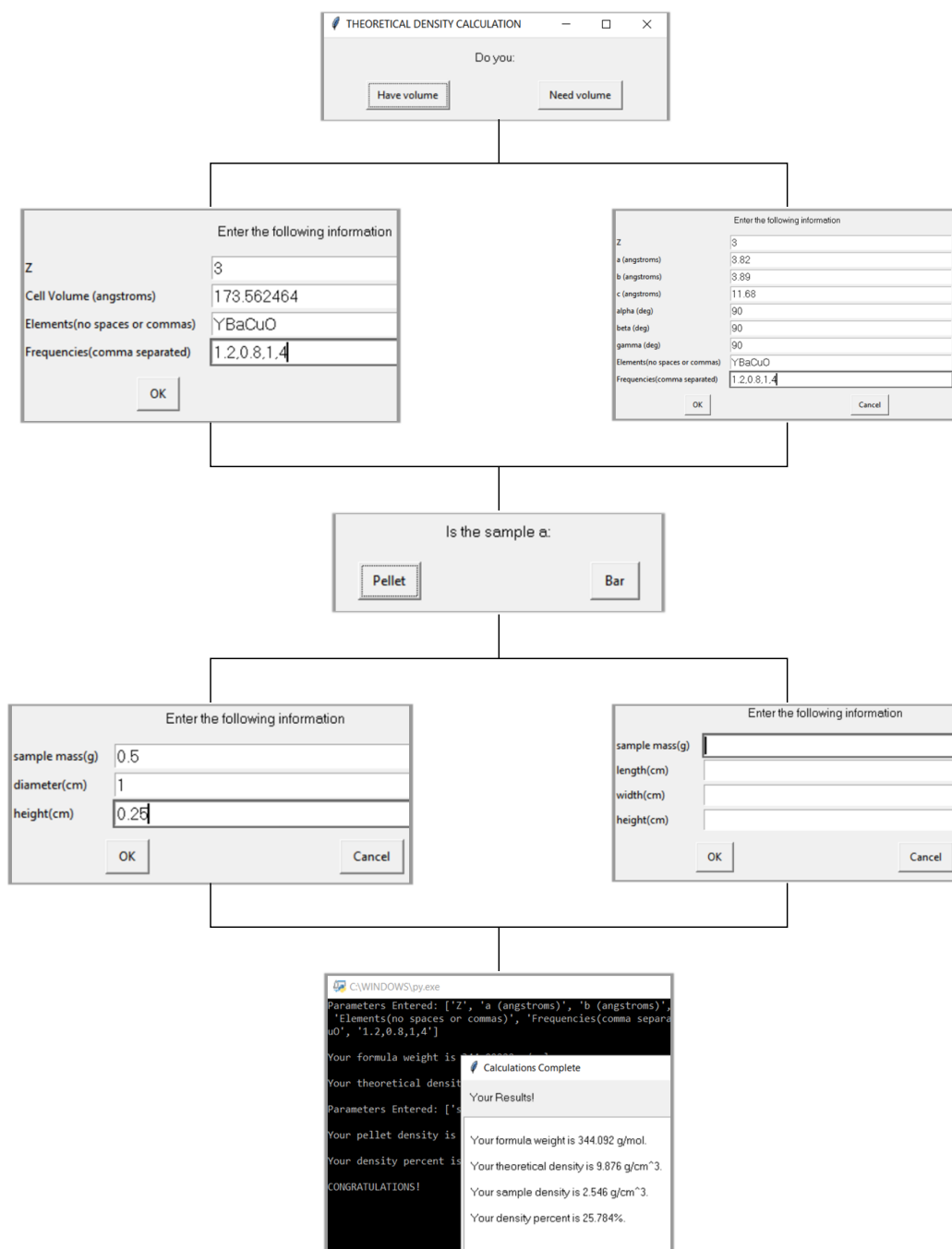


Figure C.2: General workflow for the running program.

C.3 Pseudocode

```

1  #!/usr/bin/python
2
3  print greeting
4  import math
5
6  #### --- Part 1: Theoretical Density --- ####
7
8  compd = user inputs the compound name
9  z = user inputs the number of atoms in cell
10 latta = user inputs lattice parameter a in angstroms
11 lattb = user inputs lattice parameter b in angstroms
12 lattc = user inputs lattice parameter c in angstroms
13 lalph = user inputs lattice parameter alpha in angstroms
14 lbeta = user inputs lattice parameter beta in angstroms
15 lgamm = user inputs lattice parameter gamma in angstroms
16
17 part1output = []
18 ##calculate formula weight from database .txt. Will involve
19   → addition/multiplication
20 ##convert angstroms to cm
21
22 ##cellvolume =
23   → latta*lattb*lattc*sqrt(1-cos^2(lalph)-cos^2(lbeta)-cos^2(lgamm)+2cos(lalph)
24   → cos(lbeta)cos(lgamm))
25 ##make sure in degrees, not radians
26
27
28 ##density = (z * formulaweight) / (cellvolume * avogadro)
29 ##append answer to part1output
30
31
32 #### --- Part 2: Sample Density --- ####
33
34 ms = user inputs mass of sample
35
36 whatsample = user chooses either (1) for pellet or (2) for bar
37
38 cylbar = assign whatsample as an integer

```

```
34 part2output = []
35 if cylbar==1:
36     diam = user inputs diameter of pellet in cm
37     height = user inputs height of the pellet in cm
38
39     radius = diam / 2
40     volume = math.pi * radius * radius * height
41
42     density = ms / volume
43     print density
44     append density to output
45 else:
46     length = user inputs length of bar in cm
47     width = user inputs in cm
48     height = user inputs in cm
49
50     volume = length * width * height
51
52     density = ms / volume
53     print density
54     append density to output
55
56     #### --- Part 3: Density Percent --- ####
57
58
59 percent = part1output / part2output
60 print percent
```

C.4 Main Code

```

1  #!/usr/bin/python
2
3  from TangModule import *
4  from easygui import *
5  import sys
6
7  loop = 1
8  msgbox ("SOLID SAMPLE DENSITY CALCULATOR - working
   ↪  model",title="TangCalc",ok_button="Let's Begin")
9  while loop == 1:
10
11
12     #### --- Part 1: Theoretical Density --- ####
13     """theoretical density = (z * formula weight) / (cell volume * avogadro's
   ↪ num)"""
14
15     message = "Do you:"
16     title = "THEORETICAL DENSITY CALCULATION"
17     if boolbox(message, title, ["Have volume", "Need volume"]):
18         msg = "Enter the following information"
19         title = ""
20         fieldNames = ["Z","Cell Volume (angstroms)","Elements(no spaces or
   ↪  commas)","Frequencies(comma separated)"]
21         fieldValues = []
22         fieldValues = multenterbox(msg,title,fieldNames)
23
24     while 1:     #for error checking
25         if fieldValues == None: break
26         errmsg = ""
27         for i in range(len(fieldNames)):
28             if fieldValues[i].strip() == "":
29                 errmsg = errmsg + ('"%s" is a required field.\n\n' %
   ↪  fieldNames[i])
30         if errmsg == "": break # no problems found
31         fieldValues = multenterbox(errmsg, title, fieldNames, fieldValues)
32     print ("Parameters Entered:", fieldNames,fieldValues)

```

```

33
34     z = fieldValues[0]
35     cellvol = (float(fieldValues[1]) * 1e-24)    #convert to cm^3
36     coeff = "1"
37     atoms = fieldValues[2]
38     freq = fieldValues[3]
39     fw = getfw(coeff, atoms, freq)             #get formula weight
40     print ('\n' + "Your formula weight is " + str(fw) + " g/mol.")
41
42     else:
43         msg = "Enter the following information"
44         title = "THEORETICAL DENSITY CALCULATION"
45         fieldNames = ["Z", "a (angstroms)", "b (angstroms)", "c (angstroms)", "alpha
46         ↪ (deg)", "beta (deg)", "gamma (deg)", "Elements(no spaces or
47         ↪ commas)", "Frequencies(comma separated)"]
48         fieldValues = []
49         fieldValues = multenterbox(msg, title, fieldNames)
50
51         while 1:    #for error checking
52             if fieldValues == None: break
53             errmsg = ""
54             for i in range(len(fieldNames)):
55                 if fieldValues[i].strip() == "":
56                     errmsg = errmsg + ("%s" is a required field.\n\n' %
57                     ↪ fieldNames[i])
58                 if errmsg == "": break # no problems found
59                 fieldValues = multenterbox(errmsg, title, fieldNames, fieldValues)
60         print ("Parameters Entered:", fieldNames, fieldValues)
61
62         z = fieldValues[0]
63         lp = [fieldValues[1], fieldValues[2], fieldValues[3], fieldValues[4],
64         ↪ fieldValues[5], fieldValues[6]]
65         cellvol = getcellvol(lp)
66         coeff = "1"
67         atoms = fieldValues[7]
68         freq = fieldValues[8]
69         fw = getfw(coeff, atoms, freq)             #get formula weight
70         print ('\n' + "Your formula weight is " + str(fw) + " g/mol.")

```

```

67
68 part1output = []
69 tdens = gettdens(z,fw,cellvol)      #get theoretical density
70 print ('\n' + "Your theoretical density is " + str(tdens) + " g/cm^3." +
    ↪ '\n')
71 part1output.append(tdens)
72
73
74 ### --- Part 2: Sample Density --- ###
75 """density = mass / volume """
76
77 part2output = []
78 message="Is the sample a:"
79 title="SAMPLE DENSITY CALCULATION"
80 if boolbox(message, title, ["Pellet", "Bar"]):
81     msg = "Enter the following information"
82     title = ""
83     fieldNames = ["sample mass(g)", "diameter(cm)", "height(cm)"]
84     fieldValues = []
85     fieldValues = multenterbox(msg,title,fieldNames)
86
87     while 1:      #for error checking
88         if fieldValues == None: break
89         errmsg = ""
90         for i in range(len(fieldNames)):
91             if fieldValues[i].strip() == "":
92                 errmsg = errmsg + ('"%s" is a required field.\n\n' %
    ↪ fieldNames[i])
93             if errmsg == "": break # no problems found
94         fieldValues = multenterbox(errmsg, title, fieldNames, fieldValues)
95     print ("Parameters Entered:", fieldNames,fieldValues)
96
97     ms=fieldValues[0]
98     cdiam=fieldValues[1]
99     cheight=fieldValues[2]
100    cdens = getcyldens(ms,cdiam,cheight)      #pellets are cylinders; get
    ↪ density of pellet

```

```

101     print ('\n' + "Your pellet density is " + str(cdens) + " g/cm^3." +
102           ↪ '\n')
103     part2output.append(cdens)
104
105     else:
106         msg = "Enter the following information"
107         title = ""
108         fieldNames = ["sample mass(g)", "length(cm)", "width(cm)", "height(cm)"]
109         fieldValues = []
110         fieldValues = multenterbox(msg, title, fieldNames)
111
112         while 1:     #for error checking
113             if fieldValues == None: break
114             errmsg = ""
115             for i in range(len(fieldNames)):
116                 if fieldValues[i].strip() == "":
117                     errmsg = errmsg + ("%s" is a required field.\n\n' %
118                                       ↪ fieldNames[i])
119                 if errmsg == "": break # no problems found
120             fieldValues = multenterbox(errmsg, title, fieldNames, fieldValues)
121             print ("Parameters Entered:", fieldNames, fieldValues)
122
123             ms=fieldValues[0]
124             blength=fieldValues[1]
125             bwidth=fieldValues[2]
126             bheight=fieldValues[3]
127             bdens = getbardens(ms, blength, bwidth, bheight)     #get density of bar
128             print ('\n' + "Your bar density is " + str(bdens) + " g/cm^3." + '\n')
129             part2output.append(bdens)
130
131             ##### --- Part 3: Density Percent --- #####
132             percent = float(part2output[0]) / float(part1output[0]) *100     #taking
133             ↪ density percentage
134             print ("Your density percent is " + str(percent) + "%" + '\n')
135             print ("CONGRATULATIONS!")
136
137             resultsmg="Your Results!"
138             title="Calculations Complete"

```

```
136 text='\n' + "Your formula weight is " + str(round(fw,3)) + " g/mol." + '\n'
    ↪ + '\n' + "Your theoretical density is " + str(round(tdens,3)) + "
    ↪ g/cm^3." + '\n' + '\n' + "Your sample density is " +
    ↪ str(round(part2output[0],3)) + " g/cm^3." + '\n' + '\n' + "Your density
    ↪ percent is " + str(round(percent,3))+ "%." + '\n'
137 textbox(resultsmg,title,text,codebox=0)
138
139 if ynbox(msg="Would you like to do another calculation?"):
140     pass
141 else:
142     sys.exit(0)
```

C.5 Functions Module

```

1  #!/usr/bin/python
2  from math import *
3  import re
4
5  ###---Create element:mass dictionary from periodic table file---###
6  ptable = {}
7  with open("element_mass.txt") as a:
8      for line in a:
9          (key, val) = line.split()           #split every line into
           ↪ [element,weight]
10         ptable[(key)] = float(val)         #define database dictionary as
           ↪ {element:weight}
11
12 ###---Calculate formula weight---###
13 def getfw(coeff,atoms,freq):
14     coefficient = 1
15     if coeff.isdigit() == True:
16         coefficient = float(coeff)         #if user input is a
           ↪ digit, reassign coefficient to that digit
17     s1 = re.findall('[A-Z][a-z]*', atoms)   #parse inputted
           ↪ elements into list
18     s2 = re.findall('[-]*[0-9]*[.]*[0-9]+', freq) #parse inputted
           ↪ frequencies into list
19     atomfreq = {s1[i]: s2[i] for i in range(len(s1))} #define dictionary
           ↪ as {element:frequency}
20     allweight = []
21     for key in atomfreq:
22         if key in ptable:
23             eachweight = float(atomfreq[key]) * float(ptable[key]) #if
                ↪ element match in database, multiply frequency by weight
24             allweight.append(eachweight)
25     totalweight = sum(allweight) * coefficient #sum
           ↪ each element's final weight, then multiply by coefficient
26     return totalweight
27
28 ###---Calculate cell volume---###

```

```

29 def getcellvol(lp):
30     for i,x in enumerate(lp):
31         if i < 3:
32             atocm = float(x) * 1e-8           #convert first 3 entries from
33             ↪ angstroms to cm
34             lp[i] = float(atocm)             #reassign those indices' values
35             ↪ as cm values
36         else:
37             degtorad = radians(float(x))     #convert last 3 entries from
38             ↪ degrees to radians
39             lp[i] = float(degtorad)         #reassign last 3 indices as
40             ↪ radian values, since math defaults to radians
41     try:
42         cellvol =
43         ↪ lp[0]*lp[1]*lp[2]*sqrt(1-cos(lp[3])**2-cos(lp[4])**2-cos(lp[5])**2+
44         ↪ 2*cos(lp[3])*cos(lp[4])*cos(lp[5]))
45     return cellvol
46 except ValueError:                          #caused by sqrt(negative).
47     ↪ example: if angles were 120,130,140
48     print ('\n' + "Lattice angles not reasonable. You are a terrible person.
49     ↪ ctrl+c to terminate, then try again." + '\n')
50
51 ###---Calculate theoretical density---###
52 def gettdens(z,fw,cellvol):
53     try:
54         tdens = (float(z) * float(fw)) / (float(cellvol) * 6.0221e23)
55         return tdens
56     except ZeroDivisionError:                #caused by cellvol=0. example:
57         ↪ if angles were 1,2,3
58         print ('\n' + "Lattice angles not reasonable. You are a terrible person.
59         ↪ ctrl+c to terminate, then try again." + '\n')
60
61 ###---Calculate cylinder density---###
62 def getcyl dens(ms,cdiam,cheight):
63     crad = float(cdiam) / 2                 #convert diameter to radius
64     cv = pi * float(crad)**2 * float(cheight) #calc volume of cylinder
65     cp = float(ms) / float(cv)
66     return cp

```

```
57  
58 ###---Calculate bar density---###  
59 def getbardens(ms,blength,bwidth,bheight):  
60     bv = float(blenght) * float(bwidth) * float(bheight)    #calc volume of  
        ↪ bar  
61     bp = float(ms) / float(bv)  
62     return bp
```

Bibliography

- [1] A. R. West, Solid State Chemistry and its Applications, 2nd Edition, Student Edition, Wiley, Chichester, 2014.
- [2] B. D. Cullity, S. R. Stock, Elements of X-Ray Diffraction, 3rd ed., Pearson, New Jersey, 2001.

